

THE UNIVERSITY OF HULL

**Hydrodynamic and control optimization for a
heaving point absorber wave energy converter**

A thesis submitted in partial fulfillment for the
degree of Doctor of Philosophy

by

Siya Jin

in the

School of Engineering and Computer Science

May 2019

Acknowledgements

My deepest thanks are expressed firstly to my major supervisor, Prof. Ron J. Patton of Control and Intelligent Systems Engineering (C&ISE) at University of Hull (UoH). Without his help and guidance, I have no opportunity to obtain the joint scholarship from Chinese Scholarship Council and UoH to support the PhD program. It is Prof. Ron Patton's passionate devotion to renewable marine energy and solid knowledge of this field spark my interest in pursuing academic career in this field. Prof. Ron Patton gives plenty of supports in offering experimental experience, which helps a lot to deeply understand the mechanism of wave energy conversion. Additionally, he offers lots of opportunities for me to attend international conferences and workshops which help me to build the network in this field. Without his kind help and rigorous scientific attitude, I have no opportunity to publish high quality journal papers. I will be forever indebted to Prof. Ron J. Patton for supporting this meaningful PhD research.

Sincere thanks are also expressed to my second supervisor, Professor Jim Gilbert, for the helpful meetings and discussions. Many thanks are due to Dr. Stuart McLelland and Mr. Brendan Murphy of School of Environmental Sciences for supervising the use of the wave tank at UoH. I would like to thank Chris Collins of the high performance computer (HPC) manager at UoH for supervising the use of HPC. I would like to thank all the lovely friends at C&ISE: Jianglin Lan, Bingyong Guo, Zhihuo Wang, Yan Hua, Chun Liu, Shuo Shi and Mustafa Abdelrahman.

Last but not the least, I would like to thank my husband Yang Qin for being with me through the good and bad times. It is your love and support make me never feel upset with difficulties. Finally, thanks for the coming of the little baby Zhan Qin. Your smile is the most beautiful thing I have ever seen.

Abstract

The thesis aims at studying the non-linear performance of a designed 1/50 scale point absorber wave energy converter (PAWEC) in heave motion. In particular, designs of the PAWEC geometry and control strategy are considered to optimize the power capture. Experimental and computational fluid dynamics (CFD) data are provided to evaluate the studies. Specifically, this thesis can be summarized into four parts.

Firstly, a numerical wave tank (NWT) is constructed in a commercial CFD package ANSYS/LS-DYNA. The main objective associated with the NWT is to closely reproduce the physical wave-PAWEC interactions. To achieve this, physical experimental data from two specified WECs are provided to verify the capability of the NWT. One of the devices is the PAWEC designed at University of Hull. Free decay, excitation force and water splashing tests, etc., are conducted. As a result, the developed NWT is validated to be capable of representing the non-linear behaviors of the PAWEC compared with the costly physical experiments.

The second part focuses on investigating the extent to which the non-linear hydrodynamic characteristics of the PAWEC need to be considered. By comparing with the CFD data from a series of tests, a non-linear mathematical modeling involving a quadratic viscous term is verified. The results show that the non-linear PAWEC behavior for the conditions of large oscillations (e.g., near resonance or at a large wave heights) can only be predicted realistically by considering a correct viscous effect. This study highlights that the linear counterpart derived from potential flow code ANSYS/AQWA fails to describe the PAWEC behavior and would mislead the control strategy and power take-off (PTO) designs. Additionally, the results show that the viscous damping is significantly larger than the inviscid radiation damping for the flat-bottom cylindrical heaving PAWEC.

It is found that the viscous effect can induce clear energy losses during device oscillations which is unwanted for a PAWEC system. Therefore, in the third part, besides the original flat-bottom PAWEC, two streamline-bottom counterparts are proposed to improve the capability of power capture. Free motion tests are conducted in the NWT regarding the three different geometric devices. The results indicate that for the streamlined devices, the added mass and hydrodynamic damping decrease by up to 60% compared with the flat-bottom device. More importantly by simulating PTO system in the NWT, it is found that there exists a clear mutual interaction among the designs of the device geometry and PTO damping. Applying a proper PTO damping to the streamlined PAWEC can prominently improve the optimal power absorption efficiency by up to 70% under both regular and irregular waves, compared with the flat-bottom PAWEC.

Finally, a fuzzy logic control strategy with particle swarm optimization algorithm (PSO-FLC) is implemented on the developed non-linear modeling to adaptively tune the PTO damping for power absorption maximization. The fuzzy rule base is initialized according to the power capture characteristics achieved through the NWT tests. PSO algorithm is then used to search for more efficient rules. It is found that applying a well-designed fuzzy inference system can adaptively tune the PTO damping for power capture optimization in contrast to the passive control with constant PTO damping.

List of Publications

1. **S. Jin**, B. Guo, R. Patton, J. Gilbert, and M. Abdelrahman, "Non-linear analysis of a point absorber wave energy converter," in 2nd International Conference on Offshore Renewable Energy, 2016.
2. **S. Jin**, R. Patton, Geometry influence on hydrodynamic response of a heaving point absorber wave energy converter, in: 12th EWTEC, 2017.
3. B. Guo, R. Patton, **S. Jin**, Identification and validation of excitation force for a heaving point absorber wave energy converter, in: 12th EWTEC, 2017.
4. B. Guo, R. Patton, **S. Jin**, J. Gilbert, D. Parsons, Nonlinear modeling and verification of a heaving point absorber for wave energy conversion, IEEE Trans. Sustain. Energy, 9:453-461, 2018.
5. B. Guo, R. Patton, **S. Jin**, J. Lan, Numerical and experimental studies of excitation force approximations for wave energy conversion, Renew. Energy, 125:877-889, 2018.
6. **S. Jin**, R. Patton, B. Guo, Viscosity effect on a point absorber wave energy converter hydrodynamics validated by simulation and experiment, Renew. Energy, 129(Part A): 500-512, 2018.
7. **S. Jin**, R. Patton, Enhancement of the wave energy absorption efficiency via geometry and power take-off damping tuning, Energy, 169:819-832, 2019.

Contents

Acknowledgements	i
Abstract	i
List of Publications	iv
List of Figures	viii
List of Tables	xvi
Abbreviations	xvii
Symbols	xix
1 Introduction	1
1.1 Background	1
1.2 WEC devices	2
1.3 Challenges and objectives	8
1.4 Outline of the thesis	15
2 Literature Review	19
2.1 Introduction	19
2.2 PAWEC devices	20
2.3 Review of dynamic study of PAWEC devices	24
2.4 Review of control strategies applied on PAWEC systems	29
2.5 Summary	31
3 CFD testing platform validation by experiments	33
3.1 Introduction	33
3.2 Governing equations	34

3.3	CFD model construction	37
3.4	Physical experiments set-up	43
3.5	CFD model validation	45
3.6	Conclusions	53
4	Verification of PAWEC non-linear modeling using CFD data	55
4.1	Introduction	55
4.2	Problem formulation	59
4.3	LSSM design for the 1/50 scale PAWEC	65
4.3.1	State-space model of the radiation force	68
4.3.2	State-space model of the excitation force	70
4.3.3	LSSM of the PAWEC	75
4.4	Non-linear state space model (NSSM) design for the 1/50 scale PAWEC	78
4.5	Verification and validation of the NSSM	82
4.6	Case studies	86
4.6.1	Viscosity effect on PAWEC free decay motion	86
4.6.2	Viscosity effect on wave-PAWEC interaction	89
4.6.2.1	Viscosity influence on the PAWEC amplitude response	89
4.6.2.2	Viscosity influence on the PAWEC phase response	93
4.6.2.3	Viscosity influence on the PAWEC performance under irregular wave	96
4.6.3	Viscosity effect on PAWEC power conversion efficiency	98
4.7	Conclusions	102
5	Power capture enhancement by joint tuning of geometry and power take-off damping	105
5.1	Introduction	105
5.2	Test setup	108
5.2.1	PAWEC geometric configuration	108
5.2.2	PTO damping configuration	110
5.2.3	Wave climate	112
5.3	Results and discussion	114
5.3.1	Geometric effect on hydrodynamic parameters	114
5.3.2	Geometric effect on free motion dynamics	119
5.3.3	Joint effects of geometry and PTO damping on power absorption	124
5.3.3.1	In regular waves	124
5.3.3.2	In irregular waves	134

5.4	Conclusions	137
6	PSO-FLC implementation on PAWEC	141
6.1	Introduction	141
6.2	System structure	143
6.3	Controller design	145
6.3.1	FLC	145
6.3.2	PSO-FLC	150
6.4	Results and discussion	155
6.4.1	By FLC	155
6.4.2	By PSO-FLC	159
6.5	Conclusions	161
7	Conclusion and future work	162
7.1	Introduction	162
7.2	Summary and conclusions	163
7.3	Recommendations for future work	167
A	Half NWT	170
B	Physical and CFD results of Mocean Energy device	172
B.1	Small scale WEC from Mocean Energy Ltd.	172
B.2	Validation via WEC from Mocean Energy Ltd.	173
C	Keyword file for the wave-PAWEC interaction	184
	Bibliography	190

List of Figures

1.1	International development distributions of the marine energy technologies (OES, 2014b).	2
1.2	Main categories of WEC devices and schematic of operation principle. a. Attenuator device. b. Oscillating wave surge converter. c. Oscillating water column. d. Point absorber wave energy converter. e. Bulge wave device. f. Submerged pressure differential device. g. Rotating mass device. h. Over-topping device. The used figures above are from OSU (2013) and Goggle Images.	4
1.3	Different types of WEC devices based on installed location. From left to right, the WEC devices are Masuda' navigation buoy (Henriques et al., 2016b), the Columbia Power Technologies device (Rhinefrank et al., 2010), the Bolt Sea Power device (Sjolte et al., 2013), the Oyster device (Cameron et al., 2010), the Coppe Subsea device (Estefen et al., 2010) and the LIMPET device (Falcão and Henriques, 2016).	7
1.4	Taut winch line used in the WEC device from Bolt Sea Power (Sjolte et al., 2013).	8
1.5	Tidal-powered hydrogen concept generated by EMEC. The figure is from the EMEC website http://www.emec.org.uk	9
1.6	General examples of the PTO simulators used in the laboratory tank tests. a. Orifice type used in OWC devices. b. Mechanical viscous damper or dashpot applied in the NREL two-body PAWEC (Yu et al., 2015). c. Rotary dashpot used in the bottom-hinged pitching point absorber (Flocard and Finnigan, 2012). d. Eddy current brake used in Uppsala buoy (Thomas et al., 2018).	10
1.7	Distribution of the R&D efforts regarding the WEC devices.	10
1.8	1/50 scaled PAWEC and corresponding experimental wave tank at UoH (Jin et al., 2018).	12
1.9	Close-up of the 1/50 scale PAWEC designed at University of Hull	14
1.10	Vortex formation around a flat-bottom buoy during oscillation in regular wave. The figures are from Zang et al. (2018).	14

1.11	Structure of the thesis.	16
2.1	Representative PAWEC developers. The used figures are from the corresponding websites listed above.	21
2.2	WEC systems developed from Fred Olsen Ltd (http://boltseapower.com/). (a) The large WEC platform, named as FO3. (b) The relatively small dimensional PAWEC. (c) The PAWEC operating in the storm condition.	23
2.3	Advantages and disadvantages of experimental and numerical methods.	28
3.1	A general sketch of the differences between Lagrangian and ALE approaches (Bakroon et al., 2017).	35
3.2	A sketch of the ALE mesh update while wave propagating.	36
3.3	A general sketch of the NWT built in ANSYS/LS-DYNA.	38
3.4	Three representative Ochi spectral distributions used to generate irregular waves. $H_s = 0.1$ m, $\omega_p = 4.83$ rad/s.	41
3.5	A representative sketch of the grid resolution.	41
3.6	(a) Scheme of the experimental platform for the 1/50 scale heaving PAWEC at the UoH. (b) The close-up of the PAWEC device and the employed instruments. (c) The close-up of the connecting elements, e.g., roller bearings.	44
3.7	(a) 3D view of the numerical model built in ANSYS/LS-DYNA. Blue, pink, brown, black and green parts are water, air, sloped beach, PTO system and PAWEC device, respectively. (b) Physical scenario in the laboratory. The cylindrical buoy installed in the centred area is the experimentally tested 1/50 scale PAWEC device.	46
3.8	Mesh convergence validation via the hydrostatic pressure test. The PAWEC is forced to be semi-submerged in still water where its bottom pressure is measured against three different grid sizes in the interaction zone. The theoretical value is 2774 Pa.	47
3.9	Cross-sectional view of the grid solution of 0.01 m in the interaction zone. Green and blue parts are the PAWEC device and adjacent flow, respectively.	48
3.10	(a) Sketch of the relative mesh spacing in the dense and coarse zones. (b) The close-up of the wave profile.	49
3.11	Numerically generated regular wave of $H = 0.073$ m, $\omega = 4.83$ s via the CFD model.	49
3.12	Numerically generated irregular wave of $H_s = 0.1$ m and $\omega_p = 4.83$ rad/s and $r = 8$ via the CFD model.	50

3.13	Time series of normalised displacement for the 1/50 scale cylindrical PAWEC under free decay test. Comparison between CFD and experimental results at an initial released displacement of 0.2 m. EXP = experimental results.	51
3.14	The excitation force modulus imposed on PAWEC against wave frequency at $H = 0.073$ m. Comparison of results from CFD model and experiment. The solid fitting line is plotted for trending reference	52
3.15	RAO versus wave frequency for the 1/50 scale cylindrical PAWEC obtained via CFD and experimental tests at $H = 0.073$ m. The solid fitting lines are plotted for trending references.	53
4.1	A general schematic of the 1/50 scale PAWEC system. (a) Conventional linear analogue of the wave-PAWEC interaction. (b) Developed non-linear analogue of the wave-PAWEC interaction. The non-linear viscous factor f_v is identified by the CFD data in this work.	56
4.2	Added mass $m(\omega)$, inviscid radiation damping $B_{inv}(\omega)$ and hydrostatic stiffness K_s of the 1/50 scale PAWEC achieved from BEM software ANSYS/AQWA. Hence, $M_t = 26.28$ kg.	65
4.3	Modulus \hat{F}_e and phase angle $\varphi(\omega)$ of the complex excitation force coefficient $\hat{F}_e(i\omega)$ for the 1/50 scale PAWEC achieved from BEM software ANSYS/AQWA.	66
4.4	IRF of the wave radiation force for the 1/50 scale PAWEC.	67
4.5	IRF of the wave excitation force for the 1/50 scale PAWEC.	67
4.6	Comparisons for the original radiation IRF and the data from the identified 4-order subsystem.	69
4.7	Error of the causalized $k_e(t)$ related to the original data against the causalizing time.	71
4.8	Comparisons of the IRFs from the original excitation force $k_e(t)$, the causalized term with $t_c = 1$ s and the corresponding approximation by the 6-order linear subsystem from Eq. (4.20).	72
4.9	The real wave elevation and the predicted data based on the use of the 50-order AR model at $H_s = 0.01$ m, $\omega_p = 4.83$ rad/s and $r = 0.5$	73
4.10	The real wave elevation and the predicted data based on the use of the 50-order AR model at $H_s = 0.01$ m, $\omega_p = 4.83$ rad/s and $r = 8$	74
4.11	Time series of predicted wave excitation force with and without 1s wave prediction. Wave condition is $H = 0.08$ m and $T = 2$ s.	74
4.12	General Simulink scheme of the LSSM to represent the PAWEC hydrodynamic response with respect to the incident wave.	75
4.13	PAWEC amplitude and phase responses against wave frequency from LSSM.	76

4.14	PAWEC power absorption efficiency against dimensionless PTO damping coefficient for different wave conditions of ω/ω_0 from LSSM, at $H = 0.073$ m. The white point represents the maximum efficiency of 125%. $B_{hyd} = 4.3\text{kg/s}$ is the inviscid radiation damping at ω/ω_0 obtained from Figure 4.2.	77
4.15	General Simulink scheme of the NSSM to represent the PAWEC hydrodynamic response with respect to the incident wave.	79
4.16	Velocity data of the PAWEC device and the adjacent wave within a period under wave condition of $\omega = 3.12$ rad/s, $H = 0.073$ m. (a) Snapshots of the velocity vector distributions. (b) Time series of the corresponding velocities. The device shows synchronous tracking of the evolution of the flow.	81
4.17	Velocity data of the PAWEC device and the adjacent wave within a period under wave condition of $\omega = 4.83$ rad/s, $H = 0.073$ m. (a) Snapshots of the velocity vector distributions. (b) Time series of the corresponding velocities. The device shows to lag behind the flow.	83
4.18	Comparisons of the free decay motions extracted from the numerical methods (e.g., LSSM, NSSM and NWT) and the physical tank test under initial released displacement of $z_0 = 0.2$ m.	84
4.19	Comparisons of the normalised free decay motions obtained from the numerical methods (e.g., LSSM, NSSM and NWT) and the physical tank test under initial released displacement of $z_0 = 0.2$ and 0.12 m.	88
4.20	Comparisons of the RAO responses under various wave frequencies and wave heights. The data are obtained from the numerical methods (e.g., LSSM, NSSM and CFD) and physical tank test.	90
4.21	Comparisons of the phase responses under various wave frequencies and wave heights. The data are obtained from the numerical methods, e.g., LSSM, NSSM and CFD.	93
4.22	The phase difference (the PAWEC device lags behind the wave) versus wave height at RAO_{\max}	94
4.23	Time series of the velocities of the PAWEC device and the adjacent wave at wave condition of $\omega = 4.91$ rad/s, $H = 0.15$ m.	95
4.24	Time series of the velocities of the PAWEC device and the adjacent wave at wave condition of $\omega = 4.59$ rad/s, $H = 0.15$ m.	96
4.25	The PAWEC displacement with respect to the irregular wave at $H_s = 0.1$ m, $\omega_p = 4.83$ rad/s and $r = 8$	97
4.26	The PAWEC displacement with respect to the irregular wave at $H_s = 0.1$ m, $\omega_p = 4.83$ rad/s and $r = 5$	97

4.27	PAWEC power conversion efficiency against the dimensionless PTO damping coefficient and wave frequency. It should be noted that (i) B_{hyd} is equal to 4.3 Ns/m when the resonance is achieved via linear theory (see Figure. 4.2) and (ii) the marked white point is the maximum conversion efficiency C_{max} . (a) Under $H = 0.073$ m via LSSM; $C_{max} = 125\%$ (b) Under $H = 0.02$ m via NSSM; $C_{max} = 66.6\%$.(c) Under $H = 0.073$ m via NSSM; $C_{max} = 52.5\%$. (d) Under $H = 0.15$ m via NSSM; $C_{max} = 33.5\%$	99
5.1	3D view of the three geometric PAWEC profiles.	109
5.2	Hydrodynamic parameters of the three different geometric PAWEC devices. The data are computed via ANSYS/AQWA.	111
5.3	Impedance and corresponding optimal PTO resistance for passive control for CL device. The data are obtained from linear theory using software ANSYS/AQWA.	112
5.4	Optimal PTO damping against wave frequency for CL, CH and CC devices obtained from linear theory using software ANSYS/AQWA. The results are used to predict optimal PTO damping versus wave frequency for passive control.	113
5.5	The normalised results against the initial displacement of 0.2 m for the three devices under free decay tests.	116
5.6	The amplitude difference against phase difference at troughs and peaks.	116
5.7	The variation of heave RAO against wave frequency for the three geometric devices at $H = 0.073$ m, $B_{PTO} = 0$ kg/s.	120
5.8	Time series of velocities for the three geometric PAWECs and the local water particles at the free surface under $H = 0.073$ m, $\omega = 3.14$ rad/s. Note that PTO system is not involved.	121
5.9	Wave-PAWEC interaction snapshots within a half period at $H = 0.073$ m, $\omega = 4.83$ rad/s. Δz is the displacement excursion from the trough to the peak.	123
5.10	Time series of velocities for the three geometric PAWECs and the local water particles at the free surface under $H = 0.073$ m and $\omega = 4.83$ rad/s. Note that PTO system is not involved.	124
5.11	Velocity data for the CL device and the local water particles at the free surface under $H = 0.073$ m, $\omega/\omega_0 \approx 1$. PTO system is involved.	126
5.12	Velocity data for the CL device and the local water particles at the free surface under $H = 0.073$ m, $\omega/\omega_n = 0.81$. PTO system is involved.	127

5.13	Variation of wave energy conversion efficiency against the PTO damping coefficient under different wave frequencies under $H = 0.073$ m for CL. The solid fitting lines are plotted for trending references.	128
5.14	Variation of wave energy conversion efficiency against the PTO damping coefficient under different wave frequencies under $H = 0.073$ m for CC. The solid fitting lines are plotted for trending references.	128
5.15	Variation of wave energy conversion efficiency against the PTO damping coefficient under different wave frequencies under $H = 0.15$ m for CL. The solid fitting lines are plotted for trending references.	129
5.16	Variation of wave energy conversion efficiency against the PTO damping coefficient under different wave frequencies under $H = 0.15$ m for CC. The solid fitting lines are plotted for trending references.	129
5.17	Optimal PTO damping versus wave frequency for CL and CC devices obtained via CFD analysis. The solid fitting lines are plotted for trending references.	131
5.18	Comparison of the shift in maximum power absorption between CL and CC device as the wave height increases. The zone circled by the black solid line represents the maximum power absorption efficiency.	132
5.19	The variation of the absorption efficiency increase (CC relative to CL) against PTO damping coefficient.	134
5.20	The variation of the absorption efficiency increase (CC relative to CL) against PTO damping coefficient.	135
5.21	Time series of the CL, CC and wave motions under irregular waves of $H_s = 0.1$ m, $\omega_p = 4.83$ rad/s and $r = 8$. $B_{PTO} = 0$ kg/s.	135
5.22	Time series of the CL, CC and wave motions under irregular waves of $H_s = 0.1$ m, $\omega_p = 4.83$ rad/s and $r = 0.5$. $B_{PTO} = 0$ kg/s.	136
5.23	Instantaneous powers of the CL and CC devices under irregular waves of $H_s = 0.1$ m, $\omega_p = 4.83$ rad/s and $r = 8$, respectively. $B_{PTO} = 10$ kg/s.	136
5.24	Instantaneous powers of the CL and CC devices under irregular waves of $H_s = 0.1$ m, $\omega_p = 4.83$ rad/s and $r = 0.5$. $B_{PTO} = 10$ kg/s.	137
5.25	Variation of average power (for 40 s) with PTO damping coefficient under irregular waves of $H_s = 0.1$ m, $\omega_p = 4.83$ rad/s and $r = 0.5, 8$, respectively.	138
6.1	General sketch of the PSO-FLC method applied on the PAWEC.	142
6.2	PAWEC system architecture.	144

6.3	PAWEC FIS structure.	146
6.4	MFs for the inputs and output.	148
6.5	Overall surface description of the designed fuzzy rules for the PAWEC device.	149
6.6	General concept of PSO algorithm for the i^{th} particle. $\vec{X}_i(t)$ and $\vec{X}_i(t + 1)$ represent the current and the updated position for the particle. $\vec{V}_i(t)$ and $\vec{V}_i(t + 1)$ are the corresponding velocities. $\vec{P}_i(t)$ is the best position the particle has achieved so far. $\vec{G}(t)$ represents the global best value achieved so far by the group of particles.	151
6.7	An example of the updated Gaussian MF.	153
6.8	Flow diagram illustrating the PSO-FLC.	154
6.9	Comparison of the absorbed energy with different control methods for wave condition: $H_s = 0.1$ m, $\omega_p = 4.83$ rad/s and $r = 0.5$	156
6.10	Comparison of the absorbed energy with different control methods for wave condition: $H_s = 0.1$ m, $\omega_p = 4.83$ rad/s and $r = 8$	156
6.11	Representative snapshots of the fuzzy rules and corresponding output at different time instant for wave condition: $H_s = 0.1$ m, $\omega_p = 4.83$ rad/s and $r = 8$	157
6.12	Comparison of the PTO damping dynamics with different control methods for wave condition: $H_s = 0.1$ m, $\omega_p = 4.83$ rad/s and $r = 0.5$	158
6.13	Comparison of the PTO damping dynamics with different control methods for wave condition: $H_s = 0.1$ m, $\omega_p = 4.83$ rad/s and $r = 8$	158
6.14	Comparison of the absorbed energy by the use of the FLC and PSO-FLC for wave condition: $H_s = 0.1$ m, $\omega_p = 4.83$ rad/s and $r = 8$	159
6.15	Comparison of the updated FIS by PSO algorithm. Wave condition is $H_s = 0.1$ m, $\omega_p = 4.83$ rad/s and $r = 8$	160
A.1	A half NWT built in the software package ANSYS/LS-DYNA.	170
A.2	Comparison of the simulated PAWEC displacements via full and half NWTs. Wave condition: $H = 0.073$ m, $T = 1.3$ s.	171
B.1	Scheme of the hinged-raft WEC from Mocean Energy Ltd. http://www.moceanenergy.com/	173
B.2	Scheme of the numerical model for the Mocean Energy WEC.	174
B.3	Distribution of the wave gauges in the flume tank for the Mocean Energy WEC test.	174
B.4	Pressure sensor distribution (shown as the black segments) on the device surface.	175

B.5	Comparisons of the wave elevations monitored by WG1 from the NWT and physical tank.	176
B.6	Comparisons of the wave elevations monitored by WG2 from the NWT and physical tank.	176
B.7	Comparisons of the wave elevations monitored by WG3 from the NWT and physical tank.	177
B.8	Comparisons of the surge forces from the NWT and physical tank. .	178
B.9	Comparisons of the heave forces from the NWT and physical tank.	178
B.10	Comparisons of the pitch moments from the NWT and physical tank.	179
B.11	Comparison of the water splashing evolutions from the NWT and physical wave tank at regular wave No.1.	182
B.12	Comparison of the water splashing evolutions from the NWT and physical wave tank at regular wave No.2.	183

List of Tables

3.1	Physical parameters of the 1/50 scale cylindrical heaving PAWEC device at the UoH.	45
4.1	Parameters of the 1/50 PAWEC for the LSSM.	76
4.2	Fit goodness of LSSM/NSSM relative to the CFD results. Note: the value for fitting varies between -Inf (bad fit) to 1 (perfect fit).	85
4.3	The test conditions for different case studies. Abbreviation: EXP = Experiment, SIM = numerical simulations, e.g., LSSM, NSSM and NWT.	87
4.4	Variation of RAO_{max} and ω'_0 against wave height. It should be noted that * represents the physical tank test under $H = 0.08$ m.)	92
5.1	Corresponding parameters for the three geometric devices.	110
5.2	Parameters of the simulated wave climates.	114
5.3	Measured logarithmic decrements and damped oscillation periods according to Figure 5.5. \bar{T}_d is the average oscillation period.	117
5.4	Qualified added mass and hydrodynamic damping. \bar{a} and \bar{B}_{hyd} are the corresponding average values.	118
5.5	Added mass, hydrodynamic damping obtained from linear and non-linear simulations.	119
B.1	Discrepancies between the experimental (H_{EXP} = average of the experimentally measured wave amplitudes from WG1 to WG3) and numerical (H_{NWT} = average of the numerically measured wave amplitudes from WG1 to WG3) wave data.	177
B.2	Discrepancies of the measured forces and pitch moments between experiment and numerical simulation under regular wave No.1.	180
B.3	Discrepancies of the measured forces and pitch torques between experiment and numerical simulation under regular wave No.2.	180

Abbreviations

3D	3 Dimensional
AD	Attenuator Device
ALE	Arbitrary Lagrangian Eulerian
AR	Autoregressive
BEM	Boundary Element Method
BWD	Bulge Wave Device
CFD	Computational Fluid Dynamics
FIS	Fuzzy Inference System
FLC	Fuzzy Logic Control
FSI	Fluid Structure Interaction
IRF	Impulse Response Function
LSSM	Linear State-Space Model
MF	Membership Function
MPC	Modern Predictive Control
NS	Navier Stokes
NSSM	Non-linear State-Space Model
NWT	Numerical Wave Tank
OTD	Over-topping Device
OWC	Oscillating Water Column
OWSC	Oscillating Wave Surge Converter

PAWEC	Point Absorber Wave Energy Converter
PCCD	Passive Control with Constant Damping
PTO	Power Take-Off
PSO	Particle Swarm Optimization
RAO	Response Amplitude Operator
RMD	Rotating Mass Device
SI	System Identification
SPDD	Submerged Pressure Differential Device
SPH	Smoothed-Particle Hydrodynamics
UoH	University of Hull
VOF	Volume of Fluid
WEC	Wave Energy Conversion

Symbols

a	hydrodynamic added mass	kg
A	wave amplitude of regular wave	m
B_{hyd}	hydrodynamic damping coefficient	kg/s
B_{inv}	inviscid radiation damping coefficient	kg/s
B_{vis}	viscous damping coefficient	kg/s
B_{PTO}	PTO damping coefficient	kg/s
B'_{PTO}	optimal PTO damping for passive control	kg/s
C	power absorption efficiency of a WEC device	%
C_{max}	maximum power absorption efficiency of a WEC device	%
C_d	viscous coefficient	
D	effective diameter of the WEC device	m
E	the absorbed wave energy	J
f_e	wave excitation force in time domain	N
F_e	wave excitation force in frequency domain	N
\hat{F}_e	wave excitation force coefficient in frequency domain	N/m
f_r	radiation force in time domain	N
F_r	radiation force in frequency domain	N
f_s	hydrostatic force in time domain	N
F_s	hydrostatic force in frequency domain	N
f_v	viscous force in time domain	N

f_{PTO}	PTO force in time domain	N
F_{PTO}	PTO force in frequency domain	N
g	gravity acceleration	m/s^2
H	wave height of regular wave	m
H_s	significant wave height of irregular wave	m
k_e	IRF of the excitation force	kg/s^3
k_r	IRF of the radiation force	kg/s^2
K_{PTO}	PTO restoring stiffness coefficient	N/m
K_s	hydrostatic stiffness coefficient	N/m
m	added mass	kg
m_∞	added mass at the infinite frequency	kg
M	intrinsic mass of the WEC device	kg
M_{PTO}	PTO inertia mass	kg
P_{wave}	available wave power on effective floater diameter	W
\bar{P}	average capture power of the WEC device	W
r	spectral sharpness	
t	time	s
t_c	causalizing time shift	s
T	wave period of regular wave	s
T_0	natural oscillation period of the device	s
u	vertical flow velocity	m/s
X	reactance	N/m
z	heaving displacement of the WEC device in time domain	m
z_0	initial released position in free decay test	m
Z	heaving displacement of the WEC device in frequency domain	m
\dot{z}	heaving velocity of the WEC device in time domain	m/s
\dot{Z}	heaving velocity of the WEC device in frequency domain	m/s
\ddot{z}	heaving acceleration of the WEC device in time domain	m/s^2

\ddot{Z}	heaving acceleration of the WEC device in frequency domain	m/s^2
η	wave elevation	m
λ	wave length	m
ω	wave frequency	rad/s
ω_0	natural frequency of the PAWEC device	rad/s
ω_p	peak frequency of irregular wave	rad/s
ρ	water density	kg/m^3
ϕ	PAWEC motion phase angle relative to the wave	°

Chapter 1

Introduction

1.1 Background

Marine energy is extracting increasing attentions for the capability of meeting the energy demand of the world, whilst protecting consumers from fossil fuel crisis, contributing to the reduction of carbon emissions and stimulating economic development in coastal areas ([Badcock-Broe et al., 2014](#)). Generally, there are a wide variety of marine energy extraction forms including: wave energy, tidal energy, marine current power, ocean thermal energy, osmotic power, marine biomass and submarine geothermal energy ([Edenhofer et al., 2011](#)).

Figure [1.1](#) provides an overview of the international development distributions of the marine energy technology ([OES, 2014b](#)). As seen, this technology is mainly developed and applied in mid-latitude coastal countries where the wave energy density is significant, e.g the UK, Ireland, Denmark, the Netherlands, France, Germany, Norway and Portugal, etc. It has been predicted that there is a potential to develop 20,000 to 80,000 TWh of electricity per year from ocean. In particular,

the potential associated with wave energy is estimated to be approximately 28,000 TWh a year (IEA, 2016, OES, 2013). EIA (2013) estimated that the world's electricity demand in year 2009 can be provided by capturing only 5% of the wave power. To date, wave energy has attracted over 170 developers in the world to date. This number confirms the global interest and efforts in developing wave energy technologies.



FIGURE 1.1: International development distributions of the marine energy technologies (OES, 2014b).

1.2 WEC devices

Presently, large numbers of wave energy conversion (WEC) devices have been proposed for electricity generation from wave. Historically, the first attempt of this technology is recorded to date back to 1799 (Pecher and Kofoed, 2017, Clément et al., 2002). In modern times, Yoshio Masuda has been regarded as the father of the modern WEC technology by conducting experimental studies since 1940s in Japan. The renewed interest in wave energy was motivated in response to the oil shortage in the beginning of 1970s (Evans, 1981). During this time, Prof. Stephen

Salter from Edinburgh University, one of the earliest pioneers contributed lots of efforts on this technology, by inventing the famous "Edinburgh Duck" (Salter, 1974). However, the perceived need of this energy source turned to decline in 1980s due to the oil glut. More recently, the potential for wave energy resources has experienced an upsurge, following climate change issues and a need for the development of a better portfolio of marine energy sources (Falnes, 2007).

By now, WEC devices can be generally divided into 8 categories based on the working principle and operating location (e.g., onshore, nearshore and offshore). Figure 1.2 illustrates the representative types and the corresponding working principles, as summarized by EMEC, OSU (2013):

- *Attenuator device (AD): a floating, multi-segmented device which drives the hydraulics to generate electricity by the relative movement between the two adjacent segments.* The most famous AD is Pelamis invented by Pelamis Wave Power (Henderson, 2006). A device named StringRAY from Columbia Power Technologies can be regarded as a hybrid PAWEC-AD device (StringRAY). A hinged-raft device from Mocean Energy is a two segmented AD device (<http://www.moceanenergy.com/>).
- *Oscillating wave surge converter (OWSC): a device which oscillates in pitch/surge direction in response to the waves, leading to the motivation of the hydro power system for electricity generation.* The WaveRoller from AW-Energy (WaveRoller), Oyster invented by Aquamarine Power (Cameron et al., 2010, Whittaker et al., 2007), Langlee from Langlee Wave Power (Pecher et al., 2010) and "Edinburgh Duck" (Salter, 1974) are the typical OWSC devices.
- *Oscillating water column (OWC): a submerged, hollow structure where the trapped air is compressed and decompressed by the action of waves resulting in the turbine rotation to generate electricity.* Typical examples are the LIMPET built into a

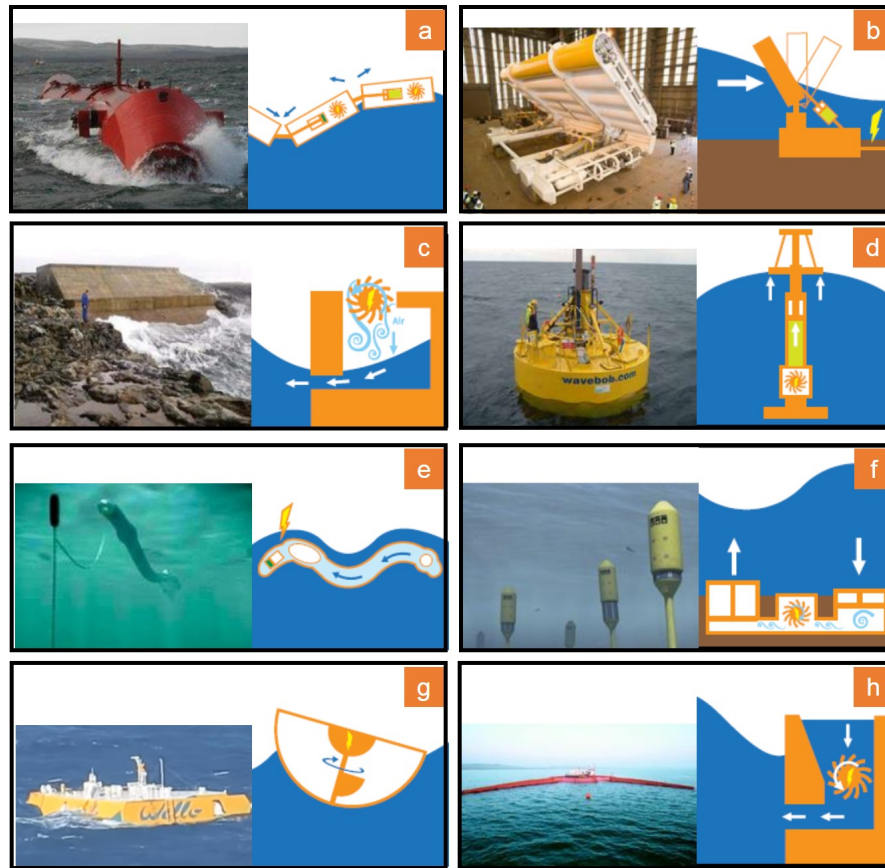


FIGURE 1.2: Main categories of WEC devices and schematic of operation principle. a. Attenuator device. b. Oscillating wave surge converter. c. Oscillating water column. d. Point absorber wave energy converter. e. Bulge wave device. f. Submerged pressure differential device. g. Rotating mass device. h. Over-topping device. The used figures above are from [OSU \(2013\)](#) and Goggle Images.

solid rock coastline of the Isle of Islay ([Boake et al., 2002](#)) and the floating device Mighty Whale ([Washio et al., 2000](#)).

- *Point absorber wave energy converter (PAWEC): a small dimensional device relative to the incoming wave length, which can operate in all directions to drive the power system for energy conversion.* Notable PAWEC devices are the WaveStar ([Marquis et al., 2010](#)), Wavebob ([Weber et al., 2009](#)), CETO ([Carnegie](#)) and the FO3 device developed by the Norwegian entrepreneur Fred Olsen ([Leirbukt and](#)

[Tubaas, 2006](#)).

- *Bulge wave device (BWD): a rubber tube filled with water, where the bulge is created by pressure variations caused by the passing waves and moves toward a turbine in the bow to generate electricity.* The Anaconda wave device is a notable BWD ([Heller et al., 2000](#)).
- *Submerged pressure differential device (SPDD): a device which works on the principle of the pressure differential generated from the wave motions.* One famous SPDD is the Achimedes Wave Swing proposed by AWS Ocean energy ([de Sousa Prado et al., 2006](#)).
- *Rotating mass device (RMD): a device which uses the wave motion to spin a rotating mass to drive the generator for electricity generation.* A famous example is the Penguin by Wello ([Wello](#)).
- *Over-topping device (OTD): a collector which concentrates the wave over the top of the structure and then funnels the waves into the reservoir resulting the generated flow to spin the hydro turbine for electricity generation.* The most notable system is the Wave Dragon ([Kofoed et al., 2006](#))

Apart from the working principles, the WEC devices can also be divided into different groups based on the locations. As show in Figure 1.3, according to the installed locations, the WEC devices can be divided into three types: onshore, nearshore and offshore ([López et al., 2013](#)). Based on different locations, the designs for mooring and cable systems can be totally different. For onshore devices, they do not need mooring systems and long lengths of sea cables to transfer the generated electricity to the national grid. The devices are directly based on a cliff or a dam where can be easily accessible. This leads to easy maintenance and installation. For nearshore WEC devices (particularly when restricted to heave motion, like Seabased, Bolt Sea Power ([Sjolte et al., 2013](#))), the mooring lines

are generally designed to be taut in order to transfer the oscillation to drive the generator. Figure 1.4 shows the working principle of the device from Bolt Sea Power. As seen, a taut winch line is connected to a winch which connects to the gearbox to drive the generator. The lifetime of the winch line is quite short, up to 6 years by abrasion about a few hundred cycles. However, it is known the typical wave site has around five million waves per year. Therefore, it would be quite important for the selection and design of the durable winch line. Similarly, a taut mooring line in the Seabased device is used to directly drive the linear generator for electricity generation. By contrast, when the device is placed in the offshore, the mooring systems are basically designed to be slack. The long length sea cables are required to transfer the energy to the grid. This increases the cost of marine energy to a high degree. Recently, attentions are paid on the ideas of "hydrogen" storage, which proposes to transfer the electricity into hydrogen and then transport the hydrogen to mainland by the existing oil&gas pipelines. EMEC has produced the world's first tidal-powered hydrogen generation, as shown in the Figure 1.5.

Based on the energy conversion principles, the WEC devices can be generally divided as two types: multi-stages conversion and direct conversion (López et al., 2013). When transferring wave energy to electricity, there exists some transmission components that link the oscillating WEC devices to the rotatory generators. These kinds of devices relate to the multi-stages conversion type. The most popularly used transmissions are: pneumatical, hydraulic and mechanical types. With the introduction of self-rectifying air-turbines, like Wells air-turbine, Dennis-Auld air-turbine and impulse air-turbine, the generator can keep efficiently rotate in one direction despite the directional air flow (Falcão et al., 2018). These have been popularly used in the OWC devices. For some WEC devices, like Ocean Power Technology, Pelamis (Henderson, 2006), hydraulics are introduced to storage the

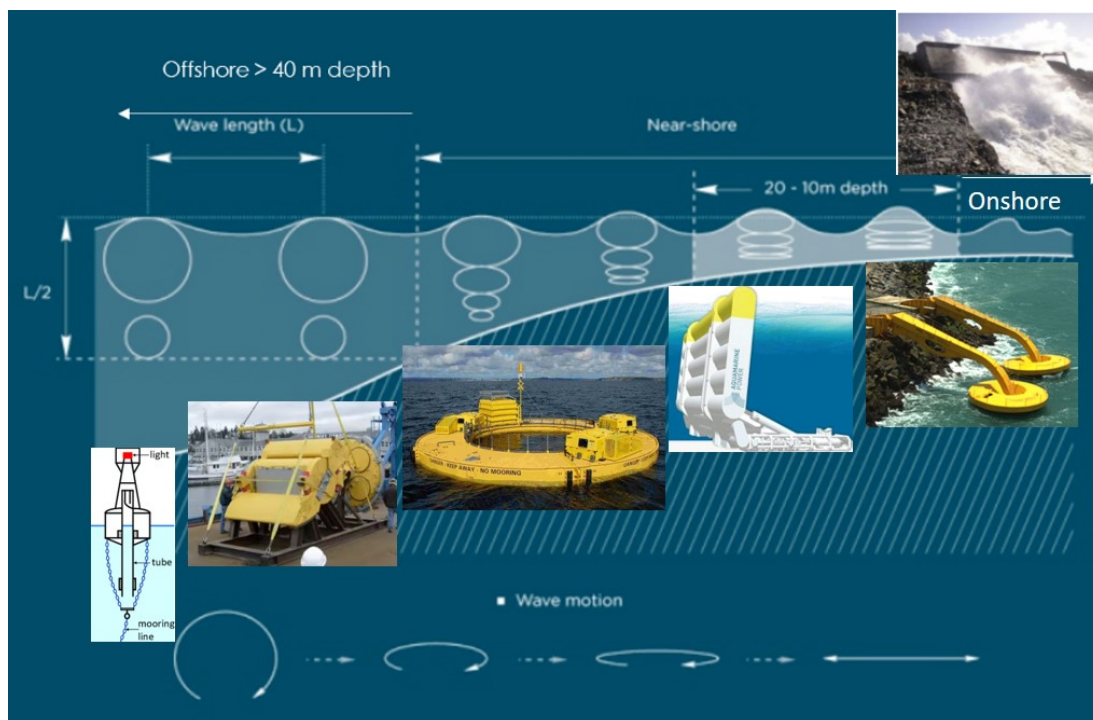


FIGURE 1.3: Different types of WEC devices based on installed location. From left to right, the WEC devices are Masuda's navigation buoy (Henriques et al., 2016b), the Columbia Power Technologies device (Rhinefrank et al., 2010), the Bolt Sea Power device (Sjolte et al., 2013), the Oyster device (Cameron et al., 2010), the Coppe Subsea device (Estefen et al., 2010) and the LIMPET device (Falcão and Henriques, 2016).

captured wave energy first into hydraulic energy. Then the hydraulic energy is converted into electricity by driving a hydraulic motor. For the direct conversion, the systems use direct-linear generator instead of the rotatory generators. By doing so, they do not need any transmissions. As the design from Seabased device, the linear generator is directly coupled to the oscillating buoy without any intervention systems (Chatzigiannakou et al., 2017).

Instead of using real rotatory or linear generators, some generator simulators (see Figure 1.6) are applied while undertaking lab tests. For OWC devices, they commonly change the dimensions of the orifices to simulate the generator (Fleming and Macfarlane, 2017). Additionally, some devices use the mechanical viscous

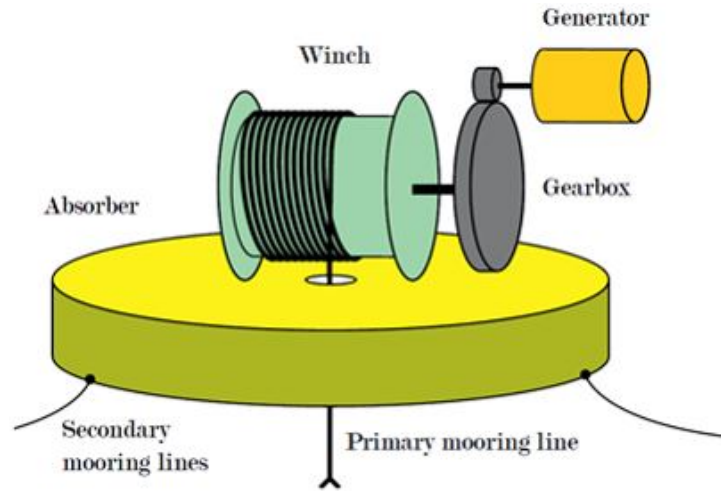


FIGURE 1.4: Taut winch line used in the WEC device from Bolt Sea Power (Sjolte et al., 2013).

damper, dashpot (linear/rotatory) to simulate the PTO. In the application of the two-body oscillating device from national renewable energy laboratory (NREL), a viscous damper is used by changing the orifices dimension and numbers to simulate varying PTO damping (Yu et al., 2015). In the laboratory tank test of the OWSC type device, a rotary dashpot is used to provided damping torque (Flocard and Finnigan, 2012). Additionally, magnet brakes are used as alternatives. Uppsala buoy employs an eddy current brake as the generator simulator (Thomas et al., 2018). For the heaving PAWEC designed by Harbin Engineering University, a permanent electromagnetic brake is used to offer damping force (Chen et al., 2018).

1.3 Challenges and objectives

Although the development of WEC devices has not converged as yet into a specific format or type of energy devices, the PAWEC type shows to be the most promising

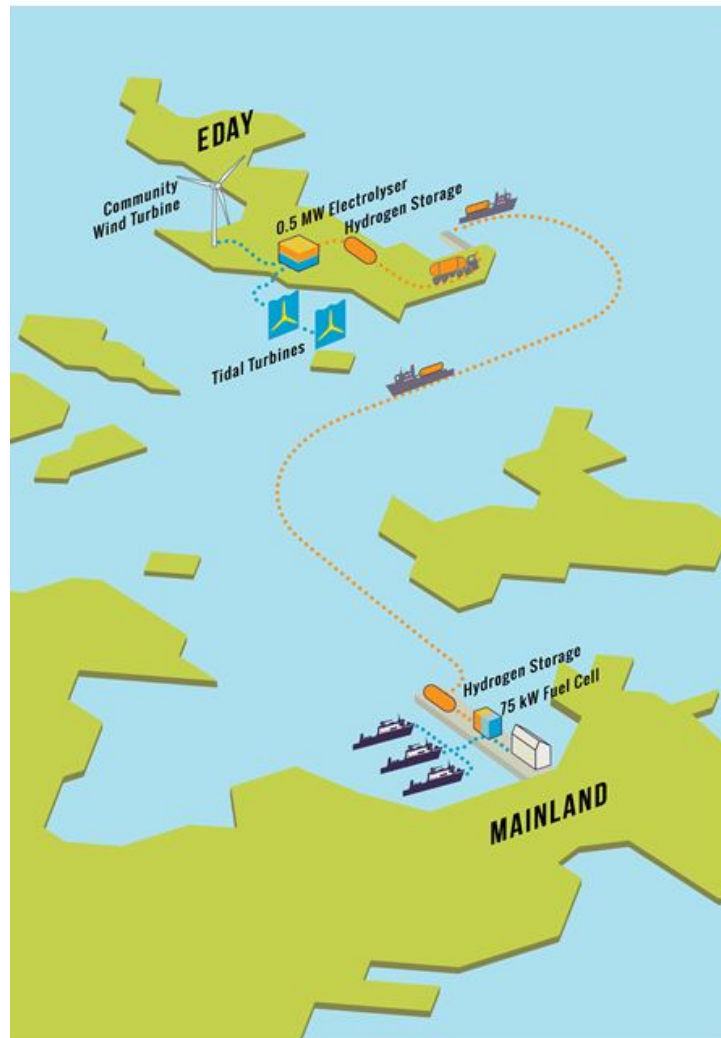


FIGURE 1.5: Tidal-powered hydrogen concept generated by EMEC. The figure is from the EMEC website <http://www.emec.org.uk>.

solution. As described in Figure 1.7, OES (2014a) indicates that PAWEC systems attract the most R&D efforts, followed by AD and OWSC.

The popular development of PAWEC device can be related to the following advantages. First of all, the systems are relatively simple. As a result, they can avoid lots of components leading to the reduction of the cost (Drew et al., 2009). For example, the hallmark of the PAWEC device from Seabased technology is simplicity.

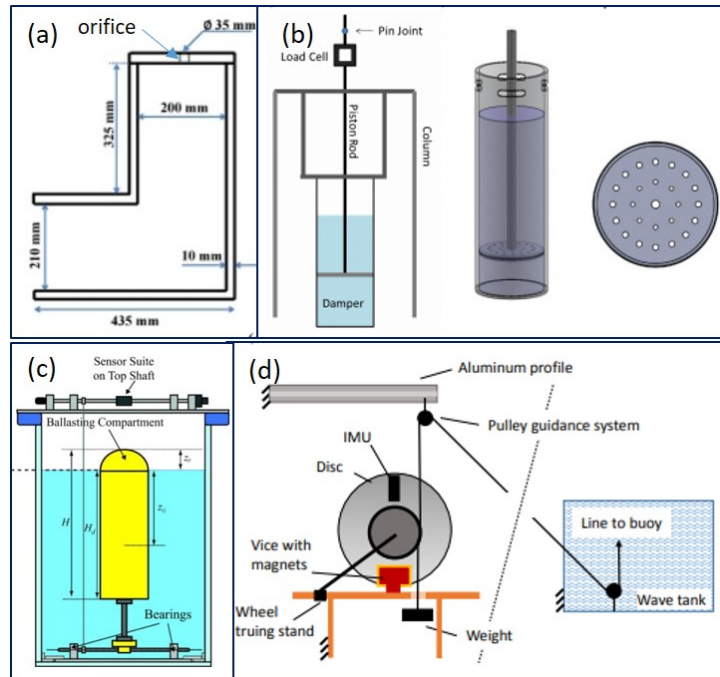


FIGURE 1.6: General examples of the PTO simulators used in the laboratory tank tests. a. Orifice type used in OWC devices. b. Mechanical viscous damper or dashpot applied in the NREL two-body PAWEC (Yu et al., 2015). c. Rotary dashpot used in the bottom-hinged pitching point absorber (Flocard and Finnigan, 2012). d. Eddy current brake used in Uppsala buoy (Thomas et al., 2018).

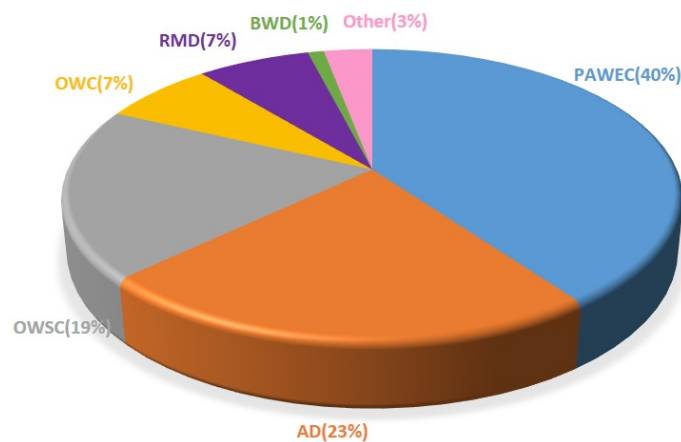


FIGURE 1.7: Distribution of the R&D efforts regarding the WEC devices.

The main components only include: one point buoy, one steel line and a direct-drive linear generator. Then it should be noted that the dimension of this kind of device relative to the wave length is considerably small, which allows the device to be wave-direction independent and capture wave energy in all directions. As generally known, in the open-sea, although there exists a dominant wave direction in a specific location, the waves are actually directionally spreading. Therefore, by selecting a small dimension, the device can be freely active without considering to shift itself to coincide with the dominant sea direction for power maximization. More importantly, compared with a PAWEC, there exists a high risk of generating bending moment in a large dimensional device. To realize the power maximization and the levelized cost of Energy (LCOE) reduction, more and more work is underway to study the practicality of developing arrays (Folley et al., 2012). Presently, most arrays are based on PAWEC devices, like the technologies from WAVESTAR, CETO, Seabased, WETFEEET. Unlike the famous surge oscillating device, Oyster which needs to be installed in nearshore, most of the PAWEC devices can be developed into floating structures installed in the offshore where there exists a huge amount of wave energy. With the simplicity of PAWEC device, the corresponding physical or numerical models can be relatively easy to be constructed (Eriksson et al., 2005). Therefore, lots of studies are based on PAWEC devices. However, it should be noted that by now the WEC device has not converged to any specific technology. There exist disadvantages for different devices. Compared to a generic hinged device, the risk for a Seabased PAWEC device under extreme condition can be quite high. For hinged device, the raft can rotate along the hinged point into a high degree which makes effective survivability under harsh conditions. However, the stroke for the Seabased PAWEC device should be constrained into a range to avoid the resulting damage of direct-drive PTO under large oscillations. This has been carefully studied with the application of an end-stop interface (Götteman et al., 2015). Also, the difficulties of improving the survivability of

the WEC devices in extreme conditions and of solving the corrosion problem in marine environment are needed to be carefully considered. Due to the installed locations are nearshore and even offshore, these definitely improve the technical difficulties and cost of maintenance. Marine energy is a multi-disciplinary requiring the consideration of lots of subjects together to realize the LCOE reduction for the aim of commercialization. It can be important to carefully study the gaps and similarities from the much more developed oil & gas and offshore wind farms, in order to inherit the development technologies.



FIGURE 1.8: 1/50 scaled PAWEC and corresponding experimental wave tank at UoH (Jin et al., 2018).

It should be note that it is very difficult to see that PAWEC device can be the most effective device . However, inspired by its simplicity for physical and numerical models, studies on a designed 1/50 scale vertically oscillating PAWEC are in progress at University of Hull (UoH) (Guo et al., 2018a,b, Jin et al., 2018, Jin and Patton, 2017, Jin et al., 2016, Guo et al., 2016, Abdelrahman et al., 2016). The main theme is to propose an efficient system to maximize the PAWEC performance in capturing wave energy with the consideration of the PTO and control actions. Figure 1.8 shows the physical experimental scenario. A series of tank tests have been conducted, including the free decay test, free motion test and wave excitation force test. By summarizing the physical experimental studies, the following

issues/challenges and corresponding objectives are proposed to be considered for the designed PAWEC in this thesis:

- **Challenge 1:** *Experimental tests are limited by the physical facility of the wave tank.* Due to the effects of wave reflection and standing wave, it is found that the physical wave tank at the UoH can only generate a limited range of stable waves. For example, regular waves with amplitude larger than 0.1 m and frequency less than 3.14 rad/s cannot be provided stably. In this case, it is impossible to understand the thorough PAWEC behaviours under varying wave conditions, especially extreme waves. To overcome this, numerical tank tests can be an appropriate alternative. As indicated by [Ransley et al. \(2017\)](#), computational fluid dynamics (CFD) model can closely reproduce the non-linear fluid dynamics associated with the interaction of extreme waves and WEC devices if the model is well-designed. Therefore, the **first objective** of this thesis is to build a capable numerical wave tank (NWT) in order to thoroughly investigate the PAWEC performances under various wave conditions.

- **Challenge 2:** *The linear model fails to predict the PAWEC hydrodynamics.* A linear mathematical model is obtained from the boundary element method (BEM) in order to describe the PAWEC hydrodynamics. It is found that the model would significantly over-predict the device response by comparing with the experimental data from free decay test. By contrast, by taking into the non-linear viscous and frictional factors into account, the derived non-linear model shows the superiority in representing the PAWEC's free decay motion, as indicated by [Guo et al. \(2018a\)](#). In addition to the free decay dynamics, the hydrodynamic interaction between the PAWEC and varying waves also need to be carefully studied. The device hydrodynamics against varying wave conditions can be of fundamental importance to predict power absorption efficiency. More importantly, as the subsystems of a WEC system, the PTO design as well as the control strategy development are

highly dependent on the device hydrodynamics responding to the waves. Therefore, a faithful hydrodynamic modeling can be critical to suggest the PTO and control systems designs (Son and Yeung, 2017, Goggins and Finnegan, 2014, Hals et al., 2011b, DelliColli et al., 2006). Consequently, the *second objective* of this thesis is to identify an overall non-linear model to effectively perform the PAWEC behaviors interacting with waves, especially under large oscillations.

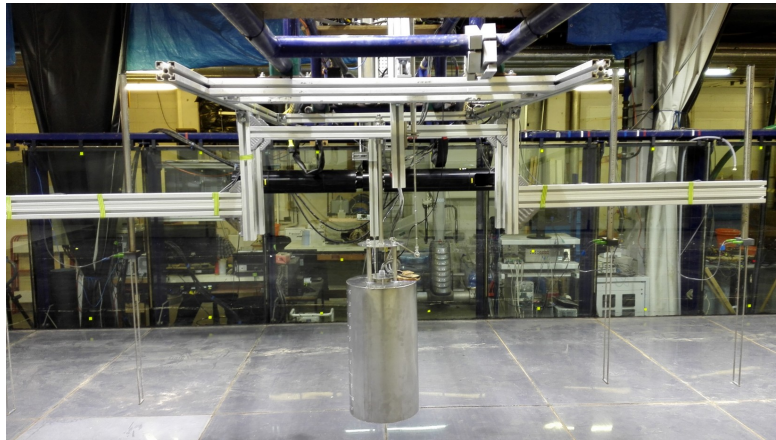


FIGURE 1.9: Close-up of the 1/50 scale PAWEC designed at University of Hull

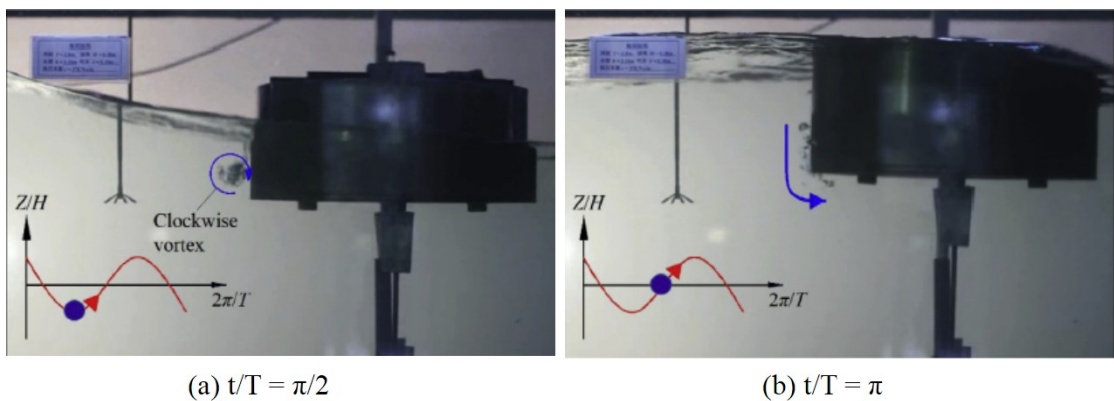


FIGURE 1.10: Vortex formation around a flat-bottom buoy during oscillation in regular wave. The figures are from Zang et al. (2018).

- **Challenge 3:** *The designed PAWEC may lead to clear energy losses while oscillating.* Figure 1.9 demonstrates the close-up of the designed 1/50 scale PAWEC. As seen, the device is a cylindrical buoy with flat bottom. By conducting free

motion test, it is noticed that there exists apparent vortex formation around the flat bottom of the PAWEC, especially under large oscillations. This phenomenon concurs with the experimental record achieved by [Zang et al. \(2018\)](#), as shown in [Figure 1.10](#). [Tom and Yeung \(2013\)](#) have indicated that the floater with flat bottom generates significant vortex shedding around the structure which may lead to energy losses. They suggested the benefits of enhancing energy capture efficiency from shape or geometry optimization. Therefore, the *third objective* of this thesis is to optimize the PAWEC profile with the aim of reducing the energy losses caused by vortex.

• *Challenge 4: Model dependent controller may lose effectiveness if the physical model is not accurately formulated.* Numbers of control methods have been applied to realize power absorption maximization from wave, e.g., reactive control ([Hals et al., 2011a](#)), latching control ([Sheng et al., 2015](#), [Babarit and Clément, 2006](#)) and model predictive control (MPC) ([Hals et al., 2011b](#), [Brekken, 2011](#)), etc. It has been found that most of these controllers are of reference-required type, such as an optimal velocity trajectory is needed in [Guo et al. \(2016\)](#). This means the controller actions are dependent on the WEC hydrodynamic model. Therefore, it is clear that the controller may fail if the given hydrodynamic plant cannot faithfully describe the system behaviors. To overcome this, a model-free controller, e.g., FLC is used in this work. Consequently, the *fourth objective* of this thesis is to investigate the capability of the FLC in controlling the PAWEC device for power absorption optimization.

1.4 Outline of the thesis

According to the objectives listed above, the thesis structure is outlined in [Figure 1.11](#) and detailed as follows:

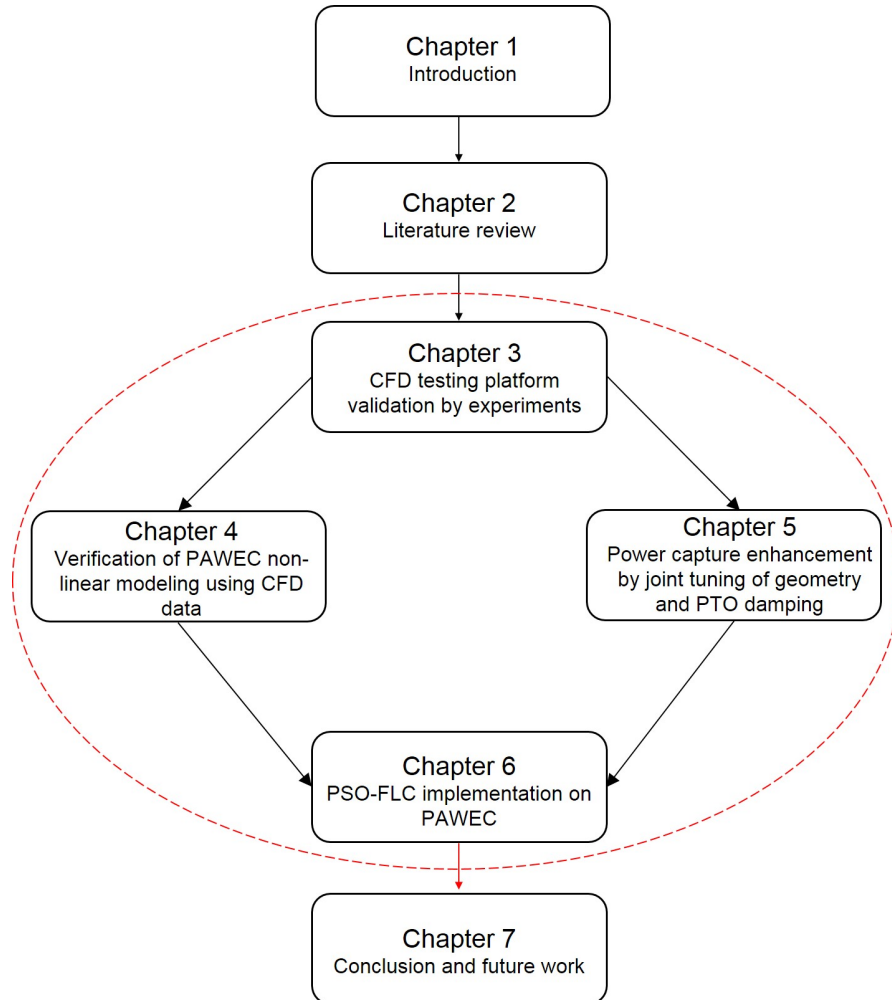


FIGURE 1.11: Structure of the thesis.

Chapter 1 provides a brief background of the wave energy development and introduces a wide variety of the WEC devices. This study focuses on the challenges and objectives corresponding to PAWEC devices and this Chapter provides some of the background details. The remaining structure of the thesis is outlined below.

Chapter 2 provides a general literature review of the technical developments related to the PAWEC system, including the review of different types of PAWEC devices, as well as the review of the PAWEC dynamics study and corresponding control strategies.

Chapters 3 to 6 are the main contributions of this thesis and can be summarized as follows:

Chapter 3 is related to the *first objective* and details the construction of a NWT by the commercial CFD software ANSYS/LS-DYNA. Data from physical wave tank are provided to verify the capability of the NWT. It is found that the developed NWT can closely reproduce the physical non-linear behaviours that the PAWEC interacts with the waves.

Chapter 4 is related to the *second objective* and focuses on the derivation of an overall non-linear mathematical modeling for practically representing the PAWEC hydrodynamics. The non-linear mathematical model is identified through the NWT built in Chapter 3. The non-linearities of the PAWEC performance are discussed by comparing the achieved data from linear model, non-linear model, NWT and physical experiment. It is found that the non-linear PAWEC behavior for the conditions of large oscillations (e.g., near resonance or at a large wave heights) can only be predicted realistically by considering a correct viscous effect. Inaccurate representation (e.g., the linear model) would result in vital errors, e.g., over-estimating the amplitude response, mis-predicting the resonance and misleading the performances of the PTO and control systems.

Chapter 5 is related to the *third objective* and studies the PAWEC geometry optimization for power absorption maximization. Two further (more streamlined) geometric counterparts are proposed in comparison with the original flat-bottom device. A series of tests related to the three PAWEC devices are conducted in the NWT built in Chapter 3. The results show that a PAWEC device with streamlined bottoms can affect the device hydrodynamics by significantly reducing the hydrodynamic added mass and damping coefficient. Additionally, it is found that there exists clear joint effects between the device geometry and PTO damping on the PAWEC power capture performance. Applying an appropriate PTO damping

to the streamline-bottom device can prominently increases the achievable optimal power under both regular and irregular waves (compared with the flat-bottom PAWEC).

Chapter 6 is related to the *fourth objectivity* and investigates the performance of the model free FLC for enhancing the PAWEC power absorption efficiency. The controller is built by using the non-linear modeling proposed in Chapter 4 as the hydrodynamic plant. The PAWEC's power capture characteristics achieved from Chapter 5 are employed to design the fuzzy rule base. Additionally, the PSO algorithm is involved into the FLC to optimize the fuzzy rule base in order to further improve the power absorption efficiency.

Chapter 7 summarizes the thesis and provides a restatement of the contributions as well as prospects for future research.

Chapter 2

Literature Review

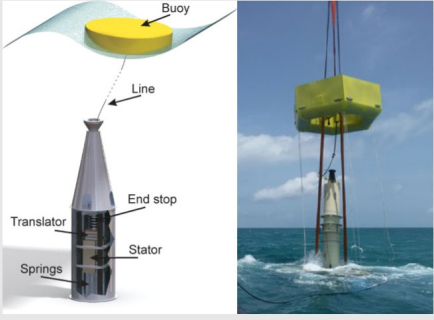
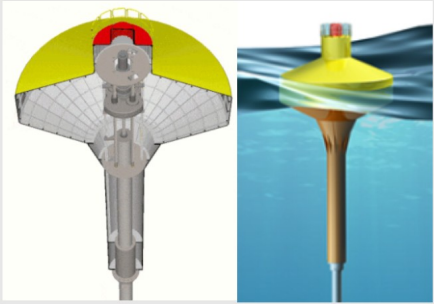
2.1 Introduction

As mentioned in Chapter 1, this thesis focuses on the study of a 1/50 scale point absorber wave energy conversion (PAWEC) device. Before describing the main work related to the device in Chapters 3 to 6, this Chapter aims at giving a brief literature review about PAWEC systems, including: (i) the different types of PAWEC devices; (ii) the corresponding dynamic performance study; and (iii) the control strategies used for the improvement of the power absorption efficiency.

The rest of this Chapter is described as: Section 2.2 provides a literature review of the popular PAWEC devices; Section 2.3 provides a review of the dynamic performance investigation of PAWEC device via experimental and numerical approaches; the corresponding control strategies applied on PAWEC systems are reviewed in Section 2.4; Section 2.5 summarizes this Chapter.

2.2 PAWEC devices

Figure 2.1 presents in detail the main PAWEC developers, most of which have conducted full-scale sea tests.

Developer name	Website	Representative figure
Seabased AB	www.seabased.com	
WaveStar Energy	www.wavestarenergy.com	
Ocean Harvesting Technologies	http://www.oceanharvesting.com/	
OPT	www.oceanpowertechologies.com	

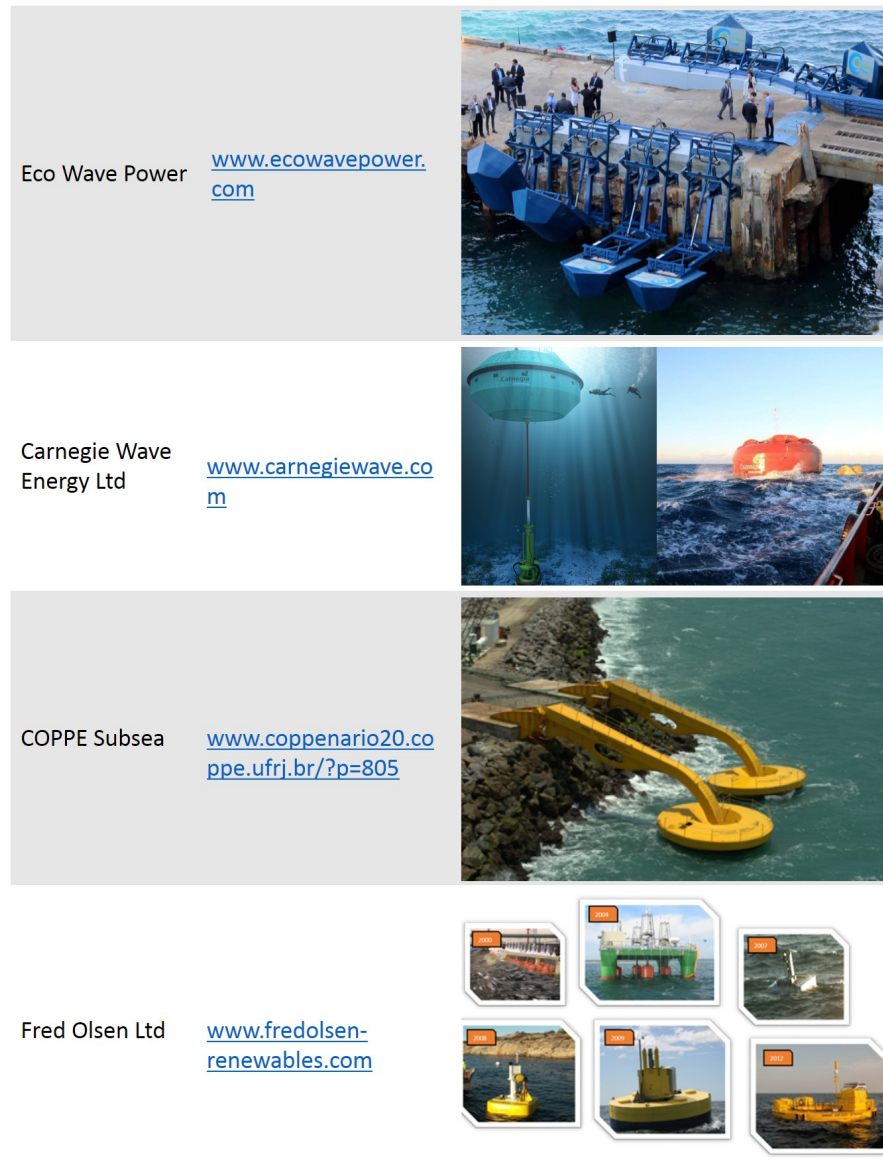


FIGURE 2.1: Representative PAWEC developers. The used figures are from the corresponding websites listed above.

As observed in Figure 2.1, PAWEC systems can be divided mainly into two categories:

- *One-body PAWECs: devices which possess only one floater and excited by the incident waves for electricity generation.* The devices are attached directly by

mooring lines or robust arms to any type of references, e.g., generators, breakwaters, jetties and fixed platforms, etc. For devices, such as Wavestar, the motions of the floats are transferred via the arms to drive the hydraulics to produce electricity (Kramer et al., 2011). For systems, such as Seabased buoy, the taut mooring line is required to directly drive the linear generator which is installed on the seabed (Eriksson, 2007).

- *Two-body PAWECs: devices which drive power take-off (PTO) systems to generate electricity based on the relative motions between the self-referenced two bodies.* For devices, such as OPT PowerBuoy, the float moves up and down the spar by the excitation of the incident wave. The heave plate maintains the spar in a relatively stationary mode. As a result, the relative motion between the float and the spar drives a PTO system for electricity generation (Edwards et al., 2014).

Fred Olsen Ltd. has carried out the research on PAWEC system for almost 16 years (<http://boltseapower.com/>). Starting out with high ambitions, Fred Olsen Ltd. built a semisub platform consisting of several heaving PAWECs in 2005, known as the famous FO3 system (see Figure 2.2a). Nevertheless, from the in-sea experience, it was indicated that the challenges of operating large wave energy conversion (WEC) system in real sea are considerably high. Hence, it was necessary to shift to small autonomous power device, namely PAWEC device (see Figure 2.2b). It was suggested that the hydrodynamics of the PAWEC devices should be carefully studied not only in small and moderate wave conditions, more importantly, under large or even extreme wave conditions (see Figure 2.2c).

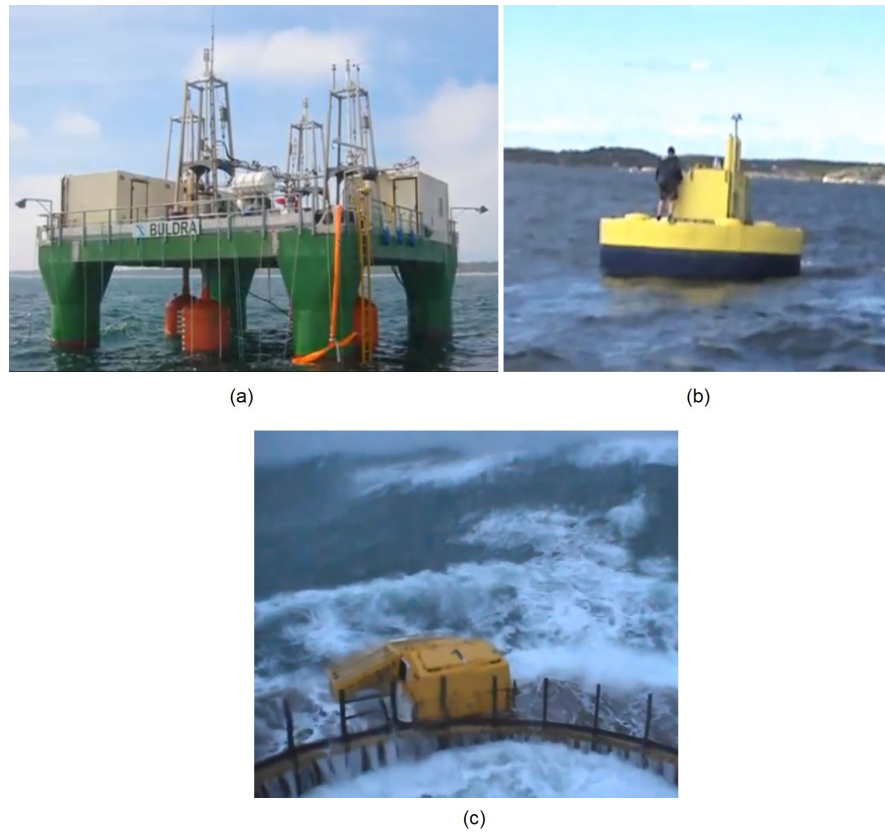


FIGURE 2.2: WEC systems developed from Fred Olsen Ltd (<http://boltseapower.com/>). (a) The large WEC platform, named as FO3. (b) The relatively small dimensional PAWEC. (c) The PAWEC operating in the storm condition.

Inspired by the PAWEC systems listed above, the simplest concept namely the one-body PAWEC device is focused on this thesis (see Figure 1.8). The objective is to gain a thorough understanding of the hydrodynamic characteristics of the designed 1/50 scale PAWEC device and communicate these efficiently in the thesis. The Section 2.3 gives a literature review of the PAWEC hydrodynamic study.

2.3 Review of dynamic study of PAWEC devices

This Section outlines the literature review of experimental and numerical studies on the PAWEC dynamic performance. Furthermore, the corresponding advantages and disadvantages of different methods and the applicability of each method are briefly introduced.

- *Experimental approaches* are generally used to physically understand the PAWEC performance in response to incident waves. De Backer (2009) demonstrated the hydrodynamic characteristics of the heaving PAWEC devices (with conical and hemispherical bottoms) from a series of free decay, excitation force and slamming tests. More importantly, the overestimation of linear model in terms of power production was clearly validated by comparing with experimental data. As indicated by Madhi et al. (2014), a so-called "Berkeley Wedge" profile was applied to produce a physically asymmetrical heaving PAWEC. The device appeared to have a considerably high capability of capturing wave energy by significantly minimizing the effects from viscosity. By conducting physical free decay tests, Guo et al. (2018a) suggested the non-linear hydrodynamics of a 1/50 scale cylindrical PAWEC caused by viscosity and friction effects. Zang et al. (2018) conducted experimental study on the power performance of a heaving flat-bottom PAWEC device under regular and irregular waves. It was suggested that the vortices generated around the bottom corner of the device can provide significant energy losses.

With no doubt, physical test should be the most accurate method to present PAWEC dynamics by naturally taking all of the non-linearities into account. However, this method has a main drawback, namely "costly". In contrast to experimental studies, cheaper methods, i.e., numerical approaches can be more appropriate to start.

• *Numerical approaches* are widely applied with the aim of closely reproducing the physical data. Several numerical methods are generally used to represent the PAWEC hydrodynamics, including the linear method, fully non-linear method and the partial non-linear method (Li and Yu, 2012). The corresponding details are summarized as bellow:

- *Linear method* is based on the boundary element method (BEM) regarding the linear potential flow theory. The typically used BEM software packages are WAMIT, AQWA, NEMOH, etc. The linear approach has several advantages. For example: it (i) predicts the hydrodynamics of a WEC system in the frequency domain which can be easily transferred into the time domain (Taghipour et al., 2008, Yu and Falnes, 1995); (ii) needs relatively low computations; and (iii) provides the hydrodynamic plant for control strategy analysis and designs (Son and Yeung, 2017, Brekken, 2011, Babarit and Clément, 2006). By using linear methods, Goggins and Finnegan (2014), McCabe (2013) and De Backer (2009) investigated shape or geometry optimization to improve the performances of PAWEC devices, respectively. Eriksson et al. (2005) studied the power capture capability against the PTO damping for different device diameters. In addition to the single WEC model, Forehand et al. (2016) described a fully coupled, bidirectional model to predict the hydrodynamic, mechanical and electrical response for an array of WECs. Additionally, the linear model has been generally applied for control strategy design, including the reactive control (Hals et al., 2011a), latching control (Babarit and Clément, 2006) and model predictive control (MPC) (Hals et al., 2011b, Brekken, 2011), etc. Nevertheless, this method has a serious drawback. It may lead to exaggerations of the amplitude response and power production of a WEC device, particularly under large oscillating conditions, like near resonance and at a high wave height (Goggins and

Finnegan, 2014, De Backer, 2009). This is mainly associated with the accompanying linear assumptions of the linear method (Falnes, 2002, Journée and Massie, 2000): (i) the wave is assumed to be linear, i.e., the wave elevation is considerably small; (ii) the motion of the WEC device is expected to be small; and (iii) the magnitude of the device effective diameter is supposed to be as large as the incident wave length. As a result, the linear method ignores all of the non-linear dissipative effects existing in practice. Hence, the overestimation of device hydrodynamics would be commonly found in linear approaches.

- *Fully non-linear method*, namely the computational fluid dynamics (CFD) method is achieved by fully solving the Navier-Stokes (NS) equations, which naturally considers the non-linearities of the fluid, e.g., compressibility and viscosity, etc. (Finnegan and Goggins, 2012, Nicolas, 2007). In this case, the non-linear hydrodynamics that the WEC device performances in response to the waves can be predicted by using CFD methods. The generally used software packages are Fluent, ANSYS/LS-DYNA and OpenFOAM, etc. Through CFD analysis, Jin et al. (2018) concluded the non-linear viscosity influence on the heaving PAWEC hydrodynamics. Anbarsooz et al. (2014) conducted CFD simulations of a submerged heaving PAWEC and suggested that the linear method is not satisfactory when subjected to steep incident wave conditions. Yu and Li (2013) reported that the resonant amplitude response of a two-body PAWEC device was decreased by the over-topping action. However, the CFD method has its own limitations. For example: it (i) requires considerably high computation; (ii) is not straightforward for control application; (iii) may fail to present the wave-PAWEC interaction if the simulated wave deformation is considerably large i.e., considering extreme wave conditions (Penalba et al., 2017). In this situation, smoothed-particle

hydrodynamics (SPH) method can be an appropriate alternative to deal with large mesh deformations. Nevertheless, it should be noticed that SPH methods will yield increased computation expense (Yeylaghi et al., 2015).

- *Partial non-linear method* is adopted by extending linear models with the inclusion of the significant non-linear terms (Jin et al., 2018, Lawson et al., 2014). One such methodology is achieved by considering the linear equivalent of the non-linear factor. For example, in order to discuss the viscous effect on the dynamic response of a heaving PAWEC device, a linear approximation of the viscous force was added into the linear model, as reported by Son et al. (2016). As validated by physical experiments, a linear mathematical model including a linear equivalent of the viscous factor can only be capable of representing the dynamics of a self-reacting PAWEC when the wave height is small (Beatty et al., 2015). When considering large oscillations with high body velocity, the limitation of this approach appear by the requirement of a changeable linearized term responding to different wave heights, as demonstrated in Tom and Yeung (2013). To overcome this, it is expected to include the practical non-linear factors into the conventional linear model. As indicted by Beatty et al. (2015), a quadratic viscous drag needs to be applied in order to faithfully represent the device hydrodynamics if the wave height is large or the body velocity is high. Validated by CFD results, Bhinder et al. (2015) demonstrated that the accuracy of the modeling (for representing the dynamic performances of a PAWEC operating in surge mode) can be improved to a great extent by the involvement of an additional quadratic viscous term. By conducting physical free decay testing for a PAWEC device, Guo et al. (2018a) concluded that the non-linearities of the free decay motions can only be practically predicted by carefully including the viscous and frictional factors. (Davidson et al., 2015a) indicated

that the achieved non-linear mathematical model can be used as a faithful PAWEC hydrodynamic plant which is of fundamental importance to control strategy design.

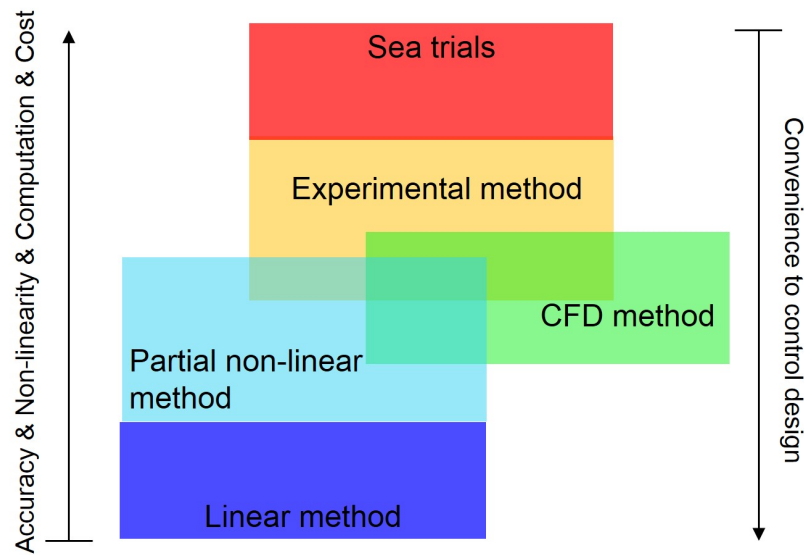


FIGURE 2.3: Advantages and disadvantages of experimental and numerical methods.

To summarize, the advantages and disadvantages of each method are given in Figure 2.3. As shown, real sea trials are definitely the most costly and challenging ways to naturally demonstrate the performances of WEC devices. In UK, there are mainly two sea test sites: the European Marine Energy Centre (EMEC) in Orkney and the Wave Hub in Cornwall. In Figure 2.3, the overlaps among different methods: experiments/CFD/partial non-linear are presented to account for the influences caused by scaling and model complexity. As generally known, a typically small scale model is preferred to be tested at the early stage of R&D due to the convenience.

In this thesis, by using the validated CFD data, a non-linear modeling considering viscous effects is verified, in order to faithfully predict the hydrodynamic performance of the designed 1/50 scale PAWEC. The corresponding studies are provided in Chapters 3 and 4. In addition, the achieved non-linear modeling is applied as the hydrodynamic plant for the control strategy design, as given in Chapter 6. The next Section gives a literature review of the control strategies applied on PAWEC systems.

2.4 Review of control strategies applied on PAWEC systems

As indicated by [Antonio \(2010\)](#), [Falnes \(2007\)](#), [Evans \(1981\)](#), the maximum power capture appears when "resonance" is achieved, i.e., the wave frequency matches the WEC device natural frequency. By contrast, the power production is significantly reduced when the wave is out of phase with the natural resonance of the device. It is clear that the natural frequency is more or less consistent for a given WEC device. Therefore, the power capture bandwidth is considerably narrow for a WEC device, as indicated in [Jin et al. \(2018\)](#). To overcome this, control applications have attracted large numbers of research efforts in order to broaden the power capture bandwidth or to optimize the power absorption efficiency.

The most important principle for controlling WEC power absorption maximization is proposed by [Evans \(1981\)](#), known as the optimal control/ reactive control. It should be noted that this concept is proposed based on the linear assumptions of the wave-WEC interaction and is derived under a frequency domain ([Hals et al., 2011b](#)). Therefore, this control approach is applicable under regular waves. In other words, the optimal control force (i.e., the PTO force) can be determined

easily under regular waves since the corresponding parameters are frequency dependent. However, the PTO control force is difficult to determine since the non-causality under irregular waves. This is the main limitation of optimal control (Guo et al., 2018b, Yu and Falnes, 1995, Falnes, 1995).

In contrast to the optimal control, suboptimal control strategies, such as the latching control is proposed, which can be regarded as a phase control. It focuses on aligning the phases of the WEC device velocity and the wave excitation force (Budal and Falnes, 1982, Budal, 1981). In practice, however, it is rather a challenge to compute the optimal latching or unlatching instants by non-causality. Babarit and Clément (2006), Babarit et al. (2004) paid great efforts on studying the application of latching control strategy on WEC device. In practical applications, Lopes et al. (2009) proposed methods to overcome the non-causality accompanying in latching control.

To control the PAWEC device operating in the safe range, constraints on device motion response should be taken into account. To solve this, MPC is adopted on WEC systems, which is well known for dealing with constraints. A significant amount of work has been done by many investigators on the use of MPC strategies for WEC control and efficiency tuning (Amann et al., 2015, Cretel et al., 2011, Brekken, 2011, Gieske, 2007). However, the greatest problem with MPC is the serious computational burden on the controller by performing in real-time. To overcome this, Fusco and Ringwood (2013) proposed a simple but effective real-time control strategy. With this technique, the control force is tuned to meet a reference (e.g., force or velocity), which is obtained by modelling the current excitation force as a narrow banded function (Ringwood et al., 2014).

However, the aforementioned control strategies have a common disadvantage. They all rely on the hydrodynamic models of the WEC devices to determine the optimal control variables, i.e., model dependent. As a result, modelling errors

would have significantly negative effect on the energy absorption of the WEC devices. Additionally, the control strategies would not be flexible with device changes over time.

It is therefore necessary to study the feasibility of model-free controller on WEC devices. As reported by [Anderlini et al. \(2017a, 2016\)](#), a model-free controller, the reinforcement learning (RL) was applied on a WEC device to learn the optimal PTO damping coefficient in every sea state directly from experience. Additionally, they applied the reactive control on a WEC device using artificial neural networks (ANNS) ([Anderlini et al., 2017b](#)). This was used to map the significant wave height, wave energy period, and the PTO damping and stiffness coefficients to the mean absorbed power and maximum displacement. Similarly, a model free FLC method was applied on a WEC system, as described in [Schoen et al. \(2011\)](#). As generally known, the rule-base for the FLC is constructed according to the physical characteristics of the system. In other words, a more efficient rule-base can be achieved by gaining a thorough understanding of the system. In this thesis, instead of constructing the rule-base by using experience from linear model ([Schoen et al., 2011](#)), the rule-base for the 1/50 scale PAWEC device is designed based on the CFD wave tank tests (see Chapter 5). The corresponding work of the FLC implementation on the PAWEC device is described in Chapter 6.

2.5 Summary

Inspired by the PAWEC background described in this Chapter, this thesis focuses on a study of the designed 1/50 scale PAWEC device operating in the heave mode (see Fig. 1.8). As mentioned in Section 1.3, one objective of this thesis is to gain thorough knowledge of the non-linear behaviors of the designed PAWEC device in order to derive a faithful non-linear mathematical modeling. CFD wave tank

testing is used to identify the non-linear mathematical model. The author of this thesis has been involved extensively in the physical wave tank experimental work, leading to important results about the significance of viscous effects. This is done in relation to numerical CFD modeling to achieve good model validation. Hence, the primary objective of this thesis is to develop a feasible CFD wave tank to conduct PAWEC hydrodynamic tests. This is therefore the focus of Chapter 3.

Chapter 3

CFD testing platform validation by experiments

3.1 Introduction

Referring to the thesis outline shown in Figure 1.11 in Chapter 1, the main work of Chapters 4 and 5 is developed based on the computational fluid dynamics (CFD) testing platform. In this case, first of all, a valid and favourable CFD model should be built, which is the objective of this Chapter.

A variety of commercial and open source CFD packages, e.g., Fluent, ANSYS/LS-DYNA and OpenFOAM, etc., can be used to simulate the wave propagation and fluid structure interaction (FSI) (Davidson et al., 2015a, Finnegan and Goggins, 2012, Nicolas, 2007). In this work, a three dimensional (3D) numerical wave tank (NWT) is built in the ANSYS/LS-DYNA. The fluid is governed by Navier Stokes (NS) equations and solved by the Arbitrary Lagrangian Eulerian (ALE)

formulation with the volume of fluid (VOF) approach for free surface tracking (Hallquist, 2006).

A series of tests (including the free decay test, excitation force test, free motion test and water splashing test, etc.) are conducted in the NWT. Physical experimental data from two specified wave energy conversion (WEC) devices are provided to validate the feasibility of the designed NWT in representing WEC hydrodynamics. One of the devices is the 1/50 scale PAWEC designed at University of Hull (Guo, 2017). Another device is provided by Mocean Energy, Ltd., which is awarded a Stage 2 project through the Wave Energy Scotland Novel WEC funding call (<http://www.moceanenergy.com/>). The results show that the designed 3D CFD model is capable of representing the non-linear interaction performances among the incident wave, WEC device and power take-off (PTO) system.

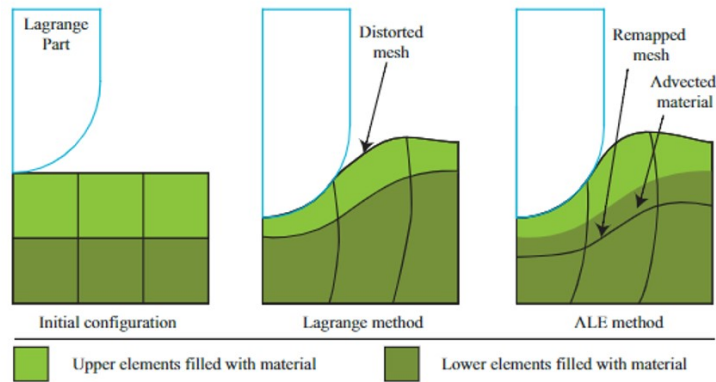
The rest of this Chapter is described as: Section 3.2 gives the governing equations of ANSYS/LS-DYNA; a 3D NWT is built to conduct CFD testing, as detailed in Section 3.3; Sections 3.4 and 3.5 describe the physical experiments and corresponding validations against the CFD data; finally, conclusive discussion are drawn in Section 3.6. Note: the physical and CFD results relate to the Mocean Energy device can be found in Appendix B.

3.2 Governing equations

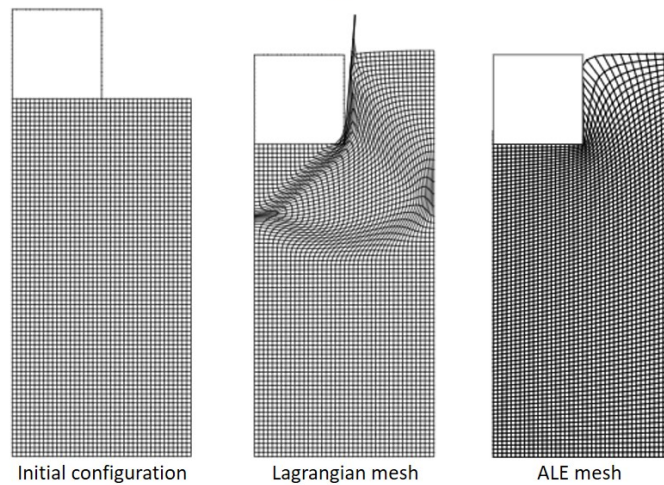
By considering fluid viscosity, the governing equations for the flow are the compressible NS equation with the continuity equation, given by:

$$\begin{aligned} \rho \left(\frac{\partial \vec{v}}{\partial t} + \vec{v} \cdot \nabla \vec{v} \right) &= -\nabla P + \nu \nabla^2 \vec{v} + \frac{1}{3} \nu \nabla (\nabla \cdot \vec{v}) + \rho \vec{g}, \\ \frac{\partial \rho}{\partial t} + \rho \nabla \cdot \vec{v} &= 0, \end{aligned} \tag{3.1}$$

where ρ , \vec{v} , P and ν represent the fluid density, velocity, pressure and kinematic viscosity, respectively. \vec{g} is the applied gravitational acceleration in the fluid.



(a)



(b)

FIGURE 3.1: A general sketch of the differences between Lagrangian and ALE approaches (Bakroon et al., 2017).

The ALE element formulation is used for solving the large deformations of the fluid during fluid-structure interaction. Figure 3.1(a) give a general idea of what the difference between the traditional Lagrangian method and the ALE approach. In the Lagrangian algorithm, nodes on meshes are attached to material points, meaning that they move and deform with the material. Therefore, Lagrangian formulation can lose accuracy at very large distortion of the elements when the fluid

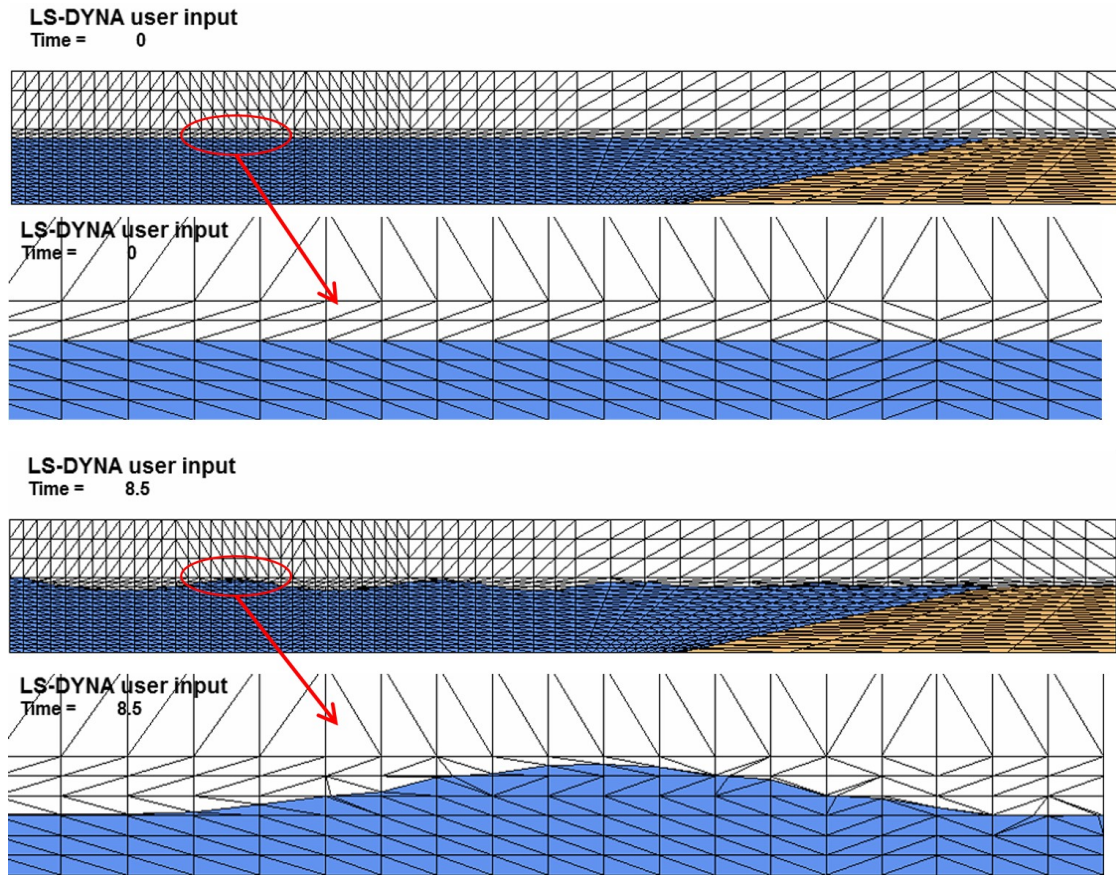


FIGURE 3.2: A sketch of the ALE mesh update while wave propagating.

has large deformation, as shown in Figure 3.1(b). Conversely, ALE method adopts another two steps to solve the distorted elements: the remap step and the advection step. The remap step interpolates the mesh into a modified mesh to obtain a new better localization for the distorted mesh. The advection step lets the material to flow to the new modified mesh. Therefore, ALE has been successfully applied to solve large deformation, as shown in Figure 3.1(b) (Bakroon et al., 2017). Figure 3.2 clearly shows an example of the mesh update while wave propagating based on ALE approach. The fluid structure interaction (FSI) coupling is calculated by the penalty method, which solves the coupling force as a spring-damper system. More details of the ALE NS solver with the penalty method used in ANSYS/LS-DYNA can be found in Souli and Benson (2013).

3.3 CFD model construction

A feasible and favourable NWT should have the ability to closely replicate the experimental wave tank system considering the physical configurations of the tank, WEC device, wave condition and the measuring instruments.

To achieve this, a general form of 3D NWT is built, as shown in Figure 3.3. The model is typically composed of four parts: (i) the paddle wave-maker for wave generation (ii) the water and air domains for wave propagation; (iii) the interaction zone for wave-WEC-PTO interaction; (iv) the artificially sloped beach for wave dissipation. In this work, the PTO action is simulated in the NWT by introducing a linear damper component. Note that: the physical wave-maker in the UoH wave tank is piston type. However, it is found that by using piston wave-maker in the numerical wave tank, the generated wave can be quite unstable after a while, e.g., after 10 s. Conversely, the paddle wave-maker shows better ability in generating stable wave for a longer duration. For example, 30 s of stable numerical wave can be achieved by paddle wave-maker (see Figure 3.11). This can be associated with the fact that the paddle wave-maker produce the water particles to obey orbital motion decaying with depth. This follows the physics of the ocean waves. However, piston wave-maker produces the water particles in all depths to have almost the constant horizontal motions. This would leads to large amount of energy accumulation while wave propagating and results in unstable wave. Therefore, the paddle wave-maker is applied in the numerical wave tank.

Several techniques used for constructing the CFD model are summarized as follows:

Remark 1: boundary descriptions

As generally known, due to the existence of walls in the physical wave tank, the hydrodynamic characteristics of a WEC device would show discrepancies compared

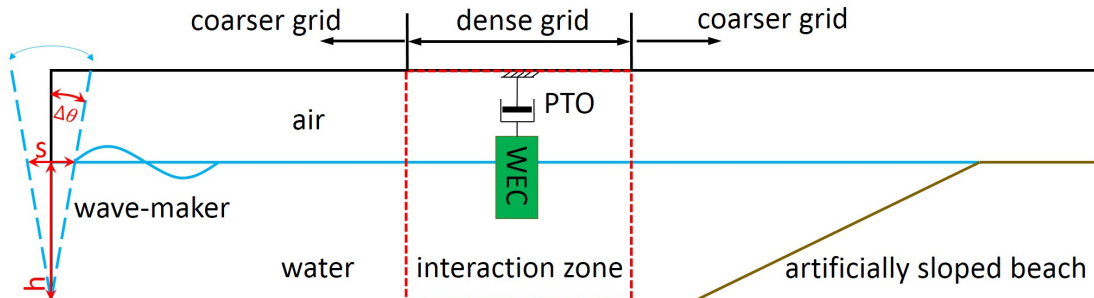


FIGURE 3.3: A general sketch of the NWT built in ANSYS/LS-DYNA.

to the open sea results (Yeung and Sphaier, 1989). If the wave tank width is too small, the waves generated during WEC device oscillations would be reflected by the side walls. These reflected waves would then act on the WEC device and thereby affect the dynamic response of the WEC device to a great extent. In order to avoid the effects, theoretically, an infinitely wide NWT is required. However, it is obvious that an infinitely wide NWT cannot be modeled. Therefore, a finitely wide NWT is developed in this work by defining the two lateral walls with non-reflecting boundaries to prevent wave reflections from intervening the model and contaminating the results. In this case, the NWT with non-reflecting boundaries can be viewed as an open wide tank. The inlet boundary is defined as the wave-maker with specified displacement. The outlet and ground boundaries are assigned with static wall conditions.

Remark 2: construction of the wave-maker

A paddle wave-maker is applied in the inlet of the NWT, as shown in Figure 3.3. It is simulated by a layer of nodes allocated in the inflow boundary. For wave generation, the wave-maker is designated with prescribed angular displacement $\theta(t)$ according to the wave-maker theory as follows (Dean and Dalrymple, 1991, Ursell et al., 1960):

$$\begin{aligned}\frac{H}{s} &= \frac{4 \sinh k_0 h}{k_0 h} \frac{k_0 h \sinh k_0 h - \cosh k_0 h + 1}{\sinh 2k_0 h + 2k_0 h}, \\ \Delta\theta &= \arctan\left(\frac{s}{2h}\right), \\ \theta(t) &= \Delta\theta \sin(\omega t),\end{aligned}\tag{3.2}$$

where s is the stroke of the wave-maker; k_0 is the wave number depending upon $\omega^2 = gk_0 \tanh k_0 h$; h represents the water depth; $\theta(t)$ and $\Delta\theta$ are the angular displacement of the wave-maker and corresponding amplitude. Clearly, to generate a regular wave with specified wave height H and wave frequency ω , corresponding angular displacement $\theta(t)$ can be obtained to govern the motion of the wave-maker based on Eq. (3.2)

The regular wave is described by:

$$\lambda(t) = \frac{H}{2} \sin(\omega t).\tag{3.3}$$

To describe irregular waves, wave spectrum is adopted. The commonly used are the Pierson-Moskowitz (PM) and the JOSWAP spectra. PM is a one parameter dependent spectrum (see Eq. 3.4), describing the fully developed seas in the North Atlantic according to the local winds (Moskowitz, 1964):

$$S(\omega) = \frac{\alpha g^2}{\omega^5} e^{-0.74(g/U\omega)^4},\tag{3.4}$$

where $\alpha = 8.1 \times 10^{-3}$ and U is the wind speed at a height of 19.5 m above the sea surface. Based on the relations of significant wave height or peak wave frequency from wind speed, the PM spectra is commonly described as follows (Pierson Jr and Moskowitz, 1964):

$$S(\omega) = \frac{\alpha g^2}{\omega^5} e^{-0.032(g/H_s \omega^2)^2},\tag{3.5}$$

$$S(\omega) = \frac{\alpha g^2}{\omega^5} e^{-1.25(\omega_p/\omega)^4}, \quad (3.6)$$

where H_s is the significant wave height and ω_p is the peak wave frequency. From the Joint North Sea Wave Observation Project (JONSWAP), it is found the wave spectrum is never fully developed and continues to develop. Hence an extra and somewhat artificial factor was added to the PM spectrum in order to improve the fit to the measurements. Then the JONSWAP spectrum is developed, by adding an extra peak enhancement factor to the PM spectrum ([Hasselmann et al., 1973](#)):

$$S(\omega) = \frac{\alpha g^2}{\omega^5} e^{-1.25(\omega_p/\omega)^4} 3.3^a, \quad (3.7)$$

$$a = e^{-(\omega - \omega_p)^2 / 2\sigma^2 \omega_p^2},$$

where $\sigma = 0.07$ for $\omega \leq \omega_p$; $\sigma = 0.09$ for $\omega > \omega_p$.

In addition to H_s or ω_p , this thesis tries to understand if the width of a spectrum would have effect on the WEC performance. Hence, Ochi spectrum is used, which is an extension of the JONSWAP spectrum in order to allow to describe wider spectrum for developing seas or narrower for swell ([Ochi and Hubble, 1977](#)). The Ochi spectrum is applied to describe irregular waves, specified by the peak frequency ω_p , the significant wave height H_s and the spectral sharpness r :

$$S(\omega) = \frac{1}{4} \frac{(r + \frac{1}{4})^r \omega_p^{4r}}{\Gamma(r)} \frac{H_s^2}{\omega^{4r+1}} e^{-(r + \frac{1}{4})(\omega_p/\omega)^4}, \quad (3.8)$$

where $\Gamma(\cdot)$ is a Gamma function. Figure 3.4 demonstrates examples of the spectrum with $H_s = 0.1$ m, $\omega_p = 4.83$ rad/s and $r = 0.5, 3, 8$, respectively.

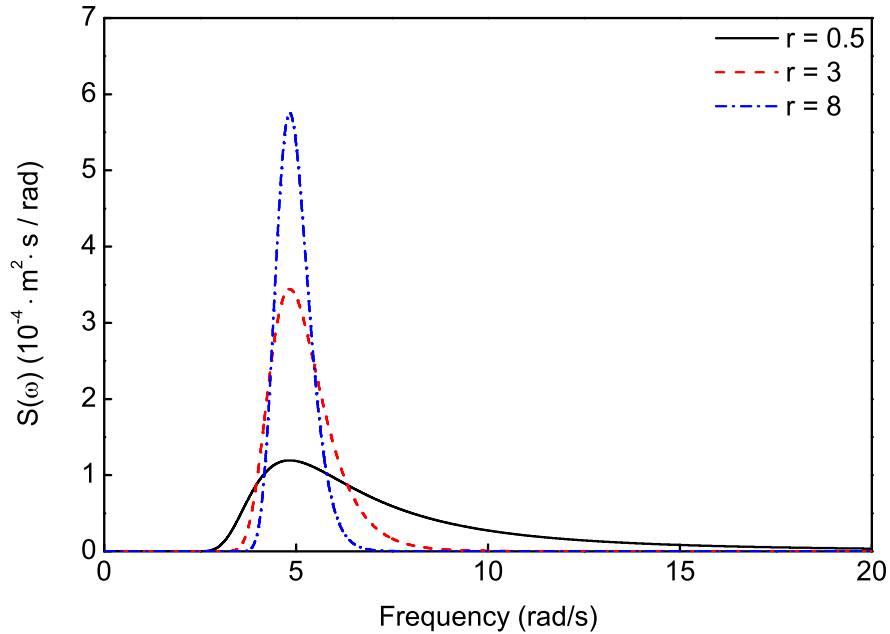


FIGURE 3.4: Three representative Ochi spectral distributions used to generate irregular waves. $H_s = 0.1$ m, $\omega_p = 4.83$ rad/s.

Remark 3: grid resolution

The hexahedral grid is used in the whole 3D CFD model. To accurately simulate the wave-WEC-PTO interaction whilst improving the computation efficiency, radiated grid solution is used in the NWT. Figure 3.5 describes a general sketch of the grid distribution. Large amounts of grids are distributed in the interaction zone. Away from this region, the mesh density is gradually decreased towards the NWT boundaries.

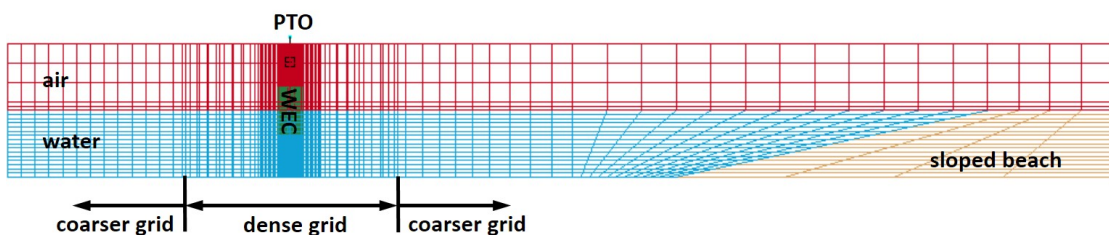


FIGURE 3.5: A representative sketch of the grid resolution.

Remark 4: generation of stable wave

To avoid wave reflection and produce stable wave motion, various techniques can be used with specified software package. For instance, in CFX or OpenFOAM, functions to change the momentum equations or increase the viscosity in the dissipation flow zone have been used (Simonetti et al., 2017, Finnegan and Goggin, 2012). However, the source function cannot be coded in ANSYS/LS-DYNA. Thus, as described in Lou (2017) and Park et al. (1999), the reflected waves were damped out by gradually increasing the mesh size toward the outlet boundary (in ANSYS/LS-DYNA). By contrast, an artificially sloped beach with specified inner damping configuration is built here in the NWT downstream to dissipate the propagating energy, as seen in Figure 3.3.

Remark 4: extraction of the output data

The displacement, velocity and acceleration of the WEC device can be directly obtained from the NWT. To monitor the numerical wave elevation, wave gauges are distributed in specified sites in the NWT corresponding to the experimental configurations. Then the wave elevation can be calculated based on the variation of the volume fraction of the water in time series. Pressure sensors are located at the WEC surface to obtain the wave excitation forces and moments.

In summary, by using the described techniques above as well as referring to the physical experimental set-up, a specified NWT can be built. Section 3.5 will describe two specified NWTs regarding two different types of physical WEC devices.

3.4 Physical experiments set-up

Physical experiment data for two kinds of WEC devices are provided, which are used to validate the NWT model in this work. One is the hinged-raft WEC device working in 7 degrees of freedom designed by Mocean Energy Ltd (<http://www.moceanenergy.com/>). Corresponding details are described in Appendix B.1. Another one is the 1/50 scale cylindrical PAWEC operating in heave motion designed by the lab colleague Bingyong Guo (Guo, 2017) and tested at UoH wave tank. This device is detailed here.

The facility used to undertake the experiments of the 1/50 scale cylindrical heaving PAWEC device is the UoH wave tank. Figure 3.6(a) shows the experimental scheme of the physical tank. 8 paddle wave-makers are allocated in the inlet boundary of the wave tank for wave generation. As seen in Figure 3.6(b), the displacement response of the PAWEC device is recorded by using the linear variable displacement transducer (LVDT). An accelerometer (Accel) is attached on the device to measure the acceleration. Five pressure sensors (PSs) are distributed at the bottom of the device to measure the hydrodynamic pressure. Five wave gauges (WGs) are provided along the wave tank to monitor the development of the wave elevation. The PAWEC device is constrained in heave motion by a vertical guide bar. In order to weaken the friction arising from the relative motion between the PAWEC device and the guide-bar, connecting components, e.g., the roller bearings are used here, as seen in Figure 3.6(c). Nevertheless, as indicated in the early experimental study (Guo et al., 2018a), the mechanical friction acting on the PAWEC device cannot be completely eliminated by using the roller bearings. Details on the PAWEC device can be found in Table 3.1.

TABLE 3.1: Physical parameters of the 1/50 scale cylindrical heaving PAWEC device at the UoH.

Diameter [m]	0.3
Height [m]	0.56
Draft [m]	0.28
Natural frequency [rad/s]	4.83
Density [kg/m³]	500
Intrinsic mass [kg]	19.7

3.5 CFD model validation

The CFD numerical model are validated by expecting to replicate the experimental data as closely as possible, according to the experimental data described in Section 3.4. Here the validation from the PAWEC at UoH is described.

Referring to Section 3.3, a 3D numerical model is built to closely reproduce the physical 1/50 scale PAWEC system, as shown in Figure 3.7. The NWT is built with: 13 m in length, 1.5 m in width (note that the physical value is 6 m, which is scaled down to 1.5 m in the NWT to reduce the computation), 0.9 m of water and 0.9 m of air. According to the physical parameters described in Table 5.1, the PAWEC device is built, located in the centred area of the NWT. The effect of the PTO system is simulated in the NWT by including a linear damper. The validation of the 3D numerical model for the PAWEC device is detailed as follows:

Step 1: mesh convergence validation

Grid resolution study is conducted from the hydrostatic pressure test to achieve suitable computation precision. For the hydrostatic pressure test, the PAWEC device is constantly forced to be semi-submerged (0.28 m beneath the still water) whilst the bottom dynamic pressure is recorded. Figure 3.8 shows the measured

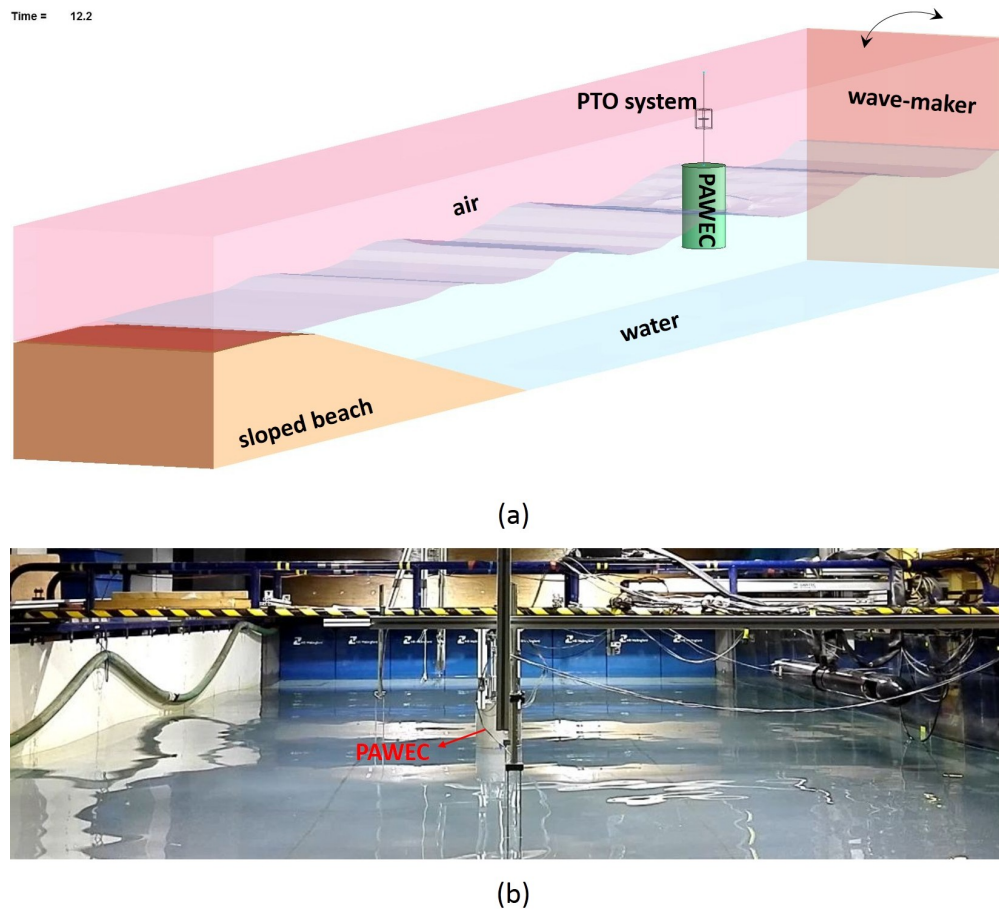


FIGURE 3.7: (a) 3D view of the numerical model built in ANSYS/LS-DYNA. Blue, pink, brown, black and green parts are water, air, sloped beach, PTO system and PAWEC device, respectively. (b) Physical scenario in the laboratory. The cylindrical buoy installed in the centred area is the experimentally tested 1/50 scale PAWEC device.

pressure against a variable grid solution in the interaction zone. As seen, the simulated pressure converges to the theoretical value of 2744 Pa as the grid size approaches 0.01 m in the interaction region. Consequently, this grid solution (see Figure 3.9) is adopted in the NWT for the numerical simulations of the 1/50 scale PAWEC device. As shown, the mesh quality out of the circle zone (interaction zone) is not good. This is designed based on the trade off between the computation and accuracy. By employing dense mesh in the interaction zone whereas coarse

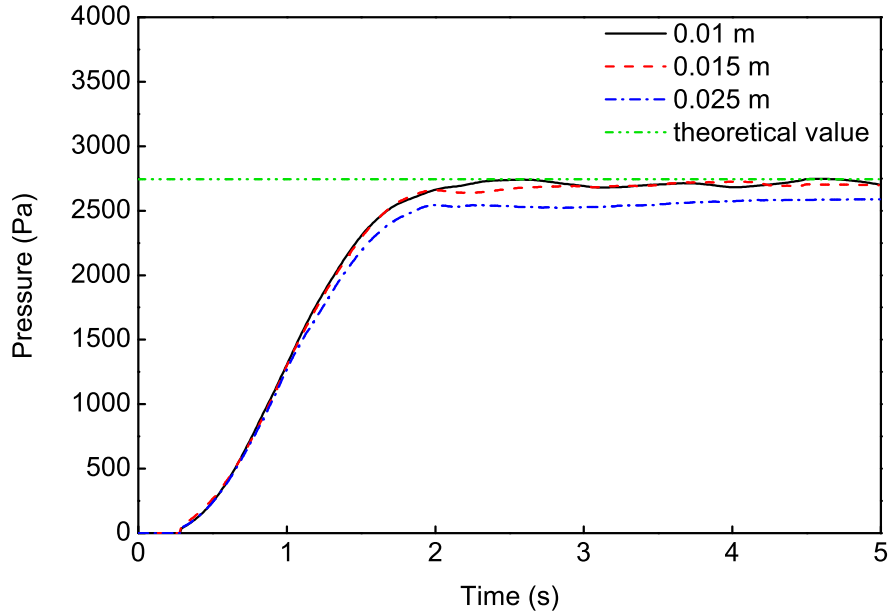


FIGURE 3.8: Mesh convergence validation via the hydrostatic pressure test. The PAWEC is forced to be semi-submerged in still water where its bottom pressure is measured against three different grid sizes in the interaction zone. The theoretical value is 2774 Pa.

mesh away this zone, it is validated (as shown in Figure 3.8) that the numerical simulation can converge to the theoretical value. Additionally, the mesh number can be significantly saved leading to efficient computation. Therefore, this work ignores the effect of the poor cell quality out of the interaction zone.

Step 2: wave generation validation

Numerical waves are generated to validate the capability of the NWT for generating stable waves. First of all, Figure 3.10(a) is offered to clarify the mesh spacing in terms of dense domain, coarse domain and wave height direction, respectively. As observed, the mesh size in the interaction zone is 0.01 m and gradually increases to 0.12 m and 0.3 m for the inlet and outlet boundaries. For wave height direction, the mesh size is kept dense (0.05m) to carefully capture the free surface flow and the grid size is increased to 0.2m away from the water-air interface boundary. As

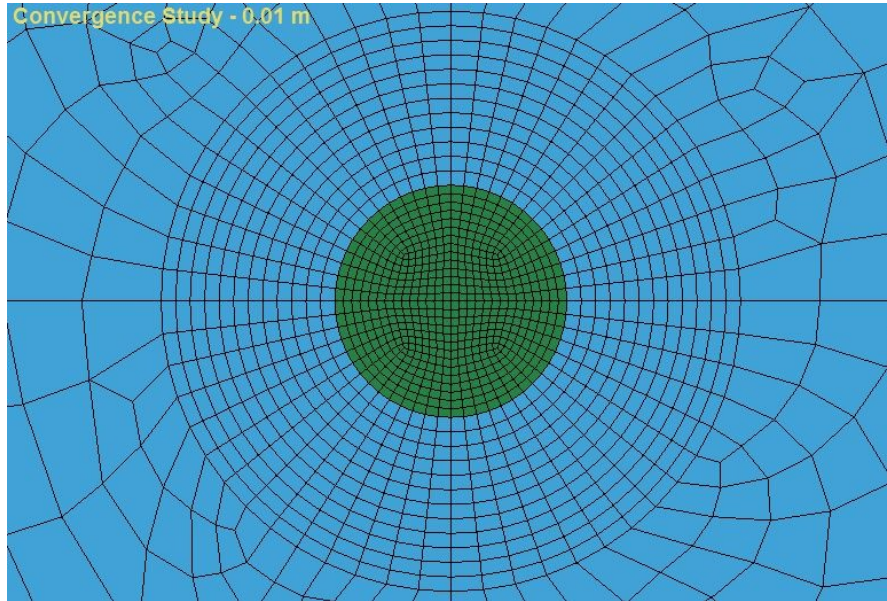


FIGURE 3.9: Cross-sectional view of the grid solution of 0.01 m in the interaction zone. Green and blue parts are the PAWEC device and adjacent flow, respectively.

a result, at least 10 grids points can be kept for one wave to preserve the wave profile, as shown in Figure 3.10(b). Figure 3.11 shows an example of the numerically generated regular wave at: $H = 0.073$ m and $\omega = 4.83$ rad/s. It can be seen that the wave amplitude and frequency basically keep consistent in a long period. In addition, to show the ability of the NWT for generating irregular waves, Figure 3.12 gives an example of the numerically generated irregular wave under: $H_s = 0.1$ m, $\omega_p = 4.83$ rad/s and $r = 8$. In summary, as expected, with the involvement of the artificially sloped beach in the downstream of the NWT, stable wave motions can be produced.

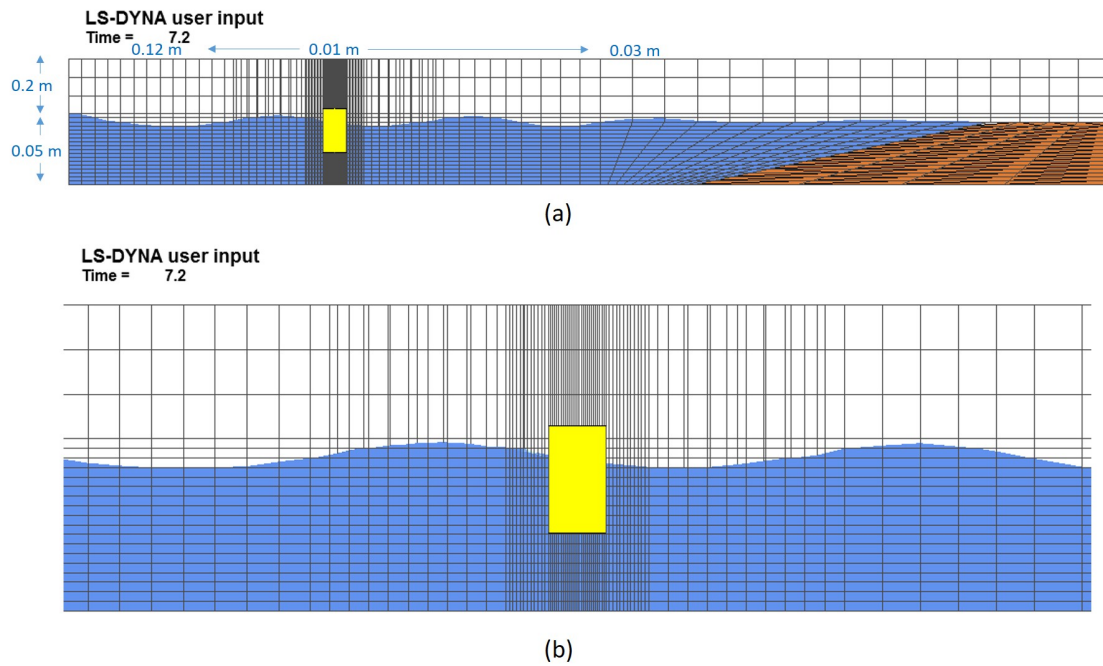


FIGURE 3.10: (a) Sketch of the relative mesh spacing in the dense and coarse zones. (b) The close-up of the wave profile.

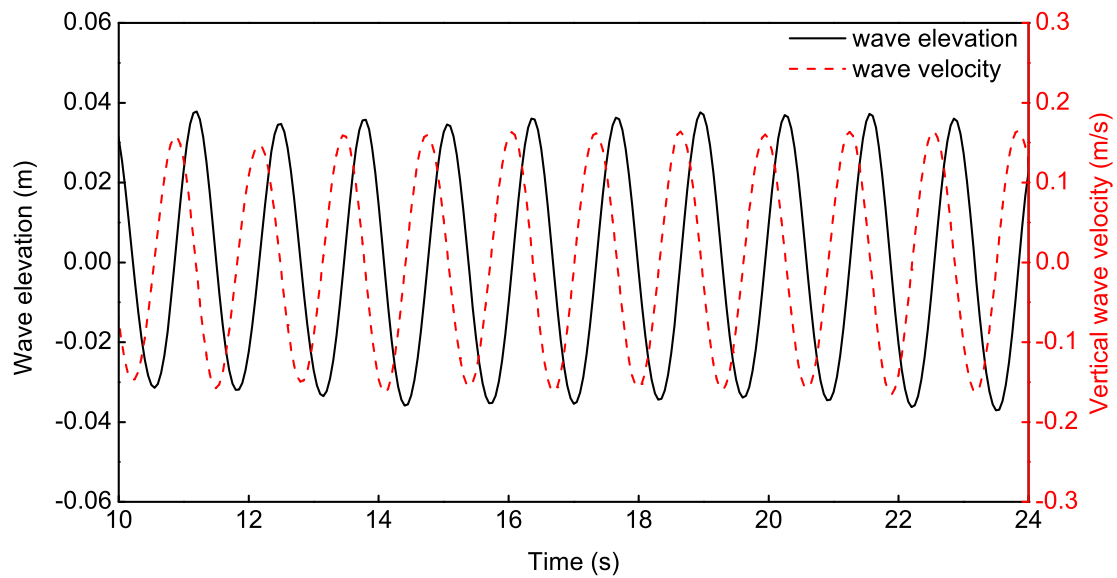


FIGURE 3.11: Numerically generated regular wave of $H = 0.073$ m, $\omega = 4.83$ s via the CFD model.

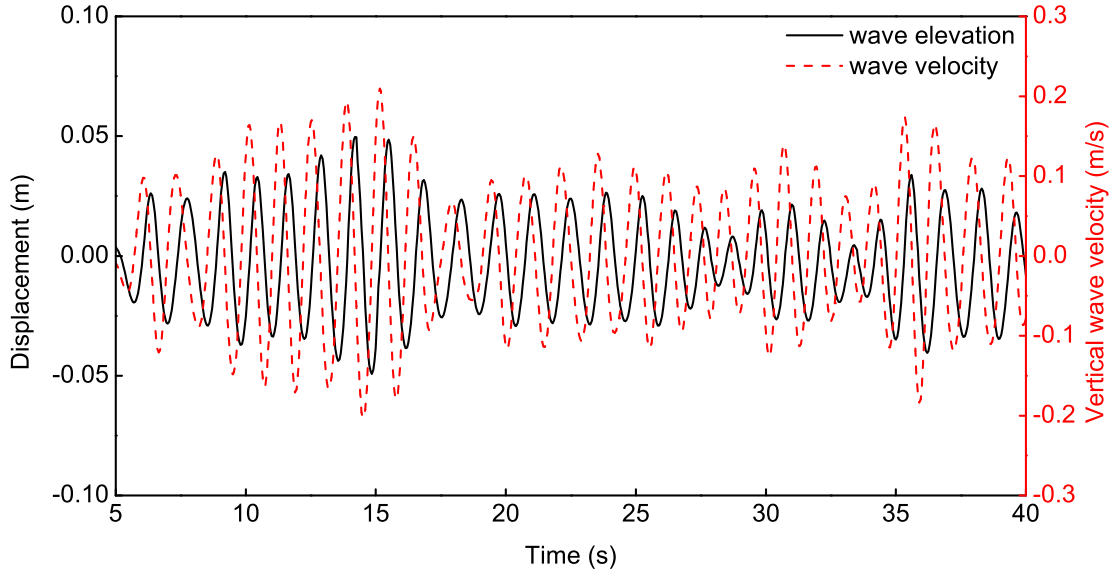


FIGURE 3.12: Numerically generated irregular wave of $H_s = 0.1\text{m}$ and $\omega_p = 4.83\text{ rad/s}$ and $r = 8$ via the CFD model.

Step 3: validation against the physical experiments

Three types of tests are further performed on the PAWEC device to verify the capability of the numerical model in representing the dynamic interaction between the wave and the PAWEC device.

Firstly, the free decay test is conducted. The device is released at an initial displacement of 0.2 m. The device heaving motion decays to its equilibrium and corresponding vertical displacement is measured. Figures 3.13 shows the comparisons of the corresponding results obtained from the CFD simulation and the experiment. Clearly, the numerical results fit well with the experimental data to a high degree. The exception is the amplitude responses after 3.5 s, showing a slight difference once the device motion decays to have relatively low velocity. Resulting from the existing friction in the physical experiments (Guo et al., 2018a), the CFD data is somewhat larger than the experimental amplitude.

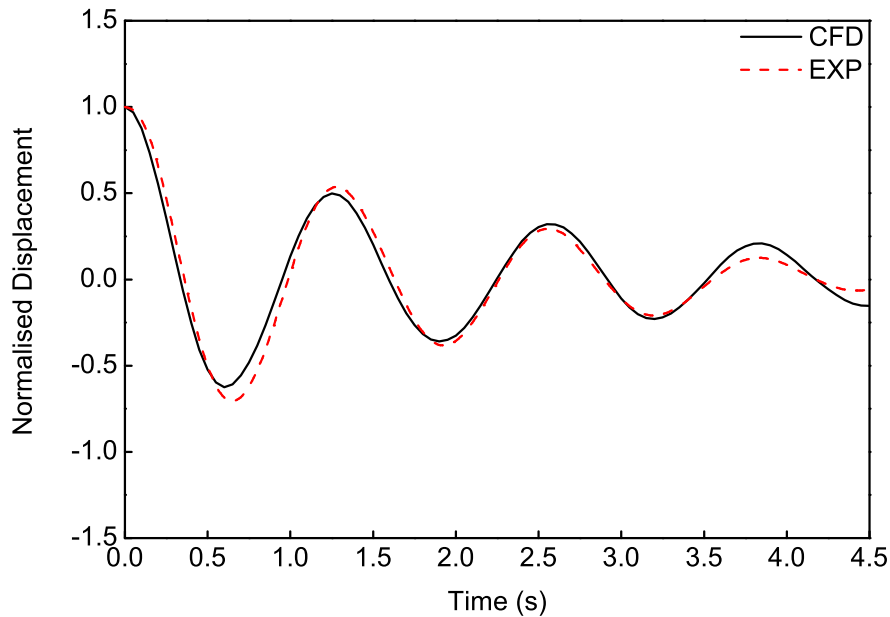


FIGURE 3.13: Time series of normalised displacement for the 1/50 scale cylindrical PAWEC under free decay test. Comparison between CFD and experimental results at an initial released displacement of 0.2 m. EXP = experimental results.

Secondly, in the excitation force test, the PAWEC is constrained at its equilibrium and experiences varying regular waves. The conditions of the tested regular waves are: wave height of 0.073 m and frequencies ranging from 3 to 7 rad/s. For each case the wave excitation force imposed on the device is measured, as shown in Figure 3.14. As observed, the CFD results are in good agreement with the experimental data.

Thirdly, the free motion test is conducted. The PAWEC is stimulated into oscillation in heave by varying regular waves and its displacement is recorded at each case given in Figures 3.15. As observed, the CFD model predicts comparable results against the experiments. In particular, the numerically predicted resonant frequency fits well the experimental prediction. The exception is the numerical amplitude response RAOs shows higher than the experimental data, by up to 30%

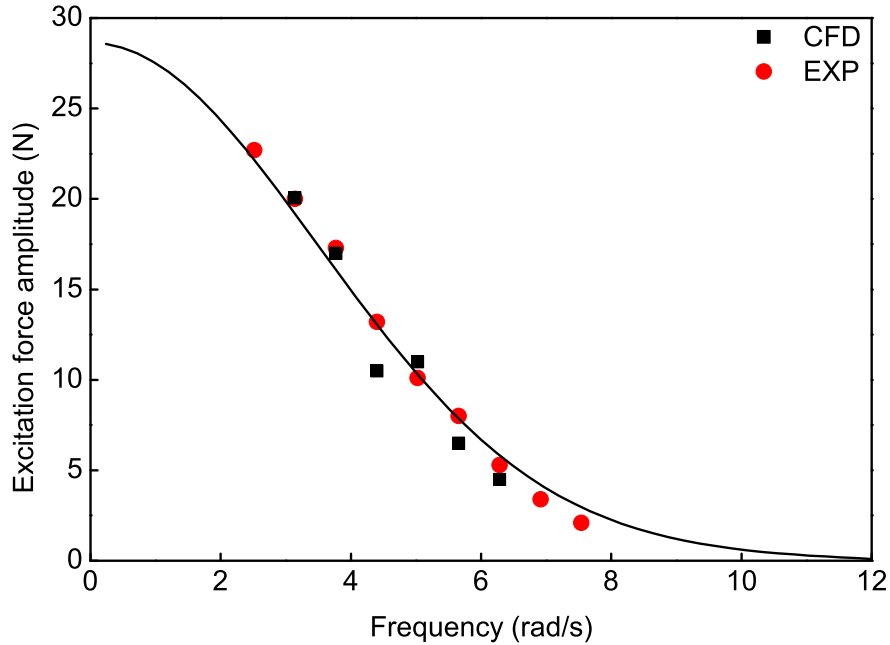


FIGURE 3.14: The excitation force modulus imposed on PAWEC against wave frequency at $H = 0.073$ m. Comparison of results from CFD model and experiment. The solid fitting line is plotted for trending reference

around resonance ($4.5 < \omega < 5.5$ rad/s). This is mainly attributed to the indispensable mechanical friction force occurring at large oscillations in the physical tests, which has been discussed in the early work (Guo et al., 2018a).

Overall, there exists good agreement between the CFD and experimental results. This suggests that the developed CFD model is capable of presenting the dynamic performances of the 1/50 scale PAWEC device. Since the considered PAWEC is a axisymmetric device, a half NWT can be employed for parts of the tests (e.g., the free motion test) in order to save computation time. The details of the validation of the half NWT can be found in Appendix A

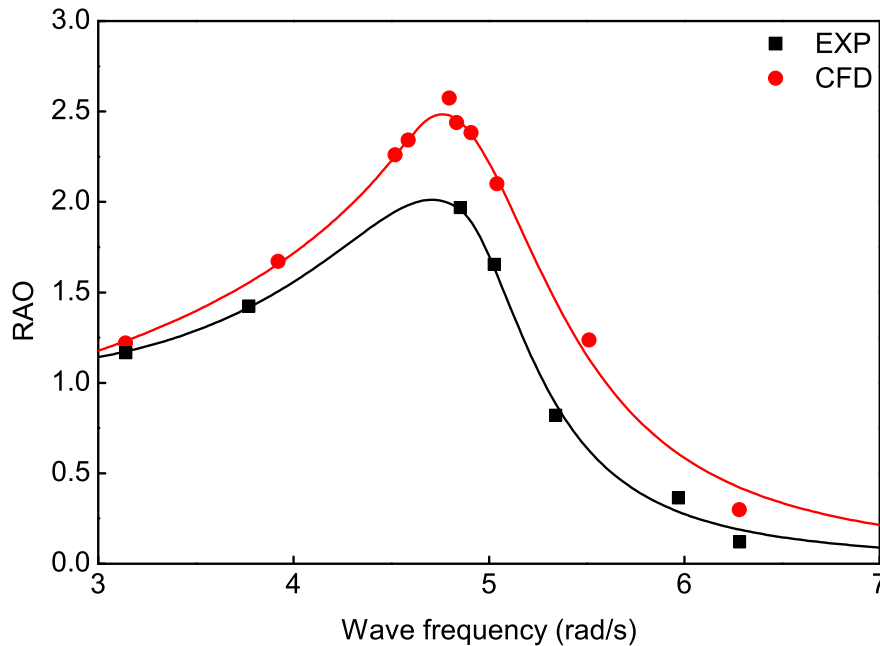


FIGURE 3.15: RAO versus wave frequency for the 1/50 scale cylindrical PAWEC obtained via CFD and experimental tests at $H = 0.073$ m. The solid fitting lines are plotted for trending references.

3.6 Conclusions

This Chapter details the construction procedure of a 3D numerical model by using the software package ANSYS/LS-DYNA. The model is used to simulate the non-linear hydrodynamics of a WEC device in response to the incident waves. Experimental data from the 1/50 scale cylindrical PAWEC in heave motion from UoH are provided for the validations of the developed CFD model. A series of wave tank tests are implemented, including free decay test, excitation force test, free motion test. The results show that the developed CFD model has a great ability of reproducing the experimental wave tank test. This suggests that a well designed CFD model can be an effective tool to present the physical hydrodynamic performances of various WEC devices (e.g., having complicated geometry profiles; operating in multi-degrees of freedom; etc.).

As generally known, the wave-PAWEC interaction is typically non-linear, especially at large oscillations. Therefore, CFD or/and experimental methods are highly recommended for physically predicting the PAWEC performances. However, these approaches are not straightforward for the control strategy implementations for maximizing the conversion efficiency. In this case, the conventional linear mathematical modeling are popularly introduced as the WEC hydrodynamic plant for control strategy design. However, this method has a main drawback that it becomes less effective in predicting the WEC performances at large oscillations. To overcome the limitation, Chapter 4 uses the validated CFD model to identify a non-linear mathematical modeling for the 1/50 scale PAWEC at the UoH. Furthermore, the proposed non-linear modeling will be used as the PAWEC hydrodynamic plant for control strategy implementation, as given in Chapter 7.

Chapter 4

Verification of PAWEC non-linear modeling using CFD data

4.1 Introduction

Figure 4.1 shows a general schematic of the 1/50 scale point absorber wave energy converter (PAWEC) system designed at the UoH, which illustrates the interactions among the waves, the PAWEC device and the power take-off (PTO) system. To gain thorough knowledge of a PAWEC system, it is critical to identify an effective hydrodynamic representation, which can be capable of faithfully predicting the device hydrodynamics in response to wave motions. More importantly, this wave-PAWEC interaction plays an important role in affecting the PTO design and the control system development (Son and Yeung, 2017, Goggins and Finnegan, 2014, Hals et al., 2011b, DelliColli et al., 2006).

The linear mathematical modeling derived from the boundary element method (BEM) is widely adopted to predict the hydrodynamic performances of a wave

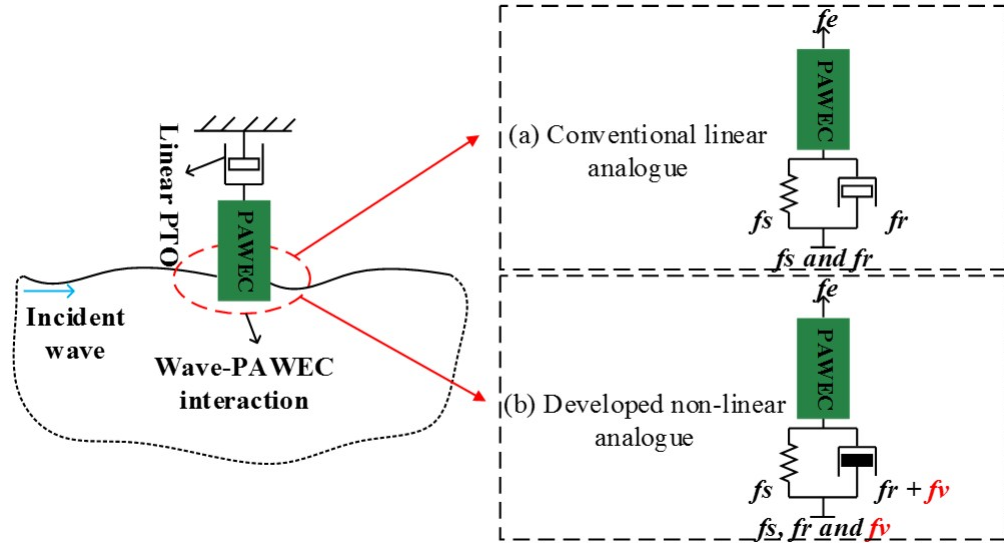


FIGURE 4.1: A general schematic of the 1/50 scale PAWEC system. (a) Conventional linear analogue of the wave-PAWEC interaction. (b) Developed non-linear analogue of the wave-PAWEC interaction. The non-linear viscous factor f_v is identified by the CFD data in this work.

energy conversion (WEC) device (Falnes, 2002, Journée and Massie, 2000). This linear model is limited by assuming:

- (i) the wave dynamics are linear;
- (ii) the WEC device motion is small;
- (iii) the effective diameter of the WEC device is comparable to the incident wave length, etc.

Therefore, in the linear approach the dynamic interaction between the WEC device and the incident wave can be simplified as a linear spring-damper system, as shown in Figure 4.1(a). By doing this, several advantages can be offered. Primarily, it conveniently predicts the hydrodynamics of a WEC device in both the frequency and time domains (Taghipour et al., 2008, Yu and Falnes, 1995). Secondly, it facilitates the integration of modeling with control analysis and design as

a WEC hydrodynamic plant (Son and Yeung, 2017, Brekken, 2011, Babarit and Clément, 2006). Nevertheless, by excluding the existing non-linearities in practice, the linear approach has a serious drawback. It would exaggerate the predictions of the device motion and absorbed power, in particular under the most favourable conditions, like close to resonance or at high wave heights (Jin et al., 2018, Goggins and Finnegan, 2014, De Backer, 2009). As a result, this linear approach would definitely limit the potential of the power take-off (PTO) and control strategy designs, which are the subsystems affected by the wave-WEC interaction.

To overcome this limitation, this Chapter aims at developing a non-linear mathematical modeling to include a more physically based wave-PAWEC interaction, as shown in Figure 4.1(b). In the developed non-linear modeling, an indispensable non-linear factor, viscosity will be considered on the study of "why and how viscosity affects the PAWEC performance". The viscous coefficient C_d is an empirical value generally predicted through experimental or computational fluid dynamics (CFD) test (Journée and Massie, 2000). In this work, this term is identified by the numerical data extracted from the CFD model developed in Chapter 3 and then validated by the physical wave tank tests at the UoH. The main contributions of this Chapter are summarized as follows:

- *A non-linear state-space model (NSSM) is developed to give a more practical prediction of the non-linear hydrodynamic performances of the 1/50 scale PAWEC.*

To clearly indicate the defects of the conventional linear model and highlight the non-linearities of the PAWEC hydrodynamics, it is first necessary to demonstrate the non-linear wave-PAWEC interaction caused by viscosity. To achieve this, the variation of the amplitude and phase performances against various regular waves is studied with the use of the linear state-space model (LSSM) and NSSM. The study is also extended to consider irregular waves. The results are validated by both CFD simulations and physical wave tank experiments. It is found that the predictions

from the linear method substantially depart from the non-linear predictions via the NSSM, NWT and the experiment. This is mainly associated with the viscosity property arising from PAWEC oscillations in response to the waves. Consequently, the results highlight that the non-linear viscous damping plays a more important role with respect to the linear radiation damping at large oscillations. This makes the case for emphasising the significance of viscosity for wave-PAWEC interaction.

- *Non-linear power capture performances of the 1/50 scale PAWEC is predicted by the NSSM.* Even though [Budar and Falnes \(1975\)](#) have suggested the resonant power conversion by the linear theory, few works study the non-linearities of the power absorption characteristics. In this work, the variation of the PAWEC power conversion efficiencies against varying parameters, e.g., the wave frequency, the wave height and the PTO damping are summarized. The results clearly indicate that the power capture performances are non-linear under different wave heights. The LSSM fails to predict the optimal PTO damping and wave condition for power maximization. This further confirms the limitation of the linear method.

The remaining part of this Chapter is described as: Section [4.2](#) formulates the interaction between a WEC device and incident regular waves under linear assumptions; Section [4.3](#) outlines the design of the conventional LSSM for the 1/50 scale PAWEC; the developed NSSM is described in Section [4.4](#); Section [4.5](#) gives the verification and validation of the proposed NSSM using numerical and physical wave tank tests; non-linear hydrodynamic and power absorption performances of the PAWEC are discussed from a series of tests, as given in Section [4.6](#); Section [4.7](#) concludes the study.

4.2 Problem formulation

Under the linear assumptions (as mentioned in Section 4.1), linear theory can be adopted. Based on Newton's second law, the linear motion of a WEC device responding to an incident wave, operating in one degree of freedom (heave motion is focused in this thesis) can be described as:

$$M\ddot{z}(t) = f_e(t) + f_r(t) + f_s(t) + f_{PTO}(t). \quad (4.1)$$

Remark 1: in the frequency domain

Through the Fourier transform of Eq. (4.1), the heaving WEC response is expressed in the frequency domain as:

$$M\ddot{Z}(i\omega) = -\omega^2 MZ(i\omega) = F_e(i\omega) + F_r(i\omega) + F_s(i\omega) + F_{PTO}(i\omega). \quad (4.2)$$

Considering the linear theory, the excitation force is proportional to the incident wave elevation (Yu and Falnes, 1995), expressed as:

$$F_e(i\omega) = A\hat{F}_e(i\omega) = A\hat{F}_e(\omega)e^{j\varphi(\omega)}. \quad (4.3)$$

where $\hat{F}_e(i\omega)$ is the complex excitation force coefficient in the frequency domain. $\hat{F}_e(\omega)$ and $\varphi(\omega)$ represent the corresponding modulus and phase angle, respectively.

The radiation force corresponds to the hydrodynamic reaction caused by the WEC oscillation against the neighbouring flow. It can be formulated as:

$$\begin{aligned}
F_r(i\omega) &= -[m(\omega)\ddot{Z}(i\omega) + B_{inv}(\omega)\dot{Z}(i\omega)] \\
&= -\dot{Z}(i\omega)[i\omega m(\omega) + B_{inv}(\omega)] \\
&= -Z(i\omega)[- \omega^2 m(\omega) + i\omega B_{inv}(\omega)].
\end{aligned} \tag{4.4}$$

The hydrostatic force F_s is caused by the mismatch between the buoyancy and gravity. For the designed heaving cylindrical PAWEC in this work, this force can be given as:

$$\begin{aligned}
F_s(i\omega) &= -K_s Z(i\omega), \\
K_s &= \rho g \pi \left(\frac{D}{2}\right)^2.
\end{aligned} \tag{4.5}$$

For a permanent-magnet linear generator, the PTO system can be simplified as a spring-damper system (Yeung et al., 2012). Then the PTO force can be modeled by:

$$\begin{aligned}
F_{PTO}(i\omega) &= -[M_{PTO}\ddot{Z}(i\omega) + B_{PTO}\dot{Z}(i\omega) + K_{PTO}Z(i\omega)] \\
&= -\dot{Z}(i\omega)[B_{PTO} + i(\omega M_{PTO} - \frac{K_{PTO}}{\omega})]. \\
&= -Z(i\omega)[(K_{PTO} - \omega^2 M_{PTO}) + i\omega B_{PTO}].
\end{aligned} \tag{4.6}$$

Substituting Eqs. (4.3) – (4.6) into Eq. (4.2), the heaving motion of a WEC in the frequency domain can be generally formulated as:

$$\begin{aligned}
\{ - [M + m(\omega) + M_{PTO}]\omega^2 + [K_s + K_{PTO}] \dots \\
+ i\omega [B_{inv}(\omega) + B_{PTO}] \} Z(i\omega) = A\hat{F}_e(i\omega).
\end{aligned} \tag{4.7}$$

Substituting $M_t(\omega)$ for $M+m(\omega)+M_{PTO}$; K for K_s+K_{PTO} and $B(\omega)$ for $B_{inv}(\omega)+B_{PTO}$, Eq. (4.7) can be replaced by:

$$[-M_t(\omega)\omega^2 + K + i\omega B(\omega)]Z(i\omega) = A\hat{F}_e(i\omega). \quad (4.8)$$

Transforming Eq. (4.8), the WEC velocity $\dot{Z}(i\omega)$ is obtained:

$$\dot{Z}(i\omega) = i\omega Z(i\omega) = \frac{A\hat{F}_e(i\omega)}{i[\omega M_t(\omega) - K/\omega] + B(\omega)}. \quad (4.9)$$

It should be noted that when the imaginary part (i.e., mechanical reactance) vanishes, the resonance can be achieved at $\omega = \omega_0 = [K/M_t(\omega_0)]^{1/2}$ (ω_0 is the undamped natural frequency). It is clear that at resonance:

- (i) there is no phase difference between the the WEC velocity and the wave excitation force;
- (ii) the magnitude of the device velocity would reach its maximum if both \hat{F}_e and $B(\omega)$ have negligible variations with ω .

Transforming Eq. (4.9), the response amplitude operator (RAO) is obtained:

$$\text{RAO} = \frac{|Z(i\omega)|}{A} = \frac{\hat{F}_e(\omega)}{|-\omega^2 M_t(\omega) + K + j\omega B(\omega)|}, \quad (4.10)$$

It should be noted that by ignoring the variations of both $\hat{F}_e(\omega)$ and $B(\omega)$ against ω , the derivation of ω can determine that the maximum RAO is achieved at $\omega = \omega'_0 = [\omega_0^2 - B_{\omega'_0}^2/2M_t(\omega'_0)^2]^{1/2}$. It is noticeable that ω'_0 is smaller than ω_0 since the existence of the damping term $B_{\omega'_0}^2/2M_t(\omega'_0)^2$ (Falnes, 2002).

To summarize, in the conventional linear theory:

(i) firstly, by ignoring the non-linearities, only the linear radiation damping $B_{inv}(\omega)$ is considered. However as indicated by [Son et al. \(2016\)](#), [Beatty et al. \(2015\)](#), the radiation damping is negligible compared to the non-linear damping.

(ii) secondly, the $\hat{F}_e(i\omega)$ is almost in phase with the incident wave at low wave frequencies ([Guo et al., 2018b](#), [Yu and Falnes, 1995](#)).

Thus considering the linear theory (through Eqs. (4.9) and (4.10)), when resonance is reached the following optimal WEC performance criteria can be achieved together:

- ω'_0 has little or no difference relative to ω_0 ;
- both the RAO and velocity values reach the maximum;
- the WEC velocity is in phase with the excitation force;
- the WEC velocity is nearly in phase with the wave elevation;
- the WEC displacement response lags by approximately 90° relative to the regular wave elevation motion;
- the WEC power reaches its maximum at $\omega/\omega_0 = 1$ and $B_{PTO} = B_{hyd} = B_{inv}$.

Question: *whether or not all of the optimal criteria listed above are still valid at the so-called resonance ($\omega = \omega_0$) when the practical non-linear factors are considered?* This question is carefully discussed in Section 4.6.

Remark 2: in the time domain

Cummins (1962) derived the motion of a heaving WEC within the time domain by taking the inverse Fourier transform of Eq. (4.8), given as:

$$\begin{aligned} (M + M_{PTO} + m_\infty)\ddot{z}(t) + \int_0^t k_r(t - \tau)\dot{z}(\tau)d\tau\dots \\ + B_{PTO}\dot{z}(t) + Kz(t) = \int_{-\infty}^{\infty} k_e(t - \tau)\eta(\tau)d\tau, \end{aligned} \quad (4.11)$$

where

$$f_r(t) = m_\infty\ddot{z}(t) + \int_0^t k_r(t - \tau)\dot{z}(\tau)d\tau, \quad (4.12)$$

and

$$f_e(t) = \int_{-\infty}^{\infty} k_e(t - \tau)\eta(\tau)d\tau. \quad (4.13)$$

Note that:

- k_r is the impulse response function (IRF) of the radiation force, which is causal. Through the inverse Fourier transform of the frequency dependent inviscid radiation damping coefficient $B_{inv}(\omega)$, k_r can be calculated (Ogilvie, 1964):

$$k_r(t) = \frac{2}{\pi} \int_0^{\infty} B_{inv}(\omega) \cos(\omega t) d\omega. \quad (4.14)$$

• k_e is a non-causal function, known as the IRF of the excitation force. Through the inverse Fourier transform of the frequency dependent complex excitation force coefficients $\hat{F}_e(i\omega)$, k_e can be obtained (Ogilvie, 1964):

$$k_e(t) = \frac{1}{\pi} \int_0^\infty \left[\text{Re}(\hat{F}_e(i\omega)) \cos(\omega t) - \text{Im}(\hat{F}_e(i\omega)) \sin(\omega t) \right] d\omega. \quad (4.15)$$

Since $k_e(t)$ is a non-causal function (Yu and Falnes, 1995), this indicates that the physical excitation force imposed on the floater is not caused by the wave motion measured at the device location, but the wave motion in future. Therefore, the causalization method in Yu and Falnes (1995) together with a time horizon of wave prediction is used to obtain the wave excitation force in this work.

For regular waves, the power absorption efficiency can be given as (McCormick, 2013):

$$\begin{aligned} \bar{P} &= \frac{1}{T} \int_0^T B_{PTO} \dot{z}(t)^2 dt, \\ P_{wave} &= \frac{1}{4\omega} \rho g^2 A^2 D, \\ C &= \frac{\bar{P}}{P_{wave}}. \end{aligned} \quad (4.16)$$

As seen from Eq. (4.16), the power conversion is dependent on both the device motions $\dot{z}(t)$ and the used PTO damping B_{PTO} . In the linear theory, it is well known that the maximum conversion efficiency is achieved at $\omega/\omega_0 = 1$ when $B_{PTO} = B_{hyd}$, i.e., $B_{PTO} = B_{inv}$ (Budar and Falnes, 1975).

4.3 LSSM design for the 1/50 scale PAWEC

According to the formulations of the linear theory expressed in Section 4.2, the LSSM for the 1/50 scale heaving PAWEC can be obtained, as detailed in this Section. First of all, a 4-order state-space model is identified to approximate the radiation force, as described in Section 4.3.1. Section 4.3.2 details the excitation force model expressed by a 6-order system with a 1 s wave prediction via AR model. Consequently, the LSSM is proposed in Section 4.3.3, which is used to represent the PAWEC motions in response to the incident waves.

Based on the physical properties of the 1/50 scale cylindrical heaving PAWEC in Table 5.1, the corresponding frequency dependent hydrodynamic parameters such as m_∞ , $m(\omega)$, $B_{inv}(\omega)$, $\hat{F}_e(\omega)$ and $\varphi(\omega)$ are calculated via the BEM software ANSYS/AQWA (see Figures. 4.2 and 4.3).

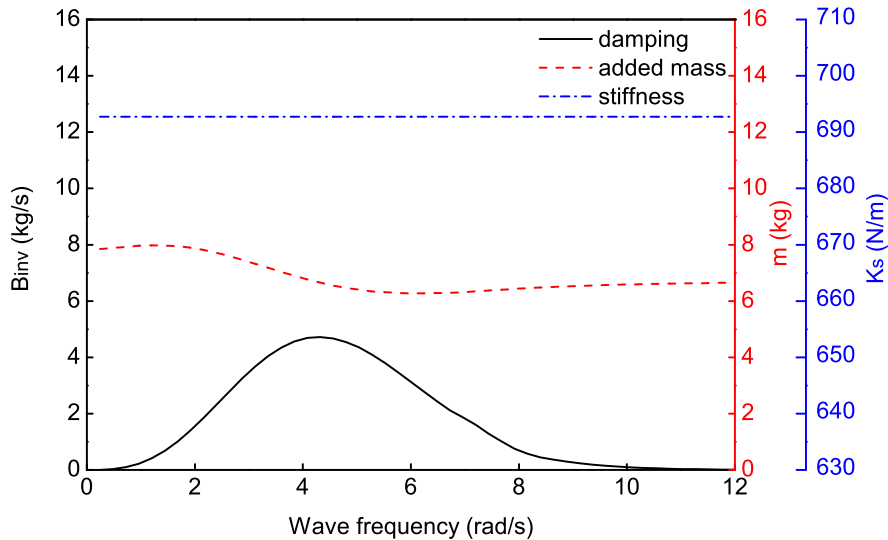


FIGURE 4.2: Added mass $m(\omega)$, inviscid radiation damping $B_{inv}(\omega)$ and hydrostatic stiffness K_s of the 1/50 scale PAWEC achieved from BEM software ANSYS/AQWA. Hence, $M_t = 26.28$ kg.

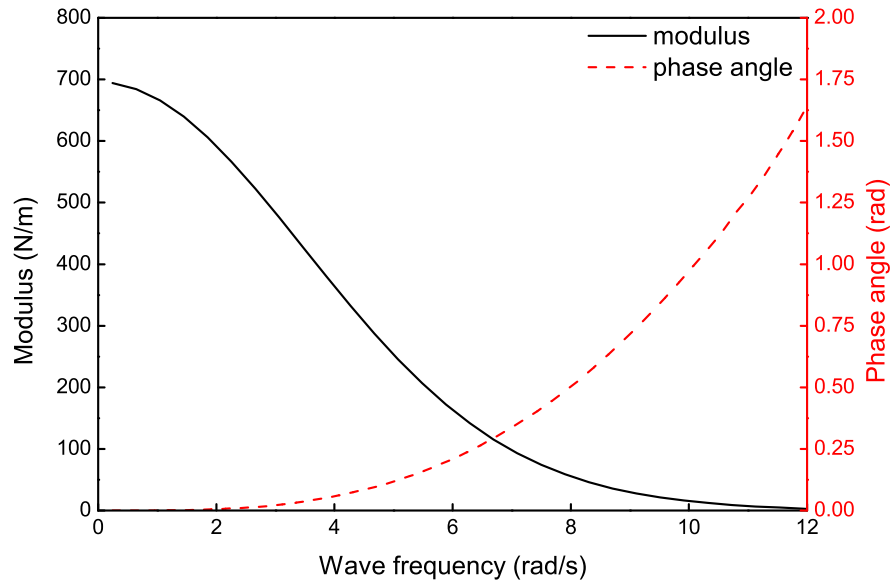


FIGURE 4.3: Modulus \hat{F}_e and phase angle $\varphi(\omega)$ of the complex excitation force coefficient $\hat{F}_e(i\omega)$ for the 1/50 scale PAWEC achieved from BEM software ANSYS/AQWA.

According to Eqs. (4.14) and (4.15), the IRFs of the radiation and excitation forces can be achieved based on the obtained hydrodynamic parameters shown in Figures 4.2 and 4.3. The achieved IRFs are described in Figures 4.4 and 4.5. As expected, $k_r(t)$ is causal and $k_e(t)$ is non-causal for $k_e(t) \neq 0$ when $t < 0$.

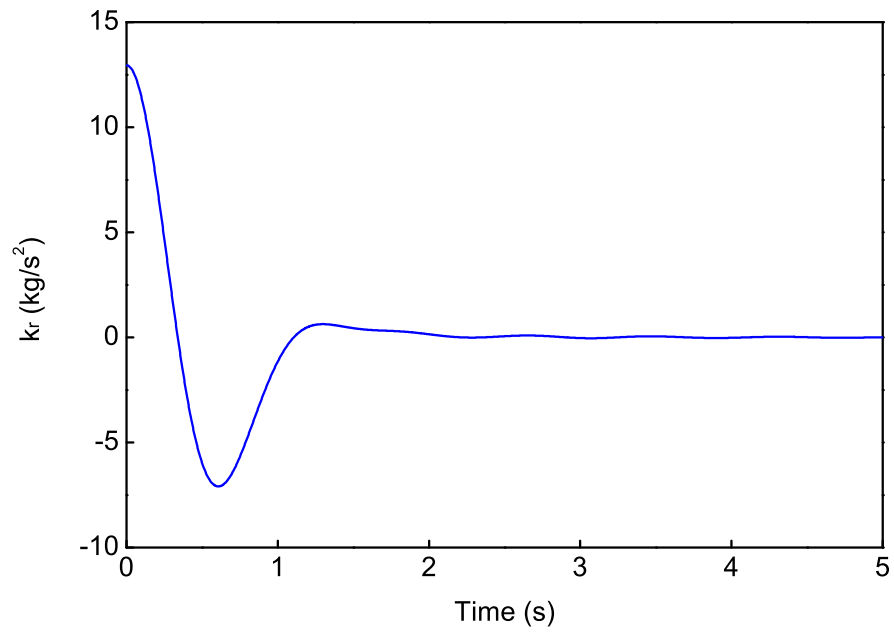


FIGURE 4.4: IRF of the wave radiation force for the 1/50 scale PAWEC.

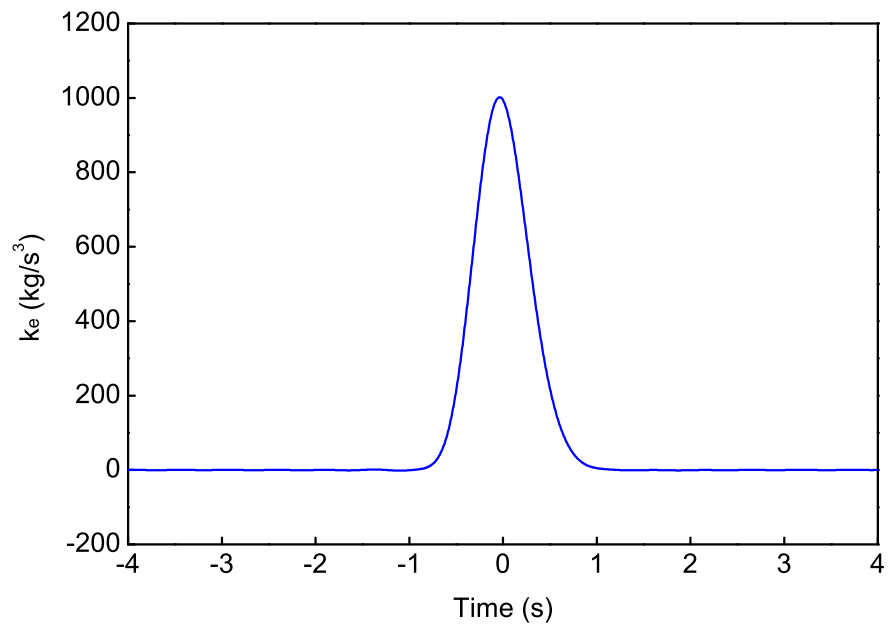


FIGURE 4.5: IRF of the wave excitation force for the 1/50 scale PAWEC.

4.3.1 State-space model of the radiation force

In order to avoid the complex calculation and inconvenient application for control strategy caused by the convolution term in Eq. (4.12) in the time domain, a linear subsystem is adopted. A state-space model is identified to approximate the convolution operation, in which the PAWEC heave velocity $\dot{z}(t)$ is set as the input and the approximation of the radiation force convolution term $f'_r(t)$ is the output. The subsystem is formulated as:

$$\begin{aligned}\dot{\mathbf{X}}_{\mathbf{r}}(t) &= \mathbf{A}_{\mathbf{r}}\mathbf{X}_{\mathbf{r}}(t) + \mathbf{B}_{\mathbf{r}}\dot{z}(t), \\ f'_r(t) &= \mathbf{C}_{\mathbf{r}}\mathbf{X}_{\mathbf{r}}(t) + \mathbf{D}_{\mathbf{r}}\dot{z}(t) \approx \int_0^t k_r(t-\tau)\dot{z}(\tau)d\tau,\end{aligned}\tag{4.17}$$

where $\mathbf{X}_{\mathbf{r}} \in \mathbb{R}^{m \times 1}$ is the state vector of the identified subsystem; $\mathbf{A}_{\mathbf{r}} \in \mathbb{R}^{m \times m}$, $\mathbf{B}_{\mathbf{r}} \in \mathbb{R}^{m \times 1}$, $\mathbf{C}_{\mathbf{r}} \in \mathbb{R}^{1 \times m}$ and $\mathbf{D}_{\mathbf{r}} \in \mathbb{R}^{1 \times 1}$ are the system matrices, respectively. A wide variety of identification methods can be applied to achieve the state-space model, as reported by [Taghipour et al. \(2008\)](#). The realization theory is used here by implementing the *imp2ss* command with the combination of the order reduction function *balmar* in MATLAB®.

In order to balance the accuracy and the computation, a 4-order state-space model is finally applied as the approximation of the radiation convolution term. The corresponding matrices of the subsystem are given as:

$$\begin{aligned}
\mathbf{A}_r &= \begin{bmatrix} -2.9050 & -4.3129 & 3.1027 & -1.0862 \\ 4.3129 & -0.0142 & 0.1668 & -0.0881 \\ -3.1027 & 0.1668 & -4.1044 & 5.2748 \\ -1.0862 & 0.0881 & -5.2748 & -2.2996 \end{bmatrix}, \\
\mathbf{B}_r &= [-3.9615 \quad 0.2639 \quad -1.8048 \quad -0.7765]^T, \\
\mathbf{C}_r &= [-3.9615 \quad -0.2639 \quad 1.8048 \quad -0.7765], \\
\mathbf{D}_r &= 0.
\end{aligned} \tag{4.18}$$

Figure 4.6 compares the radiation IRF corresponding to the identified 4-order system with the original value calculated through Eq. (4.14). As observed, the results fit well with each other. This indicates that the identified linear subsystem can be appropriate to represent the convolution term of the radiation force.

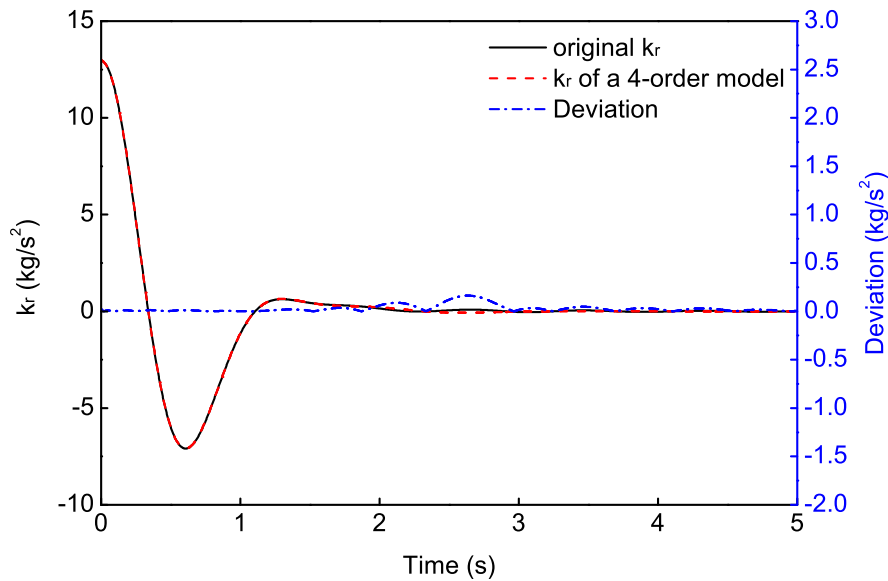


FIGURE 4.6: Comparisons for the original radiation IRF and the data from the identified 4-order subsystem.

4.3.2 State-space model of the excitation force

Similar to the radiation force, a linear subsystem is identified to approximate the convolution term of the excitation force. As observed from Figure 4.5, the excitation force kernel function $k_e(t)$ appears to be non-causal. To overcome this, $k_e(t)$ should be first causalized. This can then be formulated as:

$$\begin{aligned} f_e(t) &= \int_{-\infty}^{\infty} k_e(t - \tau)\eta(\tau)d\tau \\ &= \int_{-\infty}^{\infty} k_e(t - t_c - \tau)\eta(t_c + \tau)d\tau. \end{aligned} \quad (4.19)$$

It can be seen from Eq.(4.19) that an appropriate t_c time-shift of excitation force kernel function and a wave prediction in t_c horizon are required for the causalization. Then, a following question should be solved: "what is the magnitude of t_c ?"

To solve this, the errors of the causalized $k_e(t)$ with respect to the original data against varying causalizing time t_c are calculated based on Figure 4.5. Figure 4.7 shows the corresponding results. Referring to Figure 4.5, $k_e(t)$ is negligible for $t < 1$ s. This confirms the data shown in Figure 4.7 that the causalized $k_e(t)$ would be appropriate enough to retain the information of the original $k_e(t)$ with an error of less than 0.065% when t_c is larger than 1 s. Consequently, $t_c = 1$ s is chosen in this work.

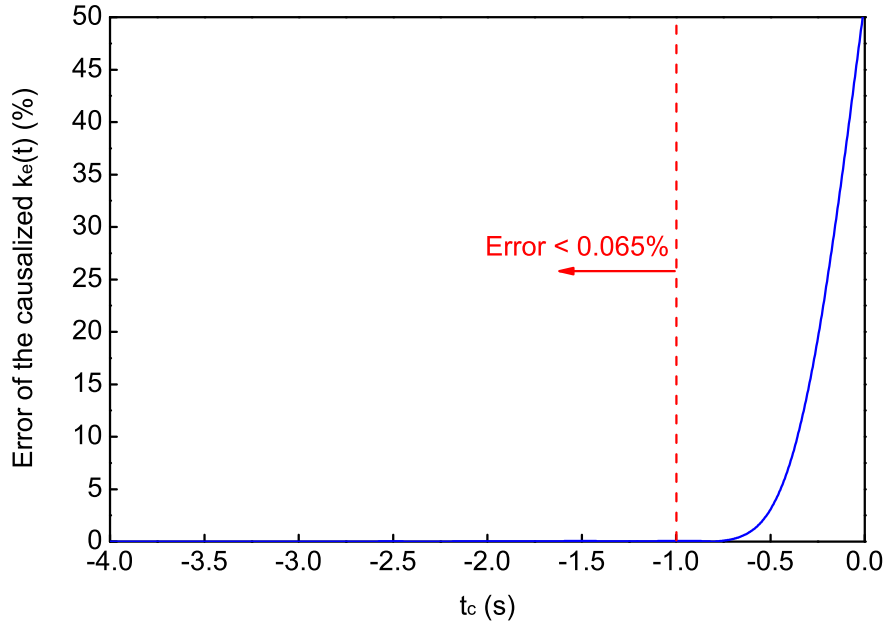


FIGURE 4.7: Error of the causalized $k_e(t)$ related to the original data against the causalizing time.

By applying $t_c = 1$ s, a 6-order linear state-space form is used to approximate the causalized excitation force. The corresponding matrices of the subsystem are given as:

$$\mathbf{A}_e = \begin{bmatrix} -0.2484 & 1.7791 & -0.5596 & -0.5514 & -0.3012 & -0.1659 \\ -1.7791 & -0.9521 & 3.1112 & 1.1397 & 0.8203 & 0.4191 \\ -0.5596 & -3.1112 & -1.9824 & -4.2878 & -1.6059 & -0.9585 \\ 0.5514 & 1.1397 & 4.2878 & -3.1706 & -5.2740 & -1.9340 \\ -0.3012 & -0.8203 & -1.6059 & 5.2740 & -4.3491 & -6.2398 \\ 0.1659 & 0.4191 & 0.9585 & -1.9340 & 6.2398 & -4.9418 \end{bmatrix}, \quad (4.20)$$

$$\mathbf{B}_e = [17.2019 \quad 25.7057 \quad 24.1690 \quad -17.5354 \quad 10.6572 \quad -5.7122]^T,$$

$$\mathbf{C}_e = [17.2019 \quad -25.7057 \quad 24.1690 \quad 17.5354 \quad 10.6572 \quad 5.7122],$$

$$\mathbf{D}_e = 0.$$

As seen in Figure 4.8, the identified 6-order state-space model can be feasible to approximate the causalized subsystem.

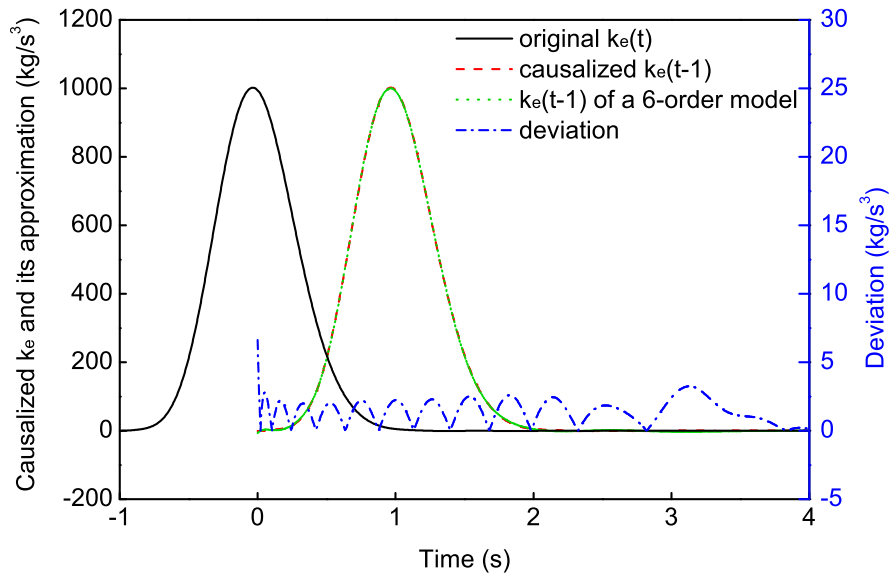


FIGURE 4.8: Comparisons of the IRFs from the original excitation force $k_e(t)$, the causalized term with $t_c = 1$ s and the corresponding approximation by the 6-order linear subsystem from Eq. (4.20).

In addition to the causalized $k_e(t)$ mentioned above, a t_c horizon of wave prediction is also required to obtain a suitable approximation of the wave excitation force, as described in Eq. (4.19). This means the input of the 6-order linear subsystem shown in Eq. (4.20) should be the wave elevation at a future time of $t_c = 1$ s.

Various approaches have been applied to realize wave prediction (Schoen et al., 2011, Fusco and Ringwood, 2010). As reported by Fusco and Ringwood (2010), autoregressive (AR) model shows great ability for predicting the waves in Irish sea. Hence, AR approach adopted in (Fusco and Ringwood, 2010) is applied in this work to predict the 1 s wave. The sample frequency is 100 Hz and hence the prediction horizon is 100 for 1 s prediction. Finally, the AR order is selected as 50 by keeping the goodness-of-fit index (Fusco and Ringwood, 2010) larger than 90 %. The order number is large due to the high sampling frequency and it can

be reduced by decreasing the sample rate. Figures 4.9 and 4.10 demonstrate two representative wave predictions via the 50-order AR model. The selected wave conditions are the irregular waves as described in Figure 3.12 with $H_s = 0.01$ m, $\omega_p = 4.83$ rad/s and $r = 0.5/8$. As observed, the 50-order AR model shows great ability in predicting the waves by fitting well with the real data, especially for a wave with narrow bandwidth (e.g., $r = 8$). More details of the corresponding study can be found in Guo et al. (2018b).

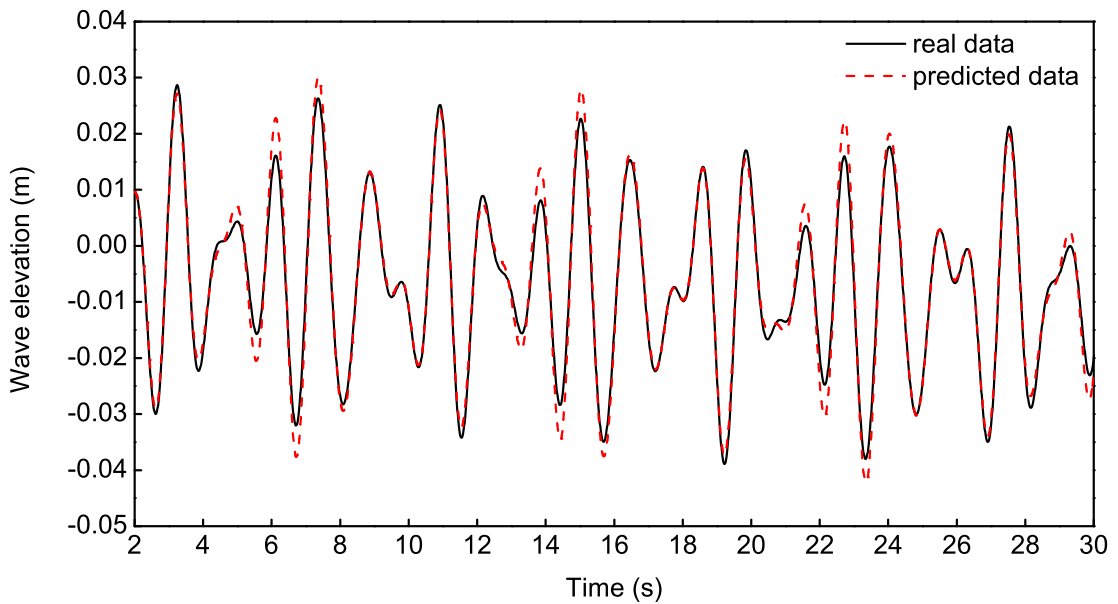


FIGURE 4.9: The real wave elevation and the predicted data based on the use of the 50-order AR model at $H_s = 0.01$ m, $\omega_p = 4.83$ rad/s and $r = 0.5$.

To clearly illustrate the requirement of wave prediction and the feasibility of the 6-order linear subsystem for the wave excitation force identification, a representative example is given in Figure 4.11. Referring to Figure 3.14, under wave condition of $H = 0.08$ m and $T = 2$ s, the magnitude of f_e is approximately 37 N and the force is nearly in phase with the incident wave. As demonstrated in Figure 4.11, the excitation force can be properly identified by using the 6-order model with 1 s of wave prediction. By contrast, the predicted excitation force totally loses accuracy in presenting the phase information in the absence of the wave prediction.

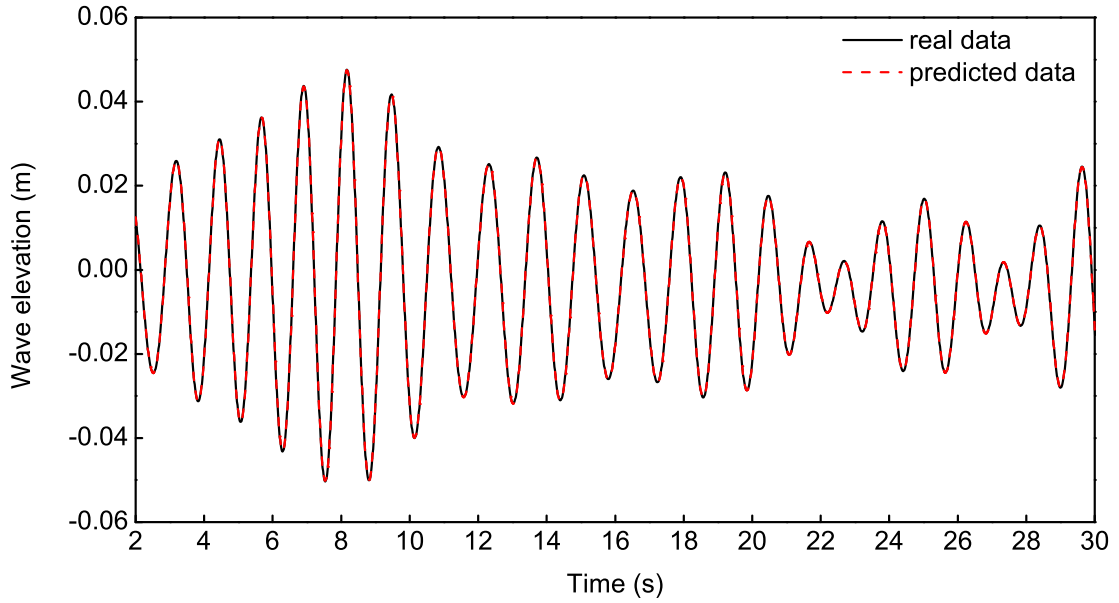


FIGURE 4.10: The real wave elevation and the predicted data based on the use of the 50-order AR model at $H_s = 0.01$ m, $\omega_p = 4.83$ rad/s and $r = 8$.

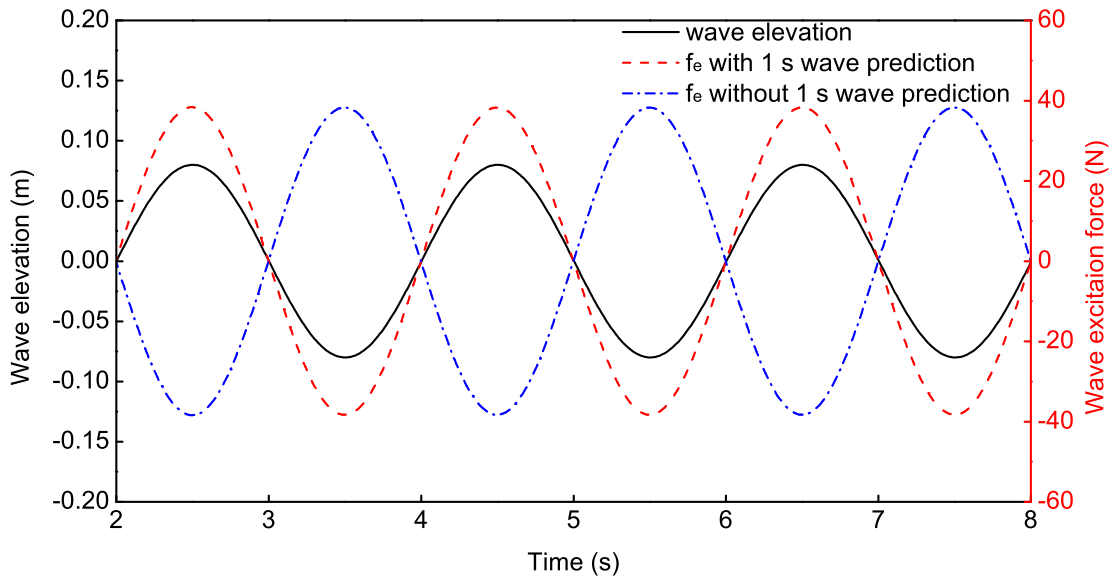


FIGURE 4.11: Time series of predicted wave excitation force with and without 1s wave prediction. Wave condition is $H = 0.08$ m and $T = 2$ s.

To summarize, when accompanied by an appropriate wave prediction, the identified 6-order causalized model can be effective in representing the relationship

between the wave and the wave excitation force, as formulated in Eq. (4.19).

4.3.3 LSSM of the PAWEC

Following Eq. (4.11) and the subsystems described in Sections 4.3.1 and 4.3.2, the LSSM representing the PAWEC hydrodynamic responses with respect to incident waves can be simulated by using a Simulink model, as shown in Figure 4.12. As it can be seen, two state space matrices (one for excitation force and one for radiation force) are constructed in order to clearly demonstrate the structure of the hydrodynamic model. The parameters applied in the LSSM can be found in Table 4.1.

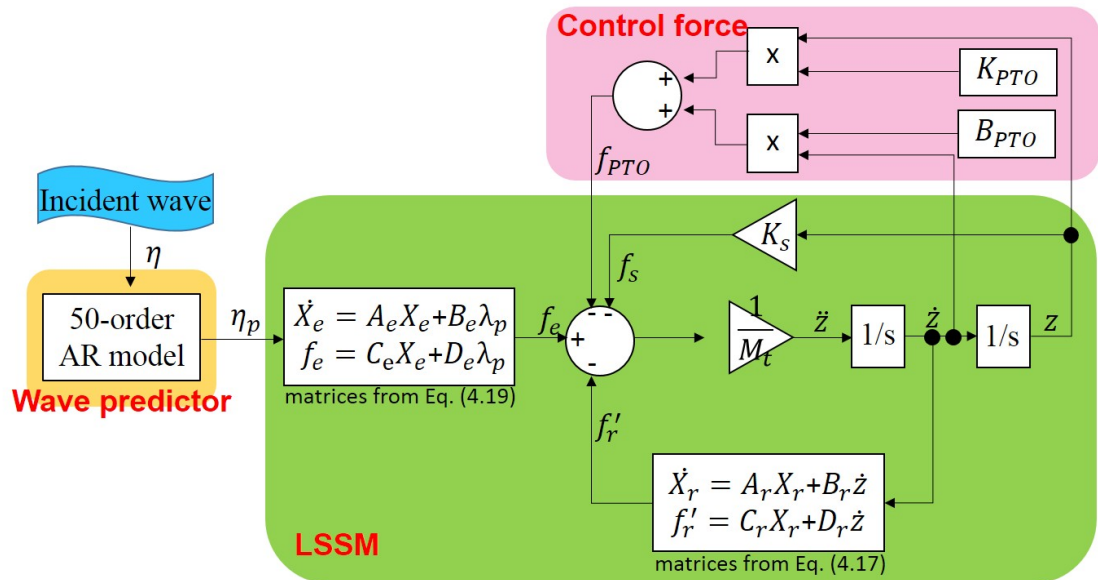


FIGURE 4.12: General Simulink scheme of the LSSM to represent the PAWEC hydrodynamic response with respect to the incident wave.

To demonstrate clearly the PAWEC performances described by the LSSM, the following representative data are given:

1. RAO and phase response

TABLE 4.1: Parameters of the 1/50 PAWEC for the LSSM.

M_t [kg]	26.28
K_s [N/m]	692.72
A_e, B_e, C_e, D_e	Eq. (4.20)
A_r, B_r, C_r, D_r	Eq. (4.18)

From Figure 4.13, the PAWEC device motion response is frequency dependent in the linear theory. The motion reaches "resonance" at a natural frequency of nearly $\omega_0 = 5.14$ rad/s, resulting in the maximum amplitude response and nearly 90° of phase lag relative to the incident wave. It is clear that the device will definitely leave and then drop back into the water when the wave amplitude is larger than approximately 0.03 m. In this situation, energy consumption is generated and would lead to the decrease of RAO. However, this case cannot be presented by the LSSM. In other words, linear theory loses effectiveness in predicting the PAWEC motion response at large oscillations.

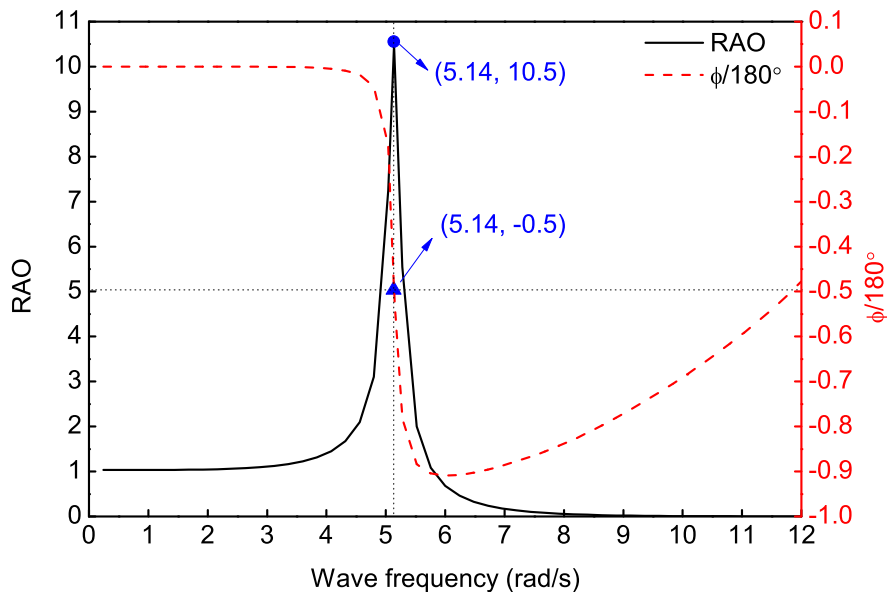


FIGURE 4.13: PAWEC amplitude and phase responses against wave frequency from LSSM.

2. power absorption efficiency

From Figure 4.14, the maximum power absorption efficiency appears at $\omega/\omega_0 = 1$ and $B_{PTO}/B_{hyd} = 1$ in the linear theory. Additionally, the maximum efficiency of 125% is found, which can be unrealistic in practice. This is one major limitation of the LSSM, namely that it would over-estimate the PAWEC power performance near resonance by employing an appropriate PTO damping (e.g., efficiency is larger than 110% with ω/ω_0 approximate to 1).

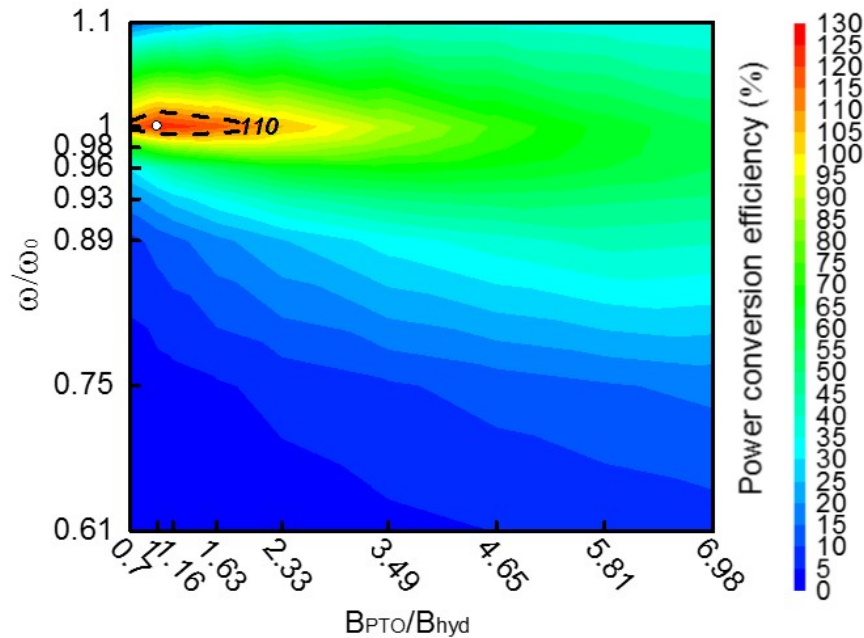


FIGURE 4.14: PAWEC power absorption efficiency against dimensionless PTO damping coefficient for different wave conditions of ω/ω_0 from LSSM, at $H = 0.073$ m. The white point represents the maximum efficiency of 125%. $B_{hyd} = 4.3\text{kg/s}$ is the inviscid radiation damping at ω/ω_0 obtained from Figure 4.2.

To summarize, the PAWEC performances are dependent on frequency in the linear theory. The optimal motion response and power capture can be achieved at resonance $\omega/\omega_0 = 1$. However, as observed from Figures 4.13 and 4.14, the predicted values are over-estimated and even unrealistic near resonance. These phenomena have also been reported by Jin et al. (2018), De Backer (2009) suggesting that

linear theory is not able to present the practical behaviors of the point absorber near resonance or at large oscillations. This can be associated with the exclusion of the non-linear dissipative factors (Guo et al., 2018a, Jin et al., 2018). Therefore, to predict practically the PAWEC behaviours at large oscillations, a NSSM is required, as discussed in the following section.

4.4 Non-linear state space model (NSSM) design for the 1/50 scale PAWEC

It is indicated by Journée and Massie (2000) that viscosity would inevitably dissipate the hydrodynamics of a slender structure whose physical property satisfies: effective diameter/wave length < 0.2 (i.e., $D/\lambda < 0.2$). For the designed 1/50 scale PAWEC, the dominant frequency to achieve efficient performance is in the range of $\omega \leq 6.24$ rad/s (see Figure 4.13). According to $\lambda \approx 2\pi g/\omega^2$ (McCormick, 2013), the minimum wave length applied to the device is approximate to 1.5 m. This implies that the designed PAWEC device with $D = 0.3$ m needs to be considered as a slender structure. In other words, the viscose effect can be indispensable and essential during the wave-PAWEC interaction. In this study, the quadratic viscous term in the Morison equation (Morison et al., 1950) is employed:

$$f_v(t) = -\frac{1}{2}\rho\pi\left(\frac{D}{2}\right)^2C_d(\dot{z}(t) - u(t))|\dot{z}(t) - u(t)|. \quad (4.21)$$

$u(t)$ represents the vertical flow velocity around the PAWEC device. In the following $\frac{1}{2}\rho\pi\left(\frac{D}{2}\right)^2C_d$ is substituted by K_v . For regular waves, this value can be approximate to $\omega A \sin(\omega t)$. Practically, the adjacent wave elevation and wave velocity can be recorded by a "wave follower". C_d is the viscous coefficient, an

empirical value. Experiments or CFD tests are widely used to predict C_d . In this thesis, numerical testing in CFD model is employed to identify the PAWEC C_d which is also validated by experiment.

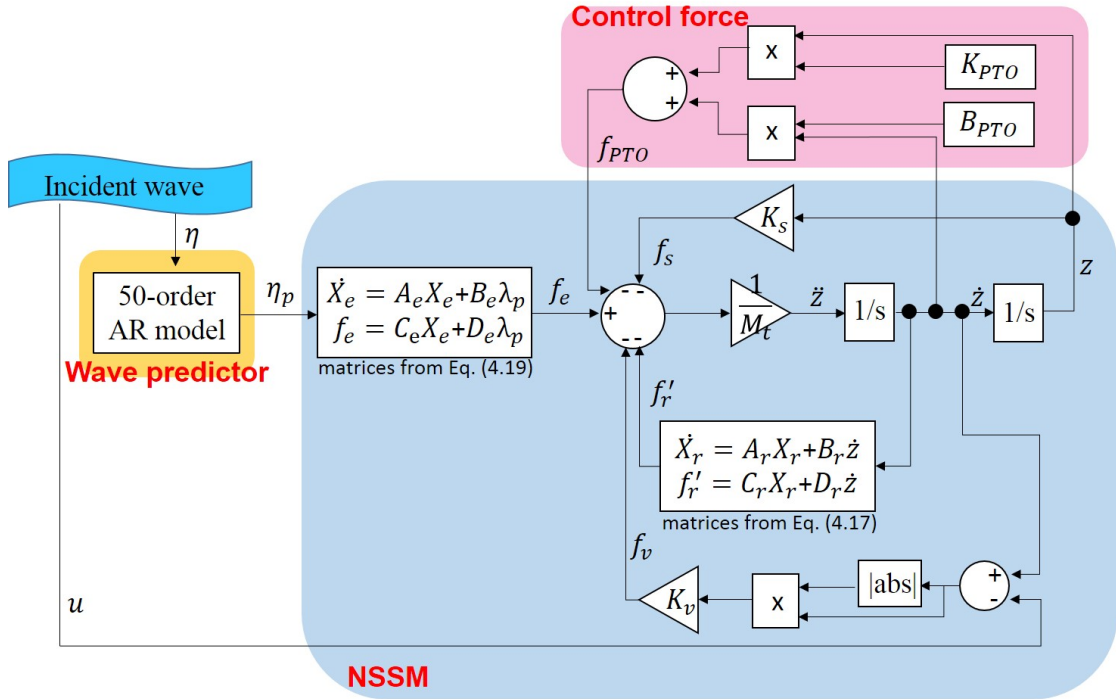


FIGURE 4.15: General Simulink scheme of the NSSM to represent the PAWEC hydrodynamic response with respect to the incident wave.

Adding the quadratic viscous force f_v into the linear Simulink structure shown in Figure 4.12, the NSSM can be achieved, as shown in Figure 4.15. Referring to Eq. (4.10), the non-linear RAO considering viscosity can now be considered equivalent to a linear form:

$$\text{RAO} = \frac{|Z(j\omega)|}{A} = \frac{\hat{F}_e(\omega)}{|-\omega^2 M_t(\omega) + K + j\omega[B_{hyd} + B_{PTO}(\omega)]|}. \quad (4.22)$$

It should be noted that B_{hyd} represents the total hydrodynamic damping coefficient by the inclusion of both the inviscid and viscous terms, which can be described as: $B_{hyd} = B_{inv}(\omega) + B_{vis}$.

From Eqs. (4.21) and (4.22), both the viscous drag f_v and the corresponding equivalent viscous damping coefficient B_{vis} show positive relationship with the motion response of the device, e.g., the relative velocity v_r between the wave and the device. In other words, a larger v_r may generate a larger f_v and B_{vis} . It is clear that the magnitude of v_r is related to both variables of ω and H . Therefore, by including the viscous term in the non-linear model, both ω and H would be the factors to affect B_{vis} and B_{hyd} , which can be described as $B_{vis}(\omega, H)$ and $B_{hyd}(\omega, H)$. In this case, the non-linear model is completely different from linear model which is only frequency dependent, e.g., $B_{hyd}(\omega)$ (i.e., $B_{inv}(\omega)$ shown in Figure 4.2). This implies that PAWEC hydrodynamic behaviors in response to incident waves should be non-linear under varying wave height.

According to Eq. (4.21), the existence of the viscosity during WEC device oscillations can be reflected by the generation of relative velocity v_r . In order to clearly prove the existence of viscosity, the CFD snapshots of the velocity vectors of both the device and the adjacent wave are given to observe the generation of v_r at different wave conditions:

Wave state 1: $H = 0.073$ m, $\omega = 3.14$ rad/s ($T = 2$ s)

This wave state corresponds to the condition known as "low wave frequency" (see Figure 4.13). As described in Figure 4.16, the PAWEC device shows to operate as a "wave follower" under this case. During oscillating in a period, the PAWEC device arrives the peak together with the adjacent wave at $t = 17$ s; afterwards the device shows synchronous tracking of the downward flow and reaches the trough at $t = 18$ s; then the device tracks the upward movement of the flow and reach

the peak again at $t = 19$ s. Clearly, in a period, the device motion is almost in phase with the wave motion by generating a negligible v_r . Based on Eq. (4.21), this implies the insignificant effects of the viscosity at low wave frequencies.

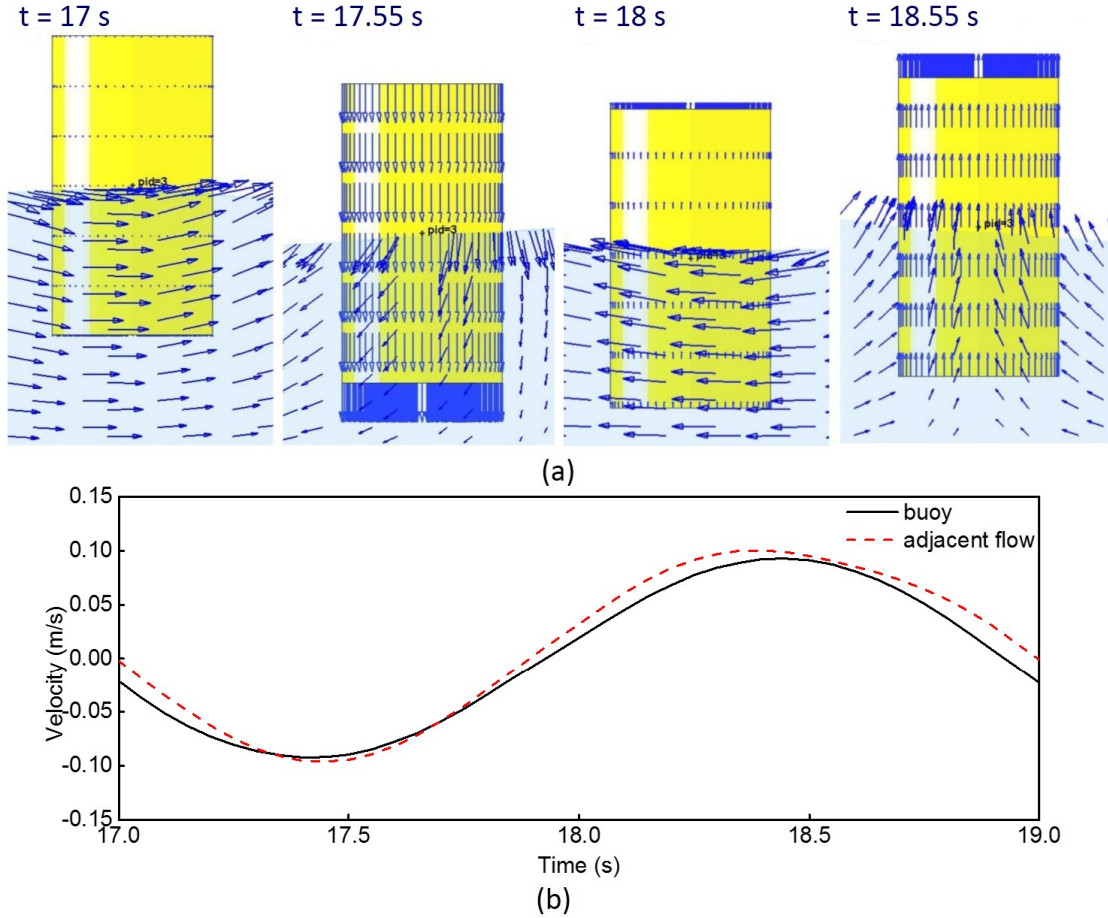


FIGURE 4.16: Velocity data of the PAWEC device and the adjacent wave within a period under wave condition of $\omega = 3.12$ rad/s, $H = 0.073$ m. (a) Snapshots of the velocity vector distributions. (b) Time series of the corresponding velocities.

The device shows synchronous tracking of the evolution of the flow.

Wave state 2: $H = 0.073$ m, $\omega = 4.83$ rad/s ($T = 1.3$ s)

This test condition is related to the case that the wave frequency closely matches the device natural frequency ω_0 (see Figure 4.13), known as "near resonance". As described in Figure 4.17, the PAWEC lags behind the adjacent wave with the

production of noticeable relative velocity v_r at this situation. During oscillating in a period, the PAWEC device moves down from the equilibrium position whereas the adjacent wave begins upward movement at $t = 14.95$ s; afterwards the device turns back to the equilibrium and begins to move upwards to the peak, while the adjacent flow starts opposite movement at $t = 15.65$ s. Clearly, in a period, there exists a significant phase shift between the motions of the device and surrounding wave. This would definitely result in flow separation and the generation of vorticity. As shown in 1.10, the similar phenomenon was physically recorded in the experiential tank testing conducted by Zang et al. (2018). They indicates that the significant viscosity generated from the oscillations of a flat-bottom WEC device should be carefully removed to reduce the related energy losses.

In summary, based on Figures 4.16 and 4.17, the v_r is insignificant when the wave frequency is relatively lower than the device natural frequency, whereas significant v_r does exist around resonant condition. This indicates that an obvious viscosity may be generated to affect the PAWEC hydrodynamics in the conditions close to resonance. Therefore, a non-linear modeling including viscosity should be developed to represent the device dynamic behaviors.

4.5 Verification and validation of the NSSM

Recalling the NSSM, it can be found that the remaining uncertain parameter is the viscous coefficient C_d . In this work, based on the least-squares technique, C_d is verified by comparing the results from the NSSM and CFD simulation, expressed as:

$$p_e = \min_p \sum_i (z_{NSSM}(t_i, p) - z_{CFD}(t_i))^2, \quad (4.23)$$

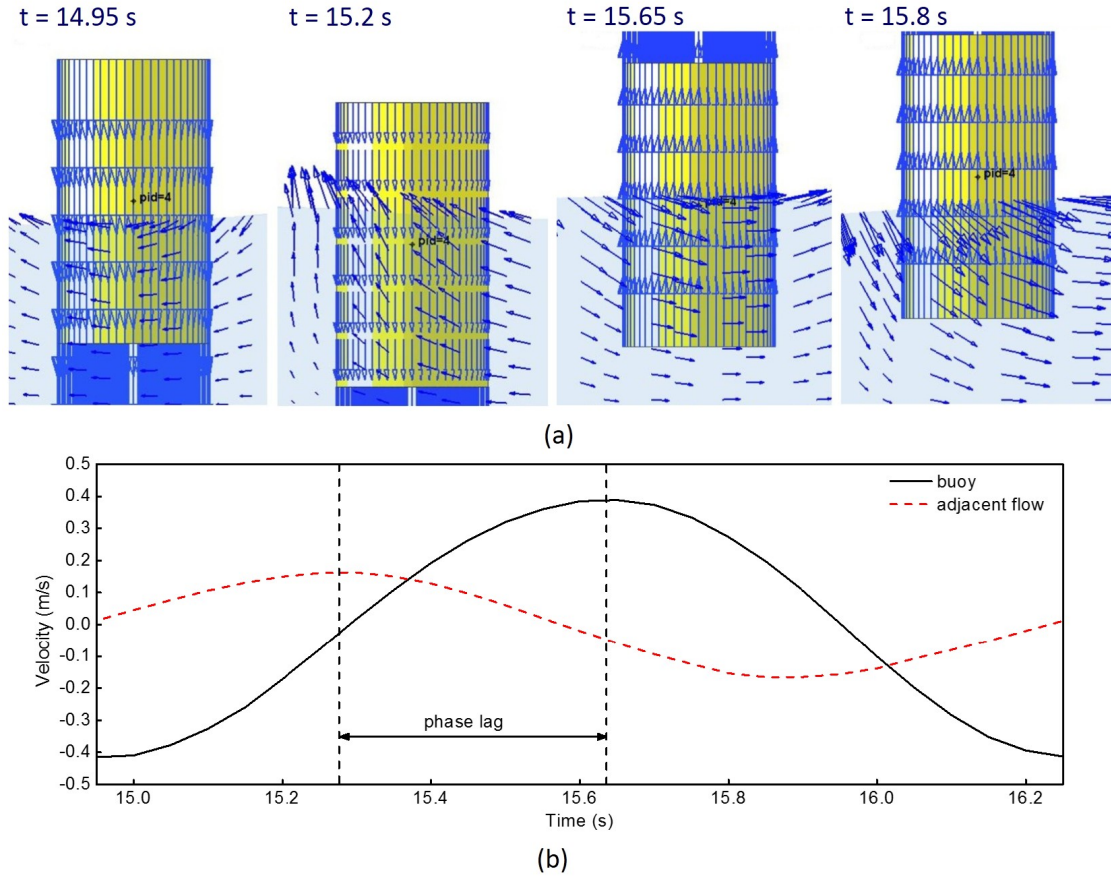


FIGURE 4.17: Velocity data of the PAWEC device and the adjacent wave within a period under wave condition of $\omega = 4.83$ rad/s, $H = 0.073$ m. (a) Snapshots of the velocity vector distributions. (b) Time series of the corresponding velocities. The device shows to lag behind the flow.

where $z_{NSSM}(t_i, p)$ is obtained PAWEC displacement by solving the NSSM via the default solver ODE45 in MATLAB®, which is easy and effective to generate the results; $z_{CFD}(t_i)$ is the device displacement obtained from the CFD simulation; p is the uncertainty and p_e represents the verified value with best fit. Clearly, in this work, C_d represents the uncertain value p in Eq. 4.23. Based on Eq. 4.23, the free decay test with initial released displacement of 0.2 m is implemented here to verify C_d . As a result, C_d equal to 1.4 is identified for the designed 1/50 scale PAWEC device.

Figure 4.18 describes the device displacements obtained from the LSSM, NSSM and CFD simulations. As observed, with $C_d = 1.4$ and $M_t = 26.28$ kg (note that the value of M_t is extracted from the BEM, referring to Table 4.1 or Figure 4.2), the amplitude responses achieved via the NSSM and CFD simulation fit with each other to a great degree. The exception is the significant discrepancy in oscillation period after $t = 2$ s. This can be associated with the under-prediction of the total mass (26.28 kg) by the linear theory (see Figure. 4.2). This concurs with the study from Davidson et al. (2015b). They also indicate that the practical total mass would be larger than the predicted value from the linear theory, especially for the large oscillations. Therefore, a more representative M_t should be determined.

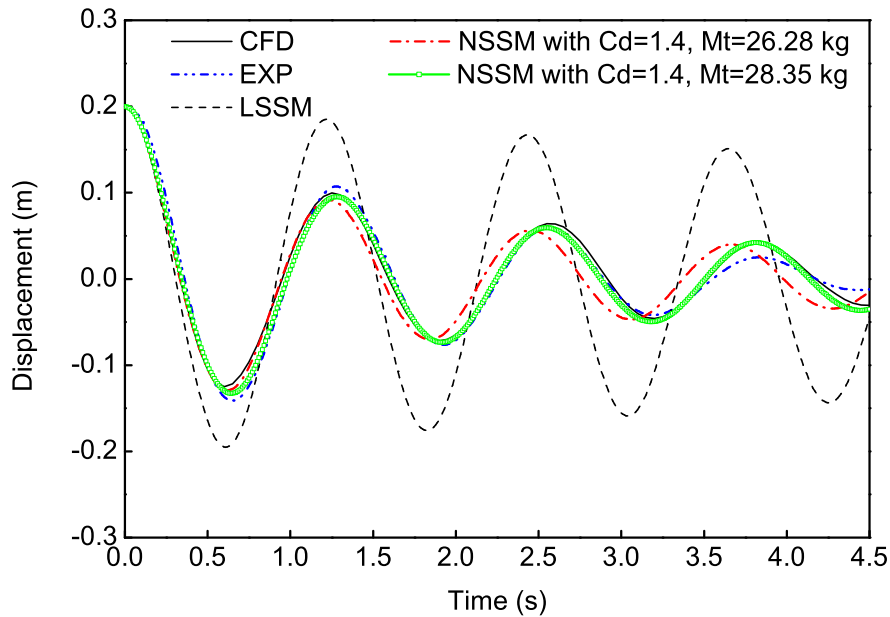


FIGURE 4.18: Comparisons of the free decay motions extracted from the numerical methods (e.g., LSSM, NSSM and NWT) and the physical tank test under initial released displacement of $z_0 = 0.2$ m.

To figure out this problem, both C_d and M_t are set as uncertainties. By recalling the above identification procedures, $C_d = 1.4$ and $M_t = 28.35$ kg are identified. As expected, by using $C_d = 1.4$, $M_t = 28.35$ kg, the data from NSSM shows great

accordance with the CFD output under both amplitude response and oscillating period (see Figure 4.18).

Furthermore, experimental data is also offered to evaluate the effectiveness of the proposed NSSM, as seen in Figure 4.18. Clearly, the numerical results from both the CFD and NSSM simulations fit well with the experimental results, whereas a slight deviation occurs after $t = 3.5$ s. The amplitude response from experiment shows to be slightly lower than that from CFD/NSSM. This arises from the practical friction effect induced by the roller bearing (see Figure 3.6). Details of the friction effect in the designed PAWEC system can be found in Guo et al. (2018a). In this work, this factor is not further discussed.

In contrast with the NSSM, the decay motion predicted from the LSSM shows significant discrepancy relative to the CFD/experimental data, e.g., the amplitude response is considerably larger. This reflects clearly the general drawback of the linear theory that it would over-estimate the device motion amplitude response. In addition to this, the deviation of the predicted oscillation period implies that the LSSM may predict inaccurate phase response during the wave-WEC interaction in contrast with the non-linear approaches (i.e., NSSM/CFD/experiment).

TABLE 4.2: Fit goodness of LSSM/NSSM relative to the CFD results. Note: the value for fitting varies between -Inf (bad fit) to 1 (perfect fit).

LSSM	NSSM ($M_t = 26.28$ [kg])	NSSM ($M_t = 28.35$ [kg])
-0.4418	0.9182	0.9875

To summarize, the fit goodness of LSSM/NSSM relative to the CFD results are offered (see Table 4.2). Note that: the fit goodness is calculated by 'normalized mean square error' and the value varies between -Inf (bad fit) to 1 (perfect fit). It can be concluded that the NSSM with $C_d = 1.4$, $M_t = 28.35$ kg shows great

superiority over the LSSM in representing the PAWEC free decay motion by increasing the fit goodness from -0.418 to 0.9875. This highlights the dissipative effect caused by the viscosity during the PAWEC device interacting with the flow, which should be considered carefully. Hence, NSSM with $C_d = 1.4$ and $M_t = 28.35$ kg is adopted to represent the PAWEC performance in the following work.

4.6 Case studies

In order to demonstrate clearly the non-linear characteristics of PAWEC performances caused by viscosity effect, three representative case studies including free decay, forced oscillation and power conversion efficiency tests are completed via LSSM, NSSM, CFD and experiment. Table 4.3 lists the corresponding tested parameters. Comparisons of the PAWEC performances achieved from different approaches are summarized, as described in following.

4.6.1 Viscosity effect on PAWEC free decay motion

As described in Table 4.3, in the free decay test, the PAWEC device is released from two representative non-zero initial positions $z_0 = 0.2$ m and 0.12 m, and the device motions then decay to the equilibrium. The corresponding displacements are recorded and normalised, as shown in Figure 4.19.

As observed, the normalised results keep consistent under different z_0 from the linear theory. It has been indicated by the experimental free decay motion study in Guo et al. (2018a) that the PAWEC device would experience a larger energy dissipation resulting in a smaller normalised displacement under a higher initial

TABLE 4.3: The test conditions for different case studies. Abbreviation: EXP = Experiment, SIM = numerical simulations, e.g., LSSM, NSSM and NWT.

<i>Free Decay motion test</i>		
EXP	z_0 [m]	0.2
SIM	z_0 [m]	0.2, 0.12
<i>Forced oscillation test</i>		
EXP	H [m]	0.08
	ω [rad/s]	3.14, 3.77, 4.85, 5.03, 5.34, 5.97, 6.28
SIM	H [m]	0.02, 0.073, 0.15
	ω [rad/s]	3.12, 3.6, 3.84, 4.52, 4.59, 4.8, 4.83 4.91, 5.04, 5.14, 5.52, 6.24
<i>Power conversion efficiency test</i>		
SIM	B_{PTO} [kg/s]	3, 4.3, 5, 6, 7, 8, 10, 15, 20, 25, 30
<i>Parameters from BEM</i>		
	M_t [kg]	26.28
	$\omega = \omega'_0$ [rad/s]	5.14
	$B_{hyd}(\omega_0) = B_{inv}(\omega_0)$ [kg]	4.3

released displacement. This suggests that the linear model LSSM totally loses effectiveness in describing non-linear free decay dynamics.

By contrast, the NSSM and CFD can be capable of representing the non-linear free decay dynamics. It shows that a higher z_0 results in a quicker motion dissipation. Clearly, the flow is viscous in practice. Therefore, a larger z_0 will disturb more adjacent flow to generate more vorticity. In this case, a larger relative velocity between the device and adjacent fluid will be induced during device oscillation. This will lead to a larger viscous drag to resist the PAWEC motion and produce energy losses. The results of the work from the NSSM and CFD simulations fit well with the work described in the experimental study from [Guo et al. \(2018a\)](#).

In addition, as observed the proposed NSSM considering the viscous term closely reproduces the non-linearities in free decay test by fitting the CFD data to a high extent in both the amplitude and oscillation period responses under different

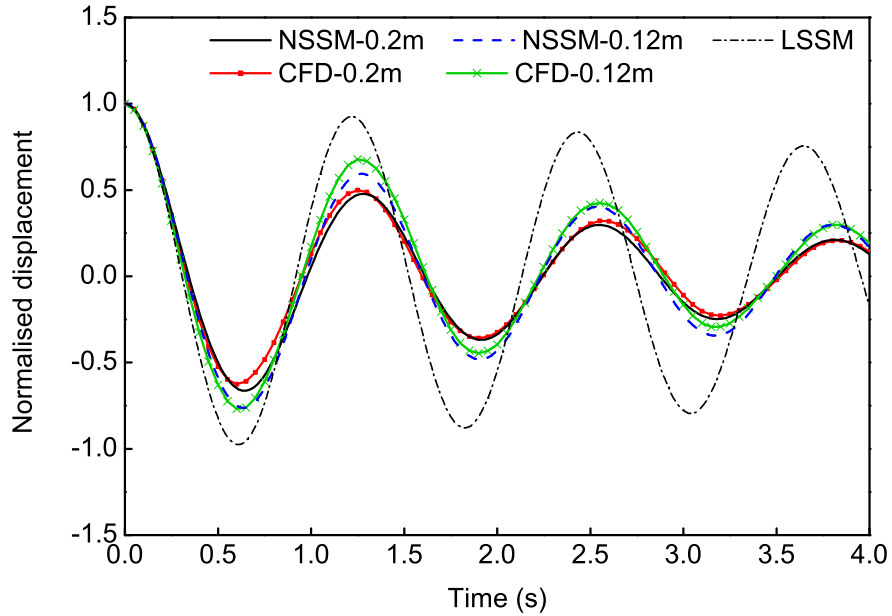


FIGURE 4.19: Comparisons of the normalised free decay motions obtained from the numerical methods (e.g., LSSM, NSSM and NWT) and the physical tank test under initial released displacement of $z_0 = 0.2$ and 0.12 m.

z_0 . Davidson et al. (2015b) identified a linear parametric hydrodynamic modeling from the CFD data. They indicates that the identified added mass and radiation damping have to be tuned with different initial released position in order to closely represent the non-linear free decay dynamics. By contrast, the developed NSSM in this work demonstrates great capability of adaptively performing the free decay dynamics under different initial positions as shown in Figure 4.19.

To summarize, the above observations regarding the result discrepancies between the LSSM and non-linear methods (e.g., NSSM and CFD) as well as the accordance of the predictions from NSSM and CFD highlight that:

- (i) in contrast to the conventional linear model, the designed NSSM is capable of adaptively describing the non-linearities in free decay motions;
- (ii) there exists potential value to use the proposed non-linear model for representing the operation of the PAWEC device in response to the incident wave, which is

detailed in the following Sections.

4.6.2 Viscosity effect on wave-PAWEC interaction

As described in Table 4.3, in the forced oscillation test, the PAWEC device is stimulated into heaving oscillations by the incident waves. As seen in Table 4.3, the generated regular waves are specified with various wave frequencies under three different wave heights (corresponding to the practical waves of small, moderate and high states (Crewe, 1990)). In addition, two different irregular wave conditions are tested. The tests are carried out to reveal the degree to which non-linearities in PAWEC hydrodynamic performance caused by viscosity effect should be considered as well as to demonstrate the capability of the developed NSSM in describing the non-linearities under varying wave conditions. First of all, the viscous effects on the PAWEC hydrodynamics, e.g., the amplitude and phase responses are discussed as follows in Section 4.6.2.1.

4.6.2.1 Viscosity influence on the PAWEC amplitude response

Under regular waves, according to Eqs. (4.10) and (4.22), there are two crucial characteristics (i.e., the maximum value RAO_{\max} and the wave frequency ω'_0 occurring RAO_{\max}) for RAO. These parameters reflect the efficient condition for the achievement of the optimal PAWEC performance. In order to investigate the viscous effect on the characteristics of RAO_{\max} and ω'_0 under various wave conditions, forced oscillation tests are conducted. As shown in Figure 4.20, the RAO variation versus wave frequency are summarized under three different wave heights (corresponding wave conditions are detailed in Table 4.3). Following findings can be summarized:

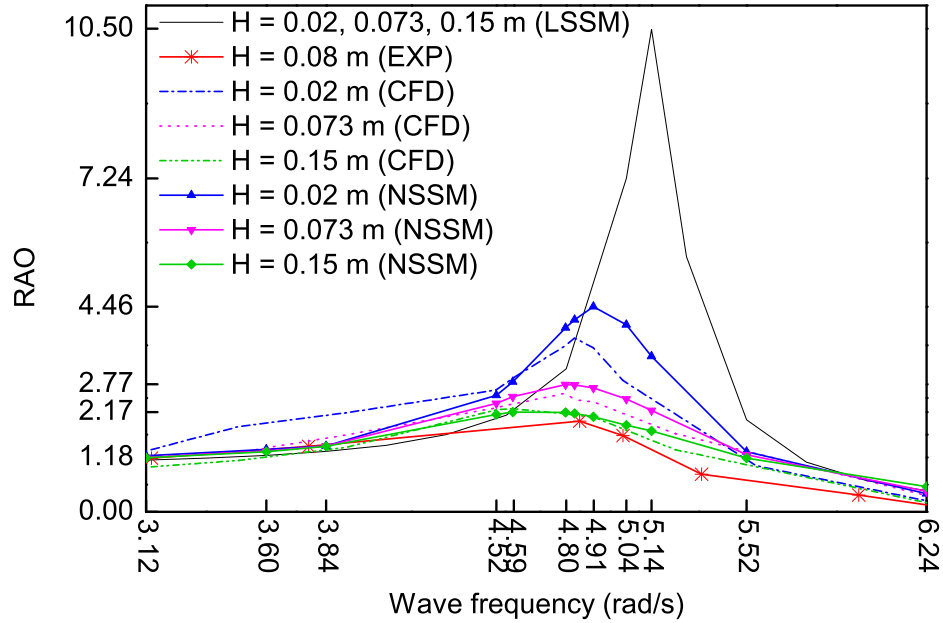


FIGURE 4.20: Comparisons of the RAO responses under various wave frequencies and wave heights. The data are obtained from the numerical methods (e.g., LSSM, NSSM and CFD) and physical tank test.

- When the wave frequency is away from the device natural frequency in the range of $\omega \leq 3.84$ rad/s, the obtained RAO values from all approaches (LSSM, NSSM, CFD and EXP) are approximately equal to 1. This can be explained by the fact that at relatively low frequencies the hydrostatic stiffness term $Kz(t)$ (shown in Eq. (4.11)) is the dominant force imposed on the PAWEC device. This force stimulates the device to synchronously follow the motion of the adjacent flow with negligible phase lag resulting in negligible viscosity effect. In other words, the PAWEC device operates as a "wave follower". This phenomenon is captured by the CFD simulation, as shown in Figure 4.16. Therefore, as expected, with insignificant viscosity effect under these wave conditions ($\omega \leq 3.84$ rad/s), the device hydrodynamics can be approximately linear, and thereby the RAO data are: (i) almost wave height independent; (ii) more or less the same from all methods.
- In comparison, when the wave frequency is close to the device natural frequency,

the LSSM fails to predict the RAO responses. As observed, first of all, LSSM over-predicts the RAO_{\max} by approximately 5.3 times of the experimental value under $H = 0.08$ m (as quantified in Table 4.4). By contrast, both the NSSM and CFD modeling provide better abilities in predicting RAO_{\max} , shown as slightly higher predictions relative to the physical data. These discrepancies mainly arise from the existence of the friction in physical tank test. Secondly, LSSM predict consistent RAO_{\max} and ω'_0 under different wave heights. Conversely, from NSSM and CFD, both RAO_{\max} and ω'_0 show significant dependence on the wave height. A larger wave height can result in smaller RAO_{\max} and ω'_0 . These observations can be attributed to the different B_{hyd} from the linear and non-linear methods. When the device operates close to resonance, the reactance term in Eqs. (4.10) and (4.22) will abruptly vanish. This would result in the damping term B_{hyd} to dominate the device response (Journée and Massie, 2000). In the linear model, it is clear that the dissipative term B_{hyd} corresponds to the inviscid radiation damping $B(\omega)$, which is only frequency dependent and considerably slight (as show in Figure 4.2). This will of course yield: (i) the over-predicted RAO_{\max} ; and (ii) the invariant RAO and ω'_0 under varying wave height. In comparison, by applying non-linear approaches (e.g., NSSM and CFD), the significant viscous term is involved and acts on the PAWEC device, which would result in the enhancement of the total resistance damping. This phenomenon is recorded through the CFD simulation as shown in Figure 4.17. Additionally, as described in Eq. (4.21), a larger viscous damping can be induced with increasing wave height. As a result, both RAO_{\max} and ω'_0 would show (i) smaller values relative to the linear predictions; and (ii) inverse relationships with the wave height (see Figure 4.20 or Table 4.4).

- *The NSSM closely reproduces the non-linear PAWEC hydrodynamic amplitude performance achieved through the CFD method.* This indicates that the developed

TABLE 4.4: Variation of RAO_{\max} and ω'_0 against wave height. It should be noted that * represents the physical tank test under $H = 0.08$ m.)

H [m]		0.02	0.073	0.15
LSSM	RAO_{\max}	10.5	10.5	10.5
	ω'_0 , rad/s	5.14	5.14	5.14
NSSM	RAO_{\max}	4.46	2.77	2.17
	ω'_0 , rad/s	4.91	4.80	4.59
CFD	RAO_{\max}	3.78	2.58	2.24
	ω'_0 , rad/s	4.83	4.80	4.59
EXP	RAO_{\max}	\	1.97*	\
	ω'_0 , rad/s	\	4.85*	\

NSSM can be capable of adaptively representing the device dynamic motions responding to different wave heights (see Figure 4.20). By contrast, in the studies conducted by [Son et al. \(2016\)](#), [Beatty et al. \(2015\)](#), a linearization of the quadratic drag term was applied. However, as indicated in their work, the linearized viscous coefficient has to be tuned against different wave heights. This highlights that the model with linearized viscous term is not as adaptive as the proposed NSSM in this work.

To summarize, since the device operates as a "wave follower" under low wave frequencies resulting in negligible viscosity, the linear method is as capable as the non-linear approaches for representing the PAWEC amplitude dynamics. However, with the existence of the significant viscosity under large oscillations, the NSSM considering viscosity provides a better capability compared to LSSM, by having the ability to predict the non-linearities of the PAWEC amplitude dynamics. In addition, it can be seen that a larger wave height yields a larger deviation of ω_0 relative to ω'_0 . This implies that the power capture response may also be wave height dependent and more importantly, the practical optimal condition for maximizing power capture may shift away from the linear prediction of $\omega = \omega_0$, which is discussed in 4.6.3.

4.6.2.2 Viscosity influence on the PAWEC phase response

Under regular wave conditions, in addition to amplitude response, the phase response can be essential to represent the PAWEC hydrodynamics. This Section focuses on illustrating the variation of the phase response caused by viscous effect. Figure 4.21 summarizes the phase responses achieved from different approaches. As observed:

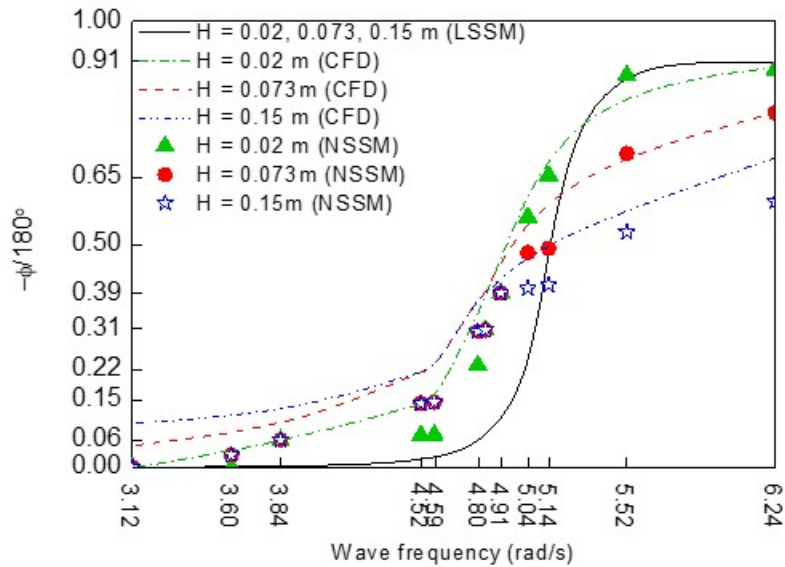


FIGURE 4.21: Comparisons of the phase responses under various wave frequencies and wave heights. The data are obtained from the numerical methods, e.g., LSSM, NSSM and CFD.

- *The phase responses predicted from LSSM show clear deviation relative to the non-linear methods, e.g., NSSM and CFD, in particular for the highest wave height of 0.15 m. With the consideration of the viscosity, NSSM shows better accordance with CFD model in representing phase response, in contrast to the LSSM. As observed, in contrast to the frequency dependent phase response from the linear theory, wave height also shows significant effect on the phase response, as seen in the NSSM and CFD results.*

• The conventional "resonance" condition ($\omega = \omega_0 = 5.14$ rad/s, RAO_{max} obtained) reflected by the buoy having an approximately 90° phase lag (see Figures. 4.13 and 4.21) relative to the flow is not applicable in the real non-linear PAWEC system. As observed from Figure 4.22, the phase lag for the frequency achieving RAO_{max} shifts further away from 90° with increasing wave height, as predicted via NSSM and CFD. This indicates that the conventional optimal criteria (from linear theory): RAO_{max} and nearly 90° phase lag of the PAWEC motion relative to the flow cannot be achieved at the natural frequency ω_0 in practice. In other words, natural frequency ω_0 cannot be the criterion for optimal PAWEC performance. More importantly, in addition to wave frequency, wave height can also affect the PAWEC performance.

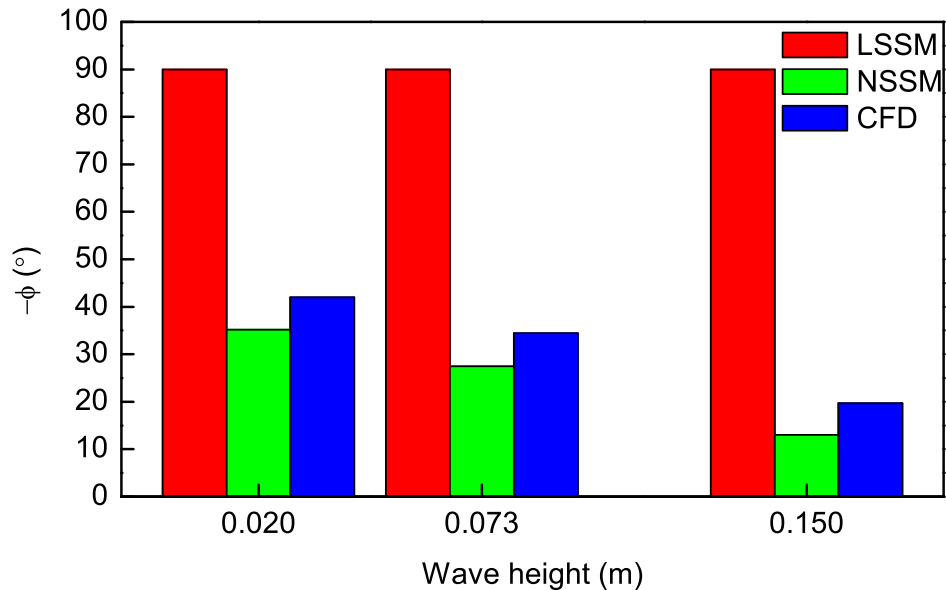


FIGURE 4.22: The phase difference (the PAWEC device lags behind the wave) versus wave height at RAO_{max} .

In order to clearly show the superiority of the developed NSSM over LSSM in representing the PAWEC hydrodynamics, two representative examples are given as bellow:

Firstly, Figure 4.23 describes the time series of the velocities for the device and the adjacent wave under wave condition of $\omega = 4.91$ rad/s, $H = 0.15$ m. As seen, there exists substantial discrepancies between the LSSM and CFD for predicting the PAWEC device velocity, shown as an approximately 80° of velocity phase difference and twice the amplitude. By contrast, the prediction from NSSM fits the CFD data to a high degree for both the amplitude and phase responses.

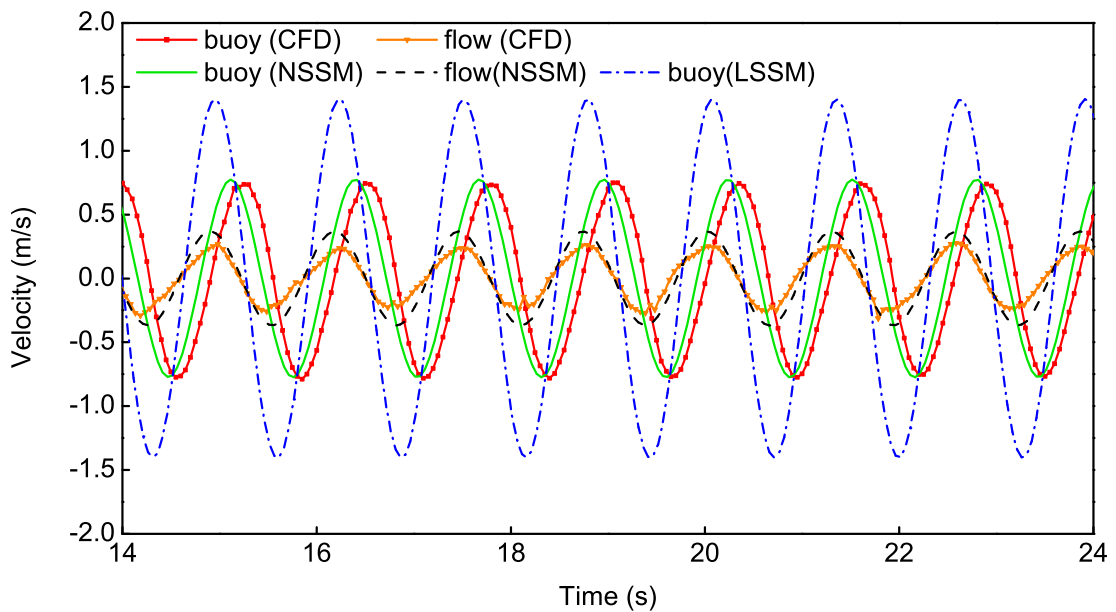


FIGURE 4.23: Time series of the velocities of the PAWEC device and the adjacent wave at wave condition of $\omega = 4.91$ rad/s, $H = 0.15$ m.

Secondly, the time series of the velocities for the PAWEC device and the adjacent wave under wave condition of $\omega = 4.59$ rad/s, $H = 0.15$ m are described in Figure 4.24. Different from the severe deviation shown under $\omega = 4.91$ rad/s, the PAWEC velocity response via the LSSM closely reproduce the CFD data, whereas the exception is an approximately 48.6° of phase difference. In comparison, the NSSM provides better accordance with the CFD model in predicting both the amplitude and phase responses.

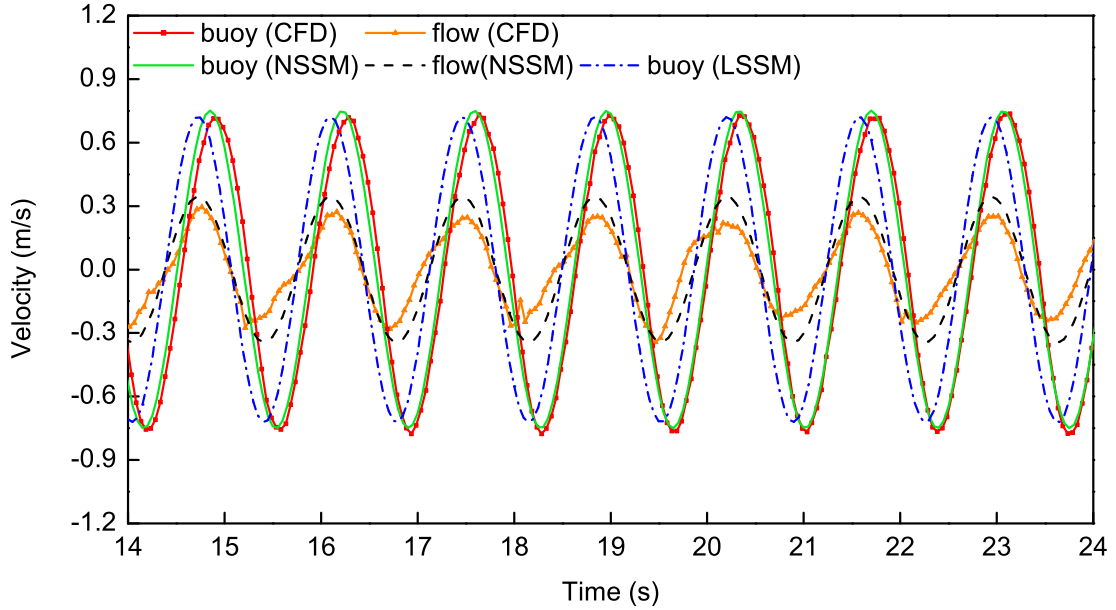


FIGURE 4.24: Time series of the velocities of the PAWEC device and the adjacent wave at wave condition of $\omega = 4.59$ rad/s, $H = 0.15$ m.

To summarize, the proposed NSSM can be capable of representing the non-linear hydrodynamic performance of the designed PAWEC under various regular wave conditions.

4.6.2.3 Viscosity influence on the PAWEC performance under irregular wave

In addition to the regular wave condition, it is also important to investigate the effectiveness of the designed NSSM under irregular wave conditions. As found in Sections 4.6.2.1 and 4.6.2.2, the linear model clearly loses effectiveness to represent PAWEC performance around resonance. Hence, the peak frequency of the tested irregular waves is specified to be consistent with the PAWEC natural frequency of 4.83 rad/s. Two representative irregular waves with $H_s = 0.1$ m, $\omega_p = 4.83$ rad/s and $r = 0.5/8$ are discussed here. The corresponding PAWEC hydrodynamics under these wave conditions are shown in Figures 4.25 and 4.26.

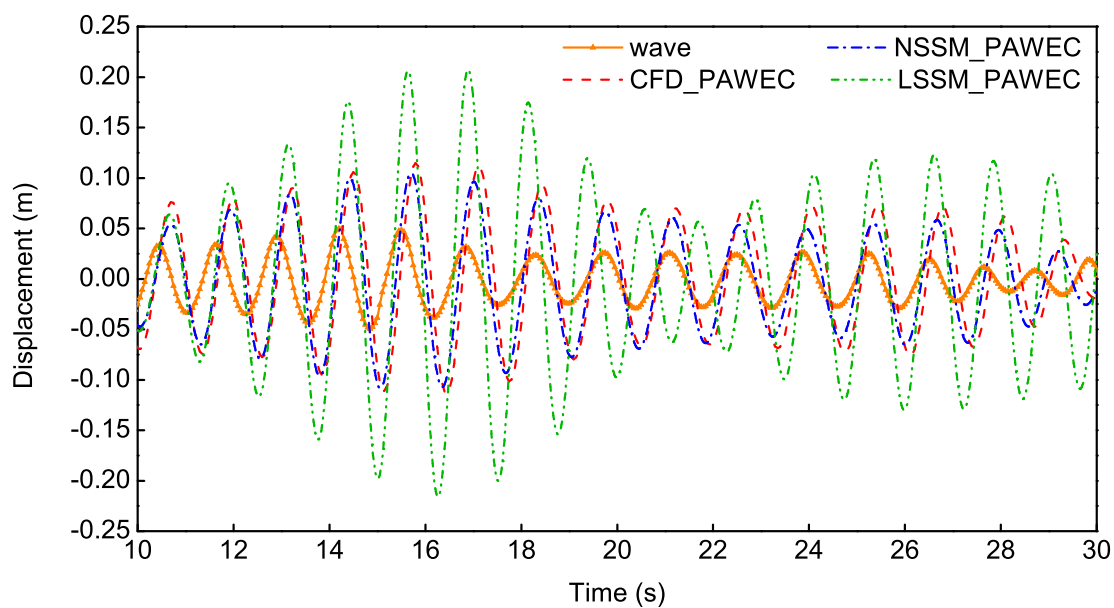


FIGURE 4.25: The PAWEC displacement with respect to the irregular wave at $H_s = 0.1$ m, $\omega_p = 4.83$ rad/s and $r = 8$.

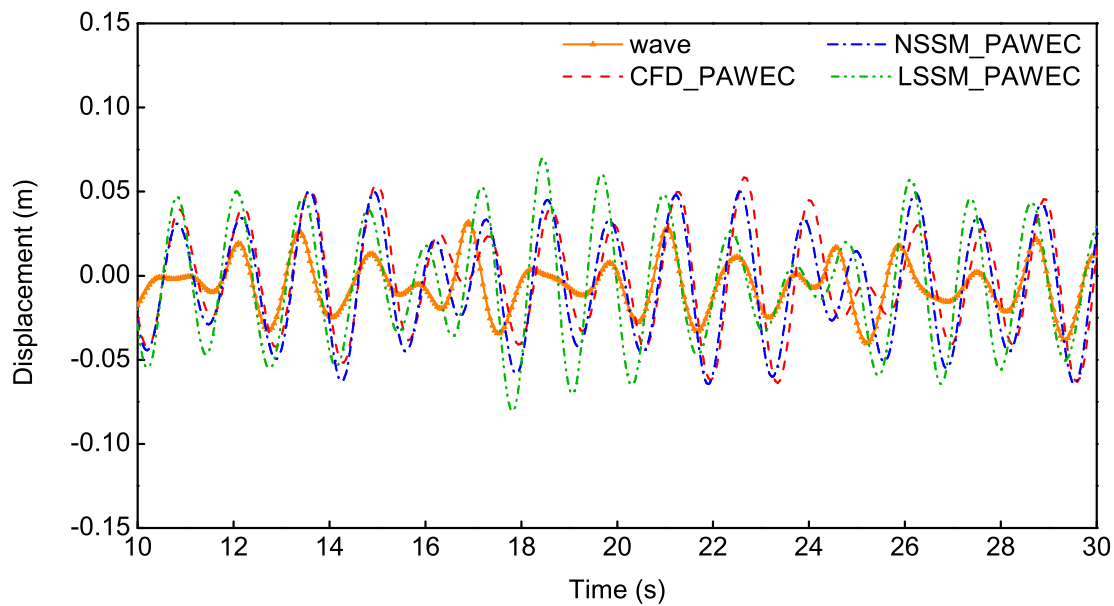


FIGURE 4.26: The PAWEC displacement with respect to the irregular wave at $H_s = 0.1$ m, $\omega_p = 4.83$ rad/s and $r = 5$.

Clearly, by involving the wave prediction, excitation casualization and identification, radiation identification and the most important non-linear factor i.e., the quadratic viscous term (as described from Sections 4.3 to 4.5), the proposed NSSM shows great superiority over the conversational LSSM in describing the PAWEC hydrodynamic performance not only in amplitude response but also in phase response. This is of fundamental importance to the control strategy implementation, where the NSSM can be applied as the basic hydrodynamic plant. This NSSM would be employed for the PSO-FLC design, as detailed in Section 6.

4.6.3 Viscosity effect on PAWEC power conversion efficiency

As described in Table 4.3, in the power conversion efficiency test, a PTO system is applied to the PAWEC system to study the power capture characteristics (see Figure 3.7). A variety of damping coefficients are applied to the PTO system. The absorbed power is measured by the product of the PAWEC velocity and the PTO damping force (determined by the device velocity and PTO damping coefficient), as given in Eq. (4.16). The viscosity effect on the PAWEC power conversion efficiency are summarized regarding varying PTO damping and wave condition. Figure 4.27 shows the results, the power conversion efficiency (as given in Eq. 4.16) as a function of dimensionless PTO damping coefficient and wave frequency through the LSSM and NSSM. Following findings can be seen:

- *As expected by the classic linear theory, the maximum power conversion efficiency is wave height independent and can be achieved at $\omega/\omega_0 = 1$ and $B_{PTO}/B_{hyd} = 1$ (see Figure 4.27a). Note that an efficiency larger than 100% is predicted which is considerably unrealistic. According to the linear model, the wave frequency enormously affects the efficiency value. As observed, the power conversion efficiency decreases sharply when the wave frequency shifts away from the PAWEC natural*

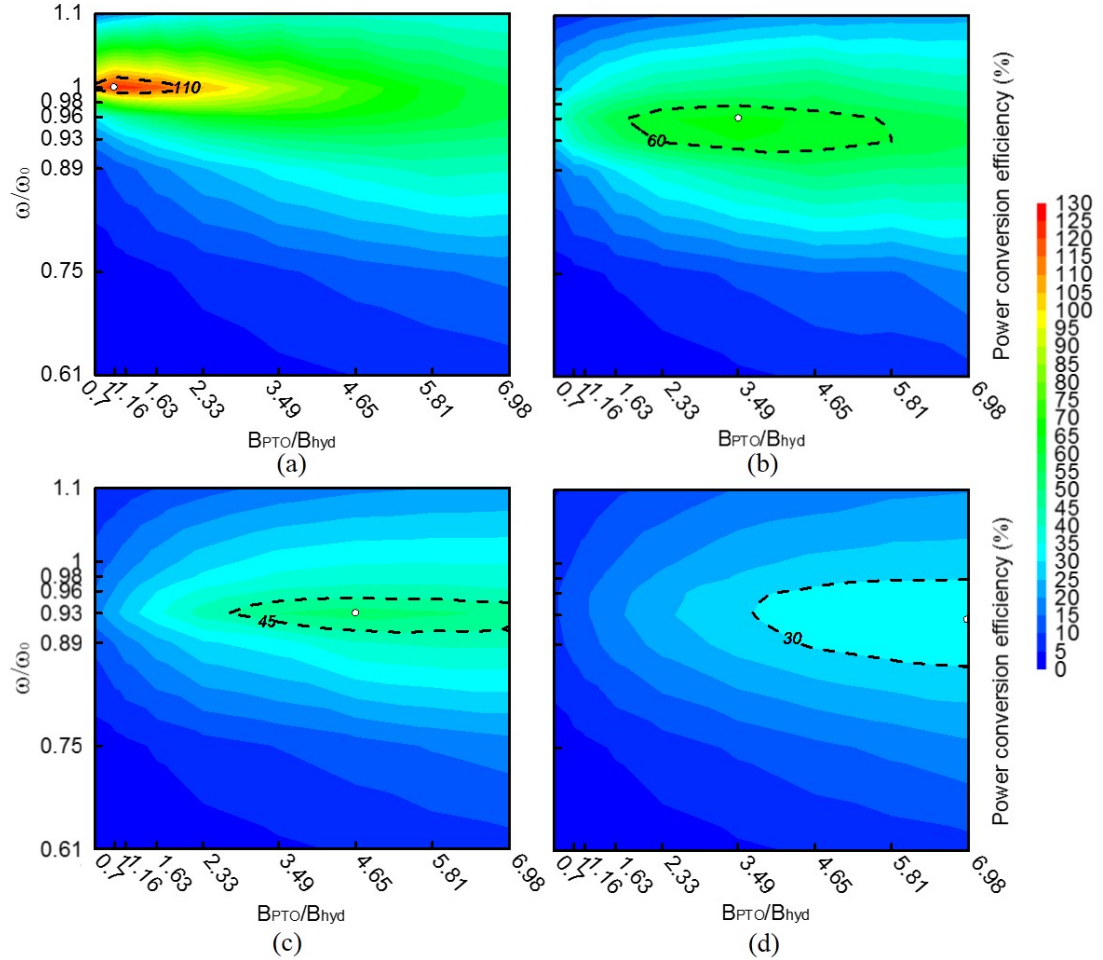


FIGURE 4.27: PAWEC power conversion efficiency against the dimensionless PTO damping coefficient and wave frequency. It should be noted that (i) B_{hyd} is equal to 4.3 Ns/m when the resonance is achieved via linear theory (see Figure. 4.2) and (ii) the marked white point is the maximum conversion efficiency C_{max} . (a) Under $H = 0.073$ m via LSSM; $C_{max} = 125\%$ (b) Under $H = 0.02$ m via NSSM; $C_{max} = 66.6\%$. (c) Under $H = 0.073$ m via NSSM; $C_{max} = 52.5\%$. (d) Under $H = 0.15$ m via NSSM; $C_{max} = 33.5\%$.

frequency, in particular under small PTO damping coefficients. In addition, the required PTO damping coefficient for the optimal power efficiency can be determined by the wave frequency. Around resonance (shown as the region inside the dash line in Figure 4.27a), the power conversion efficiency declines gradually when the PTO damping value departs from $B_{PTO}/B_{hyd} = 1$. Differently, in the frequency range

outside resonance (shown as the region outside the dash line in Figure 4.27a), the power conversion efficiency increases with increasing PTO damping. Similar findings have been reported by De Backer (2009). This observation can be explained by the RAO predictions via the linear theory. That is overrated/abruptly decreased motion responses inside/outside the resonance, respectively (see Fig. 4.13 or 4.20).

- *By contrast, the NSSM presents different power absorption performance by considering viscosity (see Fig. 4.27b-d). At $H = 0.073$ m, the maximum power conversion efficiency predicted by the NSSM is 52.5%, which is far more reasonable in comparison to the 125% via LSSM. Additionally, the power capture characteristics show to be wave height dependent. In other words, the conversion properties are non-linear. As observed, when the wave height increase, the optimal damping for maximizing increases, whereas the optimal wave frequency decreases. This suggests that the conditions for maximum efficiency are not consistent at different wave height as predicted by the linear theory. With a increasing wave height, the optimal conditions shift further away from the theoretical linear predictions. This finding in turn confirms that the linear theory can only be applicable under small oscillations. Under large oscillations, non-linearities occur and linear models are not capable of predicting the power capture in an accurate way. Similar findings have been reported in the CFD and experimental studies by Davis (1990), Anbarsooz et al. (2014). This phenomenon can be explained by:*

(i) The involved viscous damping in the NSSM would affect the B_{PTO} characteristics to be wave height dependent, especially under large oscillations. Under a small wave height, the magnitude of the device velocity with respect to the incident wave velocity is small. This would lead to insignificant viscous damping B_{vis} . Hence, B_{hyd} could be dominated by the frequency dependent radiation damping B_{inv} and thereby can be considered approximately to be linear. This results in the

optimal condition at small wave heights close to the theoretical value. As shown in Figures 4.27b-d, at the smallest wave height $H = 0.02$ m, the optimal B_{PTO} and ω/ω_0 are close to the theoretical values shown in Figure 4.27a. Conversely, due to the indispensable wave height dependent viscous term B_{vis} , B_{hyd} increases significantly with increasing wave height, which requires a larger optimal PTO damping to reduce energy losses (as shown from Figures 4.27b-d).

(ii) As generally known, the optimal conversion efficiency may correspond to the largest amplitude response of the PAWEC. As described in Section 4.6.2.1, when the wave height increases, the wave frequency for largest amplitude response decreases. Therefore, the wave frequency for optimal power capture shows to decrease with increasing wave height.

By comparing the power conversion efficiency at different wave heights (see Figures 4.27b-d), it is found that a larger wave height would result in a smaller efficiency. This is related to a larger energy losses caused by the significant viscosity effect under a larger wave height. In practice, we suppose that the optimal PAWEC operation range (corresponding to the region inside the dash line, as shown from Figures 4.27a-d) is a decrement of 10% power conversion efficiency relative to the maximum value. Then, it can be found that the range for the efficient power conversion efficiency is expanded under the non-linear model, compared to the narrow optimal range predicted by the linear theory. As observed, the optimal condition for the designed PAWEC varies in the range: $10.75 \text{ Ns/m} < B_{PTO} < 24.7 \text{ Ns/m}$ together with $4.7 \text{ rad/s} < \omega < 5.0 \text{ rad/s}$ (under the wave conditions and PTO damping coefficients studied in this work).

4.7 Conclusions

This Chapter focuses on developing a more overall non-linear mathematical modeling for the designed 1/50 scale vertical oscillating PAWEC, compared with the conventional linear modeling. Note that the viscous force is considered automatically in the CFD model and experiments. For the developed non-linear mathematical model, the viscosity is involved by using the quadratic viscous term in Morison equation. Then, the viscosity effect on the PAWEC performance is verified by comparing the predictions via LSSM and NSSM with CFD and experimental data. Some conclusions can be drawn as follows:

- For the linear model, a 4-order state-space model is applied to approximate the convolution term of the wave radiation force (see Figure 4.6). A 6-order state-space model for the causalized IRF of the excitation force together with a 50-order AR model for the wave prediction is used to represent the excitation force in response to the incident wave (see Figures 4.8 and 4.11).
- To develop the non-linear model, the viscous effect is involved by applying a quadratic viscous term from the Morison equation. The viscous coefficient of 1.4 and total mass of 28.35 kg for the designed PAWEC are verified for the NSSM by the CFD data from free decay testing (see Figure 4.18). As a result, a satisfying correspondence is found between the motion response from the NSSM and the experiment. More importantly, the developed NSSM shows the adaptive ability of presenting the non-linearities of the free decay motion under different initially released displacements (see Figure 4.19).
- Under the forced oscillation testing, the amplitude and phase responses exhibit significant non-linearities. With the exception of wave frequency, the wave height is seen to be an indispensable factor affecting the PAWEC performance. As the wave

height increases, the RAO response decreases and the wave frequency corresponding to the maximum RAO shifts to a lower value. It is found that the conventional LSSM loses capability in describing these non-linearities. Conversely, the developed NSSM closely reproduce the CFD and experimental testing in describing the PAWEC non-linearities at different wave heights. The results indicate that the conventional optimal performance criteria at the resonance frequency such as the maximum oscillation and an approximately 90° phase lag between PAWEC and regular wave motion are not valid as the wave height increases (see Figs. 4.20 and 4.21). With the viscosity influence, the PAWEC RAO and phase responses have different performances under different wave heights.

- An unreasonable power conversion efficiency of 125% is predicted by the linear model at a wave height of 0.073 m (shown in Figure 4.27a). In addition, the wave frequency shows to be the most crucial factor affecting the conversion efficiency. Of next importance in this context is the PTO damping coefficient. By contrast, based on the NSSM, the maximum efficiency of 52.5% is predicted at a wave height of 0.073 m. In addition to the wave frequency and PTO damping, the power conversion efficiency is also dependent on the wave height. More importantly, the optimal condition for the maximum efficiency is no longer consistent as predicted by the linear theory. It shows a clear dependence on the wave height. An increasing wave height yield the optimal condition to shift to a higher PTO damping and a lower wave frequency (see Figures 4.27b-d).

To summarise, this Chapter shows that for the designed 1/50 scale PAWEC, the LSSM fails to accurately predict the hydrodynamic performance and power conversion efficiency, especially at large oscillations. Conversely, the non-linear model with careful modeling of the viscous force provides better ability to closely reproduce the PAWEC non-linearities. This study indicates that the viscose effect is

significant for the designed PAWEC, especially for large oscillations (e.g., close to resonance or under high wave height).

As shown from the power conversion results, for the designed flat-bottom cylindrical 1/50 scale PAWEC, viscosity could clearly dissipate the mechanical energy leading to the decrease of the power absorption efficiency. Therefore, in Chapter 5 geometry optimization is studied to reduce viscous effects and thereby to improve the power capture. More importantly, as generally known, the optimal PTO damping for power absorption maximisation is related to the device hydrodynamic performance. Viscosity has been validated to significantly affect the PAWEC performance. Therefore, it would of course generate an effect on the PTO damping characteristics. This would also be discussed in Chapter 5.

Chapter 5

Power capture enhancement by joint tuning of geometry and power take-off damping

5.1 Introduction

As described in Chapter 4, for the designed 1/50 scale cylindrical heaving point absorber wave energy conversion (PAWEC) device, the viscosity plays an important role in dissipating the device kinetic energy (see Figure 4.27). This finding concurs with the numerical and experimental studies by [Zang et al. \(2018\)](#), [Yeung and Jiang \(2011\)](#). Therefore, it is necessary to design a PAWEC device to reduce viscous dissipation for power capture enhancement. One method to achieve this is through geometric optimization. As suggested by [Vantorre et al. \(2004\)](#), applying wave energy conversion (WEC) devices with rounded edges can reduce the energy losses resulting from high viscosity and vortex shedding.

In addition to the viscous effect, the interaction between the WEC device and the external PTO system is also considerably important for the PAWEC performance. In practice, varying PTO system has been used by considering different WEC system configuration, e.g., direct-drive linear generator, air or water turbine, hydraulic pump and dielectric elastomer, etc. (Henriques et al., 2016a, Chiba et al., 2013, Antonio, 2010). For simplification, a spring-damper system is generally used as PTO substitute to study the power absorption performance. Power tuning can be achieved by adjusting the spring and damper coefficients of the PTO (Zang et al., 2018, López et al., 2017, Davis, 1990). It has been indicated by Falnes (2002), the maximum power absorption is achieved when the wave frequency matches the device natural frequency ($\omega/\omega_0 = 1$) and the PTO damping equals the hydrodynamic damping ($B_{PTO} = B_{hyd}$). In other words, there is a form of resonance involved in maximizing energy capture allied with a mechanical form of impedance matching. Theoretically, introducing the spring component can realize optimum WEC performance under varying wave conditions, as the PTO can work as a motor for part of the operation cycle. However, this is realized at the expense of generating bidirectional power flow, which is still a challenging phenomenon requiring further experimental and modeling studies. In this study, to generate unidirectional power flow, the PTO role is only simulated by a damper operating just as a generator.

Ideally, it should be possible to jointly optimize the designs of the WEC hydrodynamics, PTO system and control strategy to produce the most efficient wave energy conversion. Optimization of the hydrodynamics should consider the optimal design of the WEC geometry. The geometry design may affect the designs of the PTO and control systems since these WEC subsystems are influenced by the hydrodynamic interaction between the WEC device and the wave motion. Hence, if possible these design issues should be considered in one "co-design" package

when developing a prototype WEC system.

To basically study the "co-design" concept, this Chapter provides a derivation of the optimal PTO damping coefficients considering the WEC geometry optimization under expected wave conditions. Optimization of the interaction between the device geometry and the PTO damping is studied for the maximization of the power performance of the tested 1/50 scale heaving PAWEC at UoH wave tank (see Figure 3.6). The study is tested in the three dimensional (3D) computational fluid dynamics (CFD) wave tank constructed in Chapter 3 (see Figure 3.7a). The main contributions of this Chapter are summarized as follows:

- *Two further counterparts are proposed to compare with the original tested cylindrical PAWEC design.* The hydrodynamic parameters of these three different geometric PAWECs are quantified by free decay tests in the CFD wave tank and by simulations from the linear software package ANSYS/AQWA. The results clearly show the variation of the viscous damping against the geometric design. Thus it is necessary to consider geometry optimisation for the design of the PAWEC system.
- *There exists clear joint effects of the structural geometry and PTO damping on the WEC dynamic performance and power absorption.* Although, a number of studies on WEC geometry configuration and PTO performance have been conducted (Zang et al., 2018, Goggins and Finnegan, 2014, McCabe, 2013, Yeung and Jiang, 2011, De Backer, 2009, Eriksson et al., 2005, Vantorre et al., 2004), few studies discuss the joint effects of these two factors. A series of power absorption tests have been conducted under different geometric designs and PTO damping coefficients. The results show that by applying an appropriate PTO damping, a streamline-bottom device can significantly enhance the PAWEC amplitude response and power capture under both regular and irregular wave conditions, compared with the original flat-bottom PAWEC.

The remainder of this Chapter is described as: the numerical test setup is provided in Section 5.2; Section 5.3 describes the results and discussion and study is concluded in Section 5.4.

5.2 Test setup

As generally known, the most promising operating range for a WEC device is around resonance or at high wave heights. Therefore, in this Chapter, the joint effects of the geometry and PTO damping on the PAWEC performance are studied mainly in this region. Appropriate parameters are selected as follows.

5.2.1 PAWEC geometric configuration

From the experimental free decay test, [Guo et al. \(2018a\)](#) has suggested that excepting the mechanical friction, of next importance in this context is the viscosity resulting in non-linearities and energy losses at large oscillations for the PAWEC. According to the studies by [Hager et al. \(2012\)](#), [Yeung and Jiang \(2011\)](#), geometry optimization for a WEC device could be an effective way to reduce the viscosity effect leading to the reduction of the energy loss.

Referring to work in Chapters 3 and 4, it is known that a cylindrical flat-bottomed PAWEC is built and tested at UoH. It is validated that there exists significant viscosity effect based on this flat-bottomed device, as discussed in Chapter 4. Additionally, it is found that the viscosity hinders the PAWEC hydrodynamics a lot at large oscillations. As generally known, device geometry can influence the viscosity term ([Journée and Massie, 2001](#)). Therefore, a study of viscosity effect in terms of device geometry is conducted here. Two further counterparts with

streamlined bottoms are studied (see Figure 5.1) in addition to the experimental prototype of the 1/50 scale cylindrical flat-bottomed PAWEC (defined as CL) as shown in Figure 3.6. One is a cylindrical buoy with a hemispherical cap (defined as CH). Another one is with a 90°-conical bottom (defined as CC). Note that the two streamlined devices CH and CC studied here are not the optimal devices. The study here is just to claim the PAWEC hydrodynamics related to geometry effects. Hence, three different geometric devices are discussed. Geometry optimisation will be studied in future in order to find the optimal design for a specified PAWEC device.

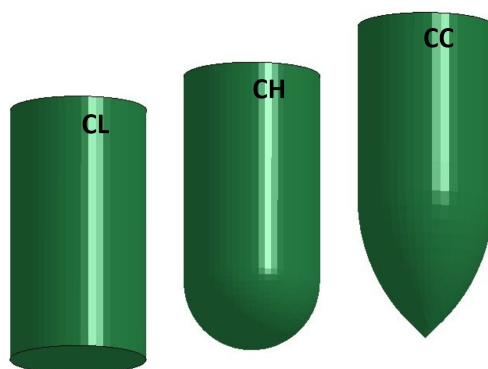


FIGURE 5.1: 3D view of the three geometric PAWEC profiles.

As generally known, natural frequency, effective water plane area, device geometry profile are crucial parameters to determine the PAWEC performance. The study here focuses on merely demonstrating the geometry effect on PAWEC performance. Therefore, natural frequency, effective diameter and volume are kept the same as shown in Table 5.1. To achieve this, the free decay testing is implemented in the numerical wave tank (NWT) by continuously tuning the densities of CH and CC until they match the density of CL. As a result, the physical parameters for the three PAWEC devices are summarized, as shown in Table 5.1.

TABLE 5.1: Corresponding parameters for the three geometric devices.

	CL	CH	CC
Diameter D [m]	0.3	0.3	0.3
Volume [m ³]	0.04	0.04	0.04
Natural frequency ω_0 [rad/s]	4.83	4.83	4.83
Density [kg/m ³]	500	602	630
Mass M [kg]	19.7	23.2	24.3

5.2.2 PTO damping configuration

According to the linear theory, by ignoring non-linear effects, only the frequency dependent inviscid radiation resistance $B_{inv}(\omega)$ and reactance $X(\omega)$ (equalling $\omega M_t(\omega) - K/\omega$) (see Eq. (4.9)) will contribute to the optimal PTO damping for passive control, which can be calculated by $B'_{PTO} = [B_{inv}^2(\omega) + X^2(\omega)]^{1/2}$ (Falnes, 2002). Figure 5.2 demonstrated the hydrodynamic parameters of the three geometric devices, achieved through ANSYS/AQWA.

According to the data shown in Figure 5.2, the impedance of the CL device and the corresponding optimal PTO damping against wave frequency (the data are computed via ANSYS/AQWA) are given to clearly illustrate the relation between the optimal PTO resistance B'_{PTO} and the hydrodynamic impedance ($B_{inv}(\omega)$ and $X(\omega)$), as shown in Figure 5.3. It can be seen that the reactance will vanish at resonance and remain low in magnitude close to resonance. As a result, inviscid resistance (radiation damping) becomes the dominant factor affecting the optimal PTO damping at resonance. As observed, the value of this factor is generally small, which results in a "trough" prediction of the optimal PTO damping (see the line with blank circle in Figure 5.3).

However, as indicated in Chapter 4, non-linearities caused by viscosity are indispensable especially at large oscillations. It has also been suggested by Son et al.

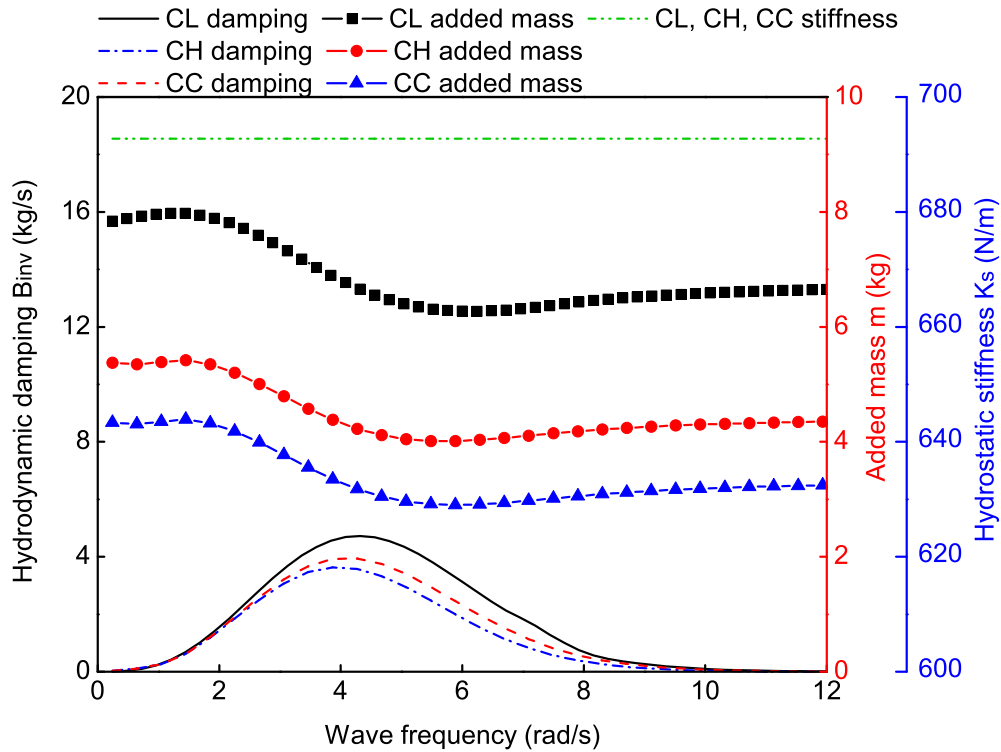


FIGURE 5.2: Hydrodynamic parameters of the three different geometric PAWEC devices. The data are computed via ANSYS/AQWA.

(2016), non-linear viscous damping is significantly larger than the inviscid radiation damping. These imply that the practical optimal PTO damping used for passive control may differ from the predictions through the linear theory shown in Figure 5.3. Therefore, it is necessary to obtain the "practical" PTO damping characteristics, taking into account of the non-linearities. In this case, CFD modeling can be capable of predicting more practical PTO damping characteristics in contrast to the linear modeling. This is the focus of this chapter.

For the three different geometric devices, optimal PTO damping obtained from the linear theory are primarily adopted to predict the range for the study (see Figure 5.4). As a result, the PTO system (see Figure 3.7a) in the NWT are designated with: 5, 7, 10, 15, 20, 25, 30, 40, 60, 70, 80 kg/s for the CFD study. As shown in Figure 5.4, the device geometric design has insignificant effect on the variation of

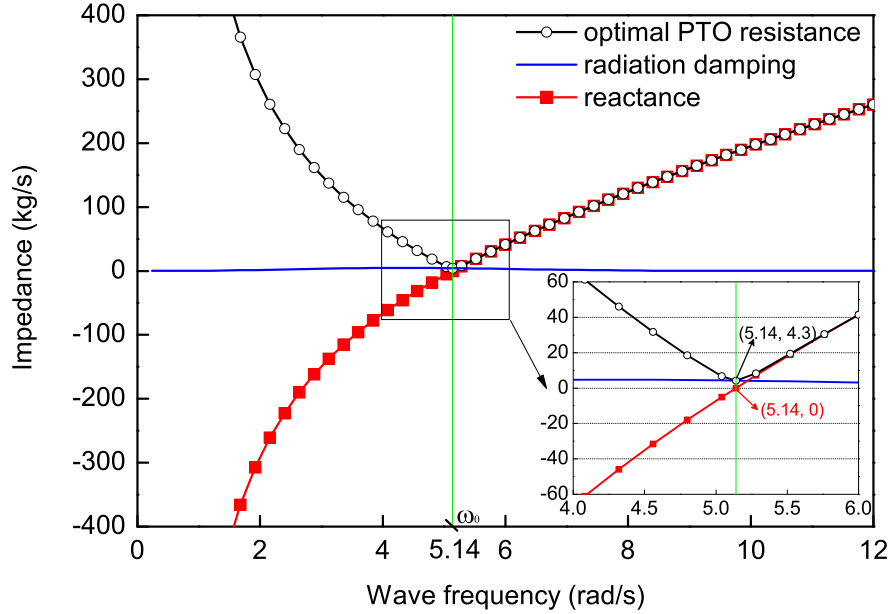


FIGURE 5.3: Impedance and corresponding optimal PTO resistance for passive control for CL device. The data are obtained from linear theory using software ANSYS/AQWA.

the optimal PTO damping against wave frequency according to the linear theory. Then the following question must be answered: "what is the practical prediction of the PTO damping by considering non-linearities?" This is discussed in Section 5.3.3.

5.2.3 Wave climate

The three PAWEC devices are tested under both regular and irregular waves. As aforementioned, this work focuses on the PAWEC characteristics around resonance or at large oscillations. In this case, the natural frequency can be a critical factor for the wave frequency selection. Regarding the device natural frequency ω_0 of 4.83 rad/s (see Table 5.1), the wave frequencies are designed around this value as detailed in Table 5.2. Referring to the report by Met Office (Crewe, 1990), the moderate to high wave heights for the fully developed open sea is defined in the

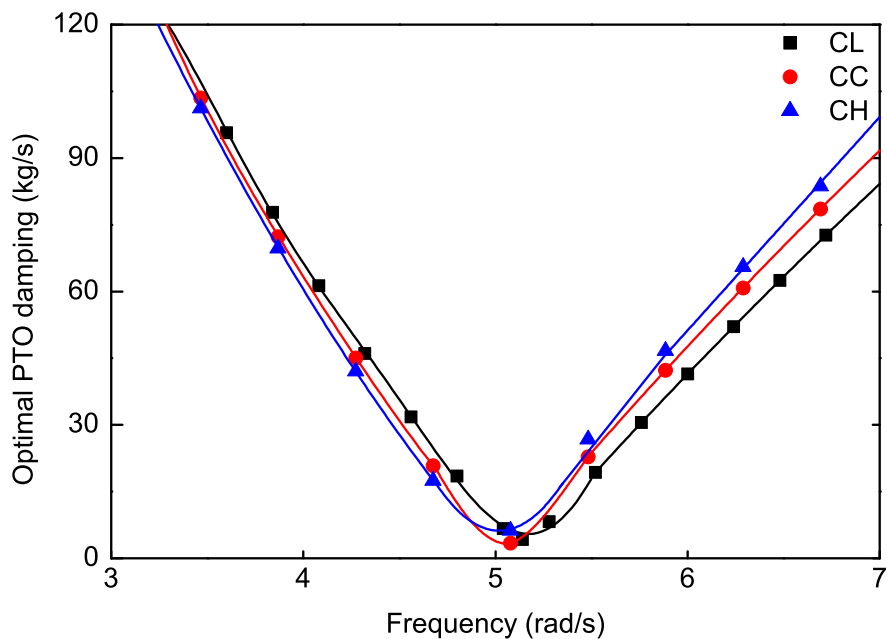


FIGURE 5.4: Optimal PTO damping against wave frequency for CL, CH and CC devices obtained from linear theory using software ANSYS/AQWA. The results are used to predict optimal PTO damping versus wave frequency for passive control.

range from 2.5 m to 10 m. Two wave height samples are discussed here with values of 3.65 m and 7.5 m. According to the scaling 1/50, wave height of 0.073 m and 0.15 m are simulated in the numerical wave tank to represent the moderate and high wave heights in practice. The irregular wave is generated according to the Ochi spectrum described in Figure 3.4.

TABLE 5.2: Parameters of the simulated wave climates.

<i>Regular wave</i>	
Wave height H [m]	0.073, 0.15
Wave frequency ω [rad/s]	3.14, 3.92, 4.52, 4.59, 4.80, 4.83, 4.91, 5.04, 5.51, 6.28
Wave frequency ratio, ω/ω_0	0.65, 0.81, 0.94, 0.95, 0.99, 1.00, 1.02, 1.04, 1.14, 1.3
<i>Irregular wave</i>	
Significant wave height H_s [m]	0.1
Peak frequency ω_p [rad/s]	4.83
Wide and narrow wave sharpness r	0.5, 8

5.3 Results and discussion

5.3.1 Geometric effect on hydrodynamic parameters

The free decay test is conducted in the NWT, in which the device is dropped from an initial position in still water. The device motion then decays to its equilibrium position. The important hydrodynamic parameters for the free decay test corresponding to all three geometric devices are the hydrodynamic added mass a and damping B_{hyd} . The values can be quantified following the mathematical formulations (Falnes, 2002):

$$z(t) = z_0 e^{-\gamma t} \left(\cos \omega_d t + \frac{\gamma}{\omega_d} \sin \omega_d t \right), \quad (5.1)$$

where the coefficient γ can be given as:

$$\gamma = B_{hyd} / [2(M + a)]. \quad (5.2)$$

According to the NWT test, both inviscid radiation damping B_{inv} and viscous damping B_{vis} are considered in B_{hyd} . The device natural frequency ω_0 can be calculated by:

$$\omega_0 = [K/(M + a)]^{1/2}. \quad (5.3)$$

Then the damped oscillation frequency ω_d (equalling $1/T_d$) can be achieved by:

$$\omega_d = (\omega_n^2 - \gamma^2)^{1/2}. \quad (5.4)$$

The logarithmic decrement of the decay motion can be calculated according to Eq. (5.1) and expressed as:

$$\gamma T_d = \ln \frac{z(t)}{z(t + T_d)}. \quad (5.5)$$

It is clear that if the time series of the displacement $z(t)$ is available, the damped oscillation period T_d and the logarithmic decrement will be measured. As a result, the hydrodynamic parameters (a and B_{hyd}) can then be derived based on Eqs. (5.2) to (5.5).

In order to compare the hydrodynamic parameters of the three different geometric devices, free decay tests are conducted by releasing all these devices from an initial position z_0 of 0.2 m in the NWT. The displacements are recorded. Figure 5.5 shows the normalised results corresponding to the different geometric models. As observed, the natural periods T_0 of these three devices are maintained more or less the same at 1.3 s ($\omega_0 = 4.83$ rad/s) as expected in Section 5.2.1. The differences of the decay motion responses can be attributed to the geometric variations.

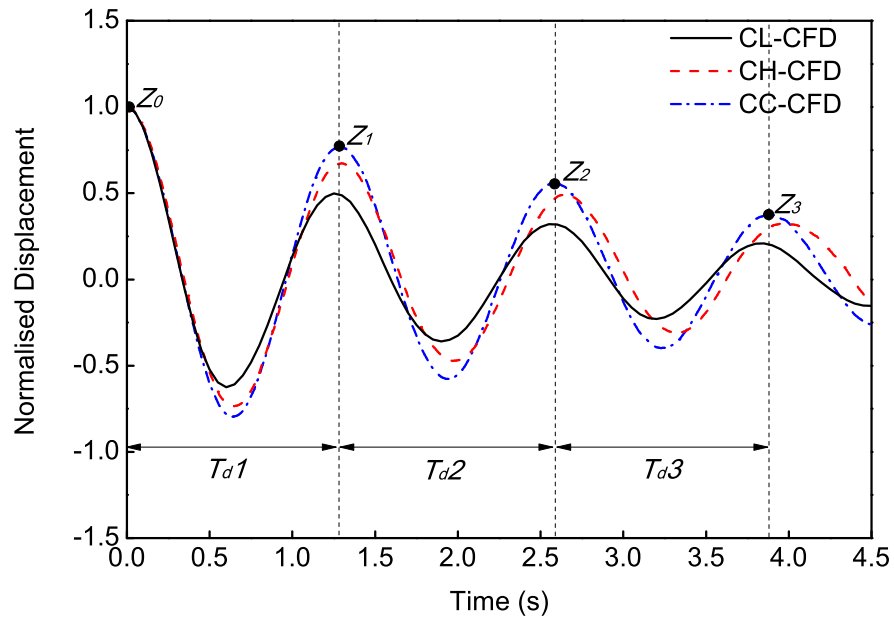


FIGURE 5.5: The normalised results against the initial displacement of 0.2 m for the three devices under free decay tests.

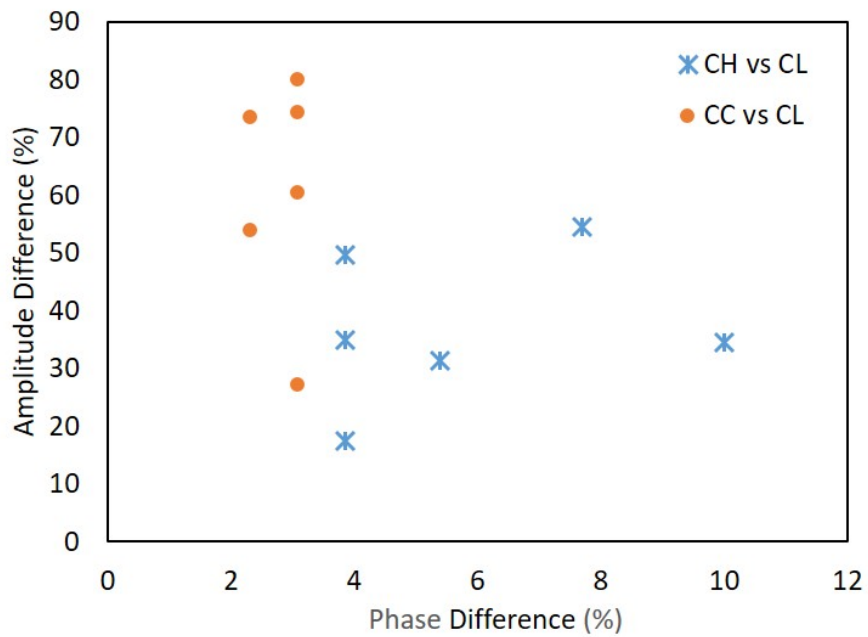


FIGURE 5.6: The amplitude difference against phase difference at troughs and peaks.

Figure 5.6 is transferred from Figure 5.5, which clearly shows the phase difference of CH and CL devices relative to the CL device, respectively. As seen, there still exists phase discrepancies among the three geometric devices although the objective is to keep them definitely consistent. In particular, for the CH device, the phase difference shows to be a bit larger compared to the CC device. Clearly, the phase deviations are controlled under 10%, which is acceptable for the current study by expecting the oscillating periods for the three geometric devices are consistent. In order to reduce the phase difference, in particular for the CH device (showing bigger phase difference), the free decay test can be repeated by changing the device density, which is not further discussed in the work.

Based on Figure 5.5, T_d and $\ln(z(t)/z(t+T_d))$ are measured, as described in Table 5.3. Referring to Eqs. (5.1) and (5.5), the added mass and the hydrodynamic resistance against different PAWEC profiles are calculated, as detailed in Table 5.4. As observed, the device with more streamlined bottom results in smaller added mass and hydrodynamic damping. For the three geometric designs, the most streamlined device CC possesses the smallest a and B_{hyd} .

TABLE 5.3: Measured logarithmic decrements and damped oscillation periods according to Figure 5.5. \bar{T}_d is the average oscillation period.

	$\ln(z_0/z_1)$	$\ln(z_1/z_2)$	$\ln(z_2/z_3)$	
CL	0.73	0.52	0.56	
CH	0.40	0.32	0.42	
CC	0.26	0.32	0.40	
	T_{d1} [s]	T_{d2} [s]	T_{d3} [s]	\bar{T}_d [s]
CL	1.32	1.29	1.36	1.32
CH	1.30	1.35	1.30	1.32
CC	1.28	1.31	1.30	1.30

TABLE 5.4: Qualified added mass and hydrodynamic damping. \bar{a} and \bar{B}_{hyd} are the corresponding average values.

	a_1 [kg]	a_2 [kg]	a_3 [kg]	\bar{a} [kg]
CL	10.41	9.240	12.44	10.70
CH	5.740	8.100	5.720	6.520
CC	3.792	5.162	4.632	4.529
	B_{hyd1} [kg/s]	B_{hyd2} [kg/s]	B_{hyd3} [kg/s]	\bar{B}_{hyd} [kg/s]
CL	33.41	23.27	26.40	27.69
CH	18.05	14.95	19.16	17.39
CC	11.86	14.60	18.16	14.87

The linear hydrodynamic damping B_{hyd} and added mass a at wave frequency of 4.83 rad/s, according to the linear theory, are obtained, as illustrated in Figure 5.2. Table 5.5 shows the comparison between the linear (obtained from ANSYS/AQWA, see Figure 5.2) and non-linear (achieved from NWT, see Table 5.4) predictions of the hydrodynamic parameters for the three devices under natural frequency of 4.83 rad/s. Clearly, there exists substantial discrepancy between the linear and non-linear predictions. The non-linear predictions of a and B_{hyd} are considerably larger than the linear predictions. This can be attributed to the fact that the viscous damping is involved in the NWT, which is ignored in the linear theory. As observed from Table 5.5, the viscous damping is significantly larger than the radiation damping. This is consistent with the indication by Yeung and Jiang (2011). In addition, it is clear that a more streamlined design will lead to a smaller viscous damping, such as the most streamlined design CC generates the smallest viscous damping. This in turn confirms the expectation that geometric configuration will affect the viscous effect.

In Figure 5.5, the most streamlined device CC and to a less extent CH (i.e., devices with streamlined bottoms) exhibit slower decays compared with the CL device (with flat-bottom). This can be associated with the clear decreases in

TABLE 5.5: Added mass, hydrodynamic damping obtained from linear and non-linear simulations.

	a_{linear} [kg]	$a_{nonlinear}$ [kg]	B_{inv} [kg/s]	B_{hyd} [kg/s]	B_{vis} [kg/s]
CL	6.45	4.25	4.54	27.69	23.15
CH	4.08	2.44	3.22	17.39	14.17
CC	3.01	1.519	3.65	14.87	11.22

added mass and hydrodynamic resistance of CC relative to CL, nearly 58% and 46%, respectively (see Table 5.4). As a result, the streamlined device (e.g., CC) will disturb less flow in its neighbourhood during oscillation, compared with the flat-bottom buoy CL. In other words, less vortex can be formed resulting in less energy losses. This result can be supported by the experimental study from Zang et al. (2018). They recorded clear vortex formation around the corner of a heaving flat-bottom buoy and emphasized the energy loss mechanics caused by the viscous effect related to the device geometry configuration.

The data from free decay tests highlight that the geometry optimization can be an efficient method to reduce the energy losses and thereby to improve the wave energy conversion efficiency. Further investigations are provided in Sections 5.3.2 and 5.3.3.

5.3.2 Geometric effect on free motion dynamics

In the NWT without the PTO system, the three devices are excited by a series of regular waves at wave height $H = 0.073$ m (corresponding properties are shown in Table 5.2), respectively. Using ideal response amplitude operator (RAO) response as a requirement, the free motions of the three devices are recorded to specify the most efficient geometric model. The RAO as a function of wave frequency and geometric configuration are plotted in Figure 5.7.

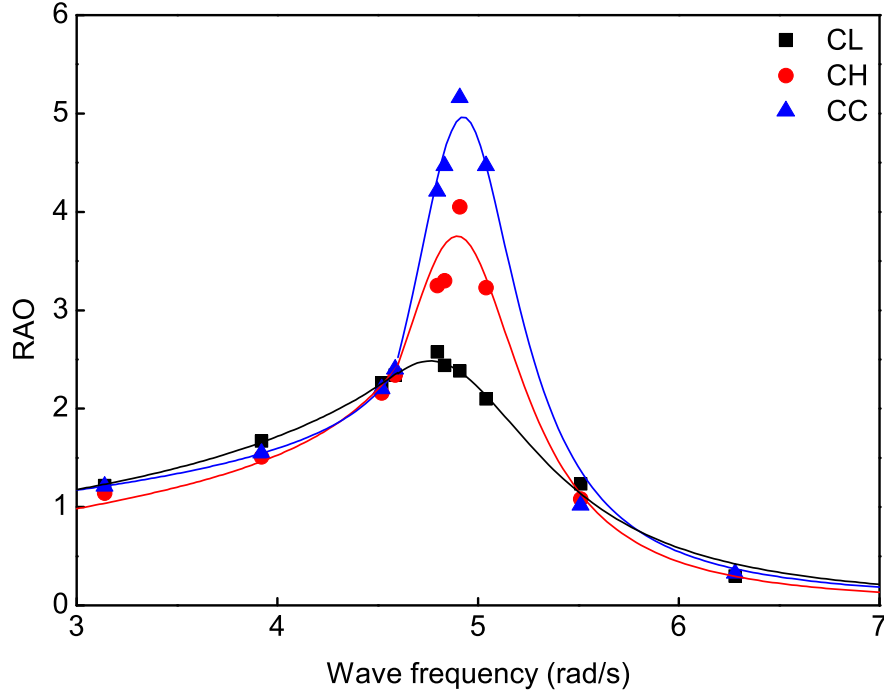


FIGURE 5.7: The variation of heave RAO against wave frequency for the three geometric devices at $H = 0.073$ m, $B_{PTO} = 0$ kg/s.

As observed:

- *At relatively low or high wave frequencies ($\omega < 4.5$ or > 5.5 rad/s), there is little or no difference in the RAO results for all the three devices. In other words, the geometric design has insignificant effect in this frequency range. This is related to the characteristics of the device RAO responses at relatively low frequencies, as described in Section 4.6.2.1. At these wave conditions, the hydrostatic stiffness term $Kz(t)$ (shown in Eq. (4.11)) imposed on the PAWEC device is the dominant force. This results in the device synchronously following the motion of the adjacent flow with negligible phase lag. As a result, the viscous and geometric effects can be negligible. To express this more clearly, the time series of the vertical velocities for the devices as well as for the local water particles are provided at one representative wave frequency of 3.14 rad/s, as shown in Figure 5.8. As expected, all the three devices operate as "wave follower", by synchronously tracking the wave motion.*

More importantly, the velocity responses of the three different PAWEC devices have little or no difference. Thus, all the devices appear to have more or less the same amplitude response relative to the incident wave, at low wave frequencies, as shown in Figure 5.7.

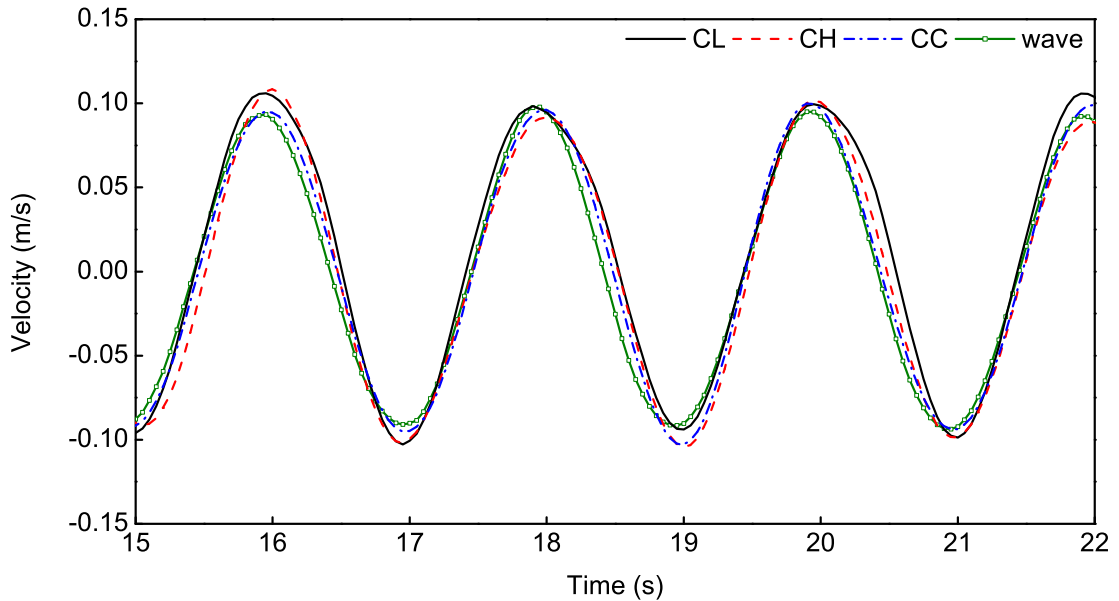


FIGURE 5.8: Time series of velocities for the three geometric PAWECs and the local water particles at the free surface under $H = 0.073$ m, $\omega = 3.14$ rad/s. Note that PTO system is not involved.

- *With the wave frequency approaching the device natural frequency at $4.5 < \omega < 5.5$ rad/s, substantial improvements in RAO can be observed for the streamlined devices CH and CC, compared with CL device. Particularly, the CC model enhances the RAO response by nearly twice that of the CL device at resonance. To demonstrate this more clearly, Figure 5.9 gives the snapshots of the wave-PAWEC interaction within a half period at $\omega = 4.83$ rad/s (wave period of 1.3 s). As observed, the three devices arrive at the trough simultaneously at time = 15 s and reach the peak at time = 15.65 s after a half period. Then the differences of the displacement excursions for the three geometric devices can be seen clearly. The displacement excursions of the CC and CH devices are approximately 1.8,*

1.4 times that of the CL structure, respectively. This highlights the geometric influence around resonance. This phenomenon can also be explained by the amplitude response properties summarized in Section 4.6.2.1. Near resonance, with the abrupt vanish of the real part (see Eq. (4.22)), hydrodynamic damping force including the inviscid radiation and viscous forces would become dominant. Based on the parameters determined from the free decay test (see Table 5.5), the differences in inviscid radiation damping of the three devices are insignificant. In contrast, the differences in viscous damping are significant with the CC device generating the smallest viscous damping whereas CL having the largest values. It follows therefore, under the same wave excitation, CC will have the largest amplitude response. Figure 5.10 shows one example of the velocity response around the device natural frequency at $\omega = 4.83$ rad/s. As observed, CC demonstrates the largest velocity amplitude, followed by CH and CL. Also, approximately 90° of phase lags are found between the devices and wave motions. As a result, CC has the largest relative velocity, followed by CH and CL. As generally known, the viscous force has positive relationship with the relative velocity and the viscous damping coefficient. Therefore, the velocity responses suggest that compared with CL and CH, a considerably small viscous damping is required for the CC device to maintain the largest amplitude response and the smallest hydrodynamic damping force. This in turn confirms the results achieved through free decay tests, as shown in Table 5.5.

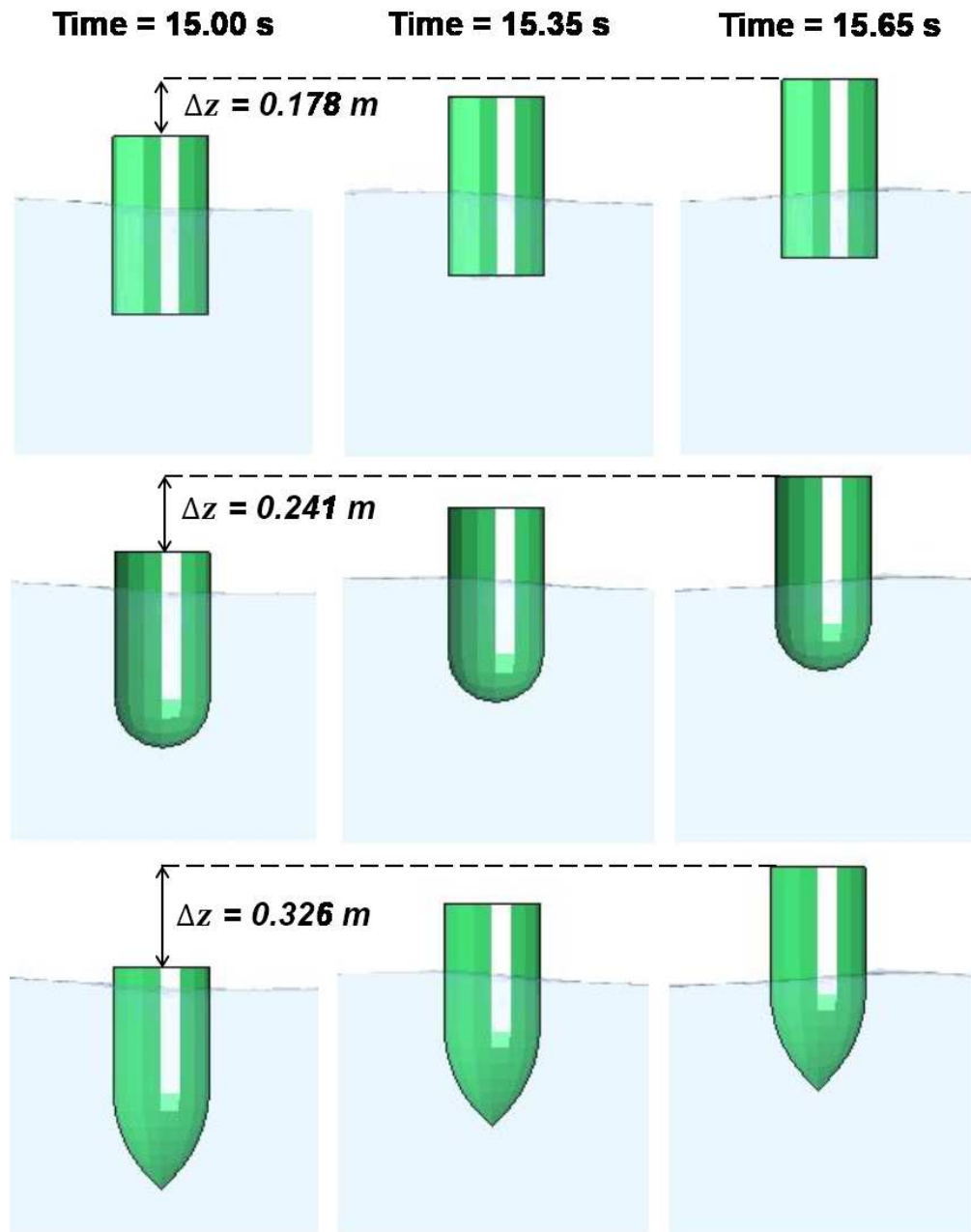


FIGURE 5.9: Wave-PAWEC interaction snapshots within a half period at $H = 0.073 \text{ m}$, $\omega = 4.83 \text{ rad/s}$. Δz is the displacement excursion from the trough to the peak.

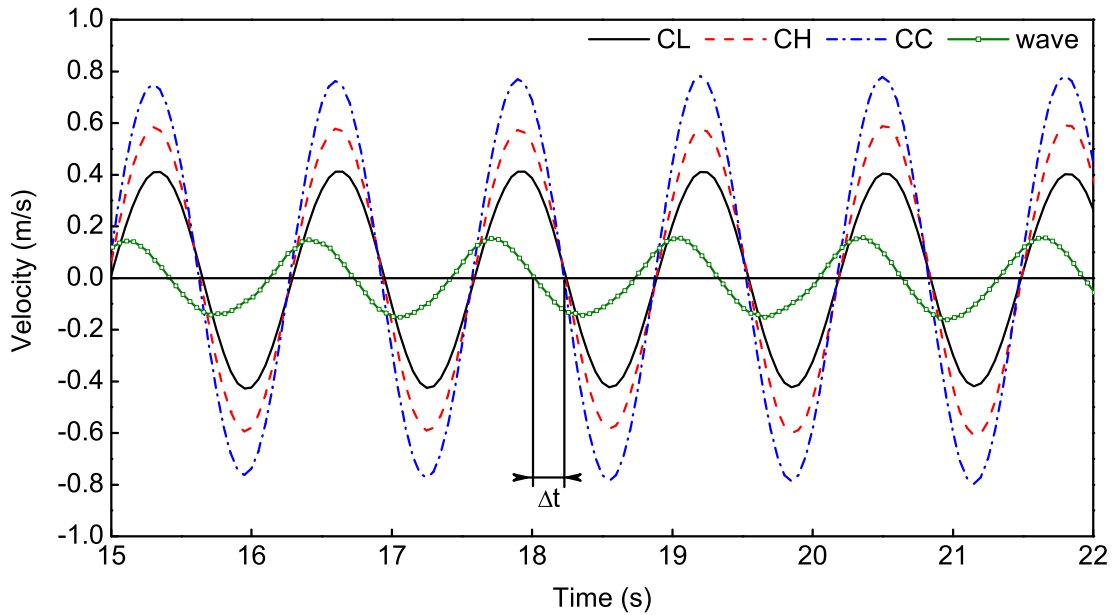


FIGURE 5.10: Time series of velocities for the three geometric PAWECs and the local water particles at the free surface under $H = 0.073$ m and $\omega = 4.83$ rad/s. Note that PTO system is not involved.

According to the above results, considering the three different geometries described in Figure 5.1, CC appears to be the optimal geometric structure for hydrodynamic response maximization. Hence in Section 5.3.3, only CL and CC devices are investigated further to develop a discussion of the joint effects of geometry and PTO damping on energy conversion efficiency.

5.3.3 Joint effects of geometry and PTO damping on power absorption

5.3.3.1 In regular waves

As indicated by Falnes (2002), under regular waves, the optimal power absorption can be achieved at "resonance" and PTO resistance identical to hydrodynamic damping. The so-called "resonance" is generally reflected by the fact that the

device velocity is in phase with the wave excitation force. In other words, the device velocity lags the velocity of a regular wave by nearly 90° under the assumption that the phase of the wave excitation force is nearly zero degree for this frequency range (as indicated by [Guo et al. \(2018b\)](#)).

As generally known, the resonant frequency is a constant for a given WEC device. This leads to a narrow power absorption bandwidth, as shown in [Figure 4.14](#). In order to broaden the bandwidth, the PTO control method is generally introduced (i.e., control for the PTO spring and damper components). This approach is the so-called optimal control or reactive control. However, this method needs to address a bidirectional power flow, which is complex and still under investigation. In this work, the passive control (a sub-optimal control approach) is applied, aiming at studying the interaction between the geometry design and PTO damping and the resulting joint effects on PAWEC power absorption performance. As shown in [Figure 3.7a](#), a linear damper component is introduced into the NWT to simulate the PTO action. Through the numerical tests, the PTO force and the device velocity can be recorded. Then the resulting average absorbed power can be calculated based on [Eq. \(4.16\)](#).

To generally illustrate the resonant power absorption and the absorption characteristics away from resonance, representative CL dynamic performances are given as follows:

- [Figure 5.11](#) shows two examples close to resonance condition of $\omega/\omega_0 \approx 1$. As seen, under this wave condition, no matter at PTO damping of 30 kg/s or 60 kg/s, the velocity phase lags of the CL device relative to the local wave particles are shown to be close to 90° , as calculated by $360\Delta t/T$. However, there exists clear difference in velocity magnitude caused by PTO damping variation. Significant decrease in device velocity is introduced by changing the PTO damping from 30 kg/s to 60 kg/s. This can be associated with the over-damped motion at

$B_{PTO} = 60$ kg/s. Referring to Figure 5.13, it can be seen that the maximum power absorption is nearly achieved around $\omega/\omega_0 = 1$ and $B_{PTO} = 30$ kg/s. By comparison, clear decrease in power absorption can be noticed when PTO damping increases to 60 kg/s around $\omega/\omega_0 = 1$. As a result, near resonance wave conditions, there exists an optimal PTO damping to maximize the power capture whereas the decline of the power capture will be generated with the PTO damping departing from this point.

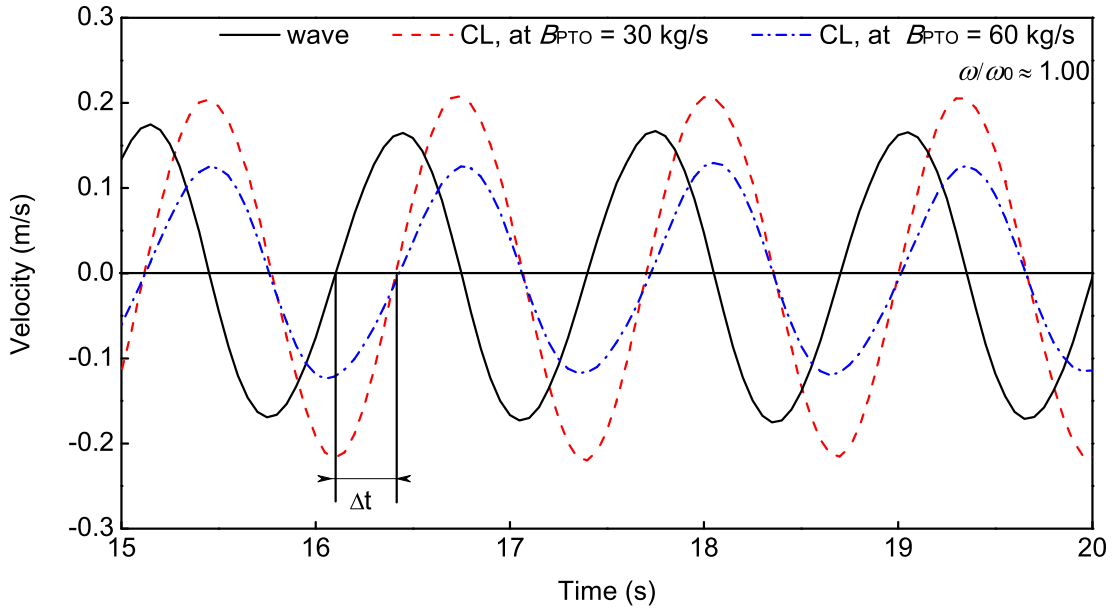


FIGURE 5.11: Velocity data for the CL device and the local water particles at the free surface under $H = 0.073$ m, $\omega/\omega_0 \approx 1$. PTO system is involved.

- Figure 5.12 shows two examples away from resonance at $\omega/\omega_n = 0.81$. As observed, under this wave condition, a larger PTO damping reduces the response amplitude but increases the velocity phase lag between the device and the wave to be further close to 90° . This finding corresponds to the experimental indications by Zang et al. (2018). As a result, a much larger PTO damping is required for the power absorption maximization at this relatively low wave frequency condition.

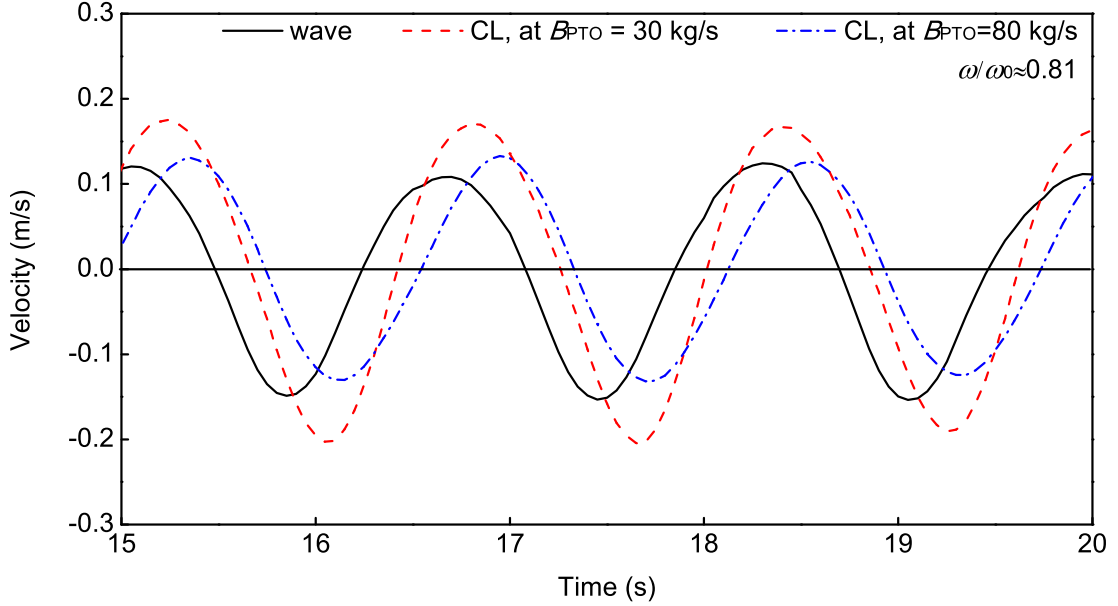


FIGURE 5.12: Velocity data for the CL device and the local water particles at the free surface under $H = 0.073$ m, $\omega/\omega_n = 0.81$. PTO system is involved.

To demonstrate the joint effect of the geometry and PTO damping on power capture more clearly, the average power absorption efficiency as a function of PTO damping under varying regular wave conditions for the CL and CC devices are summarized, as shown from Figures 5.13 to 5.16. Solid fitting lines are plotted to show the trends. It can be noticed, under both moderate and high wave heights of 0.073, 0.15 m:

- *Wave frequency shows to be a critical factor in affecting the power absorption efficiency.* As observed, when the wave frequency is around the device natural frequency (e.g., $\omega/\omega_0 = 1.02, 1, 0.95$), the power absorption efficiencies are generally higher than that in the wave conditions away from this region (corresponding to $\omega/\omega_0 = 1.14, 0.81, 0.65$) for both CC and CL under both moderated and high wave heights. This concurs with the fundamental theory and numbers of experimental results, which indicates that the maximum power absorption could be achieved when the incident wave frequency matches the device natural frequency [De Backer](#)

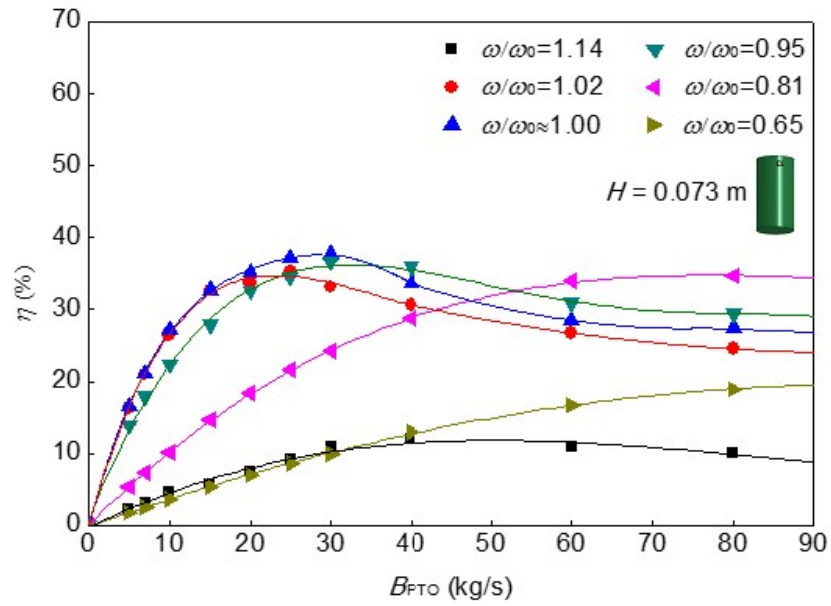


FIGURE 5.13: Variation of wave energy conversion efficiency against the PTO damping coefficient under different wave frequencies under $H = 0.073$ m for CL. The solid fitting lines are plotted for trending references.

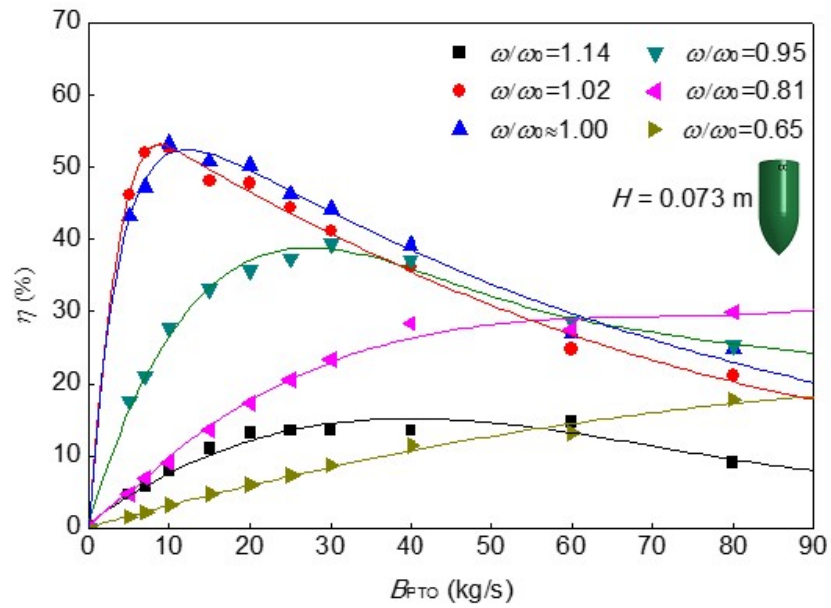


FIGURE 5.14: Variation of wave energy conversion efficiency against the PTO damping coefficient under different wave frequencies under $H = 0.073$ m for CC. The solid fitting lines are plotted for trending references.

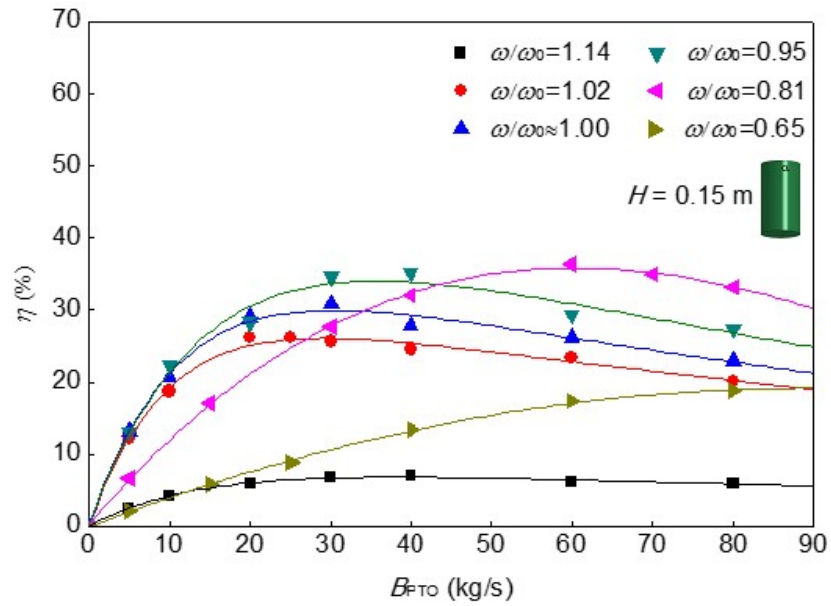


FIGURE 5.15: Variation of wave energy conversion efficiency against the PTO damping coefficient under different wave frequencies under $H = 0.15$ m for CL. The solid fitting lines are plotted for trending references.

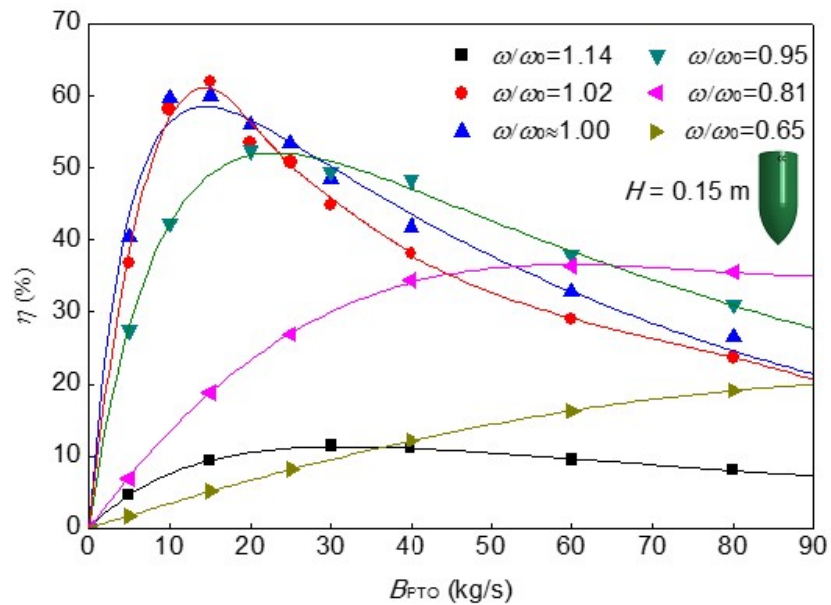


FIGURE 5.16: Variation of wave energy conversion efficiency against the PTO damping coefficient under different wave frequencies under $H = 0.15$ m for CC. The solid fitting lines are plotted for trending references.

(2009), Vantorre et al. (2004), Falnes (2002).

- *The joint effects of the geometry and PTO damping on the power absorption are significant when the wave frequency is around the natural frequency of the device.* For example, at $H = 0.073$ m, $\omega/\omega_0 \approx 1$, the CC device achieves the maximum efficiency at PTO damping of 10 kg/s, which is only one third of the optimal damping of 30 kg/s for CL. In addition, the CC device demonstrates apparent superiority over CL in harvesting wave energy. As observed, at $H = 0.073$ m, maximum efficiency of 53.3% is achieved for CC device in contrast with that of 37.7% for CL device. At $H = 0.15$ m, the maximum efficiency of CC device is 62%, by up to 70% increase with respect to that of CL.

- *The geometry effects on the optimal values of the PTO damping and absorption efficiency turn out to be insignificant when the wave frequency is away from the device natural frequency (e.g., $\omega/\omega_0 = 1.14, 0.81, 0.65$).* As observed, for the different geometric device, the power capture trends against PTO damping are shown to be more or less the same at given wave conditions. Furthermore, a high PTO damping is expected to reach the optimal power absorption for both CL and CC devices at a given wave condition. For example, at a relatively low wave frequency $\omega/\omega_0 = 0.65$, the required optimal PTO damping would exceed 80 kg/s. This is consistent with the result described for Figure 5.12, suggesting that a relatively high resistance load is required to damp the device motion for power absorption improvement at wave frequencies away from the device natural frequency.

The optimal applied PTO damping versus wave frequency obtained via CFD simulations is plotted in Figure 5.17, in comparison with the predictions by the linear theory. Clear discrepancy can be noticed around $\omega/\omega_0 = 1$. As observed, the predicted optimal PTO damping coefficients via CFD simulations are higher than those gained from the linear theory, especially for the flat-bottom device CL. For

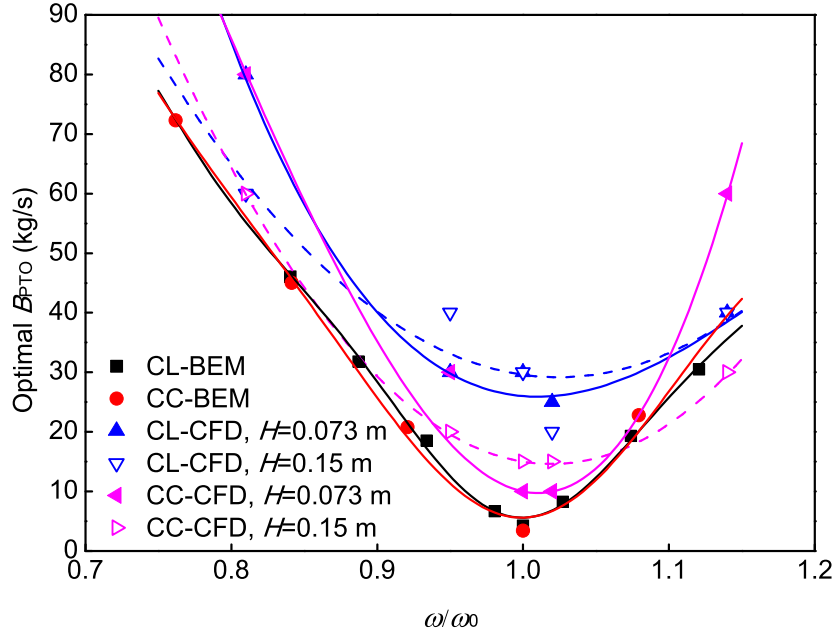


FIGURE 5.17: Optimal PTO damping versus wave frequency for CL and CC devices obtained via CFD analysis. The solid fitting lines are plotted for trending references.

the CL device close to $\omega/\omega_0 = 1$, the optimal damping is more or less 30 kg/s, nearly 5 times larger than the predicted value from the linear theory. For the CC device close to $\omega/\omega_0 = 1$, the optimal damping predicted through CFD method is still larger than the linear prediction but the discrepancy shows to be somewhat smaller in contrast with the CL device. This is mainly due to the inviscid fluid applied in the linear theory. Hence, only the inviscid radiation damping contributes to the PTO damping. However, this is impractical especially around $\omega/\omega_0 = 1$ where the device would experience indispensable viscous effect as mentioned above. By considering a viscous fluid, in the CFD simulation, viscous damping would account for a proportion of the hydrodynamic damping. Hence, this leads to a larger requirement of the optimal PTO damping than the linear theory close to $\omega/\omega_0 = 1$. Furthermore, as observed, the CL device requires a larger PTO damping (nearly 30 kg/s) than the CC device (approximately 10 kg/s). This in turn

confirms the indication that the more streamlined device would produce a smaller hydrodynamic damping compared with the flat-bottomed PAWEC, resulting in less energy losses as discussed in Sections 5.3.1 and 5.3.2.

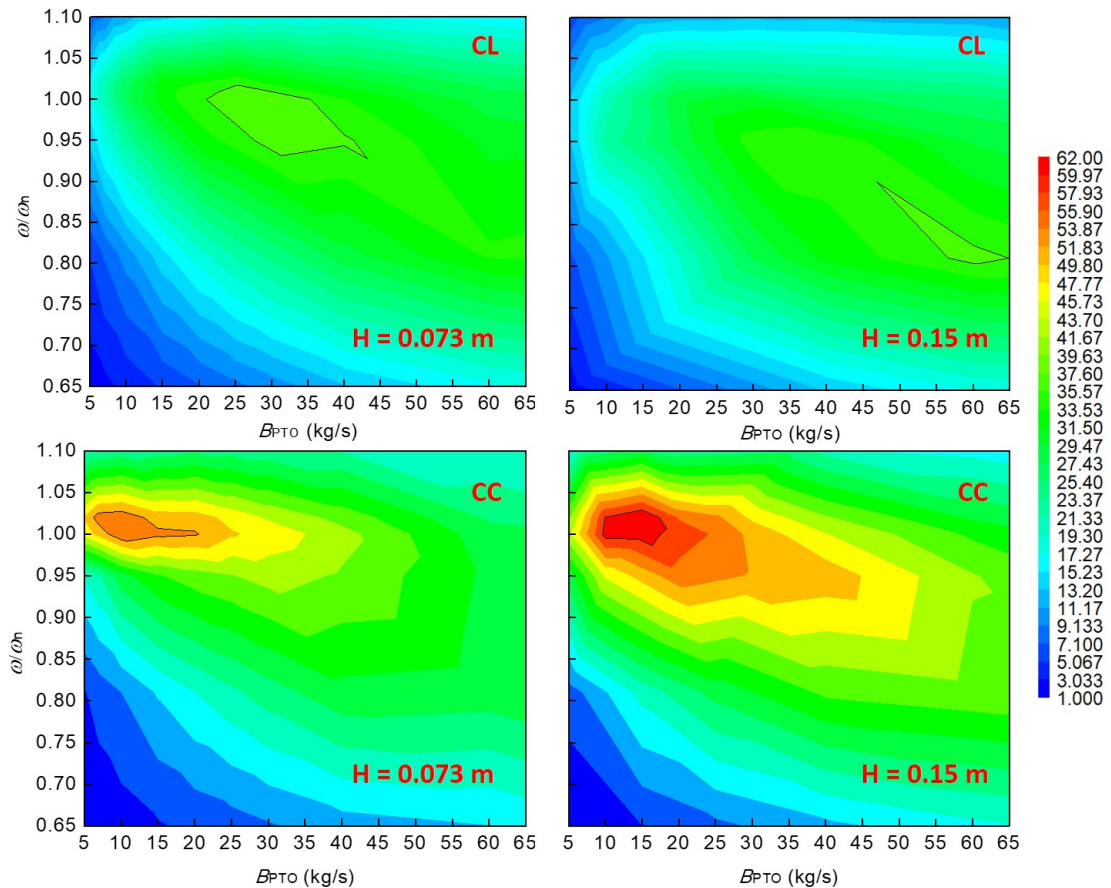


FIGURE 5.18: Comparison of the shift in maximum power absorption between CL and CC device as the wave height increases. The zone circled by the black solid line represents the maximum power absorption efficiency.

To further illustrate the joint effects of geometry and PTO damping on the characteristics of the maximum absorption efficiency at varying wave heights, Figure 5.18 is given. As observed, for the CL device it is clear that the maximum efficiency shifts towards a lower wave frequency and a higher PTO damping as the wave height increases. These CFD results correspond with the experimental and CFD data given in Davis (1990), Anbarsooz et al. (2014). By contrast, for the CC

device, no discrepancies are apparent in the optimal values of the PTO damping and wave frequency, corresponding to the two wave heights shown. The maximum power absorption efficiency seems to be maintained consistently around $\omega/\omega_n = 1$ rad/s and $B_{PTO} = 10$ kg/s. These observations can be supported by:

- (i) The optimal PTO damping and wave frequency are related to the hydrodynamic damping including viscous damping in practice.
- (ii) The viscous effect on a flat-bottom device is much larger than that on a streamlined design.
- (iii) The viscosity magnitude is highly dependent on the oscillation magnitude.

Thus, in contrast to the CC design, the optimal power efficiency characteristics of the CL design have a clearly higher dependence on wave height. This shows that the hydrodynamic behaviour of the CL device has significantly stronger non-linearity than that of the CC counterpart.

Figures 5.19 and 5.20 illustrate the power absorption efficiency increase of the CC device relative to CL at the two different wave heights. It can be noted that the CC PAWEC presents clear superiority over the CL device in extracting wave energy, by up to 200% increase under both wave heights. Additionally, the efficiency increase shows an inverse relationship to the PTO damping. This can be explained as the resistance caused by the PTO turns out to be dominant with increasing B_{PTO} , thus weakening the hydrodynamic damping influence caused by the geometrical design. In other words, at a sufficiently large B_{PTO} , the geometry effect on the device power absorption and the prediction of the optimal PTO damping would become negligible. However, this situation could be achieved at the expense of a relatively small power absorption efficiency, as shown from Figures 5.13 to 5.16. In summary, when considering a new PAWEC device design it is necessary to investigate initially the most efficient configurations of the device geometry and

PTO damping for high energy absorption. It is therefore important to consider a "co-design" approach based on the device geometry, PTO damping and expected wave conditions.

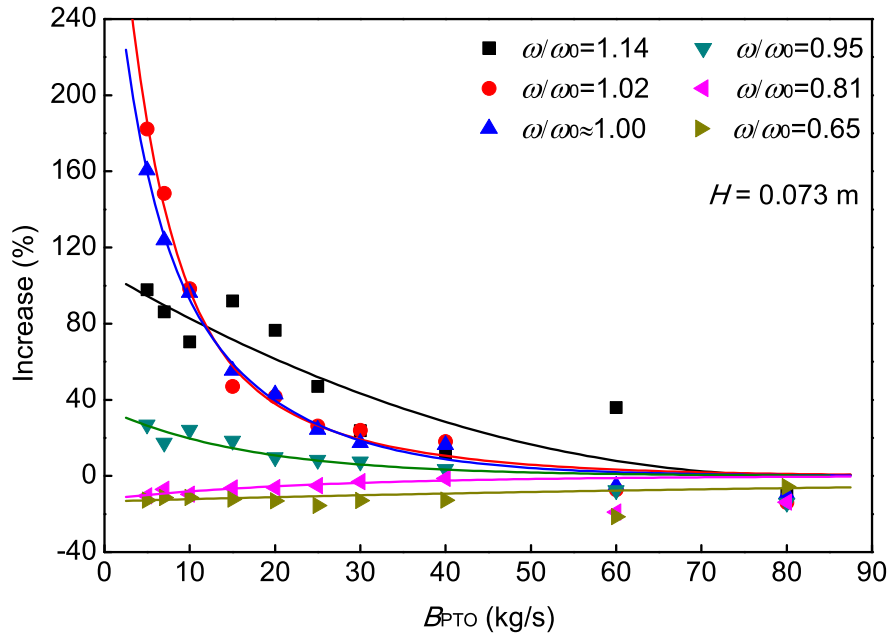


FIGURE 5.19: The variation of the absorption efficiency increase (CC relative to CL) against PTO damping coefficient.

5.3.3.2 In irregular waves

Two series of Ochi spectral (corresponding parameters are detailed in Table 5.2) are applied in the NWT to generate irregular waves. The difference of these two irregular waves is on the selection of the spectral bandwidth coefficient r . A narrow spectrum will be generated at $r = 8$, in contrast to a wide spectrum produced at $r = 0.5$.

The device motions and wave elevations in time series at $B_{PTO} = 0$ kg/s are obtained (see Figures 5.21 and 5.22). In a similar manner to the observations corresponding to regular wave excitation (see Figure 5.7), the CC device still shows

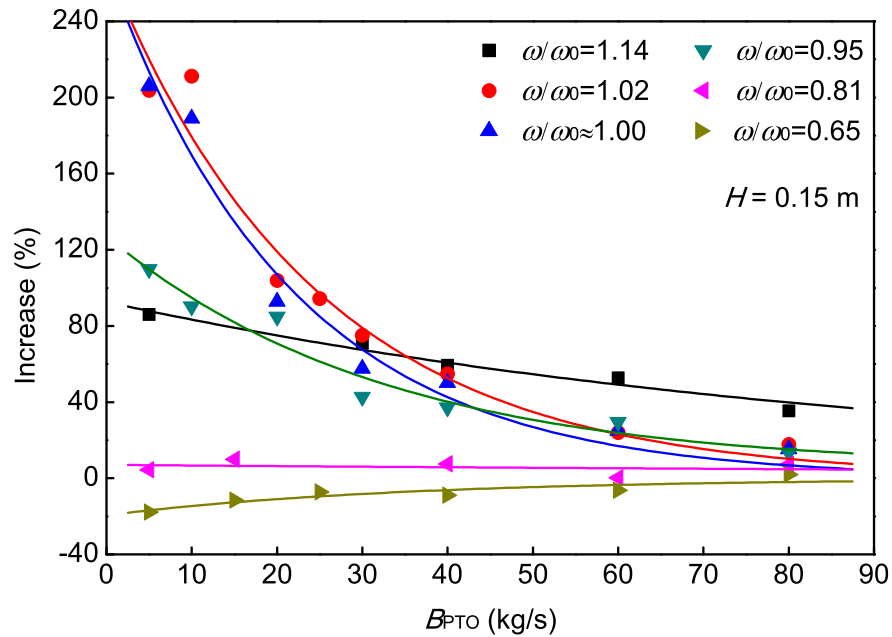


FIGURE 5.20: The variation of the absorption efficiency increase (CC relative to CL) against PTO damping coefficient.

more efficient dynamic performance compared with the CL under these two kinds of irregular waves. In the case of CC larger oscillation magnitudes are evident, thus implying the higher energy efficiency.

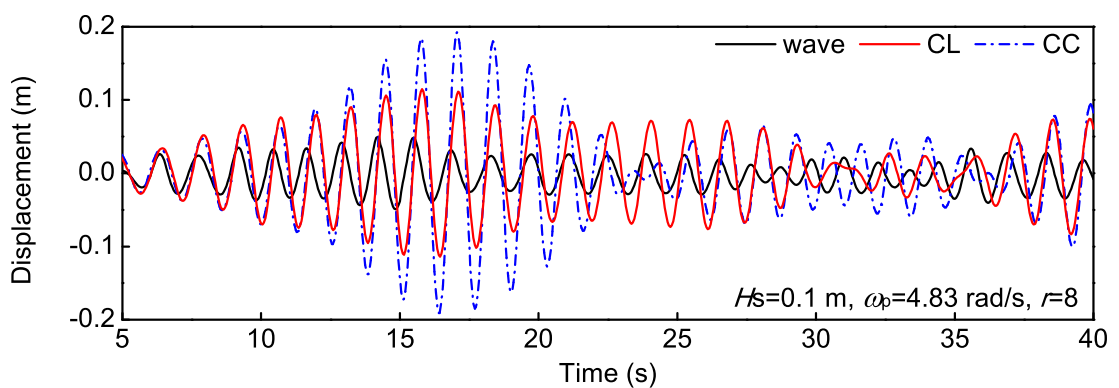


FIGURE 5.21: Time series of the CL, CC and wave motions under irregular waves of $H_s = 0.1$ m, $\omega_p = 4.83$ rad/s and $r = 8$. $B_{PTO} = 0$ kg/s.

Under these two types of irregular wave conditions, the instantaneous power outputs are obtained by the product of the device velocity and the PTO damping

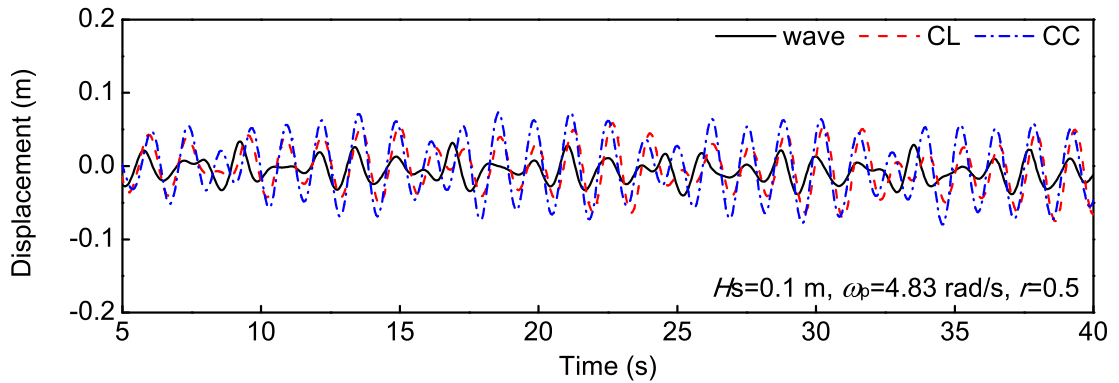


FIGURE 5.22: Time series of the CL, CC and wave motions under irregular waves of $H_s = 0.1$ m, $\omega_p = 4.83$ rad/s and $r = 0.5$. $B_{PTO} = 0$ kg/s.

force. Figures 5.23 and 5.24 demonstrate an example at PTO damping of 10 kg/s. Clearly, the captured power using the CC device is larger than that of CL device for these two wave conditions.

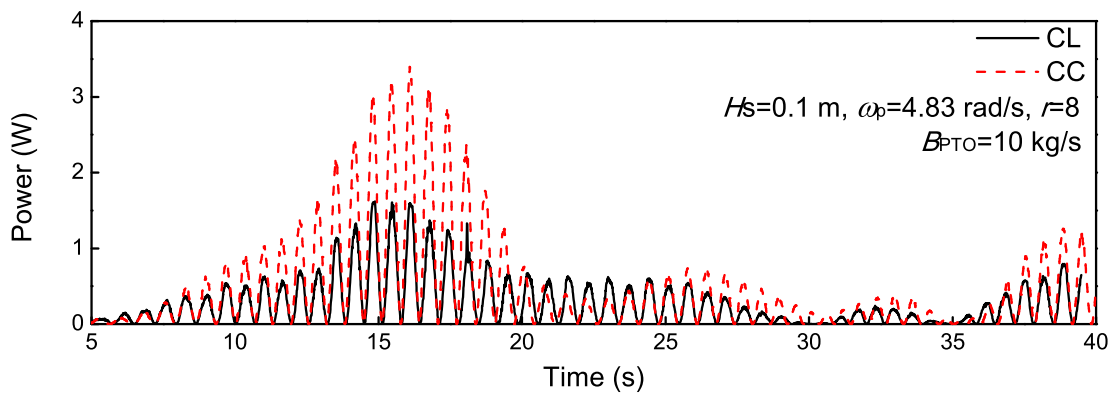


FIGURE 5.23: Instantaneous powers of the CL and CC devices under irregular waves of $H_s = 0.1$ m, $\omega_p = 4.83$ rad/s and $r = 8$, respectively. $B_{PTO} = 10$ kg/s.

Furthermore, the variations of the average captured power against the applied PTO damping are shown in Figure 5.25. As observed, the CC device shows prominent superiority in extracting wave energy almost over the whole studied PTO damping range of 0 to 80 kg/s, in contrast to the CL device at $r = 8$. Regarding a wide spectrum at $r = 0.5$, a smaller extent of superiority of CC over CL can be found from 0 to 30 kg/s. These findings imply that to highly exploit the

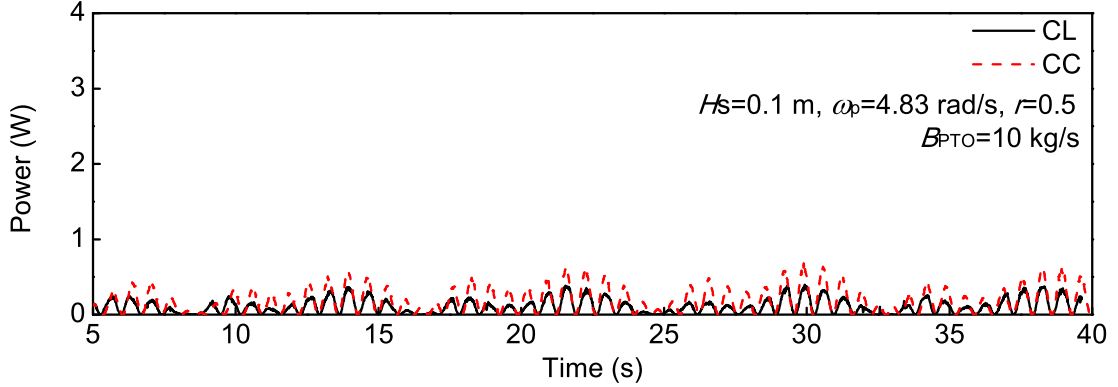


FIGURE 5.24: Instantaneous powers of the CL and CC devices under irregular waves of $H_s = 0.1$ m, $\omega_p = 4.83$ rad/s and $r = 0.5$. $B_{PTO} = 10$ kg/s.

advantage of applying the streamlined-bottom device for the reduction of energy loss and the enhancement of power absorption, it is of fundamental importance to match the majority of wave frequencies with the device natural frequency (e.g., at $r = 8$). This confirms the requirement of considering the "co-design" concept. In other words, it is necessary to jointly consider the device geometry, PTO system and wave conditions to enhance the power capture.

5.4 Conclusions

This Chapter aims at studying the joint effects of geometry and PTO damping on the power absorption under both regular and irregular waves. A series of numerical tests are conducted in the NWT, e.g., free decay test, free motion test and power absorption test. According to the simulated results, the conclusions can be drawn as below:

- Added mass a and hydrodynamic damping B_{hyd} are quantified for the three geometric devices from free decay tests. Up to 60% decrease in both a and B_{hyd} is observed as the geometry changes from CL to CC. As a result, compared with the

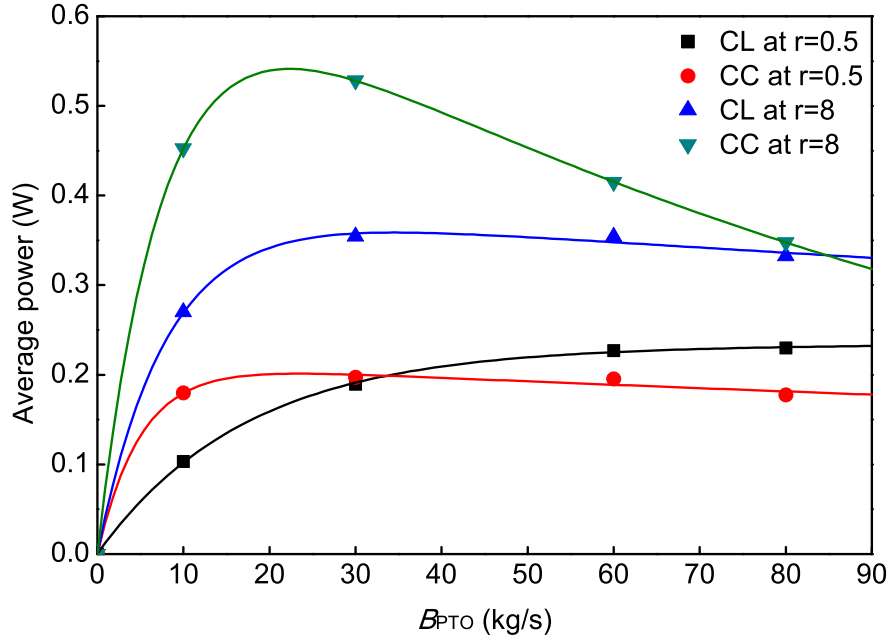


FIGURE 5.25: Variation of average power (for 40 s) with PTO damping coefficient under irregular waves of $H_s = 0.1$ m, $\omega_p = 4.83$ rad/s and $r = 0.5, 8$, respectively.

flat-bottomed CL, significantly slower decay in motion is found for the streamlined CC.

- From free motion test without PTO, it can be seen the geometry design has a prominent affect the device amplitude response, especially around resonance. The streamlined device CC results in up to 100% increase of amplitude responses compared with the CL device near resonance. In addition, the geometry optimization with streamlined bottom leads to remarkable decrease in viscous damping, which contributes to the increasing amplitude response.
- Conducting the PAWEC performance with PTO action under regular waves, it can be found that the joint effects of geometry and PTO damping on the power absorption efficiency characteristics are significant. For the CC device, the maximum power absorption efficiency is maintained consistently at a PTO damping of 10 kg/s and near resonance for different wave heights. In contrast, for the CL

device, the maximum efficiency shifts towards a larger PTO damping (changing from 30 to 60 kg/s) and a lower wave frequency (changing from $\omega/\omega_n = 1$ to 0.81) with increasing wave height. The maximum power efficiency is enhanced to 53.3% and 62%, respectively for wave heights H of 0.073 and 0.15 m for CC, relative to that of 37.7% and 36% for CL.

- With PTO action under irregular waves, the joint effects of geometry and PTO damping on the power absorption can also be seen. The superiority of the CC device over the CL device is clearly shown in enhancing the captured power over a large range of PTO damping (ranging from 0 to 80 kg/s), at a narrow wave spectrum condition with the peak wave frequency matching the device natural frequency. Under a wide wave spectrum condition, the advantage of using the streamlined device still exists but reduces to a smaller extent with the PTO damping ranging from 0 to 30 kg/s.

In summary, parameters considered, such as the geometry, the PTO damping, the wave frequency and the wave height show clear mutual interaction with each other in affecting the heaving PAWEC performance. This suggests the application of "co-design" in optimizing the device performance for power generation. In the future, based on the numerical study in this work, a further study on the PAWEC performance optimization would be extended to physical experiments in the UoH flume tank.

The non-linear power capture characteristics of the CL device against PTO damping and wave condition are summarized in this Chapter, as shown from Figures 5.13 to 5.18 and Figure 5.25. It is clear that it can be possible to find an appropriate PTO damping for optimal power capture regarding different wave conditions via large numbers of tests. Although the wave condition is stochastic in practice, it is not realistic to apply large numbers of trials. To solve this, control method

(PSO-FLC) is implemented to adaptively achieve efficient PAWEC performance with respect to the stochastic wave conditions, as discussed in the Chapter [6](#).

Chapter 6

PSO-FLC implementation on PAWEC

6.1 Introduction

By conducting series of numerical tests, the optimal power take-off (PTO) damping can be found for power capture maximisation under different wave conditions regarding the designed point absorber wave energy converter (PAWEC), as summarized in Chapter 5. This method is defined as the passive control with constant PTO damping (PCCD) in this work. The corresponding results concur with the experimental study conducted by (Zang et al., 2018). However in practice, it is unrealistic to conduct numbers of trials for achieving the optimal PTO damping with respect to a stochastic wave. Hence, it is important to adaptively adjust the PTO damping regarding the stochastic irregular waves. To achieve this, a fuzzy logic controller accompanied by particle swarm optimization (PSO-FLC) (Bouarroudj et al., 2017, Debnath et al., 2013) is implemented on the PAWEC device (via simulations) to address the tuning problem, as discussed in this Chapter. Fuzzy

logic controller has been successfully used in many fields due to its easy implementation from human experts (Lee, 1990, Azadegan et al., 2011). However, the main disadvantage of this controller is that the tuning of the membership functions (MFs) is time consuming. To overcome this, various techniques have been used to automatically optimize the parameters of MFs, such as genetic algorithm or PSO (Fang et al., 2008, Messai et al., 2011). In this work a PSO based FLC is used to adaptively tune the PTO damping for power adsorption improvement.

Figure 6.1 shows briefly the corresponding concept. As shown, the controller sets the PTO damping as the control variable. To self-adjust the controller regarding the incident wave condition, the PSO algorithm is integrated into FLC for the membership functions (MFs) optimization of the fuzzy rules.

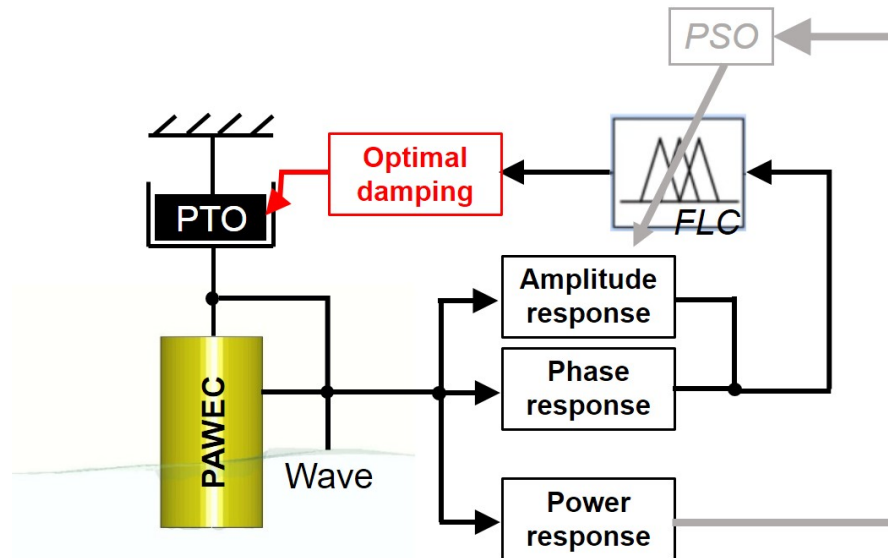


FIGURE 6.1: General sketch of the PSO-FLC method applied on the PAWEC.

The main contributions of this Chapter are summarized as follows:

- *First of all, the FLC method is implemented on the PAWEC device (in simulations) to indicate its capability of tuning the PTO damping for power absorption maximisation. In this work, the fuzzy inference system (FIS) is designed according*

to the power capture characteristics summarized from the numerical tank tests, as described in Chapter 5. The results show clearly that applying the FLC can yield adaptive PTO damping tuning with respect to the incident wave condition.

- *The PSO algorithm is then applied to the control system to adaptively tune the parameters of the FIS in order to further improve the control action.* In the proposed PSO process, each particle is designed to represent the crucial parameters (the mean value and standard deviation) of the Gaussian MFs for the inputs and outputs. The results show that each particle will be updated to search for an optimal set of MFs after numbers of iteration. As a result, the amount of the absorbed wave energy is increased.

The rest of this Chapter is described as: Section 6.2 provides the system structure; The designs of the FLC and the PSO-FLC are detailed in Section 6.3; Section 6.4 describes the results and discussion; study is concluded in Section 6.5.

6.2 System structure

The designed 1/50 scale PAWEC consists of a cylindrical buoy reacting against the incident waves and the PTO force. In this work, the device is constrained to operate only in heave mode. The motion of the device obeys Newton's second law, expressed as:

$$M\ddot{z}(t) = f_e(t) + f_r(t) + f_v(t) + f_s(t) + f_{PTO}(t). \quad (6.1)$$

The proposed non-linear state-space model (NSSM) in Section 4.4 is used to describe the PAWEC hydrodynamics, as demonstrated in Figure 4.15. Then by

involving the PSO-FLC method to tune the PTO damping, the whole system can be given in Figure 6.2.

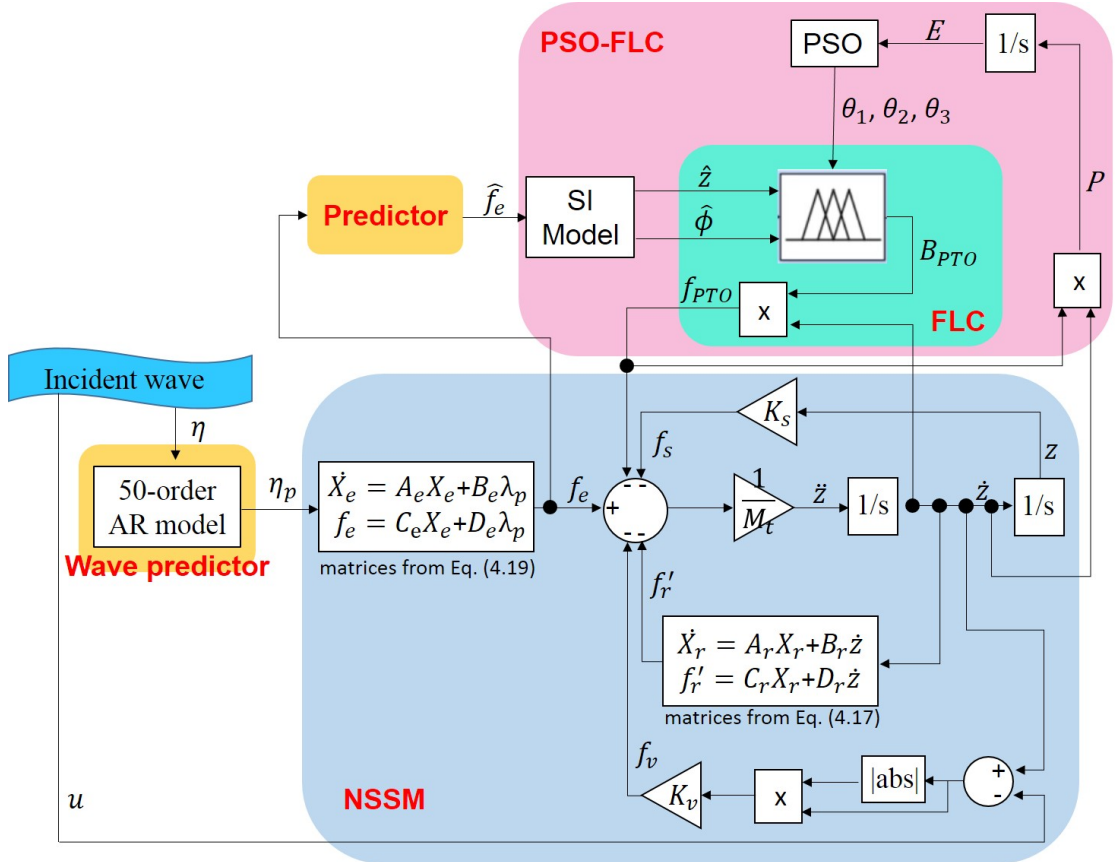


FIGURE 6.2: PAWEC system architecture.

As shown, for the considered PAWEC, the wave excitation force f_e is related to the incident wave elevation. It is approximated by a 6-order state-space model with a 1 s of wave prediction, as detailed in Section 4.3.2. For the radiation force f_r , a 4-order state-space model is derived to approximate its convolution term with the PAWEC oscillating velocity as the input (see Section 4.3.1). The non-linear factor, i.e., the viscosity force f_v is considered according to the quadratic term in the Morison equation. Corresponding viscous coefficient K_v is identified by the computational fluid dynamics (CFD) tank tests, as described in Section 4.5. The hydrostatic force f_s is expressed by $-K_s Z$, where K_s is the hydrostatic stiffness

coefficient given by $\rho g \pi (D/2)^2$. f_{PTO} is the PTO control force. In order to avoid bidirectional power flow, the PTO role is simulated only by a damper operating just as a generator (expressed as $B_{PTO} \dot{Z}$). Hence, the PTO damping coefficient B_{PTO} is the control variable in this system.

FLC is proposed to adapt the PTO force by continuously controlling the damping coefficient B_{PTO} . The control variable is computed based on the predicted wave excitation force with 0.01 s horizon. The prediction of the excitation force is realised by an AR model, which is similar with the method applied for the wave elevation prediction, as described in Section 4.3.2. System identification (SI) is applied to offer a state-space model for simulating the PAWEC hydrodynamics under the predicted wave excitation force. To search more efficient MFs parameters $(\theta_1, \theta_2, \theta_3)$ for the control action improvement, PSO algorithm is involved aiming at maximizing the absorbed energy E .

6.3 Controller design

6.3.1 FLC

As discussed in Chapter 4, the dynamics of the PAWEC are actually non-linear with respect to the incident waves, differing from the conventional linear description. In other words, the system suffers from modeling complexity regarding different wave conditions. Therefore, instead of the model based controller, the FLC method is applied to control the PAWEC device which is independent of the mathematical modeling of the hydrodynamic plant. However, this control method has a main drawback that an efficient rule base of the FIS needs to be determined by trial and error.

Section 5.3.3 details the non-linear power capture properties of the PAWEC device summarized from numerical wave tank tests. The data are used here to guide the design of the fuzzy rules. According to the results discussed in Section 5.3.3, it can be found that the power absorption efficiency is dependent of the PAWEC hydrodynamic performance, i.e., the device's amplitude and phase responses against the incident wave. Clearly, for the designed cylindrical PAWEC, the optimal power absorption is achieved when the device reaches nearly 90° phase lag relative to the wave motion at B_{PTO} approximately equalling 30 kg/s. Additionally, when the phase lag is away from 90° , a larger PTO damping is required to enhance the power absorption.

Therefore, for the proposed FIS controller, two inputs are defined to tune the control variable PTO damping. As shown in Figures 6.1 and 6.2, one is the magnitude difference between the incident wave elevation and the PAWEC displacement, defined as $|\hat{z} - \eta|$. The other is the phase difference between the incident wave excitation force and PAWEC oscillating velocity, defined as $|\hat{\phi}|$. The Mamdani type of FIS is applied with two inputs and one defuzzyfied output, as demonstrated in Figure 6.3. Note that the defuzzyfication is realized by using the centroid of the output membership function.

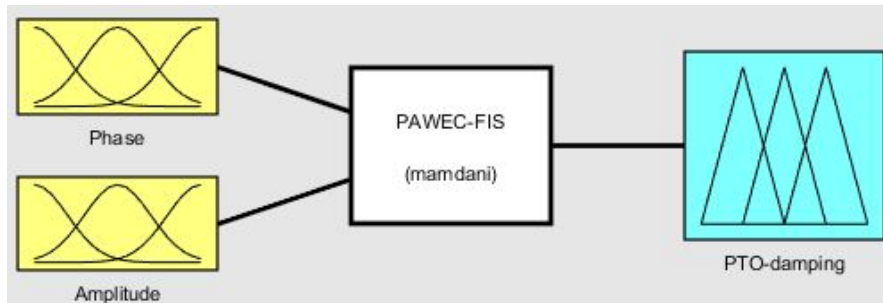


FIGURE 6.3: PAWEC FIS structure.

The two inputs and the one output are processed using a set of different MFs. As generally known, selecting MFs can be quite time consuming. There are lots of

functions can be used, such as Gaussian, Triangular and Generalized bell-shaped type, etc. In this work, Gaussian MFs are applied as examples to validate the feasibility of using FLC for controlling WEC performance. Other types of functions can be considered by PSO algorithm to search the optimised function for the WEC device. This is not discussed in this work. All the MFs are described by Gaussian type curve. The symmetric Gaussian function is dependent of the standard deviation σ and the mean value c , given by:

$$f(x; \sigma, c) = \exp \left(- (x - c)^2 / 2\sigma^2 \right). \quad (6.2)$$

The crucial parameters σ and c of these MFs are decided according to the data summarized from Figures [5.11](#) to [5.18](#).

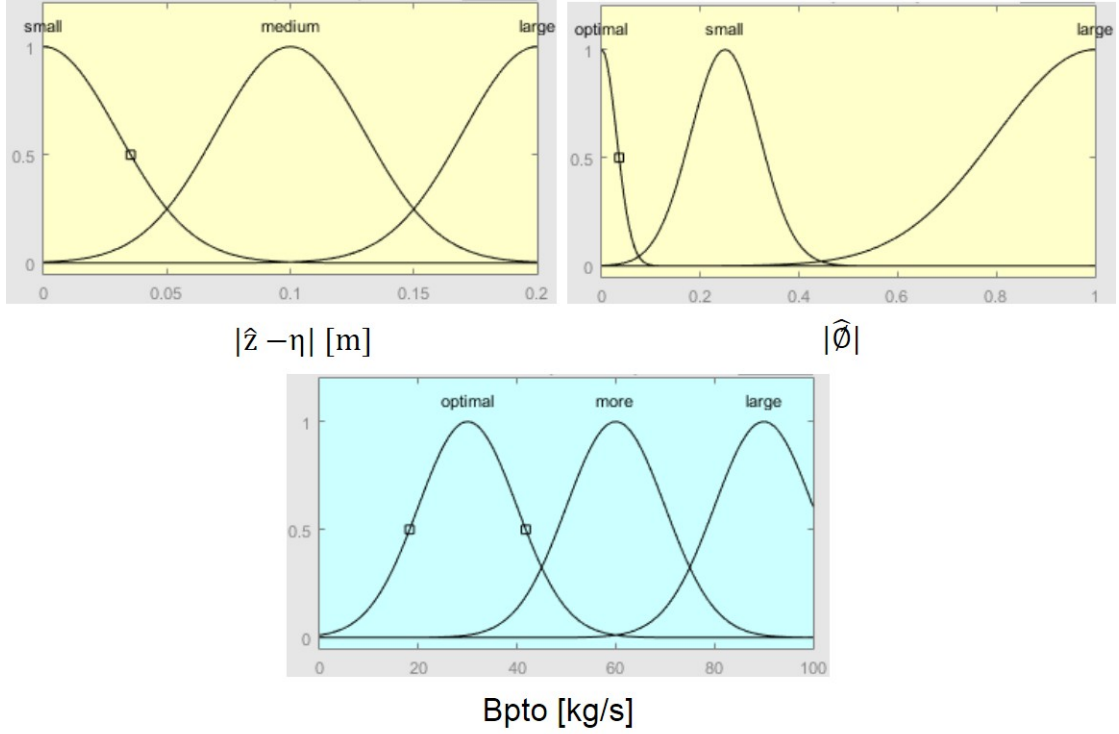


FIGURE 6.4: MFs for the inputs and output.

Figure 6.4 details the designs of the MFs for the two inputs and one output. As observed:

- *Each variable is defined by three MFs.*
- *For the first input, magnitude difference $|\hat{z} - \eta|$, the MFs are categorized as: "small", "medium" and "large".*
- *For the second input, the phase difference $|\hat{\phi}|$, the MFs are categorized as: "optimal", "small" and "large".* According to data shown in Figures 5.11 and 5.12, the optimal power capture performance can be achieved when the wave excitation force is approximately in phase with the device oscillation velocity. Therefore, the mean value c for the "optimal" MF is set at 0.

• For the control output, the PTO damping B_{PTO} , the MFs are categorized as: "optimal", "more" and "large". Referring to the optimal PTO damping B_{PTO} shown in Figure 5.18, the c for the "optimal" MF is located at 30 kg/s. The range of the control output is set as [0 100].

Then the fuzzy rule base is constructed as follows:

- (1) If (Phase is optimal) then (PTO-damping is optimal);
- (2) If (Phase is small) and (Amplitude is small) then (PTO-damping is more);
- (3) If (Phase is large) then (PTO-damping is large);
- (4) If (Amplitude is medium) then (PTO-damping is optimal);
- (5) If (Amplitude is large) then (PTO-damping is large);

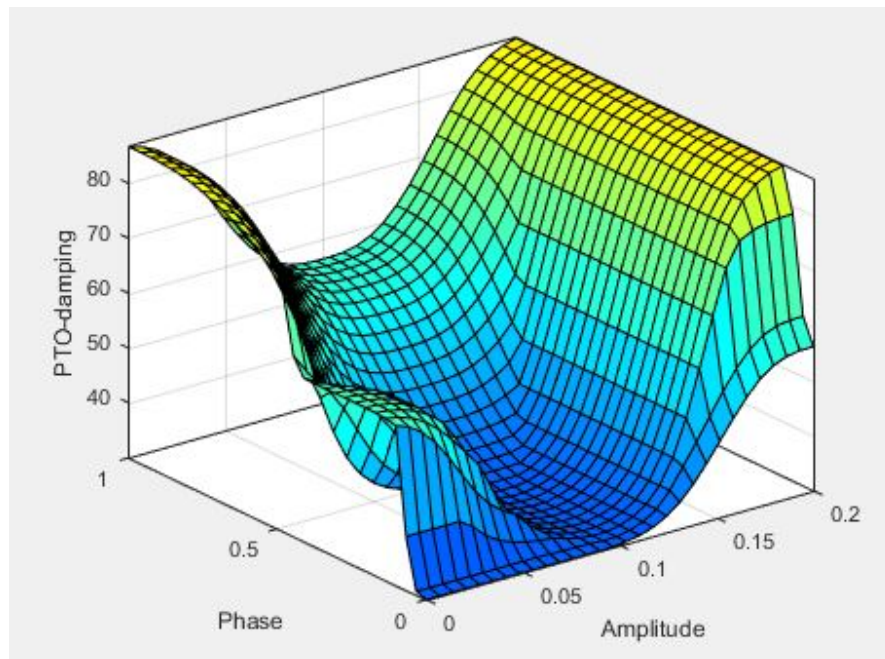


FIGURE 6.5: Overall surface description of the designed fuzzy rules for the PAWEC device.

As a result, the overall fuzzy rules can be transferred to a surface description, as shown in Figure 6.5. Clearly:

- *When the phase difference is nearly 0 and the oscillation amplitude is small, the PTO damping is controlled approximately at 30 kg/s;*
- *When the phase difference is nearly 0, a larger optimal PTO damping is required with increasing oscillation amplitude;*
- *when the phase difference is far away from 0, the PTO damping will be controlled at a considerably larger value.*

The control actions described above concur with the PAWEC power capture characteristics summarized in Figure 5.18. In other words, the designed FIS obeys the physical laws of the PAWEC system for efficient power absorption.

The parameters of the input and output MFs described in the FIS are determined by referring the numerical tank test results in Section 5.3.3. However, it cannot be guaranteed if the proposed FIS provides the most efficient control action for the PAWEC system regarding the varying wave conditions. Therefore, by contrast, a controller with updating MFs with respect to the wave condition will be proposed to further enhance the power absorption. This method is discussed below.

6.3.2 PSO-FLC

As mentioned in Section 6.3.1, there may exist a better FIS to improve the control action for an improved power absorption. In order to search for a better FIS, the PSO algorithm is applied here.

Proposed by Eberhart and Kennedy (1995), the PSO algorithm is inspired from the flocking behaviours of birds or insects swarming. Naturally, to search the food

in an area, the birds in a group will share their own experience with each other and then follow the bird which is closest to the food. If any of the other birds comes closer to the food than the first bird, it will attract the others to veer toward the new position. This pattern continues until all the birds get the food. In the PSO algorithm, each bird is viewed as a "particle".

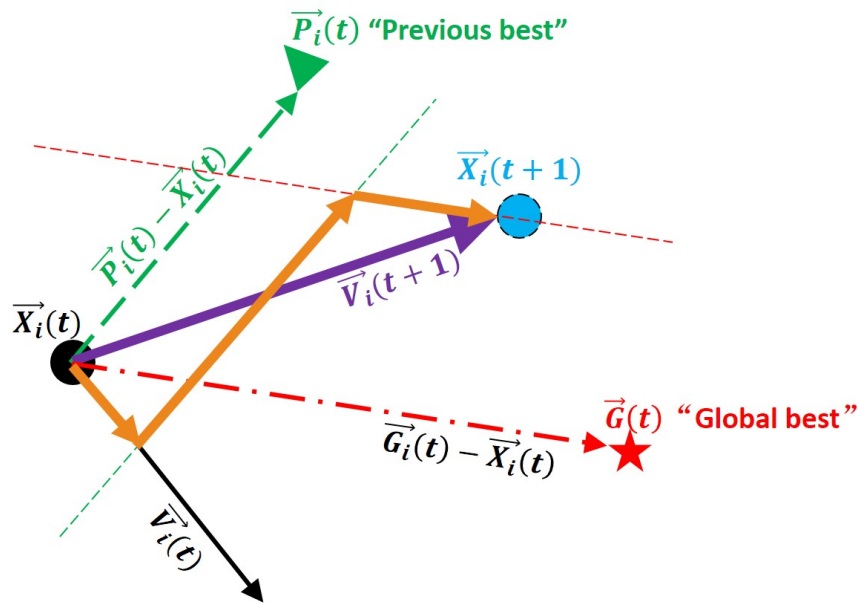


FIGURE 6.6: General concept of PSO algorithm for the i^{th} particle. $\vec{X}_i(t)$ and $\vec{X}_i(t+1)$ represent the current and the updated position for the particle. $\vec{V}_i(t)$ and $\vec{V}_i(t+1)$ are the corresponding velocities. $\vec{P}_i(t)$ is the best position the particle has achieved so far. $\vec{G}(t)$ represents the global best value achieved so far by the group of particles.

Learned from the birds swarming scenario, the PSO is successfully used for solving optimization problems. In the PSO, a group of initialized particles are used to search for the optima by self-learning and communicating with each other. In every iteration, the population is evaluated by a cost function. As a result, each particle is updated with new information by pursuing the maximum or minimum value of the cost function. Figure 6.6 depicts the action of the i^{th} particle in one iteration. It can be seen that in every iteration, each particle updates its

position $\vec{X}_i(t)$ and velocity $\vec{V}_i(t)$ by considering two "best" values. One is the previous best position $\vec{P}_i(t)$ that has been obtained for this particle to lean toward the optimal solution. Another "best" value is the global best position $\vec{G}(t)$ that has been obtained so far for all the particles in the population. Following Figure 6.6, the particle's updated position and velocity can then be formulated as:

$$\begin{aligned}\vec{X}_i(t+1) &= \vec{X}_i(t) + \vec{V}_i(t+1) \\ \vec{V}_i(t+1) &= \Omega\vec{V}_i(t) + \alpha_1\beta_1(\vec{P}_i(t) - \vec{X}_i(t)) + \alpha_2\beta_2(\vec{G}(t) - \vec{X}_i(t)),\end{aligned}\tag{6.3}$$

where Ω is the inertia weight coefficient; β_1 and β_2 are the acceleration coefficients. $\Omega\vec{V}_i(t)$ represents the inertia term; $\alpha_1\beta_1(\vec{P}_i(t) - \vec{X}_i(t))$ and $\alpha_2\beta_2(\vec{G}(t) - \vec{X}_i(t))$ are the cognitive and social component, respectively. $c_1 = \alpha_1\beta_1$, $c_2 = \alpha_2\beta_2$. In practice, Clerc and Kennedy (2002) have summarized Ω , c_1 and c_2 by the constriction equation:

$$\chi = \frac{2K}{\left|2 - 2\Phi - \sqrt{4\Phi^2 - 8\Phi}\right|},\tag{6.4}$$

where K and Φ are commonly set to 1 and 2.05. Then, $\Omega = \chi$, $c_1 = c_2 = \chi\Phi$.

As described in Section 6.3.1, Gaussian curves (determined by parameters σ and c) are used to describe the MFs of the inputs and output in the FIS. By applying the PSO algorithm, the aim is to search better MFs parameters for FLC action improvement (see Figure 6.7). The procedure of the PSO algorithm interacted into the FLC of the PAWEC system is described in Figure 6.8. As shown, each particle is designated with the information of the MFs parameters σ and c for the two inputs and one output. Therefore, for the PAWEC system the dimension of each particle D_p should be 18, namely $3 \times 3 \times 2$. Eq. (6.3) is applied to update the dynamics of the particles at each iteration. A cost function is used to evaluate the

efficiency of the updated particles by computing the amount of absorbed energy by PAWEC system. The objective is to maximize the energy absorption E .

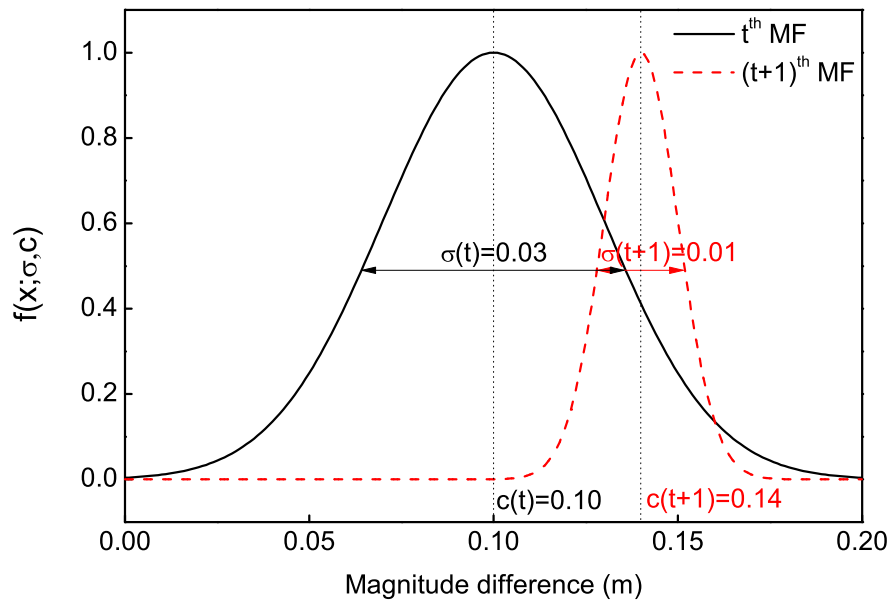


FIGURE 6.7: An example of the updated Gaussian MF.

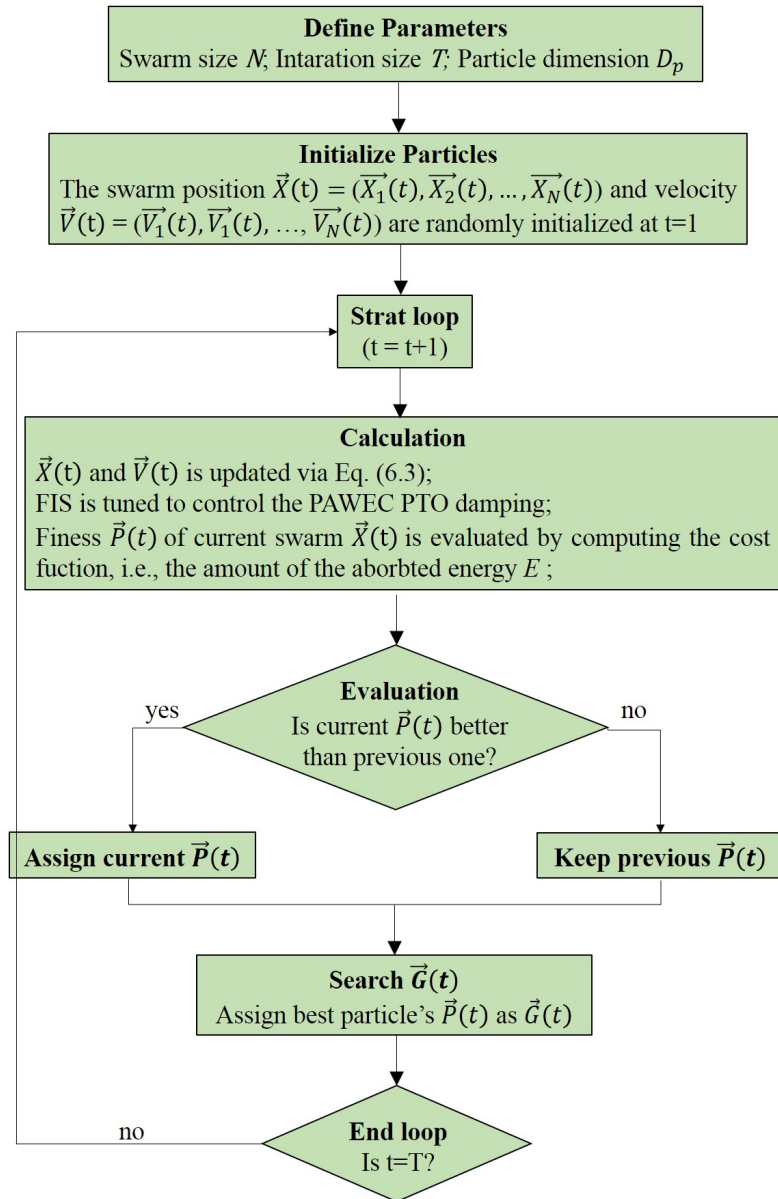


FIGURE 6.8: Flow diagram illustrating the PSO-FLC.

6.4 Results and discussion

Two irregular wave conditions are applied (corresponding data can be found in Table 5.2) for these simulations. In order to evaluate the performance of the FLC and PSO-FLC on the PAWEC, PCCD approach is used as a counterpart. The PCCD method has been discussed via the CFD tank tests, as shown in Figure 5.25.

6.4.1 By FLC

Figures 6.9 and 6.10 describe the energy absorption of PAWEC device by using the FLC and PCCD. As observed:

- *Through the PCCD, the optimal power capture is achieved by trial and error at different wave conditions.* For an irregular wave with a narrow bandwidth ($r = 8$), the captured power can be maximized at PTO damping equalling 30 kg/s; while a larger damping of 50 kg/s is required for the wave with a wider bandwidth ($r = 0.5$). These results concur with that shown in Figure 5.25. This highlights the limitation of using the PCCD. This control method is incapable of maximizing power absorption at different wave conditions by designating with a constant PTO damping.
- *On the contrary, it is clear that the proposed FLC can adaptively achieve efficient power absorption at different wave conditions.* For both irregular wave conditions at $r = 0.5$ and 8, it can be noticed that by applying the designed FIS (see Figure 6.5) the absorbed energy is more or less the same as the optimal absorbed energy with PCCD method. Figure 6.11 shows an example of the dynamic control action by the FLC. As seen, the PTO damping is adjusted with the change of the incident

inputs. As a result, in contrast to the constant PTO damping used in PCCD, the adaptive value is determined by the FLC, as shown in Figures 6.12 and 6.13.

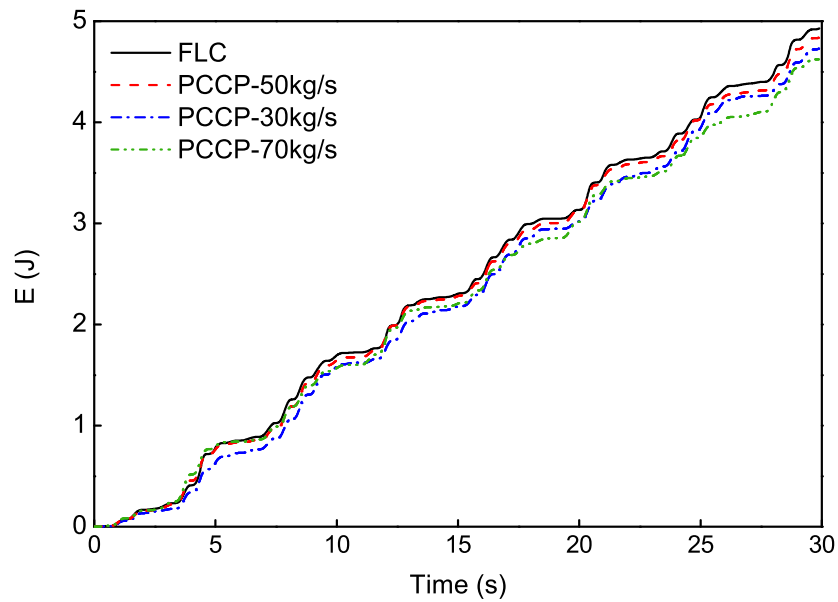


FIGURE 6.9: Comparison of the absorbed energy with different control methods for wave condition: $H_s = 0.1$ m, $\omega_p = 4.83$ rad/s and $r = 0.5$.

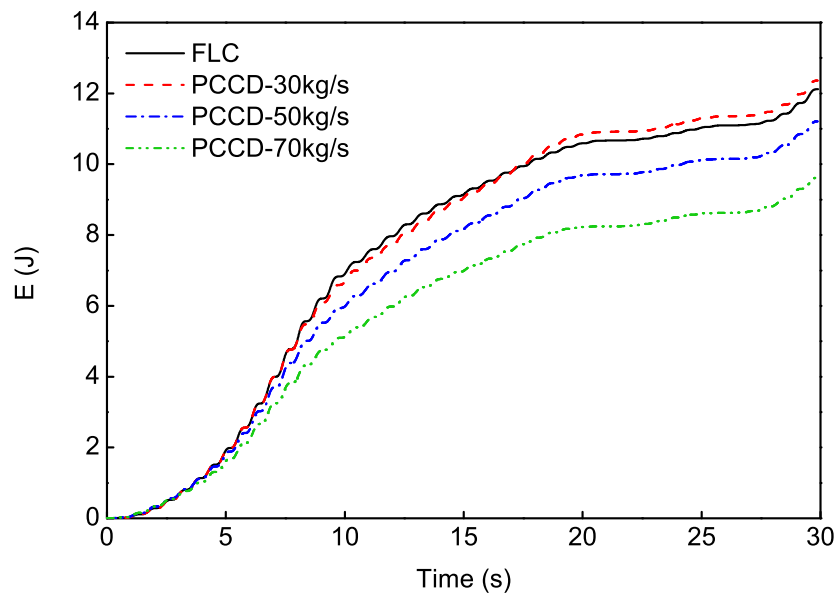


FIGURE 6.10: Comparison of the absorbed energy with different control methods for wave condition: $H_s = 0.1$ m, $\omega_p = 4.83$ rad/s and $r = 8$.

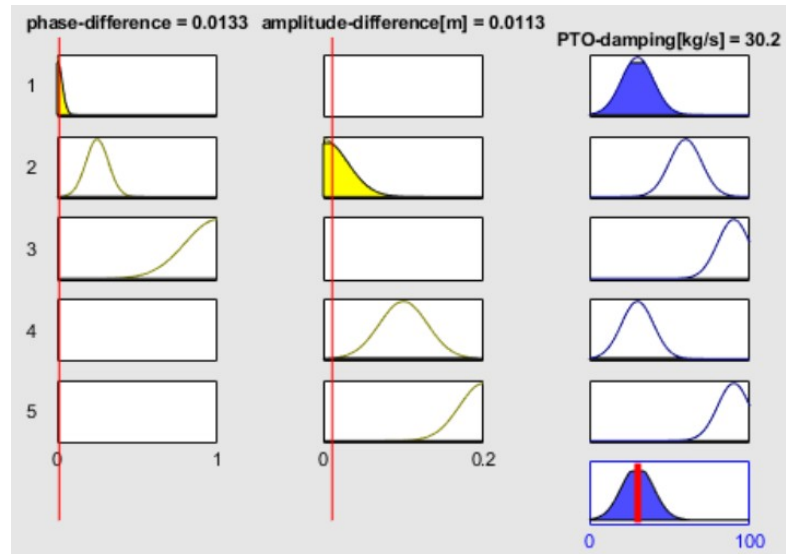
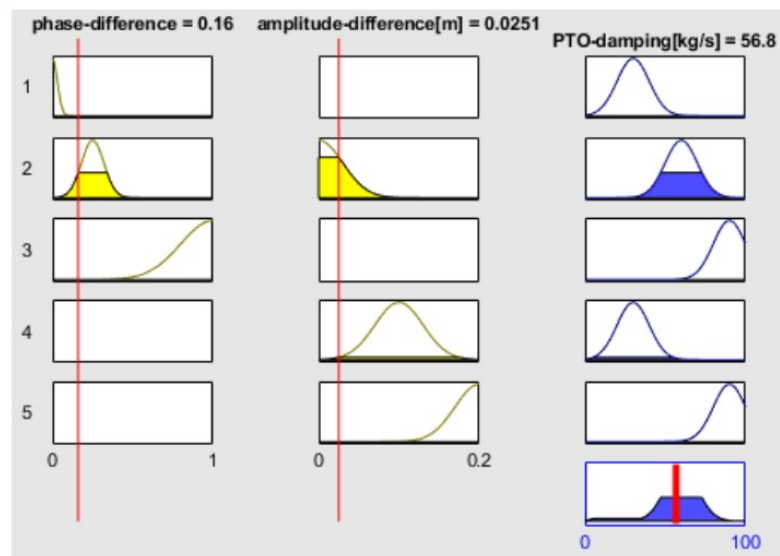
(a) $t = 6.8$ s(b) $t = 14.37$ s

FIGURE 6.11: Representative snapshots of the fuzzy rules and corresponding output at different time instant for wave condition: $H_s = 0.1$ m, $\omega_p = 4.83$ rad/s and $r = 8$.

To summarize, the above results indicate the superiority of the FLC over PCCD. By applying FLC, the PTO damping can be adaptively tuned for power capture maximization regarding different wave conditions.

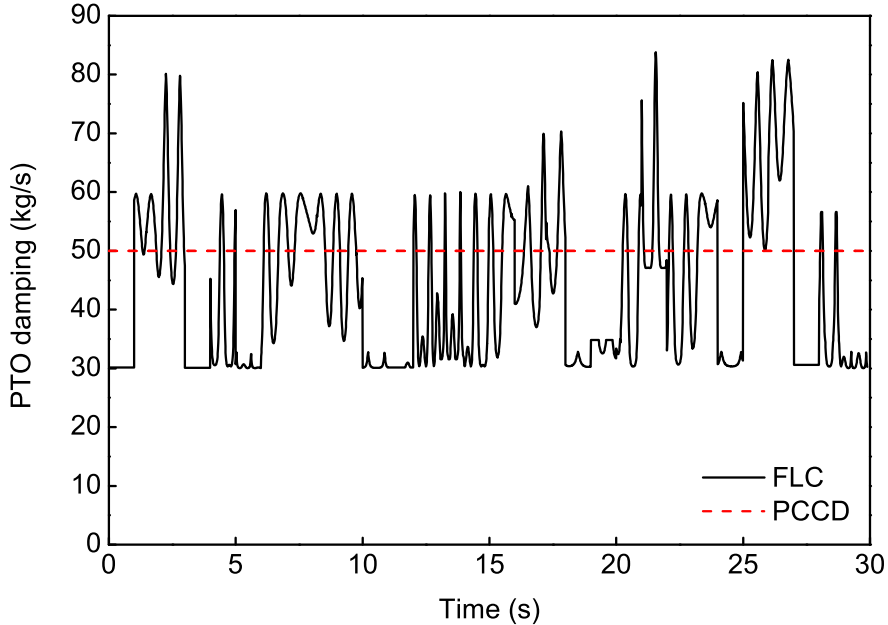


FIGURE 6.12: Comparison of the PTO damping dynamics with different control methods for wave condition: $H_s = 0.1$ m, $\omega_p = 4.83$ rad/s and $r = 0.5$.

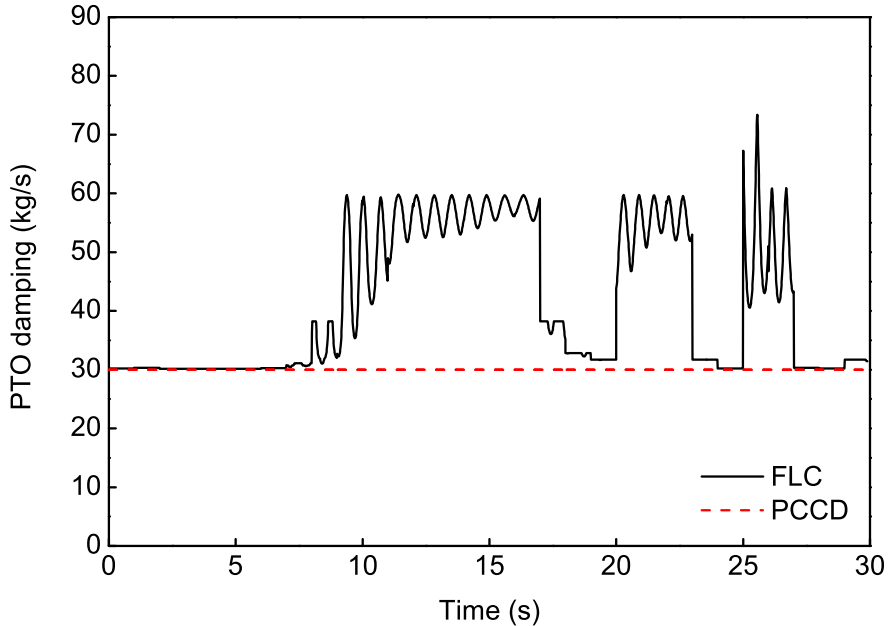


FIGURE 6.13: Comparison of the PTO damping dynamics with different control methods for wave condition: $H_s = 0.1$ m, $\omega_p = 4.83$ rad/s and $r = 8$.

6.4.2 By PSO-FLC

There is a possibility that the applied FIS is not the optima one. Thus, the PSO is included into the FLC to search for a better FIS. As generally known, increasing the PSO swarm size N and iteration size T can improve the possibility to reach the global optima. However, this will increase the computational burden. In this work, the N and T are set to 30 and 15, respectively.

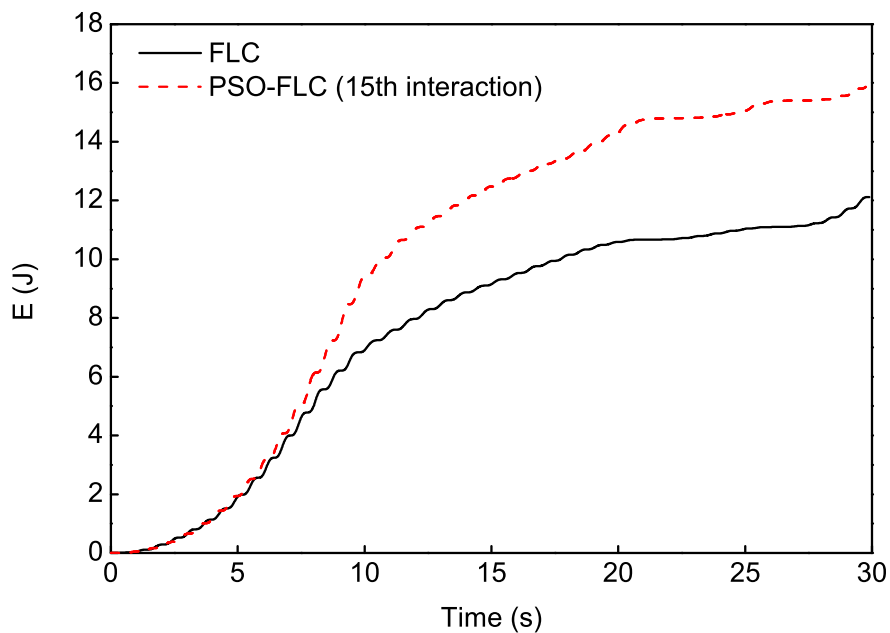


FIGURE 6.14: Comparison of the absorbed energy by the use of the FLC and PSO-FLC for wave condition: $H_s = 0.1$ m, $\omega_p = 4.83$ rad/s and $r = 8$.

As shown in Figure 6.14, the amount of the absorbed energy increases by up to 30% by using the PSO-FLC in comparison with FLC. Figure 6.15 describes the update of the FIS by using the PSO. Clearly, the MFs are tuned after 15th iteration.

Figure 6.14 together with Figure 6.15 can be used to show the effectiveness of PSO algorithm in searching better FLC controller parameters. The study is conducted under wave condition of $H_s = 0.1$ m, $\omega_p = 4.83$ rad/s and $r = 8$. Figure 6.15 demonstrates the change of the FLC parameters after 15th iteration with the use

of PSO algorithm. As shown, after 15 iteration, the PSO algorithm adaptively tune the fuzzy controller to perform as a new system (shown in the right of Figure 6.15) in contrast to the initialised system (shown in the left of Figure 6.15). After 15th iteration, the PTO damping output for phase difference larger than 0.5 are clearly different from the initial design. As a result, the absorbed energy is substantially increased by up to 30% (see Figure 6.14) by using the updated control algorithm after 15th interaction. As for different sea states, the PSO algorithm would adaptively adjust the FLC control algorithm for better performance after N interactions.

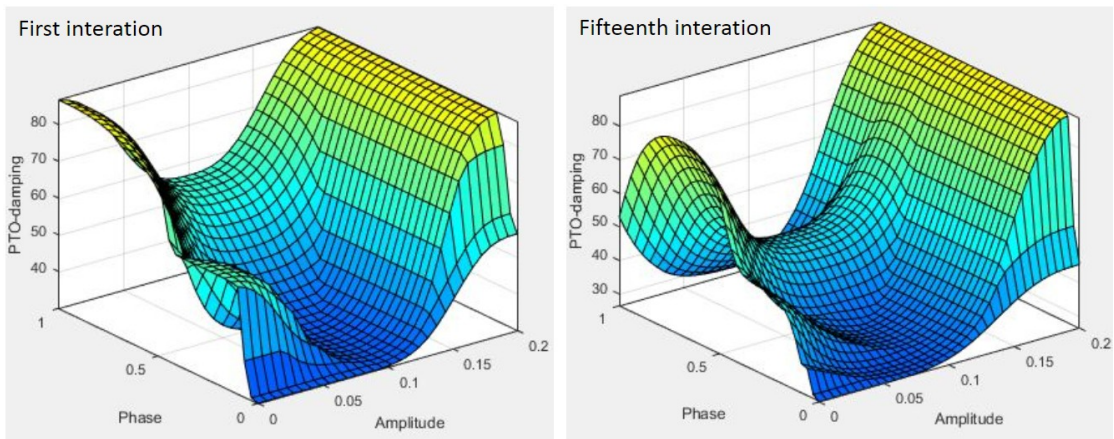


FIGURE 6.15: Comparison of the updated FIS by PSO algorithm. Wave condition is $H_s = 0.1$ m, $\omega_p = 4.83$ rad/s and $r = 8$.

6.5 Conclusions

This Chapter focuses on studying the FLC performance of controlling PTO damping for power capture maximization. According to the simulated results, the following conclusions can be given:

- The designed FLC can adaptively tune the PTO damping in response to different incident waves for power absorption efficiency maximization. The Mamdani-type

fuzzy inference system is applied to manage the PTO damping adjustment with respect to incident waves. The fuzzy rules are proposed by considering the PAWEC power capture characteristics described in Figure 5.18.

- Adding the PSO algorithm into the designed FLC can clearly increase the amount of the absorbed power by up to 32% (under wave condition $H_s = 0.1$ m, $\omega_p = 4.83$ rad/s and $r = 8$). In this work, the PSO is applied to optimize the parameters of the Gaussian type MFs in the FIS.

To summarize, this Chapter indicates the capability of using control strategy to further improve the power absorption efficiency. As expected, the controller as a subsystem of the whole PAWEC system is highly dependent of the device hydrodynamic properties, which are discussed in Chapters 4 and 5. This fact confirms the importance of considering "co-design" concept for the PAWEC development, as mentioned in Chapter 5. A summary of the research study from Chapter 3 to Chapter 6 is given in the next Chapter.

Chapter 7

Conclusion and future work

7.1 Introduction

This Chapter summarizes the findings of the research study from Chapters 3 to 6, as described in Section 7.2. Additionally, the future research inspired from the current work is outlined in Section 7.3.

The thesis is completely focussed on the 1/50 scale heaving point absorber wave energy conversion (PAWEC) device designed and constructed by Binyong Guo (Guo, 2017). The main contributions are encapsulated in the following four objectives of the current study:

(1) to develop an effective computational fluid dynamics (CFD) numerical wave tank (NWT) in order to closely reproduce the PAWEC hydrodynamic tests conducted in the physical wave tank (see Chapter 3);

(2) to demonstrate the degree to which the non-linearity in the PAWEC hydrodynamics should be represented and furthermore to identify a non-linear mathematical modeling to closely represent the PAWEC non-linear hydrodynamics (see Chapter 4);

(3) to study the joint effects of the PAWEC geometric configuration and power take-off (PTO) damping on wave energy absorption in order to optimize the PAWEC power capture (see Chapter 5).

(4) to implement the fuzzy logic controller (FLC) on the PAWEC device in order to further maximize the power absorption efficiency (see Chapter 6).

The findings and conclusions related to the above research objectives are summarized in the next Section.

7.2 Summary and conclusions

A brief summary of the research study from Chapters 3 to 6 is given in this Section. Furthermore, the conclusions and the potential impact corresponding to WEC applications or other (similar) research studies are outlined.

• Development of a NWT validated by experiments

The detailed techniques used to develop a CFD NWT, which can efficiently generate both regular and irregular waves are described in Chapter 3. As generally known, it is of fundamental importance to produce stable waves for a wave tank. To achieve this, a layer of nodes designated with prescribed angular displacement is allocated in the inlet of the NWT to simulate the paddle wave-maker for wave generation. In addition, an artificially sloped "beach" is located in the downstream of the NWT to dissipate the propagating wave energy for generating stable waves.

When using NWT, another key challenge which should be taken into account is the trade-off between the computational cost and precision. With no doubt, a higher density of grid solution would generate a corresponding higher precision but lead to a larger computation cost. A radiated grid solution is applied in this work to save the computation while guaranteeing the computation precision. Large numbers of grids are distributed in the region where the wave dynamic is considerably concerned. Away from this zone, the mesh density is gradually decreased towards the boundaries of the NWT.

In addition to wave dynamics, the NWT is applied to simulate the wave-PAWEC interaction, including the PAWEC dynamics under conditions of free decay, wave excitation and free motion testing. Furthermore, the NWT has enhanced capability (due to non-linear approach) to capture the splashing phenomena during the wave-WEC interaction. The numerical data are validated by the physical data obtained from the experimental wave tank tests.

Overall, the proposed NWT is capable of reproducing the physical wave tank test for studying the PAWEC dynamic behaviors considering non-linearities. It can be concluded that a well designed NWT can be an effective tool for accurate simulation of the physical hydrodynamic performances of different types of WEC devices. Therefore, the use of numerical modeling can be an appropriate alternative to studying the non-linear response of the PAWEC with respect to the waves (even under extreme waves) in contrast to costly physical testing.

- **Verification of a non-linear modeling using CFD data**

In Chapter 4, a non-linear modeling involving a quadratic viscous term is verified to describe the PAWEC hydrodynamic behaviors. For a given PAWEC device, it is of fundamental importance to facilitate an understanding of the hydrodynamics. As generally known, the PAWEC device is tuned to be resonant oscillation for the

achievement of the power absorption maximization. Then the main challenge to be overcome is the degree to which non-linearities in the device hydrodynamics should be considered. Currently, a number of studies by various investigators are based on the use of linear modeling, e.g. using the boundary element method (BEM) to describe the PAWEC hydrodynamics. By contrast, this thesis focuses on indicating the non-linearities of the PAWEC device caused by the non-linear viscosity. Therefore, a non-linear approach considering viscosity is proposed. The superiority of the proposed non-linear model over the linear counterpart in representing the PAWEC dynamic behaviors is validated by comparing with the data from the NWT and the physical wave tank. It is concluded that the linear hydrodynamic representation leads to significant errors in predicting the PAWEC dynamic responses which may mislead the PTO and control strategy designs.

By contrast, the proposed non-linear model offers much more realistic predictions of the PAWEC hydrodynamics. Additionally, the non-linear model provides a considerably quicker and more convenient solution to represent the PAWEC hydrodynamics in the time domain in contrast to the time-costly and complex CFD model. Furthermore, the model can be integrated straightforwardly into the control strategy design for further power capture optimization as the hydrodynamic plant of a PAWEC device. Overall, the non-linear model can be used as a feasible analysis tool for the initial concept design and parameter optimisation regarding the engineering and structural design of a PAWEC device.

- **Power capture enhancement by joint tuning of geometry and power take-off damping**

The power absorption efficiency is a crucial factor which should be carefully considered in the design of a PAWEC device. This is the motivation of Chapter 5. A methodology for maximizing the power capture is presented by optimizing the geometric configuration of the 1/50 scale PAWEC via NWT tests. More importantly,

the joint effects of the device geometry and power take-off (PTO) damping on the wave energy absorption efficiency are also discussed. Two other geometric counterparts (the cylindrical PAWEC with a hemispherical streamlined bottom and a 90°-conical streamlined bottom, defined as CH and CC, respectively) are proposed with respect to the original flat-bottom cylindrical PAWEC device (CL). A PTO force via varying damping coefficient is applied to compare the power conversion performances of the aforementioned devices. Free decay, wave-PAWEC interaction and power absorption tests are conducted via the CFD model. It is found that the streamlined devices (CH and CC) can generate by up to 60% of decrease in the hydrodynamic added mass and damping, compared to the CL device. Moreover, the CC design is the best among the three studied geometries as evidenced by its capability of enhancing the amplitude response by up to 100% in contrast to the CL design. Additionally, applying an appropriate PTO damping to the CC device prominently increases the achievable optimal power by up to 70% under both regular and irregular waves (compared with the CL device).

The study detailed in Chapter 5 provides a critical idea, which is that the parameters considered, such as the geometry, the PTO damping, the wave frequency and the wave height show clear mutual interactions with each other in affecting the heaving PAWEC performance. Therefore, it is necessary to balance the design and optimization among the PAWEC hydrodynamics, PTO system, wave conditions and the control strategy. In other words, the application of "co-design" in optimizing the device performance for power generation should be carefully considered at the initial study stage of a PAWEC system.

• PSO-FLC implementation on PAWEC

In Chapter 6, a model-free controller, the fuzzy logic controller (FLC) is implemented on the PAWEC device for the maximisation of the power absorption efficiency. It should be noted, instead of using laws achieved from the linear model,

the corresponding fuzzy rule-base is constructed based on the numerical power capture characteristics obtained from the NWT tank tests. Furthermore, the particle swarm optimization (PSO) algorithm is integrated into the FLC to optimally tune the rule-base in order to further maximize the power absorption efficiency. The simulations are conducted by using Matlab/Simulink. Two different irregular wave conditions are used to test the capability of the FLC and PSO-FLC. The analysis demonstrate the ability of the FLC in adaptively tuning the PTO damping for maximizing the absorbed energy with respect to different wave conditions. Additionally, applying PSO algorithm into FLC can optimally tune the fuzzy rule-base for further power capture enhancement.

The model-free controller (FLC) does not require a reference tracking strategy, i.e., no optimum PAWEC velocity trajectory is required. Hence, using FLC provides the user a relatively easy way of optimally tuning the PTO damping for power absorption maximization.

7.3 Recommendations for future work

Following the current study, there are several related topics which can be explored in the future:

- (1) In the thesis, the PAWEC performances under safe operating wave conditions are discussed. In addition to this, it is considerably important to study the load cases and even the survivability of the PAWEC device under extreme wave conditions. The application of CFD NWT for analyzing the extreme loads on the PAWEC can be explored. It should be noticed that smoothed particle hydrodynamics (SPH) method may need to be introduced if the CFD method has difficulties in handling the large mesh deformation for particularly extreme cases.

(2) It is validated that the linear predictions lose effectiveness and there exists significant non-linearities for the designed PAWEC, particularly around resonance or at large oscillations. However, it should be noted the corresponding findings and conclusion are validated for the 1/50 scale cylindrical model with 0.3 m of diameter. It is necessary to scale up the NWT model in order to validate the non-linearities and their full scale significance for a prototype PAWEC, capable of operating at sea. In other words, attention should be paid to a study of the effect on hydrodynamics cause by scaling (up or down). The development of studying the hydrodynamics of the prototype can be explored in the NWT.

(3) As validated from the current study, the hydrodynamic design has significant effects on the design of the PTO system and the development of the control system. It should be possible to jointly optimize the designs of the WEC hydrodynamics, PTO system and control strategy to produce the most efficient wave energy extraction. In future work, more hydrodynamic parameters, e.g. water plane, draft, added mass, etc. can be considered in addition to the bottom profile of the device. In the study from WETFEEET project, they propose an idea of 'negative spring' by changing the water plane diameter so as to tune the device natural frequency for resonance ([Gradowski et al., 2017](#)). Additionally, they propose 'enhanced added mass' to reduce the device natural frequency to tune it in accordance to the frequency of the predominant incoming waves ([Teillant et al., 2016](#)). Hence, these design issues should be considered in one "co-design" package when developing a prototype WEC system in future.

(4) The designed PSO-FLC in the work can be extended to physical tank tests. As for real application, it would be quite important to solve the discontinuous changes of PTO damping with time as shown in [Figures 6.12 and 6.13](#).

(5) The waves considered in this work are uni-directional. In addition, the WEC devices discussed in this work are quite simple and axisymmetrical. However,

the real ocean waves are directionally spreading. It is worthy of studying the WEC performances with more complex shapes, particularly, in the real directional spreading sea conditions. As reported by [McCabe et al. \(2010\)](#), with the use of genetic algorithm it is found the optimized WEC device with unisymmetric shape can improve the absorbed power quite a lot compared to the bisymmetric shape.

Appendix A

Half NWT

The computation time for a full NWT requires approximately 27 hours for a 22 s simulation of the wave-PAWEC interaction. Since the designed PAWEC is a axisymmetric device, a half NWT constructed along the symmetrical plane (with reflective boundary condition) is introduced to reduce the computation. Figure [A.1](#) shows the designed half NWT.

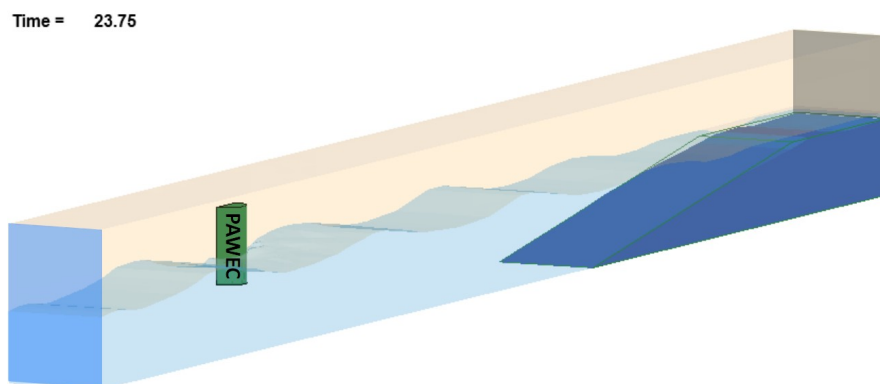


FIGURE A.1: A half NWT built in the software package ANSYS/LS-DYNA.

To validate the feasibility of the half NWT, the PAWEC displacements achieved through both the full and half NWTs are provided under wave condition of $H = 0.073$ m, $T = 1.3$ s. Figure [A.2](#) demonstrates the results. It can be seen that the

half model fits well with the full model in presenting the PAWEC performance with discrepancy less than 5.5 %. More importantly, the computation time has been reduced to 14 hours by employing the half NWT. As a result, the developed half NWT can be used to simulate the interaction between the PAWEC and the incident wave.

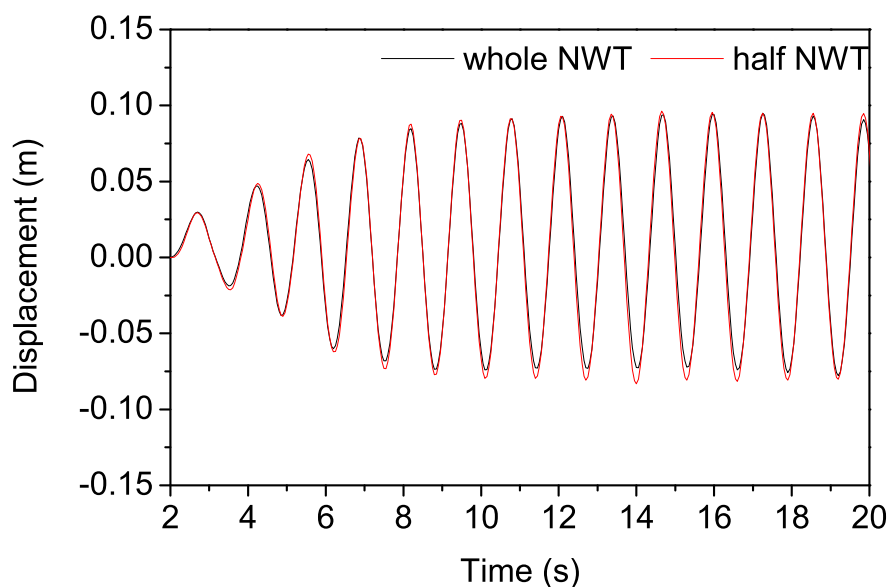


FIGURE A.2: Comparison of the simulated PAWEC displacements via full and half NWTs. Wave condition: $H = 0.073$ m, $T = 1.3$ s.

Appendix B

Physical and CFD results of Mocean Energy device

B.1 Small scale WEC from Mocean Energy Ltd.

Figure B.1 shows the hinged-raft WEC proposed by Mocean Energy Ltd. The WEC device is composed of two hulls, the front and the rear one. In contrast to the one degree freedom PAWEC device (acting in heave motion) designed at the UoH, this device can achieve 7 degrees of freedom, including surge, sway, heave, roll, pitch, yaw and the relative angular displacement at the hinge. This novel WEC device has been involved in the stage 2 of the Wave Scotland Novel Wave Energy Converter Program. More details can be found in <http://www.moceanenergy.com/>.

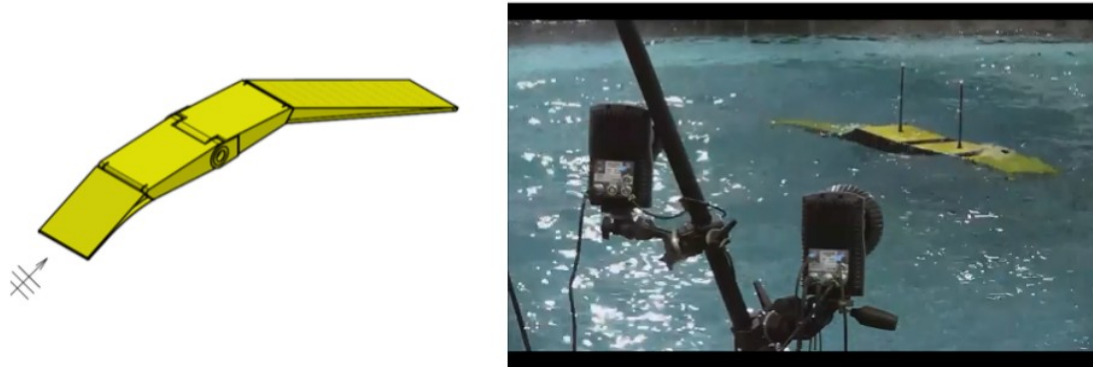


FIGURE B.1: Scheme of the hinged-raft WEC from Mocean Energy Ltd. <http://www.moceanenergy.com/>

B.2 Validation via WEC from Mocean Energy Ltd.

In addition to the NWT validation via the 1/50 heaving PAWEC system, a more complex device (possessing a more complicated geometry profile and operating in multi-degrees) is provided by Mocean Energy Ltd. The study focuses on verifying the ability of the numerical model in reproducing the surge and heave forces, pitch moment and even the water splashing phenomenon.

The analysis described here are carried out on one hull of this device. Referring to the physical experimental wave tank set-up, the device is constrained in the numerical flume tank and experiences regular waves with varying wave frequency and wave height, as shown in Figure B.2. Three wave gauges are installed along the flume tank (corresponding to the experimental installation sites) to monitor the wave propagation, as shown in Figure B.3. To record the forces and moments imposed on the device, pressure sensors are designated on the whole surface of the device, as shown in Figure B.4. In addition, the output time step of the numerical simulation is set to the same value as the experimental sample frequency in order to compare the numerically recorded dynamic videos with the experimental high speed videos. First of all, the validation of the mesh convergence is conducted,

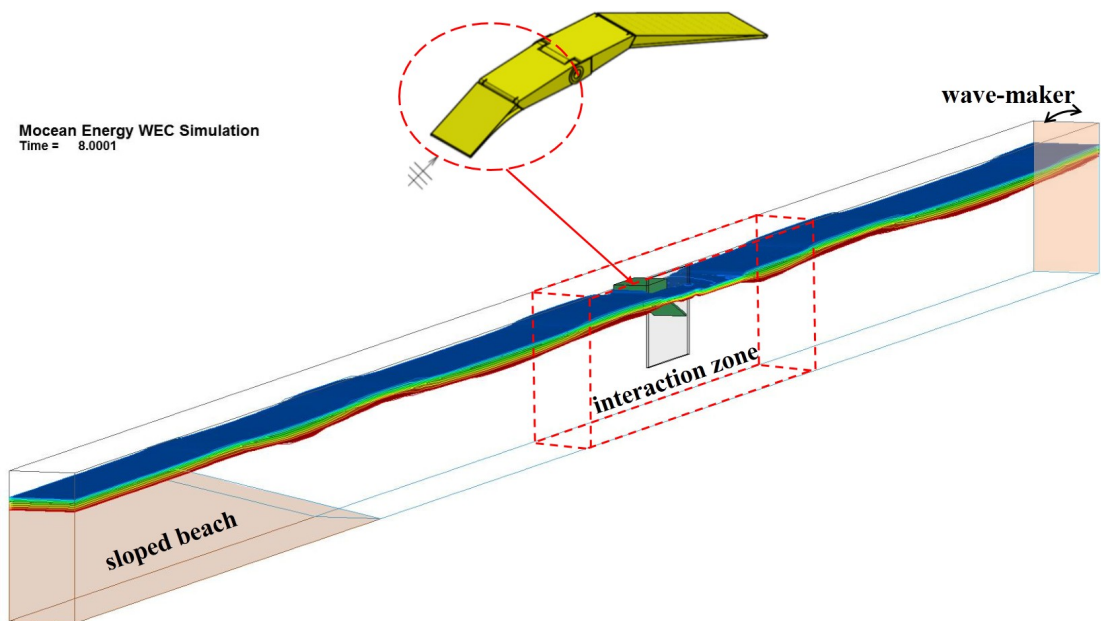


FIGURE B.2: Scheme of the numerical model for the Mocean Energy WEC.

which is not detailed here. As a result, the mesh solution with $10 \text{ mm} \times 10 \text{ mm} \times 10 \text{ mm}$ in the interaction zone is used.

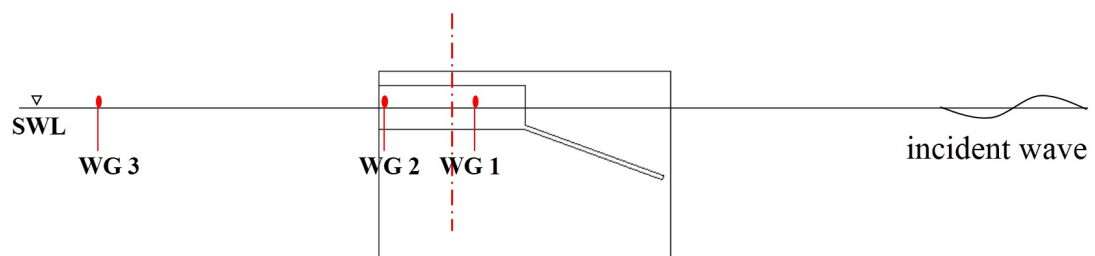


FIGURE B.3: Distribution of the wave gauges in the flume tank for the Mocean Energy WEC test.

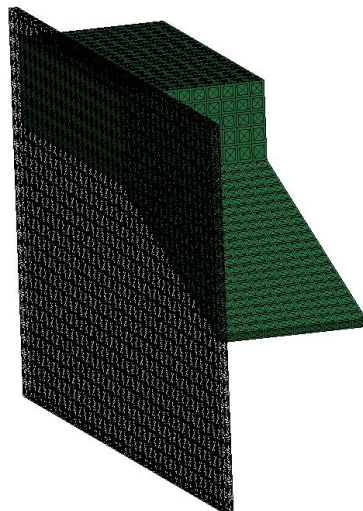


FIGURE B.4: Pressure sensor distribution (shown as the black segments) on the device surface.

Step 1: wave generation validation

Two representative regular waves are generated in both the NWT and the physical flume tank. The wave data are:

- (1) Wave No.1: $H_0 = 11.38$ mm, $f = 0.734$ Hz;
- (2) Wave No.2: $H_0 = 13.09$ mm, $f = 0.688$ Hz.

As shown in Figure B.3, three wave gauges are distributed along the NWT and the physical wave tank. They are used to measure the wave development regarding Wave No.1 and Wave No.2. Figures B.5 to B.7 show the comparisons of the monitored wave elevations from the NWT and the physical wave tank.

Table B.1 summarises the amplitude discrepancies of the numerically generated wave with respect to the experimental data. It is apparent that the waves are well generated in the NWT, in good agreement with the physically generated waves.

Step 2: wave excitation forces validation

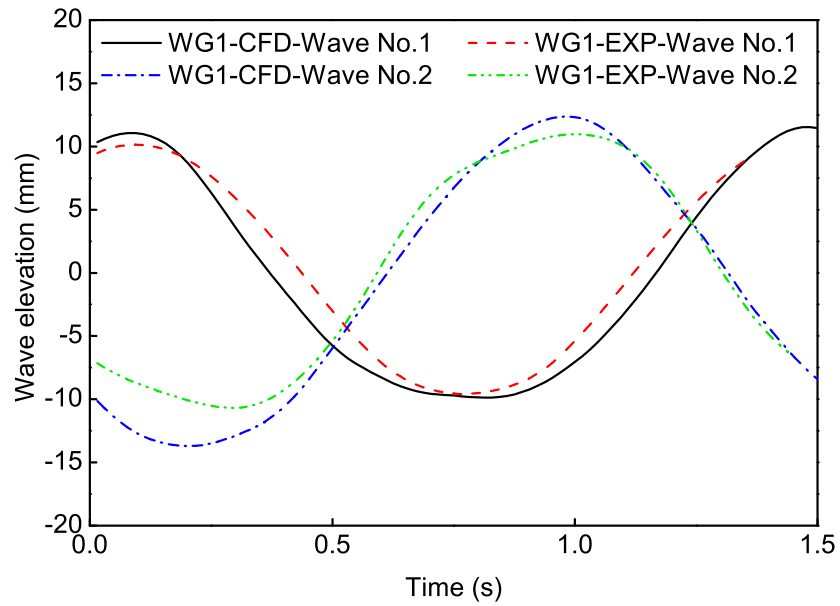


FIGURE B.5: Comparisons of the wave elevations monitored by WG1 from the NWT and physical tank.

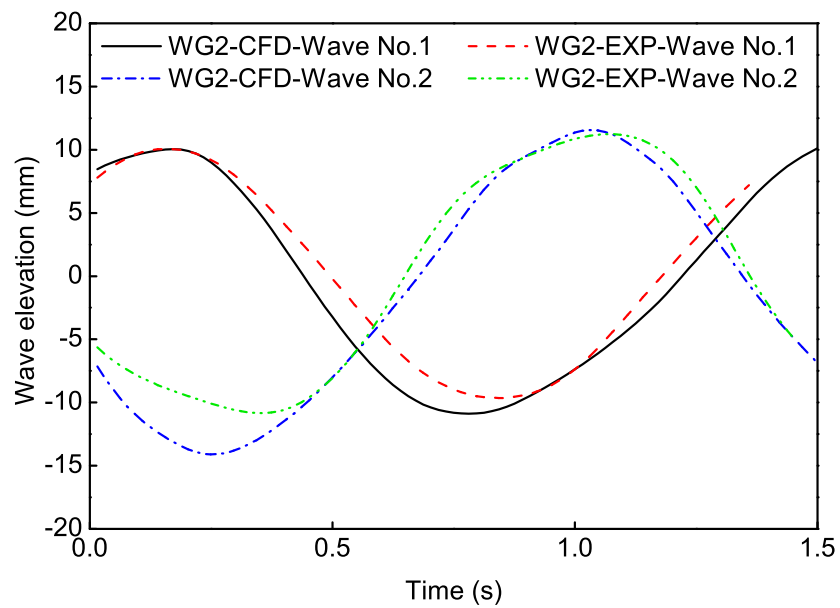


FIGURE B.6: Comparisons of the wave elevations monitored by WG2 from the NWT and physical tank.

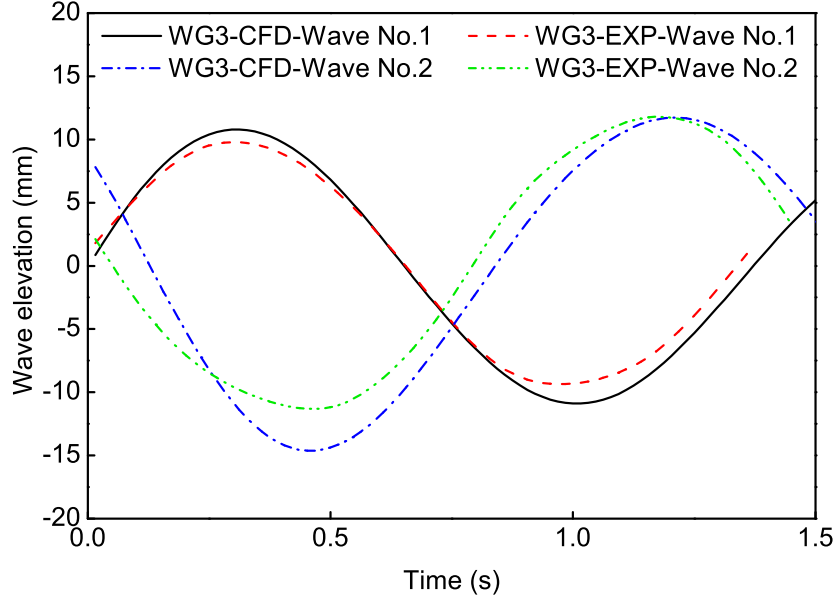


FIGURE B.7: Comparisons of the wave elevations monitored by WG3 from the NWT and physical tank.

TABLE B.1: Discrepancies between the experimental (H_{EXP} = average of the experimentally measured wave amplitudes from WG1 to WG3) and numerical (H_{NWT} = average of the numerically measured wave amplitudes from WG1 to WG3) wave data.

	H_o [mm]	H_{EXP} [mm]	H_{NWT} [mm]	Increase [%] H_{NWT} to H_{EXP}
Wave No. 1	11.38	9.77	10.59	8.39
Wave No. 2	13.09	11.14	13.01	16.79

By applying the two types of regular waves (mentioned in Step 1), the corresponding surge and heave forces and the pitch moments acting on the device are recorded, as shown from Figures. B.8 to B.10.

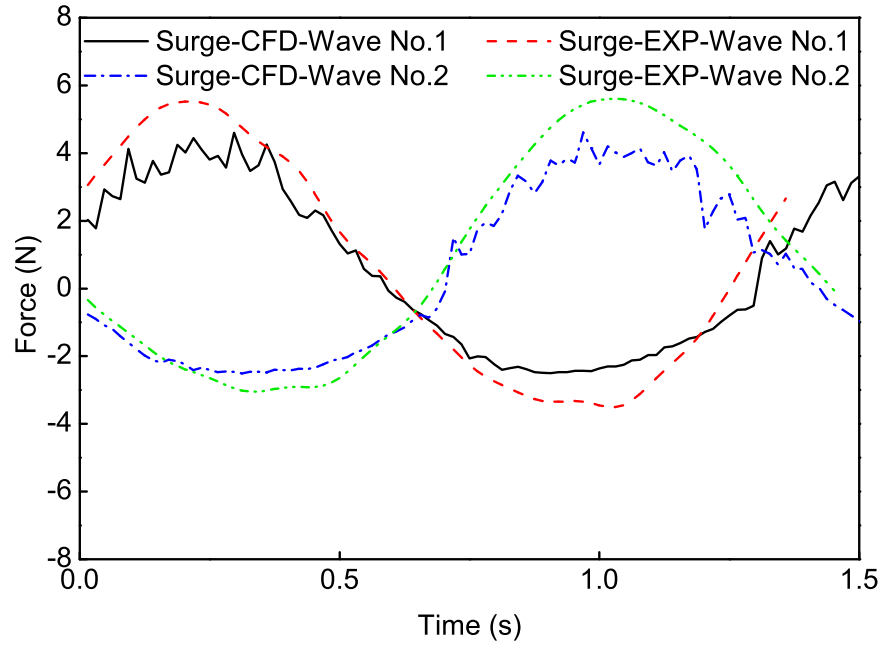


FIGURE B.8: Comparisons of the surge forces from the NWT and physical tank.

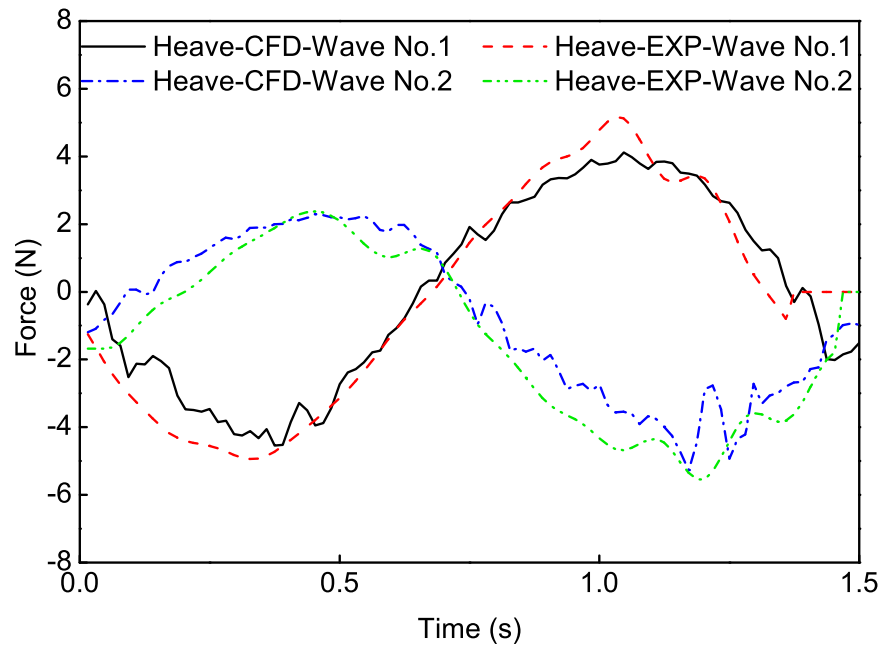


FIGURE B.9: Comparisons of the heave forces from the NWT and physical tank.

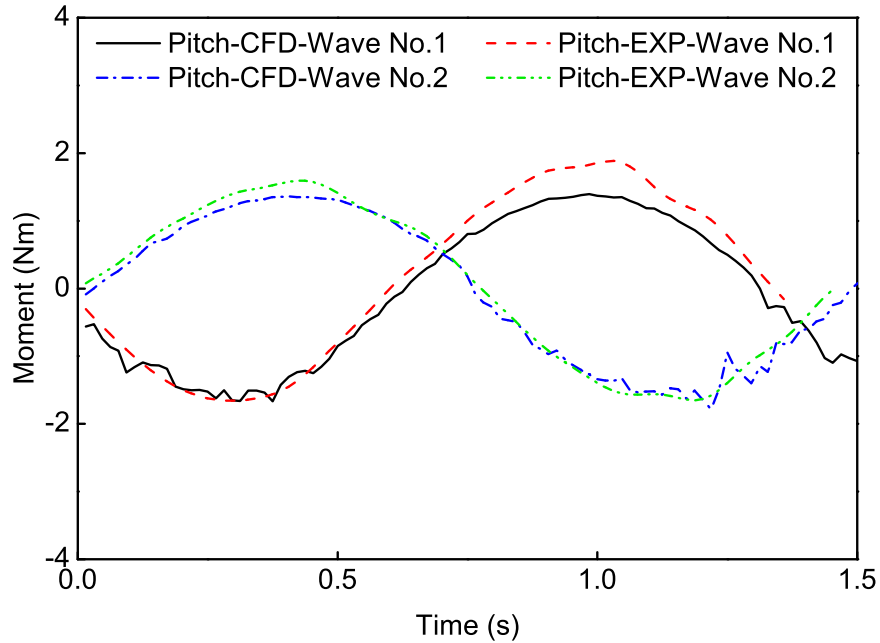


FIGURE B.10: Comparisons of the pitch moments from the NWT and physical tank.

Tables B.2 and B.3 summarise the amplitude discrepancies of the numerically measured surge and heave forces and pitch torque with respect to the experimental data under the two wave conditions. Clearly, the corresponding data from the numerical simulations and experiments get accordance with each other to a high degree. This suggests that the developed CFD model can be capable of simulating the hydrodynamics not only in heave but also in surge and pitch.

TABLE B.2: Discrepancies of the measured forces and pitch moments between experiment and numerical simulation under regular wave No.1.

		Physical value	Numerical value	Average increase [%]
Surge force [N]	peak	5.6124	4.6180	-17.72
	trough	-3.0511	-2.5100	
Heave force [N]	peak	2.3756	2.2960	-4.38
	trough	-5.5438	-5.2764	
Pitch torque [Nm]	peak	1.5914	1.3580	-3.16
	trough	-1.6507	-1.7817	

TABLE B.3: Discrepancies of the measured forces and pitch torques between experiment and numerical simulation under regular wave No.2.

		Physical value	Numerical value	Average increase [%]
Surge force [N]	peak	5.5274	4.2367	-25.38
	trough	-3.5028	-2.5020	
Heave force [N]	peak	5.1701	4.1120	-17.54
	trough	-4.9424	-4.2269	
Pitch torque [Nm]	peak	1.8840	1.3956	-13.52
	trough	-1.6532	-1.6634	

Step 3: water splashing validation

The dynamic water splashing phenomena corresponding to the aforementioned two wave conditions are obtained, as shown in Figures [B.11](#) and [B.12](#). As observed, the evolutions of the water splashing occurring along the boundary of the device are well reproduced by using the CFD model compared to the experimental data.

In summary, in a similar manner to the observations corresponding to the validation by the 1/50 scale heaving PAWEC in Section [3.5](#), the developed CFD model still shows great capability in reproducing the physical dynamic interaction between the incident wave and the Mocean Energy WEC device.

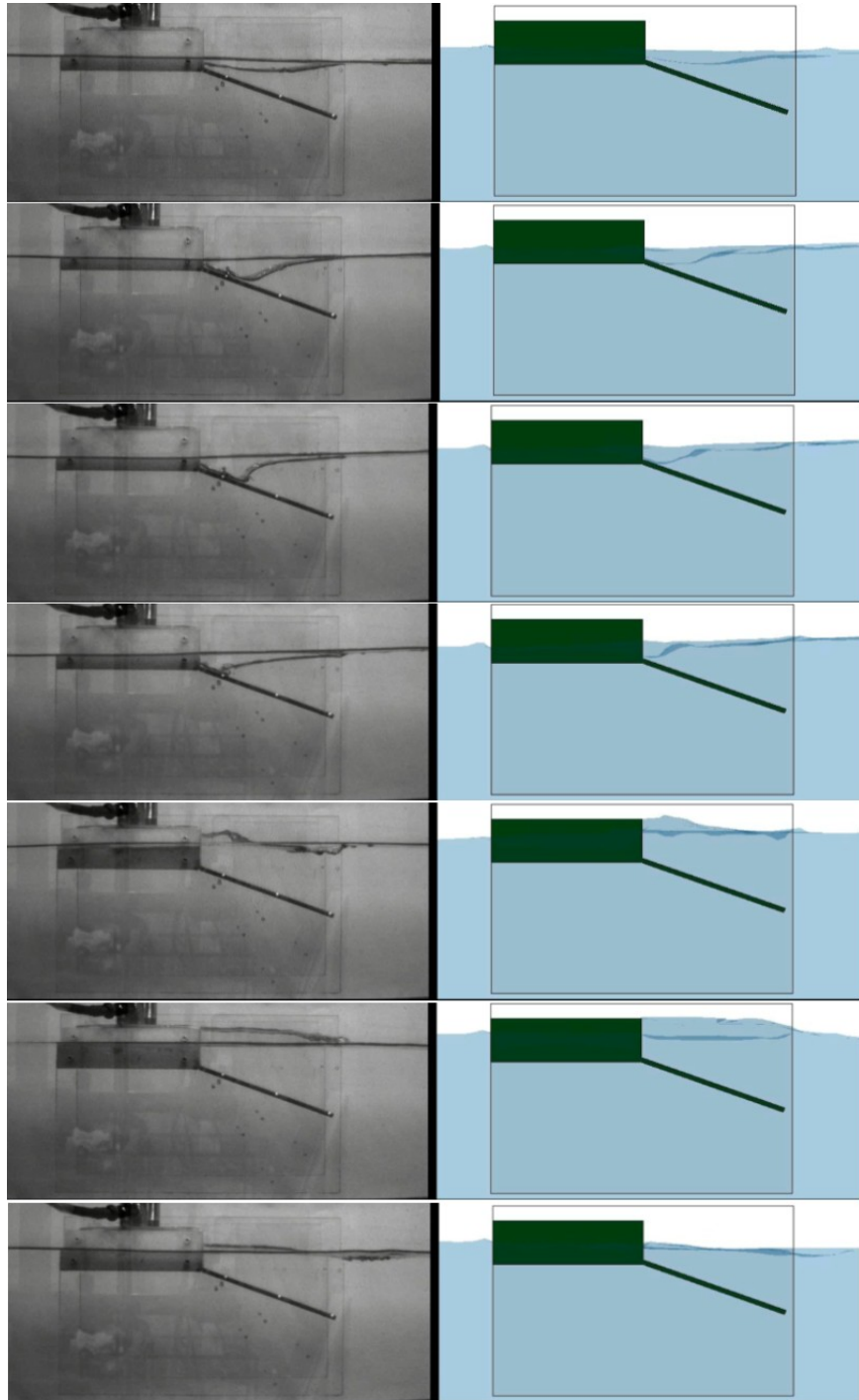


FIGURE B.11: Comparison of the water splashing evolutions from the NWT and physical wave tank at regular wave No.1.

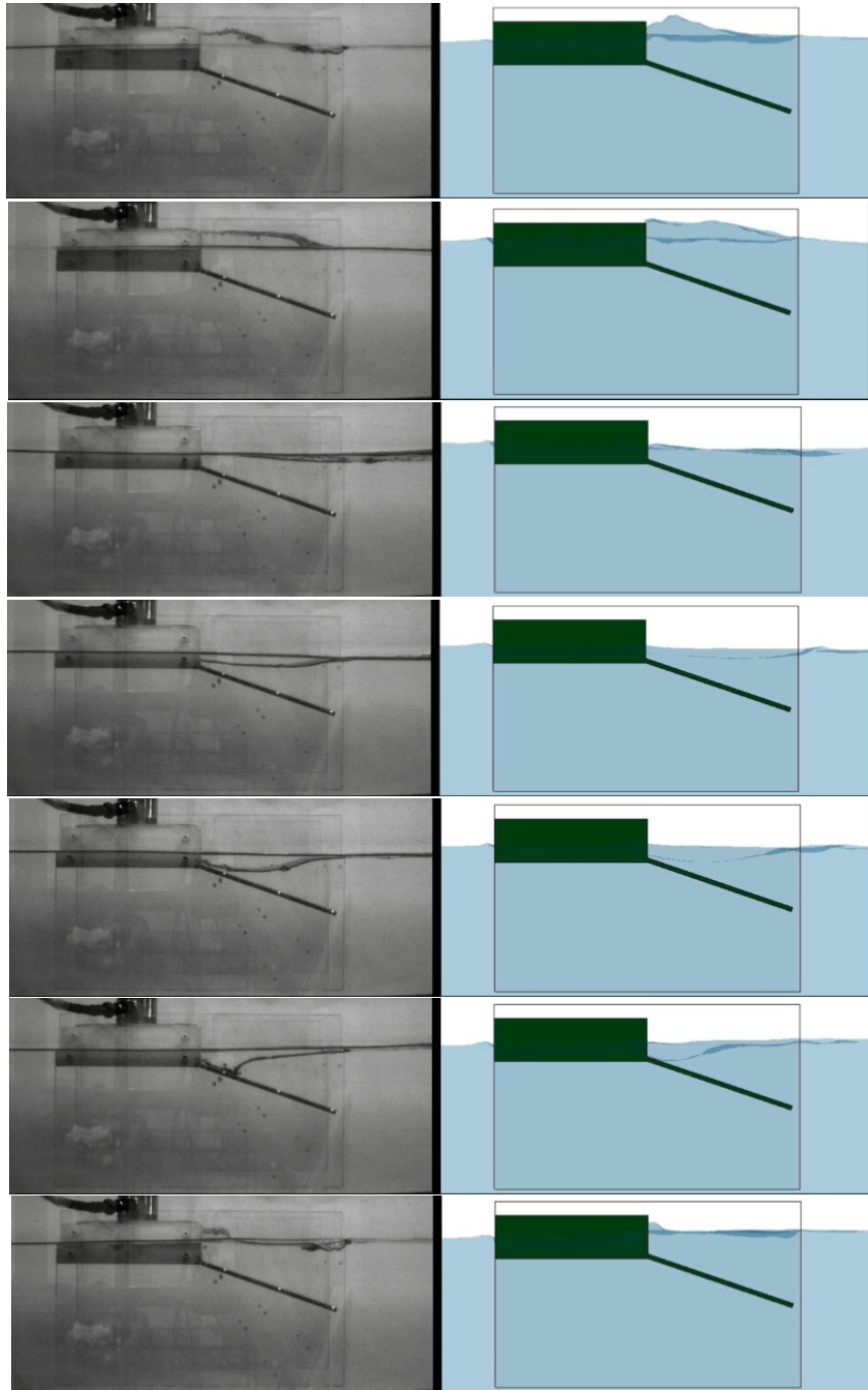


FIGURE B.12: Comparison of the water splashing evolutions from the NWT and physical wave tank at regular wave No.2.

Appendix C

Keyword file for the wave-PAWEC interaction

This section provides the keywords used to model the wave-PAWEC interaction in LS-DYNA. A lot of useful examples for building numerical models in LS-DYNA are available from <https://www.dynaexamples.com>.

Following is the keywords for the wave-PAWEC interaction with PTO configuration of 10 kg/s under wave condition of $H_s = 0.15$ m, $\omega = 4.83$ rad/s. To simulate other wave conditions, corresponding curves to represent the wave-paddle displacement in time series can be modified under *DEFINE_CURVE. In addition, different damping configuration can be changed from *MAT_DAMPER_VISCOUS. The detailed setting descriptions for different keywords can be found in LS-DYNA keyword user's manual.

```

$# LS-DYNA Keyword file
$# Created on Oct-02-2017 (09:50:55) by Siya Jin
*KEYWORD
*TITLE
Wave-PAWEC interaction with PTO
$# title
$# Unit mm-g-s
*CONTROL_TERMINATION
$# endtim   endcyc   dtmin   endeng   endmas
 24.000000   0       0.000   0.000   0.000
*CONTROL_TIMESTEP
$# dtinit   tssfacs   isdo    tslimt   dt2ms    lctm     erode    ms1st
  0.000   0.900000   0       0.000   0.000    0        0        0
$# dt2msf   dt2mslc   imsc1   unused   unused   rmscl
  0.000    0        0        0        0       0.000
*DATABASE_ABSTAT
$# dt       binary   lcur    ioopt
  0.000    0        0        1
*DATABASE_DEFORC
$# dt       binary   lcur    ioopt
  0.010000 0        0        1
*DATABASE_NODOUT
$# dt       binary   lcur    ioopt   dthf    binhf
  0.010000 0        0        1       0.000   0
*DATABASE_BINARY_D3PLOT
$# dt       lcdt    beam    npltc   psetid
  0.010000 0        0        0        0
$# ioopt
  0
*DATABASE_BINARY_D3THDT
$# dt       lcdt    beam    npltc   psetid
 24.000000 0        0        0        0
*DATABASE_FORMAT
$# iform    ibinary
  0        0
*DATABASE_EXTENT_BINARY
$# neiph    neips    maxint   strflg   sigflg   epsflg   rltflg   engflg
  0        0        3        1        1        1        1        1
$# cmpflg   ieverp    beamip   dcomp    shge     stssz    n3thdt   ialemat
  0        0        4        1        1        1        2        0
$# nintsld  pkp_sen   sclp     unused   msscl    therm    intout   nodout
  0        0       1.000000 0        0        0        OSTRESS  STRESS
$# dtdt     resplt
  0        0
*BOUNDARY_NON_REFLECTING
$# ssid    ad        as
  1       0.000   0.000

```

In LS-DYNA, the time step size roughly corresponds to the transient time of an acoustic wave through an element using the shortest characteristic distance.

$$\Delta t^{n+1} = tssfacs \times \min\{\Delta t_1, \Delta t_2, \dots, \Delta t_N\}$$

```

*BOUNDARY_PRESCRIBED_MOTION_SET
$#  nsid      dof      vad      lcid      sf      vid      death      birth
    3         11       2         2  1.000000    01.0000E+28  0.000
$#  offset1  offset2      mrb      node1     node2
0.0000      0.0000      0         0         0
*BOUNDARY_SPC_SET
$#  nsid      cid      dofz      dofry      dofz      dofz      dofry      dofz
    1         0         0         0         1         1         1         0
*BOUNDARY_SPC_SET
$#  nsid      cid      dofz      dofry      dofz      dofz      dofry      dofz
    2         0         1         1         1         1         1         1
*BOUNDARY_SPC_NODE
$#  nid      cid      dofz      dofry      dofz      dofz      dofry      dofz
  47760      0         1         1         1         1         1         1
*LOAD_BODY_Y
$#  lcid      sf      lciddr      xc      yc      zc      cid
    1  1.000000      0      0.000      0.000      0.000      0
*PART
$#  title Air
Part      1 for Mat      1 and Elem Type      1
$#  pid      secid      mid      eosid      hgid      grav      adpopt      tmid
    1         1         1         1         0         0         0         0
*SECTION_SOLID_ALE
$#  secid      elform      aet
    1         11         1
$#  afac      bfac      cfac      dfac      start      end      aafac
0.000      0.000      0.000      0.000      0.000      0.000      0.000
*MAT_NULL
$#  mid      ro      pc      mu      terod      cerod      ym      pr
    1  1.2560E-6      0.000  1.8100E-5      0.000      0.000      0.000      0.000
*EOS_GRUNEISEN
$#  eosid      c      s1      s2      s3      gamao      a      e0
    1  3.4400E+5      0.000      0.000      0.000      0.000000      0.000      0.000
$#  v0
    0.000
*PART
$#  title Water
Part      2 for Mat      2 and Elem Type      1
$#  pid      secid      mid      eosid      hgid      grav      adpopt      tmid
    2         2         2         2         0         0         0         0
*SECTION_SOLID_ALE
$#  secid      elform      aet
    2         11         1
$#  afac      bfac      cfac      dfac      start      end      aafac
0.000      0.000      0.000      0.000      0.000      0.000      0.000

```

```

*MAT_NULL
$# mid ro pc mu terod cerod ym pr
   2 0.001000-100.00000 8.9000E-4 0.000 0.000 0.000 0.000
*EOS_GRUNEISEN
$# eosid c s1 s2 s3 gamac a e0
   2 1.4800E+6 0.000 0.000 0.000 0.000 0.000 0.000
$# v0
   0.000
*PART
$# title Slope Beach
Part 3 for Mat 3 and Elem Type 1
$# pid secid mid eosid hgid grav adpopt tmid
   3 3 3 3 3 0 0 0
*SECTION_SOLID_ALE
$# secid elform aet
   3 11 1
$# afac bfac cfac dfac start end aafac
   0.000 0.000 0.000 0.000 0.000 0.000 0.000
*MAT_NULL
$# mid ro pc mu terod cerod ym pr
   3 0.001000-100.00000 8.9000E-4 0.000 0.000 0.000 0.000
*EOS_GRUNEISEN
$# eosid c s1 s2 s3 gamac a e0
   3 3.00E+6 0.000 0.000 0.000 0.000 0.000 0.000
$# v0
   0.000
*PART
$# title PAWEC
Part 1 for Mat 1 and Elem Type 1
$# pid secid mid eosid hgid grav adpopt tmid
   4 4 4 0 0 0 0
*SECTION_SOLID
$# secid elform aet
   4 1 0
*MAT_RIGID
$# mid ro e pr n couple m alias
   4 5.0000E-42.1000E+11 0.330000 0.000 0.000 0.000
$# cmo con1 con2
   0.000 0.000 0.000
$# lco or a1 a2 a3 v1 v2 v3
   0.000 0.000 0.000 0.000 0.000 0.000
*PART
$# title PTO
$# pid secid mid eosid hgid grav adpopt tmid
   9 9 9 0 0 0 0

```

```

*SECTION_DISCRETE
$#  secid      dro      kd      v0      c1      fd
    9          0      0.000    0.000    0.000    0.000
$#  cdl        tdl
    0.000      0.000
*MAT_DAMPER_VISCOUS
$#  mid      dc
    9 10000.0000
*SET_MULTI_MATERIAL_GROUP_LIST
$#  ammsid
    1
$#  ammgid1  ammgid2  ammgid3  ammgid4  ammgid5  ammgid6  ammgid7  ammgid8
    2          3          0          0          0          0          0          0
*ALE_MULTI-MATERIAL_GROUP
$#  sid      idtype  gpname
    1          1
    2          1
    3          1
*CONSTRAINED_EXTRA_NODES_NODE
$#  pid      nid
    4      47761
*CONSTRAINED_LAGRANGE_IN_SOLID
$#  slave  master  sstyp  mstyp  nquad  ctype  direc  mcoup
    4          1          1          0          2          4          2      -1
$#  start  end      pfac  fric  frcmin  norm  normtyp  damp
    0.0001.0000E+10 0.000  0.000  0.500000  0          0      0.000
$#  cq      hmin  hmax  ileak  pleak  lcidpor  nvent  blockage
    0.000  0.000  0.000  0      0.010000  0          0          0
$#  iboxid  ipenchk  intforc  ialesof  lagmul  pfacmm  thkf
    0          0          0          0          0.000  0          0.000
*ELEMENT_DISCRETE
$#  eid      pid      n1      n2      vid      s      pf      offset
    41876    9      47760  47761  0          1.000000  0          0.000
*ELEMENT_MASS
$#  eid      nid      mass      pid
    41875    47760  0.500000  0
    41876    47761  0.500000  0
*DEFINE_CURVE
$#  lcid      sidr      sfa      sfo      offa      offo      dattyp
    1          0      1.000000  1.000000  0.000  0.000  0
$#
    a1          o1
    0.000      9800.0000
    30.000000  9800.0000
*DEFINE_CURVE Curve No.2 is used to defined the angular displacement of the wave-maker.
$#  lcid      sidr      sfa      sfo      offa      offo      dattyp
    2          0      1.000000  1.000000  0.000  0.000  0
$#
    a1          o1
    0.000      0.000
    0.010000  0.006872

```

```
0.020000      0.013733
0.030000      0.020573
0.040000      0.027382
0.050000      0.034148
.
.
.
*NODE
$
*ELEMENT_SOLID
$
*END
```

Bibliography

- Abdelrahman, M., Patton, R., Guo, B., and Lan, J. (2016). Estimation of wave excitation force for wave energy converters. In *3rd SysTol*, pages 654–659. IEEE.
- Amann, K. U., Magaña, M. E., and Sawodny, O. (2015). Model predictive control of a nonlinear 2-body point absorber wave energy converter with estimated state feedback. *IEEE Trans. Sustain. Energy*, 6(2):336–345.
- Anbarsooz, M., Passandideh-Fard, M., and Moghiman, M. (2014). Numerical simulation of a submerged cylindrical wave energy converter. *Renew. Energy*, 64:132–143.
- Anderlini, E., Forehand, D. I., Bannon, E., and Abusara, M. (2017a). Control of a realistic wave energy converter model using least-squares policy iteration. *IEEE Trans. Sustain. Energy*, 8(4):1618–1628.
- Anderlini, E., Forehand, D. I., Bannon, E., and Abusara, M. (2017b). Reactive control of a wave energy converter using artificial neural networks. *International Journal of Marine Energy*, 19:207–220.
- Anderlini, E., Forehand, D. I., Stansell, P., Xiao, Q., and Abusara, M. (2016). Control of a point absorber using reinforcement learning. *IEEE Trans. Sustain. Energy*, 7(4):1681–1690.

- Antonio, F. d. O. (2010). Wave energy utilization: A review of the technologies. *Renew. Sust. Energy Rev.*, 14(3):899–918.
- Azadegan, A., Porobic, L., Ghazinoory, S., Samouei, P., and Kheirkhah, A. S. (2011). Fuzzy logic in manufacturing: A review of literature and a specialized application. *International Journal of Production Economics*, 132(2):258–270.
- Babarit, A. and Clément, A. H. (2006). Optimal latching control of a wave energy device in regular and irregular waves. *Appl. Ocean Res.*, 28(2):77–91.
- Babarit, A., Duclos, G., and Clément, A. H. (2004). Comparison of latching control strategies for a heaving wave energy device in random sea. *Appl. Ocean Res.*, 26(5):227–238.
- Badcock-Broe, A., Flynn, R., George, S., Gruet, R., and Medic, N. (2014). Wave and tidal energy market deployment strategy for europe. *SI Ocean*.
- Bakroon, M., Daryaei, R., Aubram, D., and Rackwitz, F. (2017). Arbitrary lagrangian-eulerian finite element formulations applied to geotechnical problems. *Numerical Methods in Geotechnics*, pages 33–44.
- Beatty, S. J., Hall, M., Buckham, B. J., Wild, P., and Bocking, B. (2015). Experimental and numerical comparisons of self-reacting point absorber wave energy converters in regular waves. *Ocean Eng.*, 104:370–386.
- Bhinder, M. A., Babarit, A., Gentaz, L., and Ferrant, P. (2015). Potential time domain model with viscous correction and cfd analysis of a generic surging floating wave energy converter. *Int. J. Mar. Energy*, 10:70–96.
- Boake, C. B., Whittaker, T. J., Folley, M., Ellen, H., et al. (2002). Overview and initial operational experience of the limpet wave energy plant. In *The Twelfth International Offshore and Polar Engineering Conference*. International Society of Offshore and Polar Engineers.

- Bouarroudj, N., Boukhetala, D., Djari, A., Rais, Y., and Benlahbib, B. (2017). Flc based gaussian membership functions tuned by pso and ga for mppt of photovoltaic system: A comparative study. In *Systems and Control (ICSC), 2017 6th International Conference on*, pages 317–322. IEEE.
- Brekken, T. K. (2011). On model predictive control for a point absorber wave energy converter. In *PowerTech, 2011 IEEE Trondheim*, pages 1–8. IEEE.
- Budal, K. (1981). Model experiment with a phase-controlled point absorber. In *2nd International Symposium on Wave and Tidal Energy, Cambridge, UK, 23-25 September 1981*, pages 191–206.
- Budal, K. and Falnes, J. (1982). Wave power conversion by point absorbers: a norwegian project. *International Journal of Ambient Energy*, 3(2):59–67.
- Budar, K. and Falnes, J. (1975). A resonant point absorber of ocean-wave power. *Nature*, 256(5517):478–479.
- Cameron, L., Doherty, R., Henry, A., Doherty, K., Van't Hoff, J., Kaye, D., Naylor, D., Bourdier, S., and Whittaker, T. (2010). Design of the next generation of the oyster wave energy converter. In *3rd international conference on ocean energy*, volume 6, page 1e12. Bilbao.
- Carnegie.
- Chatzigiannakou, M., Dolguntseva, I., and Leijon, M. (2017). Offshore deployments of wave energy converters by seabased industry ab. *Journal of Marine Science and Engineering*, 5(2):15.
- Chen, Z., Zhou, B., Zhang, L., Li, C., Zang, J., Zheng, X., Xu, J., and Zhang, W. (2018). Experimental and numerical study on a novel dual-resonance wave energy converter with a built-in power take-off system. *Energy*, 165:1008–1020.

- Chiba, S., Waki, M., Wada, T., Hirakawa, Y., Masuda, K., and Ikoma, T. (2013). Consistent ocean wave energy harvesting using electroactive polymer (dielectric elastomer) artificial muscle generators. *Appl. Energy*, 104:497–502.
- Clément, A., McCullen, P., Falcão, A., Fiorentino, A., Gardner, F., Hammarlund, K., Lemonis, G., Lewis, T., Nielsen, K., Petroncini, S., et al. (2002). Wave energy in europe: current status and perspectives. *Renew. Sust. Energy Rev.*, 6(5):405–431.
- Clerc, M. and Kennedy, J. (2002). The particle swarm-explosion, stability, and convergence in a multidimensional complex space. *IEEE Trans. Evolut. Comput.*, 6(1):58–73.
- Cretel, J. A., Lightbody, G., Thomas, G. P., and Lewis, A. W. (2011). Maximisation of energy capture by a wave-energy point absorber using model predictive control. In *18th IFAC*, pages 3714–3721.
- Crewe, M. (1990). The national meteorological library and archives. *State librarian*, 38(3):37–39.
- Cummins, W. (1962). The impulse response function and ship motions. Technical report, DTIC Document.
- Davidson, J., Cathelain, M., Guillemet, L., Le Huec, T., and Ringwood, J. (2015a). Implementation of an openfoam numerical wave tank for wave energy experiments. In *11th EWTEC*.
- Davidson, J., Giorgi, S., and Ringwood, J. V. (2015b). Linear parametric hydrodynamic models for ocean wave energy converters identified from numerical wave tank experiments. *Ocean Eng.*, 103:31–39.
- Davis, J. (1990). Wave energy absorption by the bristol cylinder-linear and non-linear effects. *P. I. Civil Eng.*, 89(3):317–340.

- De Backer, G. (2009). *Hydrodynamic design optimization of wave energy converters consisting of heaving point absorbers*. PhD thesis, Department of Civil Engineering, Ghent University: Ghent, Belgium.
- de Sousa Prado, M. G., Gardner, F., Damen, M., and Polinder, H. (2006). Modelling and test results of the archimedes wave swing. *Proceedings of the Institution of Mechanical Engineers, Part A: Journal of Power and Energy*, 220(8):855–868.
- Dean, R. G. and Dalrymple, R. A. (1991). *Water wave mechanics for engineers and scientists*, volume 2. World Scientific Publishing Co Inc.
- Debnath, S. B. C., Shill, P. C., and Murase, K. (2013). Particle swarm optimization based adaptive strategy for tuning of fuzzy logic controller. *International Journal of Artificial Intelligence & Applications*, 4(1):37.
- DelliColli, V., Cancelliere, P., Marignetti, F., DiStefano, R., and Scarano, M. (2006). A tubular-generator drive for wave energy conversion. *IEEE Trans. Ind. Electron.*, 53(4):1152–1159.
- Drew, B., Plummer, A. R., and Sahinkaya, M. N. (2009). A review of wave energy converter technology. *Proc. IMechE, Part A: J. Power and Energy*, 223:887–902.
- Eberhart, R. and Kennedy, J. (1995). A new optimizer using particle swarm theory. In *Micro Machine and Human Science, 1995. MHS'95., Proceedings of the Sixth International Symposium on*, pages 39–43. IEEE.
- Edenhofer, O., Pichs-Madruga, R., Sokona, Y., Seyboth, K., Matschoss, P., Kadner, S., Zwickel, T., Eickemeier, P., Hansen, G., Schlömer, S., et al. (2011). Ipcc special report on renewable energy sources and climate change mitigation. *Prepared By Working Group III of the Intergovernmental Panel on Climate Change, Cambridge University Press, Cambridge, UK*.

- Edwards, K., Mekhiche, M., et al. (2014). Ocean power technologies powerbuoy®: System-level design, development and validation methodology.
- EIA (2013). International energy statistics. Technical report.
- EMEC, E. M. E. C.
- Eriksson, M. (2007). *Modelling and experimental verification of direct drive wave energy conversion: Buoy-generator dynamics*. PhD thesis, Acta Universitatis Upsaliensis.
- Eriksson, M., Isberg, J., and Leijon, M. (2005). Hydrodynamic modelling of a direct drive wave energy converter. *Int. J. Eng. Sci.*, 43(17):1377–1387.
- Estefen, S. F., Castello, X., Lourenço, M. I., and Rossetto, R. M. (2010). Design analysis applied to a hyperbaric wave energy converter. In *Proceedings 11th International Symposium on Practical Design of Ships and Other Floating Structures*.
- Evans, D. (1981). Power from water waves. *Annu. Rev. Fluid Mech.*, 13(1):157–187.
- Falcão, A. F. and Henriques, J. C. (2016). Oscillating-water-column wave energy converters and air turbines: A review. *Renewable Energy*, 85:1391–1424.
- Falcão, A. F., Henriques, J. C., and Gato, L. M. (2018). Self-rectifying air turbines for wave energy conversion: a comparative analysis. *Renew. Sust. Energy Rev.*, 91:1231–1241.
- Falnes, J. (1995). On non-causal impulse response functions related to propagating water waves. *Appl. Ocean Res.*, 17(6):379–389.
- Falnes, J. (2002). *Ocean waves and oscillating systems: linear interactions including wave-energy extraction*. Cambridge university press.

- Falnes, J. (2007). A review of wave-energy extraction. *Mar. Struct.*, 20(4):185–201.
- Fang, G., Kwok, N. M., and Ha, Q. (2008). Automatic fuzzy membership function tuning using the particle swarm optimization. In *2008 IEEE Pacific-Asia Workshop on Computational Intelligence and Industrial Application*, volume 2, pages 324–328. IEEE.
- Finnegan, W. and Goggins, J. (2012). Numerical simulation of linear water waves and wave–structure interaction. *Ocean Eng.*, 43:23–31.
- Fleming, A. and Macfarlane, G. (2017). In-situ orifice calibration for reversing oscillating flow and improved performance prediction for oscillating water column model test experiments. *International journal of marine energy*, 17:147–155.
- Flocard, F. and Finnigan, T. (2012). Increasing power capture of a wave energy device by inertia adjustment. *Applied Ocean Research*, 34:126–134.
- Folley, M., Babarit, A., Child, B., Forehand, D., O’Boyle, L., Silverthorne, K., Spinneken, J., Stratigaki, V., and Troch, P. (2012). A review of numerical modelling of wave energy converter arrays. In *ASME 2012 31st International Conference on Ocean, Offshore and Arctic Engineering*, pages 535–545. American Society of Mechanical Engineers.
- Forehand, D. I., Kiprakis, A. E., Nambiar, A. J., and Wallace, A. R. (2016). A fully coupled wave-to-wire model of an array of wave energy converters. *IEEE Trans. Sustain. Energy*, 7(1):118–128.
- Fusco, F. and Ringwood, J. V. (2010). Short-term wave forecasting for real-time control of wave energy converters. *IEEE Trans. Sustain. Energy*, 1(2):99–106.
- Fusco, F. and Ringwood, J. V. (2013). A simple and effective real-time controller for wave energy converters. *IEEE Trans. Sustain. Energy*, 4(1):21–30.

- Gieske, P. (2007). Model predictive control of a wave energy converter: Archimedes wave swing.
- Goggins, J. and Finnegan, W. (2014). Shape optimisation of floating wave energy converters for a specified wave energy spectrum. *Renew. Energy*, 71:208–220.
- Götteman, M., Engström, J., Eriksson, M., Hann, M., Ransley, E., Greaves, D., Leijon, M., et al. (2015). Wave loads on a point-absorbing wave energy device in extreme waves. In *25th International Ocean and Polar Engineering Conference*. International Society of Offshore and Polar Engineers.
- Gradowski, M., Alves, M., Gomes, R. P., and Henriques, J. (2017). Integration of a hydrodynamic negative spring concept into the owc spar buoy. In *Proceedings of the 12th EWTEC, Aug.*
- Guo, B. (2017). *Study of scale modelling, verification and control of a heaving point absorber wave energy converter*. PhD thesis, School of Engineering and Computer Science, University of Hull: HULL, UK.
- Guo, B., Patton, R., Abdelrahman, M., and Lan, J. (2016). A continuous control approach to point absorber wave energy conversion. In *11th UKACC*, pages 1–6. IEEE.
- Guo, B., Patton, R., Jin, S., Gilbert, J., and Parsons, D. (2018a). Nonlinear modeling and verification of a heaving point absorber for wave energy conversion. *IEEE Trans. Sustain. Energy*, 9(1):453–461.
- Guo, B., Patton, R. J., Jin, S., and Lan, J. (2018b). Numerical and experimental studies of excitation force approximation for wave energy conversion. *Renew. Energy*, 125:877–889.
- Hager, R., Fernandez, N., and Teng, M. H. (2012). Experimental study seeking optimal geometry of a heaving body for improved power absorption efficiency. In

- The Twenty-second International Offshore and Polar Engineering Conference.*
International Society of Offshore and Polar Engineers.
- Hallquist, J. O. (2006). Ls-dyna theory manual. *Livermore software technology corporation*, 3:25–31.
- Hals, J., Falnes, J., and Moan, T. (2011a). A comparison of selected strategies for adaptive control of wave energy converters. *J. Offshore Mech. Arct. Eng.*, 133(3):031101.
- Hals, J., Falnes, J., and Moan, T. (2011b). Constrained optimal control of a heaving buoy wave-energy converter. *J. Offshore Mech. Arct. Eng.*, 133(1):011401.
- Hasselmann, K., Barnett, T., Bouws, E., Carlson, H., Cartwright, D., Enke, K., Ewing, J., Gienapp, H., Hasselmann, D., Kruseman, P., et al. (1973). Measurements of wind-wave growth and swell decay during the joint north sea wave project (jonswap). *Ergänzungsheft 8-12*.
- Heller, V., Chaplin, J., Farley, F., Hann, M., and Hearn, G. (2000). Physical model tests of the anaconda wave energy converter. In *Proc. 1st IAHR European Congress*.
- Henderson, R. (2006). Design, simulation, and testing of a novel hydraulic power take-off system for the pelamis wave energy converter. *Renew. Energy*, 31(2):271–283.
- Henriques, J., Gato, L., Lemos, J., Gomes, R., and Falcão, A. (2016a). Peak-power control of a grid-integrated oscillating water column wave energy converter. *Energy*, 109:378–390.
- Henriques, J., Portillo, J., Gato, L., Gomes, R., Ferreira, D., and Falcão, A. (2016b). Design of oscillating-water-column wave energy converters with an application to self-powered sensor buoys. *Energy*, 112:852–867.

- IEA (2016). Ocean potential. Technical report.
- Jin, S., Guo, B., Patton, R., Gilbert, J., and Abdelrahman, M. (2016). Non-linear analysis of a point absorber wave energy converter. In *International Conference on Offshore Renewable Energy*.
- Jin, S. and Patton, R. (2017). Geometry influence on hydrodynamic response of a heaving point absorber wave energy converter. In *12th EWTEC*.
- Jin, S., Patton, R. J., and Guo, B. (2018). Viscosity effect on a point absorber wave energy converter hydrodynamics validated by simulation and experiment. *Renew. Energy*.
- Journée, J. and Massie, W. (2000). *Offshore hydromechanics*. TU Delft.
- Journée, J. M. and Massie, W. (2001). Offshore hydrodynamics. *Delft University of Technology*, 4:38.
- Kofoed, J. P., Frigaard, P., Friis-Madsen, E., and Sørensen, H. C. (2006). Prototype testing of the wave energy converter wave dragon. *Renew. Energy*, 31(2):181–189.
- Kramer, M., Marquis, L., and Frigaard, P. (2011). Performance evaluation of the wavestar prototype. In *9th EWTEC*. Citeseer.
- Lawson, M., Yu, Y.-H., Nelessen, A., Ruehl, K., and Michelen, C. (2014). Implementing nonlinear buoyancy and excitation forces in the wec-sim wave energy converter modeling tool. In *33rd International Conference on Ocean, Offshore and Arctic Engineering*.
- Lee, C.-C. (1990). Fuzzy logic in control systems: fuzzy logic controller. ii. *IEEE Transactions on systems, man, and cybernetics*, 20(2):419–435.

- Leirbukt, A. and Tubaas, P. (2006). A wave of renewable energy. *ABB Review*, (3):29.
- Li, Y. and Yu, Y.-H. (2012). A synthesis of numerical methods for modeling wave energy converter-point absorbers. *Renew. Sust. Energy Rev.*, 16(6):4352–4364.
- Lopes, M., Hals, J., Gomes, R., Moan, T., Gato, L., and Falcão, A. d. O. (2009). Experimental and numerical investigation of non-predictive phase-control strategies for a point-absorbing wave energy converter. *Ocean Eng.*, 36(5):386–402.
- López, I., Andreu, J., Ceballos, S., de Alegría, I. M., and Kortabarria, I. (2013). Review of wave energy technologies and the necessary power-equipment. *Renew. Sust. Energy Rev.*, 27:413–434.
- López, M., Taveira-Pinto, F., and Rosa-Santos, P. (2017). Influence of the power take-off characteristics on the performance of ceco wave energy converter. *Energy*, 120:686–697.
- Lou, J. (2017). *Numerical Simulation, Laboratory and Field Experiments, Analysis and Design of Wave Energy Converter and Mooring System*. PhD thesis, Civil Engineering, Oregon State University: Corvallis, USA.
- Madhi, F., Sinclair, M. E., and Yeung, R. W. (2014). The berkeley wedge: an asymmetrical energy-capturing floating breakwater of high performance. *Marine Systems & Ocean Technology, Journal of SOBENA*, 9(1):05–16.
- Marquis, L., Kramer, M., and Frigaard, P. (2010). First power production figures from the wave star roshage wave energy converter. In *3rd International Conference and Exhibition on Ocean Energy*. ICOE 2010.
- McCabe, A. (2013). Constrained optimization of the shape of a wave energy collector by genetic algorithm. *Renew. Energy*, 51:274–284.

- McCabe, A., Aggidis, G., and Widden, M. (2010). Optimizing the shape of a surge-and-pitch wave energy collector using a genetic algorithm. *Renew. Energy*, 35(12):2767–2775.
- McCormick, M. E. (2013). *Ocean wave energy conversion*. Courier Corporation.
- Messai, A., Mellit, A., Guessoum, A., and Kalogirou, S. (2011). Maximum power point tracking using a ga optimized fuzzy logic controller and its fpga implementation. *Solar energy*, 85(2):265–277.
- Morison, J., Johnson, J., Schaaf, S., et al. (1950). The force exerted by surface waves on piles. *JPT*, 2(05):149–154.
- Moskowitz, L. (1964). Estimates of the power spectrums for fully developed seas for wind speeds of 20 to 40 knots. *Journal of geophysical research*, 69(24):5161–5179.
- Nicolas, A. (2007). Ale modeling of surface waves. In *6th European LS-DYNA Users’ Conference*, pages 9–20.
- Ochi, M. K. and Hubble, E. N. (1977). Six-parameter wave spectra. In *Coastal Engineering 1976*, pages 301–328.
- OES (2013). Implementing agreement on ocean energy systems. Technical report.
- OES (2014a). Development of recommended practices for testing and evaluating ocean energy system. Technical report.
- OES (2014b). Ocean energy systems annual report 2014. Technical report.
- Ogilvie, T. F. (1964). Recent progress toward the understanding and prediction of ship motions. In *5th Symposium on naval hydrodynamics*, volume 1, pages 2–5. Bergen, Norway.

- OSU (2013). A primer on wave energy wave energy devices. Technical report.
- Park, J.-C., Kim, M.-H., and Miyata, H. (1999). Fully non-linear free-surface simulations by a 3d viscous numerical wave tank. *Int. J. Nume. Meth. Fl.*, 29(6):685–703.
- Pecher, A. and Kofoed, J. P. (2017). *Handbook of ocean wave energy*. Springer.
- Pecher, A., Kofoed, J. P., Espedal, J., Hagberg, S., et al. (2010). Results of an experimental study of the langlee wave energy converter. In *The Twentieth International Offshore and Polar Engineering Conference*. International Society of Offshore and Polar Engineers.
- Penalba, M., Giorgi, G., and Ringwood, J. V. (2017). Mathematical modelling of wave energy converters: a review of nonlinear approaches. *Renew. Sust. Energy Rev.*, 78:1188–1207.
- Pierson Jr, W. J. and Moskowitz, L. (1964). A proposed spectral form for fully developed wind seas based on the similarity theory of sa kitaigorodskii. *Journal of geophysical research*, 69(24):5181–5190.
- Ransley, E., Greaves, D., Raby, A., Simmonds, D., and Hann, M. (2017). Survivability of wave energy converters using cfd. *Renew. Energy*, 109:235–247.
- Rhinefrank, K., Schacher, A., Prudell, J., Stillinger, C., Naviaux, D., Brekken, T., Von Jouanne, A., Newborn, D., Yim, S., and Cox, D. (2010). High resolution wave tank testing of scaled wave energy devices. In *ASME 2010 29th International Conference on Ocean, Offshore and Arctic Engineering*, pages 505–509. American Society of Mechanical Engineers.
- Ringwood, J. V., Bacelli, G., and Fusco, F. (2014). Energy-maximizing control of wave-energy converters: The development of control system technology to optimize their operation. *IEEE Control Syst. Mag.*, 34(5):30–55.

- Salter, S. H. (1974). Wave power. *Nature*, 249(5459):720–724.
- Schoen, M. P., Hals, J., and Moan, T. (2011). Wave prediction and robust control of heaving wave energy devices for irregular waves. *IEEE Trans. Sustain. Energy*, 26(2):627–638.
- Sheng, W., Alcorn, R., and Lewis, A. (2015). On improving wave energy conversion, part i: Optimal and control technologies. *Renew. Energy*, 75:922–934.
- Simonetti, I., Cappiotti, L., Elsafti, H., and Oumeraci, H. (2017). Optimization of the geometry and the turbine induced damping for fixed detached and asymmetric owc devices: A numerical study. *Energy*, 139:1197–1209.
- Sjolte, J., Tjensvoll, G., and Molinas, M. (2013). Power collection from wave energy farms. *Applied Sciences*, 3(2):420–436.
- Son, D., Belissen, V., and Yeung, R. W. (2016). Performance validation and optimization of a dual coaxial-cylinder ocean-wave energy extractor. *Renew. Energy*, 92:192–201.
- Son, D. and Yeung, R. W. (2017). Optimizing ocean-wave energy extraction of a dual coaxial-cylinder wec using nonlinear model predictive control. *Appl. Energy*, 187:746–757.
- Souli, M. and Benson, D. J. (2013). *Arbitrary Lagrangian Eulerian and fluid-structure interaction: numerical simulation*. John Wiley & Sons.
- StringRAY, C. P. t.
- Taghipour, R., Perez, T., and Moan, T. (2008). Hybrid frequency–time domain models for dynamic response analysis of marine structures. *Ocean Eng.*, 35(7):685–705.

- Teillant, B., Debruyne, Y., Sarmiento, A., Gomes, R., Gato, L., Fontana, M., Philippe, M., and Combourieu, A. (2016). Integration of breakthrough concepts into the owc spar buoy. In *Progress in Renewable Energies Offshore: Proceedings of the 2nd International Conference on Renewable Energies Offshore, Lisbon, Portugal, 24-26 October 2016*, page 351. CRC Press.
- Thomas, S., Giassi, M., Göteman, M., Hann, M., Ransley, E., Isberg, J., and Engström, J. (2018). Performance of a direct-driven wave energy point absorber with high inertia rotatory power take-off. *Energies*, 11(9):2332.
- Tom, N. and Yeung, R. W. (2013). Performance enhancements and validations of a generic ocean-wave energy extractor. *J. Offshore Mech. Arct. Eng.*, 135(4):041101.
- Ursell, F., Dean, R. G., and Yu, Y. (1960). Forced small-amplitude water waves: a comparison of theory and experiment. *J. Fluid Mech.*, 7(01):33–52.
- Vantorre, M., Banasiak, R., and Verhoeven, R. (2004). Modelling of hydraulic performance and wave energy extraction by a point absorber in heave. *Appl. Ocean Res.*, 26(1):61–72.
- Washio, Y., Osawa, H., Nagata, Y., Fujii, F., Furuyama, H., Fujita, T., et al. (2000). The offshore floating type wave power device" mighty whale": open sea tests. In *The Tenth International Offshore and Polar Engineering Conference*. International Society of Offshore and Polar Engineers.
- WaveRoller, A. E.
- Weber, J., Mouwen, F., Parish, A., and Robertson, D. (2009). Wavebob—research & development network and tools in the context of systems engineering. In *8th EWTEC*.
- Wello.

- Whittaker, T., Collier, D., Folley, M., Osterried, M., Henry, A., and Crowley, M. (2007). The development of oyster—a shallow water surging wave energy converter. In *7th EWTEC*, pages 11–14. Porto, Portugal.
- Yeung, R. and Sphaier, S. (1989). Wave-interference effects on a truncated cylinder in a channel. *J. Eng. Math.*, 23(2):95–117.
- Yeung, R. W. and Jiang, Y. (2011). Effects of shaping on viscous damping and motion of heaving cylinders. In *30th International Conference on Ocean, Offshore and Arctic Engineering*, pages 825–836.
- Yeung, R. W., Peiffer, A., Tom, N., and Matlak, T. (2012). Design, analysis, and evaluation of the uc-berkeley wave-energy extractor. *J. Offshore Mech. Arct. Eng.*, 134(2):021902.
- Yeylaghi, S., Buckham, B., Moa, B., Oshkai, P., Beatty, S., and Crawford, C. (2015). Sph modeling of hydrodynamic loads on a point absorber wave energy converter hull. In *15th EWTEC*.
- Yu, Y., Lawson, M., Li, Y., Previsic, M., Epler, J., and Lou, J. (2015). Experimental wave tank test for reference model 3 floating-point absorber wave energy converter project. Technical report, National Renewable Energy Lab.(NREL), Golden, CO (United States).
- Yu, Y.-H. and Li, Y. (2013). Reynolds-averaged navier–stokes simulation of the heave performance of a two-body floating-point absorber wave energy system. *Computers & Fluids*, 73:104–114.
- Yu, Z. and Falnes, J. (1995). State-space modelling of a vertical cylinder in heave. *Appl. Ocean Res.*, 17(5):265–275.

- Zang, Z., Zhang, Q., Qi, Y., and Fu, X. (2018). Hydrodynamic responses and efficiency analyses of a heaving-buoy wave energy converter with pto damping in regular and irregular waves. *Renew. Energy*, 116:527–542.